

AD-A254 348



2

PL-TR-92-2069

REGIONAL SEISMOGRAMS: ATTENUATION AND SCATTERING.

M. Nafi Toksöz
Edmond E. Charrette III
Ningya Cheng
Anton M. Dainty
Batakrishna Mandal
Chengbin Peng
Craig A. Schultz

Earth Resources Laboratory
Department of Earth, Atmospheric, and
Planetary Sciences
Massachusetts Institute of Technology
Cambridge, Massachusetts 02139

6 March 1992

DTIC
ELECTE
JUL 30 1992
S. D

Final Report
1 July 1989—31 December 1991

APPROVED FOR PUBLIC RELEASE; DISTRIBUTION UNLIMITED



PHILLIPS LABORATORY
AIR FORCE SYSTEMS COMMAND
HANSCOM AIR FORCE BASE, MA 01731-5000

92 7 28 049

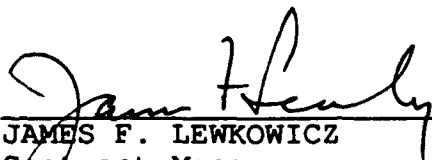
92-20406

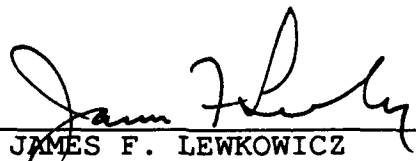
SPONSORED BY
Defense Advanced Research Projects Agency
Nuclear Monitoring Research Office
ARPA ORDER NO. 5307


MONITORED BY
Phillips Laboratory
Contract F19628-89-K-0020

The views and conclusions contained in this document are those of the authors and should not be interpreted as representing the official policies, either expressed or implied, of the Defense Advanced Research Projects Agency or the U.S. Government.

This technical report has been reviewed and is approved for publication.


JAMES F. LEWKOWICZ
Contract Manager
Solid Earth Geophysics Branch
Earth Sciences Division


JAMES F. LEWKOWICZ
Branch Chief
Solid Earth Geophysics Branch
Earth Sciences Division


DONALD H. ECKHARDT, Director
Earth Sciences Division

This report has been reviewed by the ESD Public Affairs Office (PA) and is releasable to the National Technical Information Service (NTIS).

Qualified requestors may obtain additional copies from the Defense Technical Information Center. All others should apply to the National Technical Information Service.

If your address has changed, or if you wish to be removed from the mailing list, or if the addressee is no longer employed by your organization, please notify PL/IMA, Hanscom AFB, MA 01731-5000. This will assist us in maintaining a current mailing list.

Do not return copies of this report unless contractual obligations or notices on a specific document requires that it be returned.

REPORT DOCUMENTATION PAGE			Form Approved OMB No. 0704-0188	
<small>Public reporting burden for this report is estimated to average 1 hour per response, including the time for reviewing instructions, searching existing data sources, gathering and maintaining the data needed, completing and reviewing the collection of information, sending comments regarding this burden estimate or any other aspect of the collection of information, including suggestions for reducing the burden. Send comments to Washington Headquarters Services, Directorate for Information Operations and Reports, 1215 Jefferson Davis Highway, Suite 1204, Arlington, VA 22202-4302, and to the Office of Management and Budget, Paperwork Reduction Project (0704-0188), Washington, DC 20503.</small>				
1. AGENCY USE ONLY (Leave blank)		2. REPORT DATE 6 MAR 1992		3. REPORT TYPE AND DATES COVERED Final Technical 1 JULY 89-31 DEC 91
4. TITLE AND SUBTITLE Regional Seismograms: Attenuation and Scattering			5. FUNDING NUMBERS F19628-89-K-0020 PE 62714E PR 9A10 TADA WU AR	
6. AUTHOR(S) M.N. Toksöz, E.E. Charrette, N. Cheng, A.M. Dainty, B. Mandal, C. Peng, C.A. Schultz				
7. PERFORMING ORGANIZATION NAME(S) AND ADDRESS(ES) Earth Resources Laboratory, Dept. of Earth, Atmospheric, and Planetary Sciences, Massachusetts Institute of Technology, 77 Massachusetts Ave., Cambridge, MA 02139			8. PERFORMING ORGANIZATION REPORT NUMBER 72237	
9. SPONSORING/MONITORING AGENCY NAME(S) AND ADDRESS(ES) Phillips Laboratory Hanscom AFB, MA 01731-5000 Contract Manager: James Lewkowicz/GPEH			10. SPONSORING/MONITORING AGENCY REPORT NUMBER PL-TR-92-2069	
11. SUPPLEMENTARY NOTES				
12a. DISTRIBUTION/AVAILABILITY STATEMENT Approved for Public Release; Distribution Unlimited			12b. DISTRIBUTION CODE	
13. ABSTRACT (Maximum 200 words) The objective of this study was to examine the influence of attenuation and scattering on regional high frequency seismograms. This final report consists of a Ph.D. thesis, a paper, and three preprints of papers either submitted or in preparation, on work supported by this project; they include both basic work on attenuation, scattering and anisotropy, and applications to regional seismograms. The Ph.D. thesis discusses the application of the finite difference method to problems in scattering and attenuation due to scattering in a random medium. In the first three chapters of the thesis, the application of Born theory to scattering and scattering attenuation is assessed. The fourth chapter applies two-dimensional finite difference calculations to explain the observed scattering phenomena at the NORSAR and NORESS arrays in Norway. The second section is a paper that examines the radiation pattern of explosive sources in anisotropic media. The third section evaluates the problem of Lg blockage across crustal extension zones by the method of coupled modes. The fourth section is concerned with the fundamental problem of scattering of the reflected wave from a rough interface. The final section applies transport theory to Rg data from a U.S. Geological Survey experiment in Maine.				
14. SUBJECT TERMS Scattering, Attenuation, Finite Difference, Lg, Rough Interfaces, Coda Modelling			15. NUMBER OF PAGES 364	
			16. PRICE CODE	
17. SECURITY CLASSIFICATION OF REPORT UNCLASSIFIED	18. SECURITY CLASSIFICATION OF THIS PAGE UNCLASSIFIED	19. SECURITY CLASSIFICATION OF ABSTRACT UNCLASSIFIED	20. LIMITATION OF ABSTRACT SAR	

Table of Contents

Preface	v
List of Contributing Scientists	vii
List of Previous Related Contracts	vii
Bibliography of Publications Sponsored by Contract	viii
"Elastic Wave Scattering in Laterally Inhomogeneous Media"	
by E.E. Charrette III	1
"Effects of an Explosive Source in an Anisotropic Medium"	
by B. Mandal and M.N. Toksöz	224
"An Analysis of the Nature and Attenuation of Lg Waves"	
by N. Cheng and M.N. Toksöz	232
"Reflections from a Randomly Grooved Interface: Ultrasonic Modeling and Finite-Difference Calculation"	
by C.A. Schultz and M.N. Toksöz	284
"Synthetic Coda Wave Modeling and Separation of Scattering Effect from Intrinsic Attenuation"	
by C. Peng, A.M. Dainty and M.N. Toksöz	320

Accession For	
NTIS GRA&I	<input checked="" type="checkbox"/>
DTIC TAB	<input type="checkbox"/>
Unannounced	<input type="checkbox"/>
Justification	
By	
Distribution/	
Availability Codes	
Dist	Avail and/or Special
A-1	

Preface

The objective of this study was to examine the influence of attenuation and scattering on regional high frequency seismograms. This is a wide-ranging topic because of deficiencies in our knowledge of basic aspects of attenuation and scattering, complicating attempts to assess their effects on regional seismograms. This final report consists of a Ph.D. Thesis, a paper, and three preprints of papers either submitted or in preparation, on work supported by this project. Each of these five publications forms a section in this report; they include both basic work on attenuation and scattering, and applications to regional seismograms. In addition, preliminary work on the problem of the radiation from an explosive source in an anisotropic medium was performed *under this contract*.

The first section is E.E. Charrette's Ph.D thesis and discusses the application of the finite difference method to problems in scattering and attenuation due to scattering in a random medium. In the first three chapters of the thesis, the basic issue of the application of Born theory, widely used in seismology, to scattering and scattering attenuation is assessed. A method of incorporating Born theory into the finite difference formalism is used to accomplish this. Results indicate that the failure of Born theory to remove energy from the incident wave is often the greatest inaccuracy resulting from this theory. The fourth chapter applies two-dimensional finite difference calculations to explain the observed scattering phenomena at the NORSAR and NORESS arrays in Norway. Although these calculations are two-dimensional, they examine all of the aspects of scattering—amplitude and travel time fluctuations of the

first arrival, coda level, and coherency of the first arrival and coda. This is the first time all of these aspects have been considered together.

The remaining sections of the report are papers, either published or preprints. The second section discusses the radiation pattern of explosive sources in anisotropic media. In such a situation, both SV and SH waves may be generated, and the radiation pattern for S waves may look like that of an earthquake. If the source is near the surface in a layered medium, both Raleigh and Love surface waves may be produced, including Lg-like phases. This work is now being continued under a separate contract. The third section examines the problem of Lg blockage across crustal extension zones by the method of coupled modes. The calculations indicate that this blockage may occur due solely to the geometrical effects of the crustal thinning; attenuation in sedimentary basins is not necessary. The fourth section is concerned with the fundamental problem of scattering of the reflected wave from a rough interface. The subject is treated both experimentally in water tank experiments and theoretically by finite difference for the case of randomly spaced parallel grooves. The presence of the grooves has a strong effect on the refracted wave and hence its interaction with the reflected wave near the critical angle. The grooves can also affect the reflected wave by producing amplitude fluctuations and coda. The final section applies transport theory to Rg data from a U.S. Geological Survey experiment in Maine. The purpose is to determine the attenuation mechanism for these waves. In this area, attenuation due to anelastic mechanisms and/or scattering to body waves dominates over Rg to Rg scattering.

List of Contributing Scientists

Edmond E. Charrette III, Graduate Research Assistant, Massachusetts Institute of Technology

• Anton M. Dainty, Founding Member Fellow, Massachusetts Institute of Technology

Batakrishna Mandal, Research Scientist, Massachusetts Institute of Technology

• Ningya Cheng, Graduate Research Assistant, Massachusetts Institute of Technology

Chengbin Peng, Graduate Research Assistant, Massachusetts Institute of Technology

Craig A. Schultz, Graduate Research Assistant, Massachusetts Institute of Technology

M. Nafi Toksöz, Professor of Geophysics, Massachusetts Institute of Technology

List of Previous and Related Contracts

DARPA/AFGL Contract F19628-86-K-0004 "Influence of Scattering on Seismic Waves", February 1986 to January 1988.

• DARPA/AFGL Contract F19628-87-K-0054 "Analysis of Regional Phases Using Three-Component Data", August 1987 to August 1989.

• DARPA/GL Contract F19628-88-K-0036 "Seismic Wave Propagation, Attenuation and Scattering over Regional Distances", August 1988 to July 1989.

GL Contract F19628-90-K-0057 "Research in Regional Seismology: The Effect of Anisotropy", April 1991 to March 1993.

DARPA/PL Contract F29601-91-K-DB15 "Research on Monitoring at Regional Distances",
September 1991 to September 1993.

Bibliography of Publications Totally or Partially Sponsored by the Contract

Toksöz, M.N., N. Cheng, A.M. Dainty and B. Mandal, 1990. Regional seismograms: attenuation, scattering and anisotropy. *Papers Presented at 12th Ann. DARPA/GL Seismic Res. Symp.*, 166-176.

Charrette, III, E.E., 1991. *Elastic Wave Scattering in Laterally Inhomogeneous Media*. Ph.D. Thesis, Massachusetts Institute of Technology.

Toksöz, M.N., A.M. Dainty, B. Mandal, N. Cheng, E.E. Charrette and C.A. Schultz, 1991. Regional seismograms: attenuation and scattering. *Papers Presented at 13th Ann. PL/DARPA Seismic Res. Symp.*, 453-460.

Mandal, B., and M.N. Toksöz, 1991. Effects of an explosive source in an anisotropic medium. *Explosion Source Phenomenology*, S.R. Taylor, H.J. Patton, P.G. Richards eds., Am. Geophys. Un. Geophys. Mon. 65, pp. 261-268.

Cheng, N., and M.N. Toksöz, 1992. An analysis of the nature and attenuation of Lg waves. *Submitted to Geophys. J. Int.*

Schultz, C.A., and M.N. Toksöz, 1992. Reflections from a randomly grooved interface: ultrasonic modeling and finite-difference calculation. *Submitted to J. Acous. Soc. Am.*

Peng, C., A.M. Dainty and M.N. Toksöz, 1992. Synthetic coda wave modeling and separation of scattering effect from intrinsic attenuation. *In preparation for PAGEOPH.*

Elastic Wave Scattering in Laterally Inhomogeneous Media

by

Edmond E. Charrette, III

B.S., University of Colorado (1983)

Submitted to the Department of Earth, Atmospheric, and Planetary
Sciences

in partial fulfillment of the requirements for the degree of

Doctor of Philosophy

at the

MASSACHUSETTS INSTITUTE OF TECHNOLOGY

January 1991

© Massachusetts Institute of Technology 1991

All rights reserved

Signature of Author

Department of Earth, Atmospheric, and Planetary Sciences

Jan 28, 1991

Certified by

M. Nafi Toksöz

Director, Earth Resources Laboratory

Thesis Supervisor

Accepted by

Thomas H. Jordan

Chairman

Department of Earth, Atmospheric, and Planetary Sciences

Elastic Wave Scattering in Laterally Inhomogeneous Media

by

Edmond E. Charrette, III

Submitted to the Department of Earth, Atmospheric, and Planetary Sciences
on Jan 28, 1991, in partial fulfillment of the
requirements for the degree of
Doctor of Philosophy

Abstract

The earth is often modeled as a series of simple homogeneous layers. Such an approach can lead to synthetic seismograms which match the dominant arrivals in the field data very well, but lack the random travel time and amplitude fluctuations and signal generated noise commonly observed on seismic recordings. These secondary features are often due to scattering from small-scale variations in the earth. The small-scale variations are too numerous and distributed too irregularly to allow deterministic characterization, so these features are often characterized by their statistical distribution. This thesis is concerned with modeling elastic waves in randomly heterogeneous media

We first explore the general principles and assumptions concerning statistical characterization and introduce several commonly used statistical models. Both analytical and numerical techniques have been applied to this problem. Most analytical techniques assume scattering is weak and use the Born or Rytov approximation to generate relatively simple closed form solutions. These solutions can be limiting in some applications because they neglect the effects of multiple scattering, and assume the incident wave travels through a smooth background medium. In the random media studied here, it is shown that these assumptions can cause serious errors in the amplitude and phase of the scattered wavefield. In order to investigate these errors, a new numerical technique is developed. The technique starts with the elastodynamic equation of motion. Using the Born approximation and perturbation analysis, the elastic wave equation is reduced to a single scattering wave equation which can be solved with finite differences. The utility of the new technique is that both the single and multiple scattering (as calculated by conventional finite difference techniques) solutions can be generated for the same complex velocity model. In Chapter 3, this is done for two different random media. The first is an impedance scattering medium; a medium which has impedance variations, but no velocity variations. In such a medium, the dominant scattering mechanism is back scattering and the efficiency with which energy is scattered varies inversely with the size of the heterogeneity. In this

medium, the two solutions (single and multiple scattering) agreed well, except around the first arrival. Near the first arrival, the amplitude of the single scattering solution is consistently greater than the multiple scattering solution. This is a consequence of the Born approximation, which does not account for the removal of energy in the incident wave due to scattering. The general shape and arrival time of the scattered field is consistent with the multiple scattering solution.

In the second model, the material properties were chosen so that the medium contained significant velocity anomalies, but almost no impedance anomalies. Because scattering is stronger in this medium, agreement between the two solutions is not as good as the previous case. Again, the single scattering solution had too much energy in the first arrival, which in turn lead to an overestimated scattered field. Unlike the previous example, the velocity anomalies also created significant travel time differences between the two solutions. These errors were present in both the scattered and incident waves and occurred because the Born approximation assumes the incident wave travels in the background field (which is often assumed to be homogeneous).

It is generally agreed that the Earth's crust and lithosphere have heterogeneities. However, the distribution and exact nature of these heterogeneities have not yet been resolved. Using the techniques presented in this thesis and data from the NORSAR and NORESS arrays we develop a model for the statistical heterogeneities present under Fennoscandia. In the course of choosing the final model, we investigated many randomly heterogeneous models. We began with a simple, single layered model with a Gaussian autocorrelation function. We also considered other single layered models with more roughness, like that proposed by Frankel and Clayton (1986), as well as multi-layered models like that proposed by Flatté and Wu (1988). Based on coherency measurements and travel time and amplitude fluctuations, we propose that the random velocity variations in the lithosphere can be modeled by as a three layered random medium. Satisfactory results were obtained when the power spectrum of the fluctuations in the uppermost layer (0–3 km) was a bandlimited white spectrum ($0.05 \text{ km}^{-1} \leq |\underline{k}| \leq 1.1 \text{ km}^{-1}$, where \underline{k} is the wavenumber vector) and the rms velocity variation was 2%. The middle layer was meant to simulate the remaining portion of the crust (3–35 km) and the fluctuations in this layer were described by the 0th order von Kármán function. The correlation length of the von Kármán function was 10 km and there was 3% rms variation in velocity. The third layer extended from the base of the crust to a depth of 250 km and was characterized by an anisotropic Gaussian correlation function. The horizontal and vertical correlation lengths in this region were 20 km and 5 km, respectively and there was 2% rms variation in velocity.

Thesis Supervisor: M. Nafi Toksöz

Title: Director, Earth Resources Laboratory

Acknowledgments

This thesis directly and indirectly reflects the work of many authors. I say this not to share the blame for its weaknesses, but instead to acknowledging the people who helped me to develop, test, and clarify the ideas present here. In particular I would like to thank Chris "dude" Bradley, Richard Coates, Vern Cormier, Anton Dainty, Joe Matarese, Jeff Meredith, Mike Prange, Bill Rodi and most of all my advisor Nafi Toksöz. A special thanks goes to Bob Cicerone and Sue Turbak who helped me greatly by offering to finish several last minute changes so that I could spend a week skiing with friends in Jackson Hole.

Much of the work done in this thesis was computationally intensive. For this reason, I would like to thank the nCUBE Corporation their generous educational discount on a 128 node parallel processor. Although the machine was installed only six months ago, I was able to use it for all of the simulations in Chapter 4. The speed and flexibility of the machine allowed me to use the finite difference technique to simulate wave propagation in the lithospheric, something I couldn't have done with a VAX 8800. I would also like to acknowledge financial support from the Defense Advanced Research Projects Agency who funded the work in Chapters 1-3 through contract F19628-89-K-0020 administered by the the Air Force Geophysics Laboratory (AFGL) and the Reservoir Delineation Group at ERL.

It is easy to forget (I know I sometimes did) that there is more to life than reading articles, writing papers, and programming computers. I would like to thank my wife, Annie, for doing her best to provide balance in my life. I know it wasn't easy. I would also like to thank my parents, who watched me get into lots of tight spots, but always seemed to know when to step in and when to let me dig myself out. I benefitted greatly from learning how to do my own "spin control" and even more by knowing they were always there.

Lastly, I would like to thank my maternal grandfather. Gramps lived with my family during most of my childhood and had a profound affect on my life. Among other things, he taught me how to combine a pile of unrelated components into a servicable widget. I know he would have been proud to see how far his teachings have gotten me.

Contents

1	Introduction	8
1.1	Thesis Objectives	8
1.2	Large-Scale Variations	9
1.3	Characterization of Small-Scale Variations	10
1.4	Characterization of the Scattered Field	11
1.5	Wave Propagation in Random Media	12
1.5.1	Statistical Modeling	12
1.5.2	Deterministic Modeling	14
1.6	Thesis Plan	14
2	Seismic Velocities as Random Fields	18
2.1	Introduction	18
2.2	Seismic Velocities as Random Fields	19
2.2.1	Decomposition of the Velocity Field	19
2.2.2	General properties of a Random Field	20
2.3	Commonly Used Autocorrelation Functions	24
2.4	Conclusions	31
3	Scattering in Random Media	34
3.1	Introduction	34
3.2	Single Scattering	36

3.2.1	Theory	36
3.2.2	Limitations of the Born Approximation	38
3.2.3	Numerical Implementation	39
3.2.4	Validation of the Single Scattering Solution	42
3.3	Single vs Multiple Scattering: A Case Study	49
3.3.1	Attenuation and Coda	68
3.4	Overview of the Scattering Process	76
3.5	FK Analysis	81
3.6	Conclusions	84
4	Elastic Wave Scattering Below NORSAR	88
4.1	Introduction	88
4.2	Scattering Beneath NORSAR	90
4.2.1	Tectonic and Geophysical Setting	93
4.3	Scattering at NORSAR	97
4.3.1	Travel time and Amplitude Variations	97
4.3.2	Transverse Coherency (NORSAR)	104
4.4	The Coda	114
4.5	Forward Modeling in Random Media	116
4.5.1	Finite Difference Simulations	118
4.6	An Improved Random Lithospheric Model	141
4.7	Conclusions	153
5	Summary and Conclusions	155
5.1	Overview	155
5.2	Summary	157
A	Born Scattering	171
A.1	Introduction	171
A.2	The Born Approximation and Single Scattering	172

A.2.1	Plane P-Wave Source	174
A.2.2	Plane S-Wave Source	182
A.3	Mie Scattering in a Weakly Heterogeneous Media	187
A.3.1	Mie Scattering from a Gaussian Inclusion	192
A.3.2	Gaussian Parameter Function	192
A.3.3	Exponential Parameter Function	196
B	Finite Difference Modeling	207
B.1	Introduction	207
B.2	2-D Finite Difference Modeling	209
B.2.1	Numerical Dispersion	211
B.2.2	Sources and Boundary Conditions	215
B.3	A Point Diffractor	221

Chapter 1

Introduction

1.1 Thesis Objectives

Most wave propagation studies concentrate on identifying the coherent features in seismic data. These features are often indicative of major structural trends, and are of great interest in many branches of geophysics. The small incoherent arrivals which occur between the major reflections and refractions also contain information about the earth, yet these features are often dismissed as noise, or classified as coda. In fact, numerous techniques, such as stacking, beamforming, etc have been developed to suppress these arrivals.

The primary objective of this thesis is to investigate the attributes of seismic waves which have propagated through a highly heterogeneous medium. This is accomplished using two different finite difference modeling techniques. One of the techniques is a conventional second order finite difference technique (Alford et al., 1974; Kelly et al., 1976), which provides a full, iterative solution to the elastic wave equation. The second is a new technique which is based on the elastic wave equation and the Born approximation. The Born approximation has received great attention for both forward and inverse modeling, because it serves to linearize the elastodynamic equations of motion (e.g., Nayfeh, 1973; Beydoun and Tarantola, 1988). Although

this approximation has been commonly used to study scattering, there is reason to question the validity of this approach. The Born approximation assumes scattering is weak, and as a result three important assumptions arise. First, it is assumed the incident wavefield passes through the heterogeneous region undisturbed. Second, the only source of scattering is the interaction of the incident wave with the perturbations in the medium. As a result secondary scattering is ignored. Third, the total field is the sum of the incident and scattered fields. Together, these assumptions violate the law of energy conservation.

The final and most important objective of this thesis is to apply what is learned from the forward modeling to actual field data. To do this, waveforms from an underground nuclear explosion were analyzed. These data were also compared to synthetic waveforms generated for a variety of previously published random lithospheric models (e.g., Aki, 1973; Frankel and Clayton, 1986; Flatté and Wu, 1988). Using travel time and amplitude fluctuations, coherency measurements and coda generation to constrain the modeling, we propose that the lithosphere below NORSAR is best modeled as the three layered model described below.

1.2 Large-Scale Variations

In whole earth seismology, the earth's velocity field is often approximated by a series of radially symmetric shells. Similarly, in exploration seismology the velocity field is often simplified to constant velocity layers. Data from these simplified models lacks the high degree of variability often seen on field data. Between the major reflections and refractions, field observations have small incoherent arrivals that cannot be accounted for by the model.

Instead of attempting to understand these arrivals, they are routinely dismissed as "noise". As a result, geophysical efforts have been directed towards data processing techniques to enhance the impact of the coherent arrivals and diminish the incoherent

arrivals (Robinson, 1957; Mayne, 1962). This limited use of seismic data has identified many major features within the earth and has established seismic imaging as a major tool for oil and gas exploration. These successes in both whole earth and exploration seismology, occurred because the "signal" was used to identify major changes in lithology and/or structure. In fact, that is the only information the "signal" carries. It can tell us little of what lies between the interfaces.

It is sometimes the case that the material between major lithographic boundaries is more important than the boundaries themselves. Of particular interest are the small-scale velocity anomalies in the crust. These features are often smaller than the shortest recorded wavelength and can be indicative of changes in lithology, porosity, pore pressure, fracture density or permeability. The two key features of these variations are their small size and large number. Both factors coalesce to produce an incoherent scattered field which cannot be explained by a simple layered model.

1.3 Characterization of Small-Scale Variations

Due to the large number and random distribution of small-scale variations, these features are often characterized by their statistics (e.g., Chernov, 1960; Hudson and Heritage, 1981). The advantage of statistical characterization is that it allows some aspects of the velocity field to be described by only a few parameters. Much like a horizontal formation in reflection seismology might be characterized by its depth, thickness and velocity, highly heterogeneous media can be characterized by their spatial autocorrelation function, correlation length, perturbation index, and average velocity.

In scattering theory, it is common to normalize both the wavelength λ of the incident wave and the extent L of the heterogeneous region by the scale length of the scatterers a (e.g., Chernov, 1960; Wu and Aki, 1985c). The product $ka = 2\pi a/\lambda$ is the normalized wavenumber, and L/a is the normalized propagation length

These normalized parameters define different scattering regimes. When $ka < .01$, the heterogeneities are too small to individually affect the passage of seismic energy, thus the spatially varying properties of the medium can be replaced by some effective bulk properties. For $.01 < ka \ll 1$, the low frequency approximation (i.e., Rayleigh scattering) is valid and the power of the scattered wave is proportional to k^4 . When $ka \approx 1$, the size of the scatterers is comparable to a wavelength. This is often called the Mie scattering regime, and is dominated by isotropic scattering, with some preference to the forward direction. When $ka \gg 1$, scattering is strongly concentrated in the forward direction. In this regime, mode conversion and backscattering are small, so parabolic approximations to the wave equation can provide accurate solutions. For relatively short propagation paths, $L/a < 100$, ray theory can be successfully used, but for longer propagation paths analytical techniques are usually used (Wu and Aki, 1990).

A third parameter is commonly used to quantify the strength of a scatterer. The perturbation index \tilde{v} is defined as the rms deviation in velocity v (or Lamé's parameters, density, etc),

$$\tilde{v} = \left(\frac{\delta v}{v_0} \right)_{rms}, \quad (1.1)$$

where v_0 is the average velocity of the medium. If $\tilde{v} < .1$ the scattered field will be small compared to the incident field and the Born approximation may give good results. Stronger variations lead to strong multiple scattering, thus invalidating the Born approximation.

1.4 Characterization of the Scattered Field

The amplitude and travel time of seismic waves are affected by propagation through a random medium. If the correlation length of the medium is small, the incident wave will be strongly scattered by the medium. If the correlation length is large, the wavefront will alternately be focused and defocused by the medium, creating large

variations in both amplitude and travel time but little scattering. In either case, the statistics of the wavefield may contain information relating to the statistics of the medium.

One technique commonly used to estimate the statistics of the wave field is the coherency. Coherency is a measure of similarity between a pair of time series. The technique has been used to study spatial and temporal trends in both strong ground motion (Harichandran and Vanmarcke, 1984) and regional (Dainty and Toksöz, 1990) studies and is a frequency domain equivalent of the correlation function used by Bungum et al. (1985) and Ingate et al. (1985). The coherency function is useful in practice because it provides a dimensionless measure of similarity between two traces. Due to the variability in traces which have propagated through a random medium, coherency studies of this kind are often done on arrays of seismic data.

1.5 Wave Propagation in Random Media

Seismic wave propagation through random media can be approached either statistically or deterministically.

1.5.1 Statistical Modeling

Most studies of wave scattering in random media use the statistical approach. The typical methodology is to first assume a spectral model for the random medium, then attempt through analytical means to predict the statistical behavior of the propagating wave field. This course of action has the advantage that if successful, the statistical variations in the observed wave field can be directly related to those in the medium.

In general, there is no exact closed form solution for elastic wave propagation in an highly heterogeneous medium. Several approximate solutions have been presented, however. If scattering is very strong, the transportation of energy can be modeled

with the diffusion equation. The diffusion models presented by Aki and Chouet (1975) and Dainty and Toksöz (1975) use energy conservation to derive seismic envelopes for strong scattering media. These techniques are valid only when all of the energy in the medium is multiply scattered and no direct energy remains. Thus, these techniques are of limited use when intrinsic attenuation is strong, or scattering is weak.

When scattering is weak, the single scattering model may provide an accurate solution (e.g., Aki, 1969; Aki, 1973; Sato, 1977a). These theories have the advantage that they are well suited to perturbation analyses, where the medium and the wave field are decomposed into a background part plus a perturbative part. This decomposition leads naturally to the Born approximation. Chernov (1960) investigated the applicability of the Born approximation for scattering in random acoustic media. The generality of his analysis lead to an overly strict validity criterion. Kennett (1972b), was the first one to extend Chernov's analysis to the elastodynamic case. His analysis was limited to two-dimensions and aimed at the problem of a horizontally stratified perturbation in a layered structure. For this geometry, he found the following validity condition,

$$\frac{\omega}{\beta_0} k_{max} \frac{HW}{\pi} \tilde{v} \ll 1, \quad (1.2)$$

where ω is the radial frequency, β_0 is the background shear wave velocity, k_{max} is the largest wavenumber contributing to the solution, and H , W and \tilde{v} are the the height, width and strength the scatterer. The strength of the scatterer is measured often defined in terms of the perturbation index, which is equal to the rms variation normalized by its mean (where the variations may defined in terms of Lamé's parameters, density, or velocity). Hudson and Heritage (1981) investigated the accuracy of the Born approximation for the 3-D elastic case. They present several inequalities which give the range of validity of the Born approximation and show that in all cases, these criteria are violated by typical teleseismic frequencies and scatterer sizes. They argue that to satisfy the validity criteria, observations would have to be made at periods on the order of 100 seconds, or greater.

1.5.2 Deterministic Modeling

One way to minimize the uncertainties and errors associated with statistical modeling is to approach the problem deterministically, that is, construct a "random" medium with known statistical parameters and investigate that model. This is the approach taken here.

In this thesis, numerical (finite difference) modeling is used to propagate energy in a variety of random media. The finite difference technique was chosen because it can produce a full solution to the elastodynamic equation of motion, and unlike high frequency approximations (such as raytracing), the technique is valid over a wide range of scatterer to wavelength ratios. Another advantage of the technique is the ability to make synthetic seismograms and snapshot pictures of the vector displacement field at any point in time.

This is not the first time the finite difference technique has been used to study scattering in random media. Frankel and Clayton (1986) used the technique to assess the accuracy of Chernov (1960) scattering theory. They also found that the travel time and amplitude variations in teleseismic arrivals at NORSAR and LASA could be explained by random heterogeneities having a von Kármán distribution and length scales less than 50 km ($a \geq 10$ km). Dougherty and Stephens (1988) used the technique to study scattering in the ocean crust and found that much of the seafloor "noise" could be traced to scattering of the primary wave into both scattered body and Stoneley modes. In this thesis, the finite difference technique is used both to model single and multiple scattering.

1.6 Thesis Plan

In the scattering literature, highly heterogeneous media are often approximated by random fields. The advantage of this approach is that a complex, multi-dimensional velocity function can be expressed in terms of a few simple statistical parameters. The

conditions under which statistical characterization is justified are outlined in Chapter 2. One statistical parameter which can be used to describe the variability of a velocity field is the autocorrelation function. The properties of three commonly used autocorrelation functions, the Gaussian, exponential, and von Kármán functions are investigated, and their likely applicability to the earth is discussed. All three spectra are nearly flat at low wavenumbers, but at higher wavenumbers the Gaussian falls off exponentially, while the exponential and von Kármán fall off with a power law dependence. The fall off rate controls the roughness of the medium. Those characterized by the Gaussian autocorrelation are smoothly varying, while the exponential and von Kármán functions are more highly textured. Although not directly related to wave scattering, the ideas presented in Chapter 2 are important to the developments in the later chapters.

In Chapter 3, a new semi-analytical technique is introduced to calculate the single-scattered field. The technique is based on the Born approximation and makes use of the full elastic wave equation. In this technique, an incident wave is either analytically or numerically propagated in a background medium. When the incident wave interacts with the perturbations in the medium, body forces are generated and introduced into a separate finite difference calculation. Unlike similar analytical techniques (Appendix B), the body forces are calculated numerically making the technique applicable to arbitrarily complex velocity models. The ability to produce synthetic seismograms based on the single scattering approximation in arbitrarily complex media is unique and of great interest because these traces can then be compared one to one with traces from the multiple scattering solution. These comparisons are made in Chapter 3. In addition, the effect of the single scattering approximation on coda and coherency statistics is investigated.

In Chapter 4, numerical simulations and data collected at the NORSAR and NORESS arrays are used to evaluate several different lithospheric models. We begin the study with the simple single layer models proposed by Aki (1973), Capon (1974)

and others. These models matched the variations in travel times and amplitude well, but could not generate the same amount of coda observed in short period data. The overlapping two-layered model proposed by Flatto and Wu (1988) also matched the observed variations in travel times and amplitude and produced more coda, but the wavefield produced by this model was considerably more coherent than the field data. After experimenting with numerous statistical models of the lithosphere, we found a three-layered model which matched the variations observed at NORSAR better than any previously proposed models. The autocorrelation of the fluctuations in the top layer (0-3 km) is a bandlimited white spectrum with 2% rms velocity variations. We found this layer necessary in order to match the observed variations across small array such as NORESS. The middle layer (3-35 km) is characterized by the 0th von Kármán function and has larger (3%) velocity variations. This layer contributes to both the generation of the coda, and to the travel time and amplitude variations observed at the surface. The bottom layer (35-250 km) is characterized by a Gaussian autocorrelation and 2% rms velocity variations. We found the best results when this layer was made to have a 20 km correlation length in the horizontal direction and a 5 km vertical correlation length. Evidence from seismic profiles near NORSAR (e.g., Cassell and Fuchs, 1979) and coupled-mode inversions (e.g., Kennett and Nolet, 1990; Kennett and Bowman, 1990) also suggest that heterogeneities in the upper mantle might have different scale lengths in the horizontal and vertical directions. In particular, Kennett and Bowman (1990) analyzed data from seismic arrays with apertures between 100 to 1000 km and suggested that the heterogeneities in the upper mantle have horizontal scale lengths on the order of 300-400 km, but a vertical scale length of about 100 km at a depth of 200 km. They also suggest the vertical scale length might increase with depth. These studies used surface wave data with frequencies on the order of 0.02 Hz and body waves with frequencies on the order of 0.04 Hz, which might explain the larger scale sizes observed in these studies.

Chapter 5 contains the conclusions which can be formed from the material pre-

sented in this thesis. In this chapter, there is a review of the technique used to generate the single scattered field, as well as a summary of some of the differences between the single and multiple scattering solutions. Limitations in single scattering theory lead us to use finite difference modeling to calculate the multiple scattering solutions presented in Chapter 4. These data are reviewed in Chapter 5, as is a model for the random heterogeneities thought to exist in the lithosphere beneath the NORSAR array.

Chapter 2

Seismic Velocities as Random Fields

2.1 Introduction

Velocity variations in the earth can be separated into two broad classes; those which are “organized” enough to be treated discretely and those which are not. Large scale lithographic boundaries and small isolated objects fall into the first category, which we will refer to as deterministic variations (or deterministic scatterers). The second category is characterized by small-scale features such as subtle velocity variations, or localized changes in composition, saturation, pore pressure, etc. These variations are often irregularly distributed and so numerous and small that they can only be treated effectively with statistical techniques; hence the name stochastic or random variations.

Waves scattered by discrete scatterers tend to produce strongly coherent arrivals. The coherency of the scattered waves makes them clearly visible across neighboring seismometers, thus these were the first waves to be studied by seismologists. The scattered field due to stochastic variations lacks coherency. These waves are thought to be the cause of the significant travel time and amplitude anomalies which are of-

ten observed, even between elements of tightly spaced arrays (Aki, 1973; Wu, 1982a; Ringdal and Husebye, 1982; Frankel and Clayton, 1986; Flatté and Wu, 1988). Because of their small amplitudes, uncorrelated nature and erratic arrival time, these waves have historically been treated as noise. Only recently has their importance in crustal studies (e.g., Aki, 1973; Aki and Chouet, 1975; Wu, 1985; Frankel and Clayton, 1986), upper mantle studies (e.g., Berteussen et al., 1975b; Mereu and Ojo, 1981; Ojo and Mereu, 1986), core-mantle boundary studies (Haddon and Cleary, 1974; Bataille et al., 1990) and reservoir characterization (Greaves and Fulp, 1987) been realized.

2.2 Seismic Velocities as Random Fields

In the scattering literature, highly heterogeneous media are often represented by random fields (e.g., Capon, 1974; Sato, 1978; Macaskill and Ewart, 1984; Wu and Aki, 1990). The justification for such an approach hinges on the assumption that the scale length of the heterogeneities is much smaller than the extent of the study area. When satisfied, the complex, multi-dimensional velocity function can be expressed in terms of a few simple statistical parameters. Due to practical considerations, the most commonly used statistical parameters are the low order statistical moments (the mean, variance, and correlation function).

2.2.1 Decomposition of the Velocity Field

With the above discussion in mind, consider the velocity function $v(\underline{x})$ which may vary with position \underline{x} over some region of the earth \mathcal{R} . The velocity function can be decomposed into two parts; a deterministic part $v_o(\underline{x})$ and a stochastic part $\delta v(\underline{x})$,

$$v(\underline{x}) = v_o(\underline{x}) + \delta v(\underline{x}) \quad \underline{x} \in \mathcal{R}. \quad (2.1)$$

It should be pointed out that the two different types of heterogeneities, deterministic and stochastic, are not inherent properties of the medium. This decomposition is

arbitrary and done simply as a modeling approach. With this in mind, we will assume that the deterministic (or background) part of the velocity field contains all large-scale velocity variations. Such variations might arise from gross changes in lithology; where a shale meets a limestone, for instance.

Although interesting, scattering from discrete variations is well understood, and numerous techniques have been developed (e.g., travel time analysis, migration, τ - p methods, etc.) which are capable of estimating that portion of the velocity field (e.g., Aki and Richards, 1980; Claerbout, 1985). In this thesis, the focus will be on scattering from the small-scale features of the velocity field. Most materials in nature contain stochastic variations, yet the distribution of these features is poorly understood.

Stochastic variations are capable of affecting the passage of seismic energy, although usually to a lesser extent than deterministic variations. Three mechanisms are commonly attributed to scattering from stochastic variations. One is the generation of coda; scattered energy arriving at the receiver after the direct arrival (Aki and Chouet, 1975; Herrmann, 1980). A second is attenuation due to scattering; energy which is scattered by the medium and never arrives at the receiver (Dainty, 1981; Wu, 1982b; Dainty, 1984). A third is through travel time fluctuations; changes in arrival time of the initial pulse due to fluctuations in the medium (Aki, 1973; Ojo and Mereu, 1986; Flatté and Wu, 1988). The first two mechanisms are interrelated and have been shown to be controlled by backscattering. Travel time fluctuations arise from scattering within a narrowly defined cone about the propagation direction, and are thus controlled by forward scattering. These three mechanisms contribute to the complexity of most seismograms observed in the earth.

2.2.2 General properties of a Random Field

A random field provides a probabilistic description of a physical phenomenon which varies spatially according to the laws of probability. For statistical reasons, it is often

necessary to treat a random field as one element randomly selected from an infinite population or ensemble of fields. Each member of the ensemble shares the same statistical properties, but is a unique realization of that ensemble. In this context, the earth's velocity field is but one realization of an infinite ensemble of functions which might have been observed.

The statistical description is achieved by associating each point in space \underline{x} with a random variable $V(\underline{x})$. It is assumed that the range of \underline{x} and sample space of the random variable are infinite,

$$\begin{aligned} 0 &\geq |\underline{x}| < \infty \\ -\infty &< V(\underline{x}) < \infty, \end{aligned} \quad (2.2)$$

and the probability density function (*pdf*) and all the joint *pdfs* are known. When this is true, a field can be described by an ordered set of random variables $V(\underline{x})$.

At any point in space, the univariate moments of the random field can be written in terms of its *pdf* $f_{V(\underline{x})}(\delta v)$,

$$E[V(\underline{x})^m] = \int_{-\infty}^{\infty} (\delta v)^m f_{V(\underline{x})}(\delta v) d(\delta v), \quad (2.3)$$

where m is the order of the statistical moment and E denotes the expectation operator. Since little is known about the statistical distribution of scatterers in the crust, it is commonly assumed in the scattering literature that velocities are Gaussian distributed. Then, the *pdf* of the velocity field can be completely described by its mean (first statistical moment) and variance (second statistical moment).

Similarly, the bivariate moments of the random field can be written in terms of its joint probability density function (*jpdf*),

$$E[V(\underline{x}_1)^m V(\underline{x}_2)^n] = \int_{-\infty}^{\infty} \int_{-\infty}^{\infty} (\delta v_1)^m (\delta v_2)^n f_{V(\underline{x}_1)V(\underline{x}_2)}(\delta v_1, \delta v_2) d(\delta v_1) d(\delta v_2). \quad (2.4)$$

The multivariate moments describe the dependence between values of the velocity field at two points in space.

The simplest, and in practice most important, of the bivariate moments is the covariance. We define the autocovariance function (*acvf*) by,

$$\gamma_{VV}(\underline{x}_1, \underline{x}_2) = E[(V(\underline{x}_1) - E(\underline{x}_1))(V(\underline{x}_2) - E(\underline{x}_2))] = Cov[V(\underline{x}_1), V(\underline{x}_2)], \quad (2.5)$$

where *Cov* denotes the covariance between two random variables. Since the *acvf* depends on the variance of the distribution, a normalized form of the *acvf* is often used to describe random fields. The normalized *acvf*, or autocorrelation function (*acf*), is given by,

$$\rho_{VV}(\underline{x}_1, \underline{x}_2) = \frac{Cov[V(\underline{x}_1), V(\underline{x}_2)]}{\sqrt{Var[\underline{x}_1]Var[\underline{x}_2]}}, \quad (2.6)$$

where *Var* is the variance of a random variable. From these two relations, it is clear that

$$\rho_{VV}(\underline{x}_1, \underline{x}_2) = \frac{\gamma_{VV}(\underline{x}_1, \underline{x}_2)}{\sqrt{\gamma_{VV}(\underline{x}_1, \underline{x}_1)\gamma_{VV}(\underline{x}_2, \underline{x}_2)}}. \quad (2.7)$$

If the *acvf* depends only on the spatial separation, the random field is said to be stationary (Tatarski, 1961). Then, the *acvf* and the *acf* can be simplified to

$$\gamma_{VV}(\underline{x}_1, \underline{x}_2) = \Psi_{VV}(\underline{x}_2 - \underline{x}_1), \quad (2.8)$$

and

$$\rho_{VV}(\underline{x}_1, \underline{x}_2) = \frac{\Psi_{VV}(\underline{x}_2 - \underline{x}_1)}{\Psi_{VV}(0)}. \quad (2.9)$$

Stationarity is almost always assumed in seismic scattering studies, in part because it simplifies most analytical approaches.

One can imagine regions in the lithosphere where the fluctuations in the velocity field have a preferred orientation. One example might be the deposition of overlapping lenses with different lithologies. The lens shape suggests that the correlation length of these features might be different in the horizontal and vertical direction. Although each lens may have isotropic elastic moduli, the composite medium may display an "effective" or "apparent" anisotropy. The preferred orientation of the fluctuations should be reflected in the *acvf*. For simplicity, it will be assumed that all azimuthal

variation in the *acf* can be explained through the dimensionless ellipsoidal norm,

$$\Psi(\underline{x}_2 - \underline{x}_1) = \Phi \left[\left((\underline{x}_2 - \underline{x}_1)^T \underline{\underline{Q}} (\underline{x}_2 - \underline{x}_1) \right)^{1/2} \right], \quad (2.10)$$

where $\underline{\underline{Q}}$ is a symmetric, positive-definite matrix. The eigenvectors $\hat{e}_i, i = 1, 2, 3$ of $\underline{\underline{Q}}$ point along the axes of the ellipsoid, and the eigenvalues λ_i are inversely proportional to the square of the correlation length along that axis, such that

$$\underline{\underline{Q}} = \sum_{i=1}^3 \lambda_i \hat{e}_i \hat{e}_i^T \quad (2.11)$$

If the fluctuations have no preferred orientation, Equation 2.11 reduces to

$$\underline{\underline{Q}} = \lambda \underline{\underline{I}}, \quad (2.12)$$

where $\underline{\underline{I}}$ is the identity matrix. Then for a stationary, isotropic random field, the *acvf* and the *acf* depend only on the spatial separation $r = |\underline{x}_2 - \underline{x}_1|$,

$$\gamma_{VV}(\underline{x}_1, \underline{x}_2) = \Psi_{VV}(r), \quad (2.13)$$

and

$$\rho_{VV}(\underline{x}_1, \underline{x}_2) = \frac{\Psi_{VV}(r)}{\Psi_{VV}(0)}. \quad (2.14)$$

Under these assumptions, the autocovariance and autocorrelation functions have several useful properties.

1. The zero lag value of the *acvf* is equal to the variance of the distribution. Then, from Equation 2.7, the zero lag of the *acf* is unity, $\rho_{VV}(0) \equiv 1$. This property makes it possible to normalize different distributions based on their total variance (zero lag value of the *acf*). It can also be shown that $|\rho_{VV}(r)| \leq 1$ for all r .
2. If the random field is continuous, then $\rho_{VV}(r)$ must be a continuous function of the lag r (Jenkins and Watts, 1968).
3. Lastly, the power spectrum of a random field is the Fourier transform of its correlation function (Tatarski, 1961). This property is central to the technique used to construct the realizations presented in the later chapters.

2.3 Commonly Used Autocorrelation Functions

The autocorrelation function is commonly used to characterize random fields and is a measure for quantifying the similarity between neighboring points in a random medium. It has the property that it is the Fourier transform of the power spectrum (Tatarski, 1961). This relationship allows us to build realizations from a desired correlation function in the wavenumber domain. Throughout this thesis, realizations were constructed by convolving the square root of the power spectrum with a phase term of the form $e^{i\theta}$, where θ is a random number drawn from a uniform distribution over the range $0 \leq \theta < 2\pi$. Since the norm of the phase term is one, the shape of the power spectrum and the total power within that spectrum are unchanged.

Although the statistical derivation outlined above was carried out for the continuum case, all computations were performed on a digital computer. As a result, it was necessary to convert the continuum equations to their discrete counterparts. The conversion is known to be inaccurate if the discrete medium is not well sampled (e.g., Jenkins and Watts, 1968; Bracewell, 1978). To minimize these errors, special care was taken to ensure that the power at the Nyquist frequency was small. This was necessary because truncation of the power spectrum at the spatial Nyquist is equivalent to convolution with a rectangular window function. Prange (1989) showed that when this occurs, oscillations are introduced into the *acf*.

Three correlation functions have received a great deal of attention in the scattering literature; the Gaussian, the exponential and the von Kármán functions (e.g., Chernov, 1960; Tatarski, 1961; Dainty, 1984; Frankel and Clayton, 1986; Wu and Aki, 1990). The commonly used form of these functions and their power spectra are given in Table 1, and shown graphically in Figure 1.

In both the Gaussian and exponential functions, the correlation length a marks the lag where the correlation function has the value e^{-1} (Figure 1). In the wavenumber domain, both spectra are flat out to a corner wavenumber which is approximately equal to $1/a$. The difference between the two spectra is most noticeable at higher

Table 1. Correlation Functions and Their Spectra

	Gaussian	Exponential	von Kármán
Correlation Function	e^{-r^2/a^2}	$e^{-r/a}$	$\frac{1}{2^{\nu-1}\Gamma(\nu)} \left[\frac{r}{a}\right]^\nu K_\nu(r/a)$
1-D Power Spectrum	$a\sqrt{\pi}e^{-k_r^2 a^2/4}$	$\frac{2a}{1+k_r^2 a^2}$	$\frac{\Gamma(\nu+1/2)}{\Gamma(\nu)} \frac{2\pi^{1/2}a}{(1+k_r^2 a^2)^{\nu+1/2}}$
2-D Power Spectrum	$\frac{a^2}{2}e^{-k_r^2 a^2/4}$	$\frac{a^2}{(1+k_r^2 a^2)^{3/2}}$	$\frac{\Gamma(\nu+1)}{\Gamma(\nu)} \frac{4\pi a^2}{(1+k_r^2 a^2)^{\nu+1}}$
3-D Power Spectrum	$(a\sqrt{\pi})^3 e^{-k_r^2 a^2/4}$	$\frac{8\pi a^3}{(1+k_r^2 a^2)^2}$	$\frac{\Gamma(\nu+3/2)}{\Gamma(\nu)} \frac{8\pi^{3/2}a^3}{(1+k_r^2 a^2)^{\nu+3/2}}$

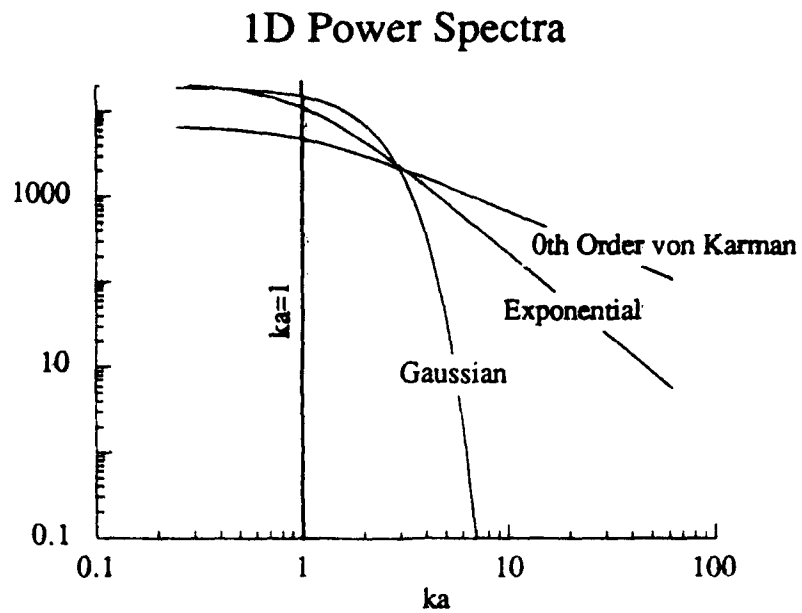
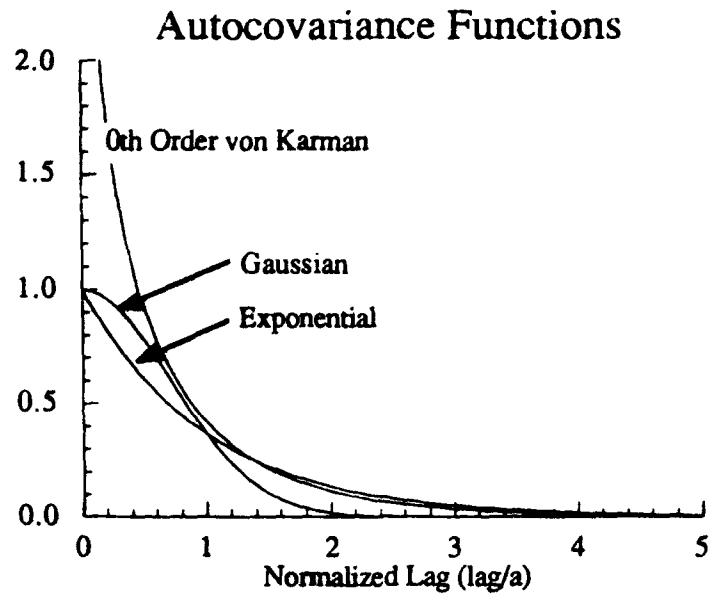


Figure 1: The model autocovariance functions (top) and their 1-D power spectra (bottom).
The spectra are normalized so that they have the same power.

wavenumbers, where the Gaussian falls off exponentially, and the exponential falls off as $k^{-(N+1)}$, where N is the number of space dimensions. The fall off rate of the spectra controls the amount of roughness in the realization. Spectra with more energy at high wavenumbers are expected to show more roughness (Figure 3) than those which are localized near zero wavenumber (Figure 2).

The von Kármán function was first introduced to characterize the random velocity field of a turbulent medium (von Kármán, 1948). In the spatial domain, the von Kármán function is peaked about the origin. The peak is especially severe when $\nu = 0$, since then the modified Bessel function K_ν goes to infinity as r/a goes to zero. Although the parameter ν can take on any value in the range 0 to 1, it has some special properties at 0, 0.3, 0.5 and 1. When $\nu = 0$ the spectrum defines a multi-dimensional Markov field (Goff and Jordan, 1988) $\nu = 0.3$ defines Kolmogorov's turbulence (Wu and Aki, 1990), while for $\nu = 0.5$ the von Kármán function simplifies to an exponential and when $\nu = 1.0$ to an autoregressive field.

In this thesis we will be most interested in the von Kármán function where $\nu = 0$. Our reason for choosing this parameterization is two-fold. Earlier studies have shown that it might best describe the random heterogeneities which exist in the crust, (Frankel and Clayton, 1986; Goff and Jordan, 1988; Toksöz et al., 1988). In addition, the 0th order ($\nu = 0$) von Kármán function is least similar to the Gaussian and thus will offer us a suitable comparison to that function.

The peakedness of the correlation function leads to a wide spectral representation, indicating that media characterized by the von Kármán function contain a significant amount of roughness (Figure 4). As in the Gaussian and exponential functions, the power spectrum of the von Kármán function is flat up to a corner wavenumber roughly equal to $1/a$. The difference is that at higher wavenumbers the spectrum falls off as $k^{-(N+2\nu)}$, considerably slower than the Gaussian or exponential functions. Thus for the von Kármán (and exponential) function, $1/a$ defines a corner wavenumber and the parameter ν controls the rate of decay of the power spectrum (Figure 1).

ACF=Gaussian

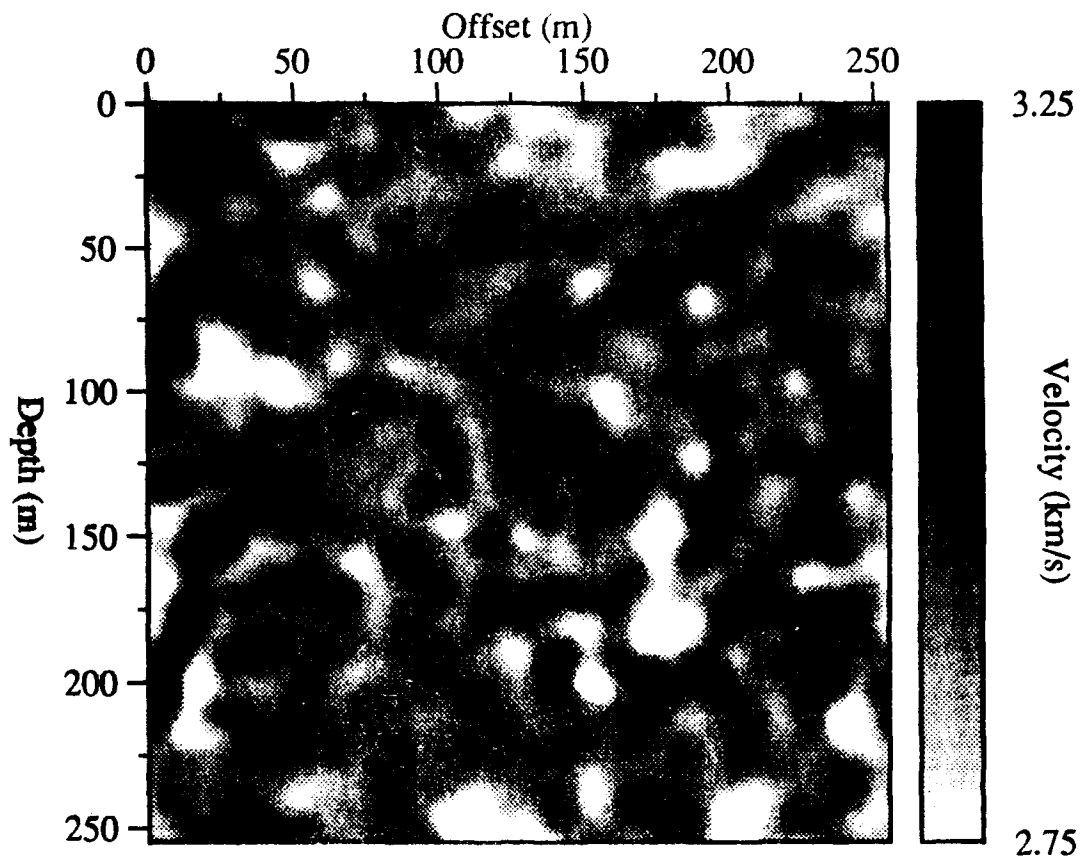


Figure 2: A 2-D realization of a random medium with a Gaussian autocorrelation function. The correlation length in this realization is 20m, and there is 5% RMS deviation in the velocity. Note the smoothness of this realization compared to those in Figures 3 and 4.

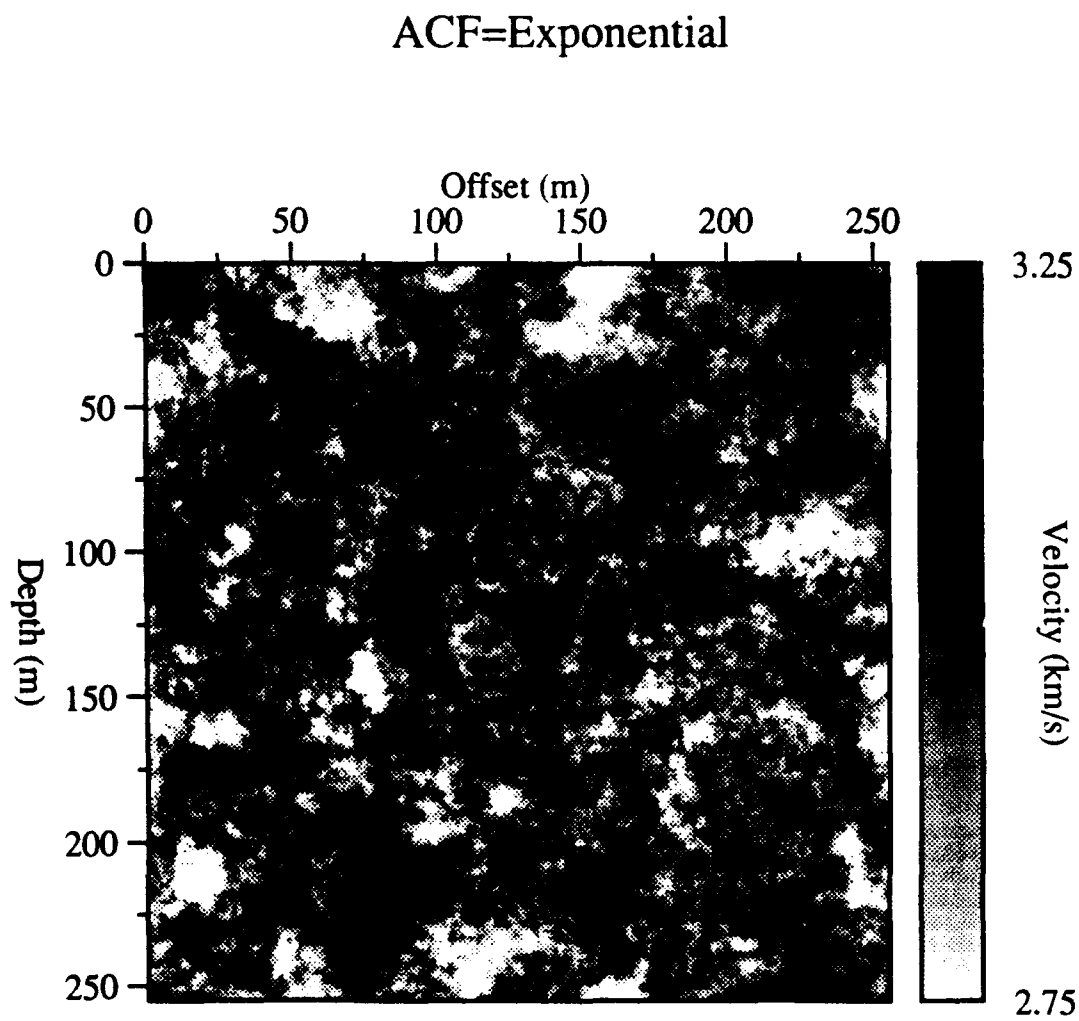


Figure 3: Same as Figures 2 and 4, but with an exponential autocorrelation function.

ACF=0th Order von Karman

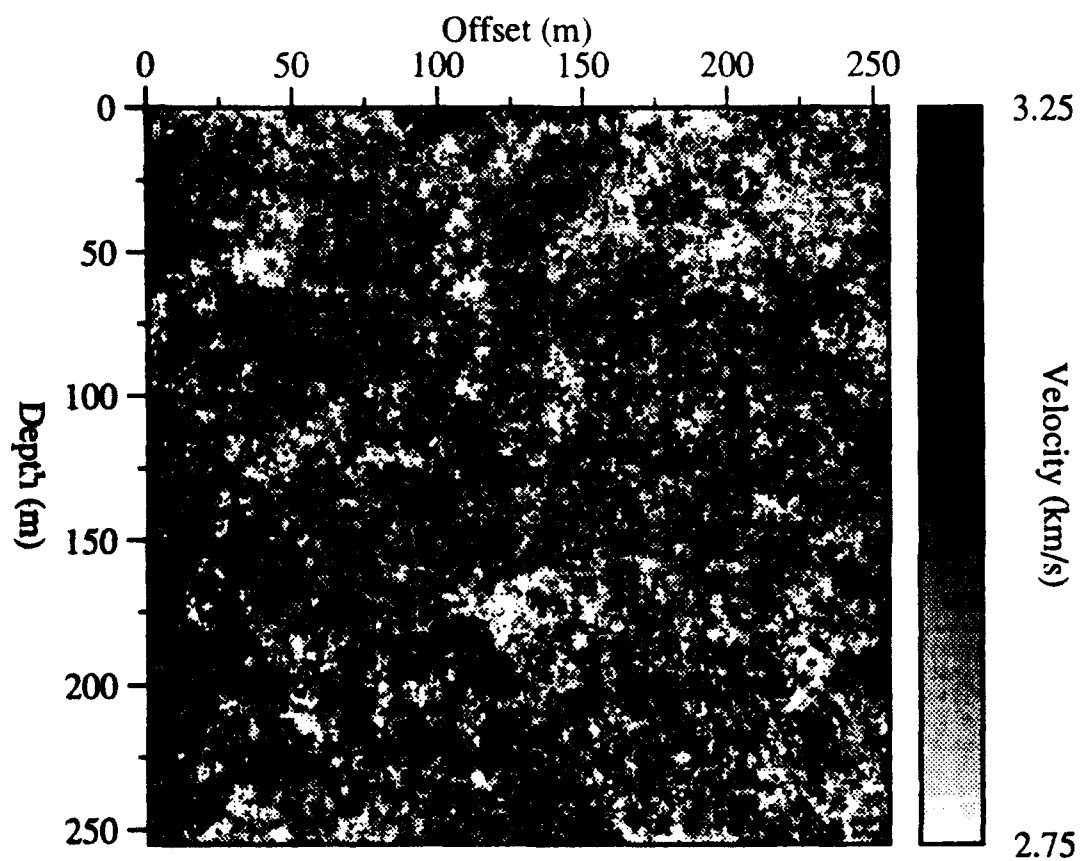


Figure 4: Same as Figures 2 and 4, but with a 0th order von Kármán autocorrelation function.

The von Kármán function has an additional property that its slope is discontinuous at zero lag. This property qualifies the von Kármán function as a fractal (Mandelbrot, 1977). Fractals are unique and of interest because they contain variations on all wavelengths. Since many physical characteristics in the crust also display variation on a wide variety of length scales, this autocorrelation function may be well suited to crustal applications. The self-similar nature of fractals can be easily seen by examining the variance as a function of wavenumber. Figure 5 shows a series of 1-D realizations taken from the three *acf* described above. All three realizations have the same correlation length ($a = 20$ m) and were generated by the same random seed. At low wavenumbers there is little variation in shape and variance between the traces. This is consistent with the power spectra (Figure 1), which are flat at low wavenumber for all three functions. At high wavenumbers, there is no variance in the Gaussian trace, and the variance in the exponential trace is smaller than it was at low wavenumber. Thus, for these media, the variance over equal logarithmic intervals of wavelength decreases as the wavelength decreases (Frankel, 1989). This is not so for the 0th order von Kármán function. The variance for that function is roughly constant over length scales smaller than $2\pi a$ (Figure 5).

At this point it is worth restating a subtle distinction. Three *acf* are commonly used in scattering literature to represent spatial velocity fluctuations in the earth; the exponential function, the von Kármán function, and the Gaussian function. It is important not to confuse the Gaussian *acf* with the Gaussian statistics of the medium. The former describes the spatial dependence of the medium, while the latter describes the *pdf* of the random variable.

2.4 Conclusions

In this chapter we have outlined the statistical background necessary to generalize the complex velocity fluctuations in the earth to a random field. Statistical charac-

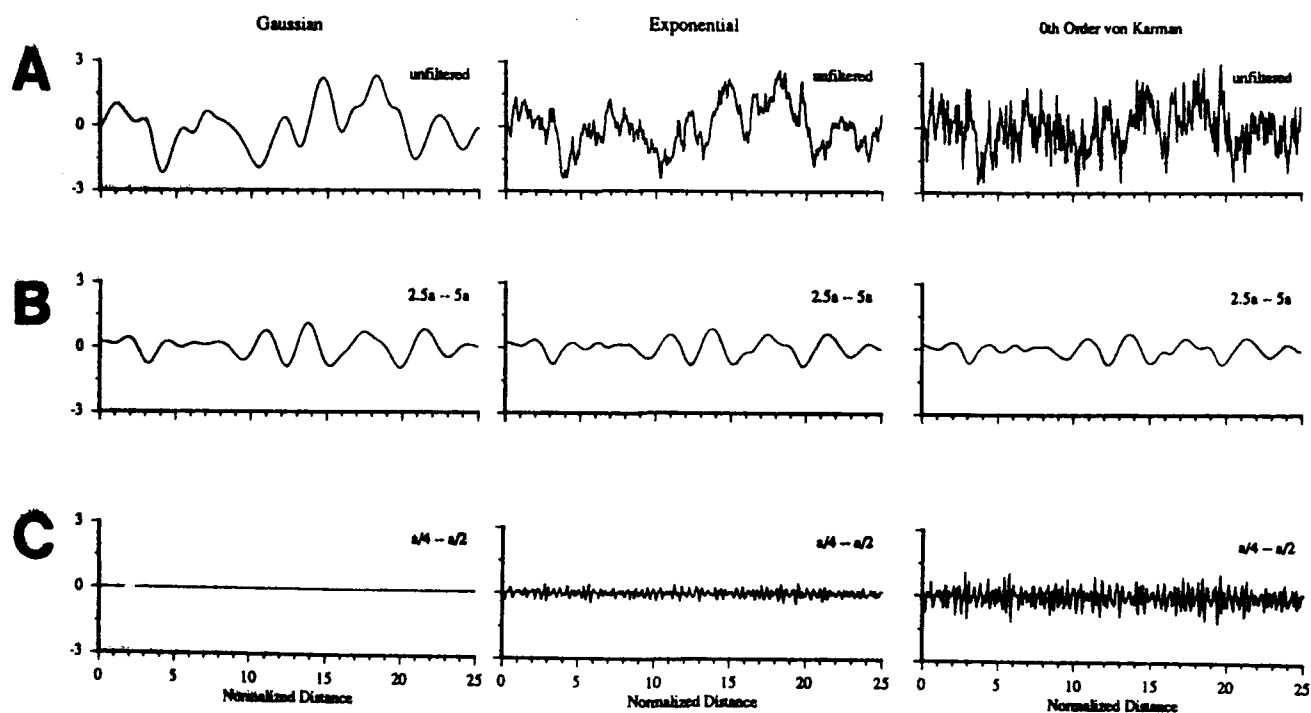


Figure 5: Random realizations from the 1D Gaussian, exponential, and 0th order von Kármán autocorrelation functions. a) unfiltered, b) bandpass filtered allowing wavelengths $2.5a$ – $5a$, c) bandpass filtered allowing wavelengths $a/4$ – $a/2$. All realizations were constructed with the same random seed, and are plotted at constant scale.

terization is considered reasonable because changes in lithology, fracture density, pore pressure, regional stresses, etc, all cause seismic velocities in the earth's crust to vary irregularly with position. Many of these features are too small and too numerous to define deterministically, thus we have little recourse but to treat them stochastically.

Although all the features mentioned above can affect seismic velocities, their spatial extent may vary by many orders of magnitude. Contrast a typical micro-crack which may be only a few microns wide and a fault zone which may be a kilometer wide; the range of length scales is 10 orders of magnitude. This wide range of length scales presents a problem when numerical techniques are used to model wave propagation in the earth. Most often only the large-scale variations (i.e. variations larger than a seismic wavelength) are included in the velocity model. As a result, synthetic seismograms generated from these models often lack the "background noise" observed in real-earth seismograms. By including these small-scale random features, we are able to achieve a better match between the synthetic seismograms and those recorded in the earth. We do this not only to better model wave propagation in the earth, but also in an attempt to understand the velocity distributions within the earth. These distributions are capable of describing a little known and poorly understood aspect of the earth and may hold great potential in reservoir characterization, fracture density studies, seismic anisotropy, mantle studies (with respect to convection), etc.

In this chapter we also introduced the autocovariance functions most commonly cited in the scattering literature. We will use these functions in the chapter on forward modeling in stochastic media. It was shown that random processes with Gaussian autocorrelation functions give rise to smoothly varying realizations, while random processes with von Kármán autocorrelation functions produce realizations with a strongly textured appearance.

Chapter 3

Scattering in Random Media

3.1 Introduction

Seismic wave scattering is a complex phenomenon which depends on the size, distribution and magnitude of the heterogeneities in the earth. In general, the exact distribution of these heterogeneities is unknown, and we have no recourse but to use some simplified model. Historically, the earth has often been modeled as a simple stratified medium, each of the strata having constant velocity and density. Seismograms from these models tend to match the gross features recorded in field data, but lack the variations in amplitude and travel time and the incoherent energy which is often observed after the major arrivals. Both of these features are symptomatic of scattering from small-scale changes in velocity or density.

The scattering problem is difficult to solve exactly, in part because the problem is recursive. That is, a wave scattered from a particular heterogeneity is further influenced by other heterogeneities in the medium. When scattering is weak, it is common to consider only the incident wave and the first scattered wave. This is the single scattering solution (e.g., Aki, 1969; Aki and Chouet, 1975; Sato, 1977a; Sato, 1977b; Aki, 1980; Wu and Aki, 1985c; Chouet, 1990). The problem is often further simplified by invoking the first Born approximation, which will be referred to as simply

the Born approximation. In the Born approximation, it is assumed that the incident wave is unchanged during propagation through the heterogeneous region. As a result, energy scattered from the incident wave is not subtracted from the background field and the total energy in the medium increases with time. Although this limitation is clearly stated in much of the scattering literature, the Born approximation continues to be used for both forward and inverse modeling of random continua.

Whereas most analytic solutions for scattered waves are valid only when scattering is weak, it may be possible to solve the problem exactly via numerical methods. The first numerical simulations of seismic wave propagation in stochastic media were accomplished using a two-dimensional ray tracing technique (Mereu and Ojo, 1981). In that study it was found that the variations in travel time and amplitude of the incident wave are controlled mainly by the long wavelength variations in the medium. Frankel and Clayton (1984) used the finite difference technique to model acoustic waves in random media and were able to produce coda waves and study apparent attenuation. For the three random media they studied (characterized by the Gaussian, exponential, and von Kármán autocorrelation functions), they found that apparent attenuation increased with frequency until the correlation length of the scatterers was comparable to a wavelength. At higher frequencies, there was no decrease in apparent attenuation in the exponential and von Kármán media, but there was a noticeable decrease in the Gaussian media. These results agree well with analytic solution (Dainty, 1984). Finite difference modeling has also been applied to the elastic wave equation; both to study the relationship between the medium and the observed scattered field (Frankel and Clayton, 1986; McLaughlin and Anderson, 1987; Dougherty and Stephens, 1988) and to study the response of typical seismic processing streams used on data collected in highly heterogeneous regions (Gibson and Levander, 1988).

In this chapter, the focus is on the differences between the single and multiple scattering solution. To accomplish that end, a new semi-analytical technique to calculate

the single scattering solution is developed. The technique uses single scattering theory and the Born approximation to calculate the equivalent body forces in the medium due to the interaction between the incident field and the heterogeneities. These equivalent sources are then propagated in the background medium via the finite difference technique. The most important advantage of this new technique is that it can be used to generate the single scattering solution for any particular velocity model. This will allow us to compare the single scattering solution to the multiple scattering solution, as calculated by a conventional finite difference technique, for a variety of random media. It is important to point out that both techniques make use of finite difference modeling, but in one case (the single scattering solution) special steps are taken to include only single scattered waves in the solution.

3.2 Single Scattering

3.2.1 Theory

Consider an isotropic, elastic medium which is homogeneous except for some small region \mathcal{R} . Outside the region \mathcal{R} , let λ_0 , μ_0 , and ρ_0 be Lamé's parameters and density. Inside \mathcal{R} , the material properties can be written as the sum of the homogeneous parameters plus a spatially varying perturbative term,

$$\begin{aligned}\lambda(\underline{x}) &= \lambda_0 + \delta\lambda(\underline{x}) & \delta\lambda &\equiv 0 \quad x \notin \mathcal{R} \\ \mu(\underline{x}) &= \mu_0 + \delta\mu(\underline{x}) & \delta\mu &\equiv 0 \quad x \notin \mathcal{R} \\ \rho(\underline{x}) &= \rho_0 + \delta\rho(\underline{x}) & \delta\rho &\equiv 0 \quad x \notin \mathcal{R}.\end{aligned}\tag{3.1}$$

Both inside and outside \mathcal{R} , particle displacements can be described by the general elastodynamic equation of motion (Aki and Richards, 1980)

$$\rho \ddot{u}_i - (\lambda \nabla \cdot \underline{u})_{,i} - [\mu(u_{i,j} + u_{j,i})]_{,j} = S_i,\tag{3.2}$$

where $\underline{u} = \underline{u}(\underline{x}, t)$ is the displacement vector, and $\underline{S} = \underline{S}(\underline{x}, t)$ is the body force vector.

Outside \mathfrak{R} , the material properties are spatially invariant and Equation 3.2 can be simplified to

$$\rho_0 \ddot{u}_i - (\lambda_0 + \mu_0)(\nabla \cdot \underline{u})_{,i} - \mu_0 \nabla^2 u_i = S_i. \quad (3.3)$$

Inside \mathfrak{R} Equation 3.1 can be inserted into Equation 3.2.

$$\rho_0 \ddot{u}_i - (\lambda_0 + \mu_0)(\nabla \cdot \underline{u})_{,i} - \mu_0 \nabla^2 u_i = S_i + Q_i, \quad (3.4)$$

where

$$Q_i = -\delta \rho \ddot{u}_i + (\delta \lambda + \delta \mu)(\nabla \cdot \underline{u})_{,i} + \delta \mu \nabla^2 u_i + (\delta \lambda)_{,i} \nabla \cdot \underline{u} + (\delta \mu)_{,j} (u_{i,j} + u_{j,i}). \quad (3.5)$$

Notice that Equation 3.4 is similar to Equation 3.3, with terms involving the heterogeneities appearing as a body force term.

If the scattered field is small compared to the incident field, the problem can be simplified by introducing the first Born approximation. Under that assumption, the displacement field can be decomposed into two parts; the incident field \underline{u}^0 and the scattered field \underline{u}^1 ,

$$\underline{u} = \underline{u}^0 + \underline{u}^1 \quad (3.6)$$

$$|\underline{u}^0| \gg |\underline{u}^1|. \quad (3.7)$$

It is assumed that scattering is weak enough that the perturbations in the medium have no effect on the incident wave and all scattering is due to the interactions between the incident wave and the perturbations in the medium (i.e. secondary scattering is ignored).

Inserting Equation 3.6 into Equations 3.4 and 3.5 and neglecting terms involving the interaction between the scattered field and the perturbations in the medium yields,

$$\rho_0 \ddot{u}_i^0 - (\lambda_0 + \mu_0)(\nabla \cdot \underline{u}^0)_{,i} - \mu_0 \nabla^2 u_i^0 + \rho_0 \ddot{u}_i^1 - (\lambda_0 + \mu_0)(\nabla \cdot \underline{u}^1)_{,i} - \mu_0 \nabla^2 u_i^1 = S_i + Q_i^0, \quad (3.8)$$

where

$$Q_i^0 = -\delta \rho \ddot{u}_i^0 + (\delta \lambda + \delta \mu)(\nabla \cdot \underline{u}^0)_{,i} + \delta \mu \nabla^2 u_i^0 + (\delta \lambda)_{,i} \nabla \cdot \underline{u}^0 + (\delta \mu)_{,j} (u_{i,j}^0 + u_{j,i}^0). \quad (3.9)$$

The first three terms in Equation 3.8 account for the displacements of the incident field in the homogeneous background. From Equation 3.2 these terms can be subtracted, leaving an equation of motion for the scattered field,

$$\rho_0 \ddot{u}_i^1 - (\lambda_0 + \mu_0)(\nabla \cdot \underline{u}^1)_{,i} - \mu_0 \nabla^2 u_i^1 = Q_i^0. \quad (3.10)$$

Under the Born approximations then, both the incident and scattered fields travel in the background medium. As a result, the incident wave is not affected by the perturbations in the medium, and the scattered field is generated only by the interaction between the incident field u^0 and the perturbations.

3.2.2 Limitations of the Born Approximation

Although the Born approximation is commonly used in both forward and inverse modeling, surprisingly few studies have been published which explore the range of validity of the technique (e.g., Chernov, 1960; Hudson and Heritage, 1981).

Chernov (1960) showed that it was possible to estimate the power carried by the scattered field in a random acoustic medium. In that derivation, gradients in the material properties were neglected (i.e. smooth perturbations only) and it was assumed that the receiver point was far from the heterogeneous region. Then, for a medium with a Gaussian correlation function, the ratio of the power in the scattered field to the power in the incident field is given by

$$\frac{\Delta I}{I} = \sqrt{\pi} \tilde{n} k^2 a L (1 - e^{-k^2 a^2}), \quad (3.11)$$

where \tilde{n} is the rms deviation in the refractive index, k is the wavenumber of the incident wave, a is the correlation length of the medium and L is the propagation length within the heterogeneous region.

From Equations 3.11 and 3.7, the range of validity for the Born approximation in an acoustic medium is given by

$$\sqrt{\pi} \tilde{v} (ka)^4 \frac{L}{a} \ll 1, \quad \text{for } ka \ll 1 \quad (3.12)$$

$$\sqrt{\pi} \tilde{v} (ka)^2 \frac{L}{a} \ll 1, \text{ for } \text{otherwise.} \quad (3.13)$$

When ka is small, the wavelength is much larger than the scatterer, and the scattered field has the characteristic Rayleigh scattering k^4 dependence. When ka is large, the scattering coefficient increases as the square of the ka . In either case, it is clear that the Born approximation is probably not adequate when the propagation path is long compared to the correlation length of the medium. This is precisely the case in a random continuum studied here.

Hudson and Heritage (1981) carried out a similar analysis for the elastic wave case. Using several simplifying assumptions, they were able to define a range of validity for the Born approximation,

$$\left(\frac{\Omega d}{\beta_0} \right)^2 \tilde{\rho} + \left(\frac{d}{a} \right)^2 \max(\tilde{\lambda}, \tilde{\mu}) \ll 1, \quad (3.14)$$

where Ω is the maximum angular frequency, β_0 is the background shear wave velocity, d is the size of the region bounded at each instant of time by the scattering centers corresponding to scattering from the incident wavefront to the observer by the least time path and $\tilde{\lambda}$, $\tilde{\mu}$ and $\tilde{\rho}$ are the normalized rms deviations in Lamé's parameters and density. In that study, the authors warn that Equation 3.14 is extremely strict and the Born approximation will work well in many media which violate this limit.

These studies suggest that although the Born approximation has been shown to produce excellent agreement with other analytical solutions when the scatterer is a discrete, isolated feature (e.g., Wu and Aki, 1985c), the technique may not be valid for random continuous media.

3.2.3 Numerical Implementation

In Appendix A, the single scattering and Born approximations are used to generate closed form solutions to a variety of scattering problems. In all cases, the inhomogeneous region is assumed to be a single, discrete, isolated anomaly. These solutions are

useful for gaining insight into the nature of scattering, but they may not be adequate to study scattering in the earth. An alternative to these analytical solutions is to solve the problem numerically. The advantage of numerical solutions is that they can be used to study scattering in media which may be too complex to study with known analytic techniques.

Many numerical techniques exist which can be used to compute synthetic seismograms in laterally heterogeneous media. High frequency techniques such as raytracing are valid only when the size of the scatterer is large compared to a wavelength (e.g., $ka > 10$) (Červený et al., 1982). Methods based on Kirchoff-Helmholtz integration are very accurate for sharp interfaces, but these techniques ignore the effects of multiple scattering and are invalid in smoothly varying media where the size of the scatterer is similar to that of a wavelength (Scott and Helmberger, 1983). Perturbation methods consider only scattering of the incident wave, thus cannot be used to study media in which multiple scattering may be important (Kennett, 1972a; Prange, 1989). Finite difference modeling overcomes many of these shortcomings and has been used successfully in a number of scattering studies (e.g., Flatté and Tappert, 1975; Macaskill and Ewart, 1984; Frankel and Clayton, 1984; McLaughlin et al., 1985; Frankel and Clayton, 1986; McLaughlin and Anderson, 1987; Dougherty and Stephens, 1988; Toksöz et al., 1991).

The chief advantage of the finite difference technique is that it is capable of propagating the complete wavefield through an arbitrarily complex model. The technique is accurate over a wide range of scattering regimes ($0.1 \leq ka \leq 1000$), and all wave types (direct, reflected, diffracted, and guided modes) are included in the solution. In addition, seismograms can be calculated at any point in the medium and "snapshot" pictures of the displacement field can be generated over the whole extent of the model. The snapshot pictures have proven to be extremely useful as they provide an excellent opportunity to view both mode conversion and coda generation. The main disadvantage of finite difference modeling is its computational burden. This has

proved to be the limiting constraint in extending the technique to three dimensions.

The finite difference scheme used throughout this study is presented in Appendix B. It is an explicit, second-order scheme in which displacements are propagated on a discrete grid. The material properties of the medium, λ , μ , and ρ are allowed to vary freely as a function of position and are discretized at the same spatial position as the wavefield. The second-order scheme was chosen because it was easy to implement and it allowed the two components of the displacement vector to be calculated at the same spatial position (unlike a staggered scheme, where displacements and stresses are calculated at different points in space). Also, the non-staggered scheme technique works well with published free surface and absorbing boundary conditions. The cost of these simplifications is a loss of accuracy, which we will show can cause observable errors in the wavefield.

The algorithm to numerically compute the single scattering solution is straightforward. First, the incident field is propagated one time step on a finite difference grid. The Born approximation states that the incident field is unaffected by the perturbations in the medium, therefore the velocity field for this simulation is the background field. Next, the source term arising from the interactions between the incident wave and the scatterers is calculated from Equation 3.9. This body force is then introduced into a second finite difference simulation which has the same background velocity model (Equation 3.10). The second finite difference simulation is updated one iteration and the process is repeated. If desired, the background (displacement) field may also be simultaneously propagated on the second finite difference grid, thus providing the total (single scattered) field.

It is important to note that the new technique is not meant to replace conventional finite difference techniques. It is simply a technique which can be used to obtain the single scattered solution for any complex velocity model. Therefore, this new technique and conventional finite difference modeling are complimentary, and for the case of an isolated point scatterer should converge to the same solution. In the next

section, we will exploit this, and use the conventional finite difference technique to assess the accuracy of the numerically derived single scattering solution.

3.2.4 Validation of the Single Scattering Solution

In this section, the scattered field due to a plane P-wave incident on a point diffractor is calculated using both the single and multiple scattering finite difference techniques. The incident wave was a Ricker wavelet with a center frequency of 60 Hz and the scatterer was a point diffractor with a 33% perturbation in μ . The resulting displacements were recorded by a circular array of receivers centered about the diffractor with a radius of 100 m (Figure 6).

To limit errors due to inaccuracies in the finite difference technique, the dominant wavelength of the source was sampled at 60 points per wavelength (PPW). Since the frequency band of the source extends to three times the center frequency and the medium was a Poisson solid, the highest frequency shear waves (waves with the shortest wavelengths) were sampled at a rate of greater than 10 PPW. At these sampling rates, the maximum errors due to the finite difference technique should be less than 5%, and at the center frequency errors should be less than 2% (Appendix B).

Figures 7 and 8 show the radiation patterns for P-P and P-S scattering for both the single and multiple scattering solutions. The radiation patterns were calculated by first converting the horizontal and vertical components of the displacement field to radial and transverse motion relative to the position of the scatterer. Then the traces were enveloped and the maximum displacement on the radial components was taken to be the P-wave radiation and the maximum displacement on the transverse component was taken to be the S-wave radiation.

From Figure 7 it is clear that the single scattering solution underestimates the scattered field in the forward direction, but overestimates the scattered field in the backward direction. There are two causes for this disagreement. First, the two techniques use different finite difference operators to find the gradient of the perturbation.

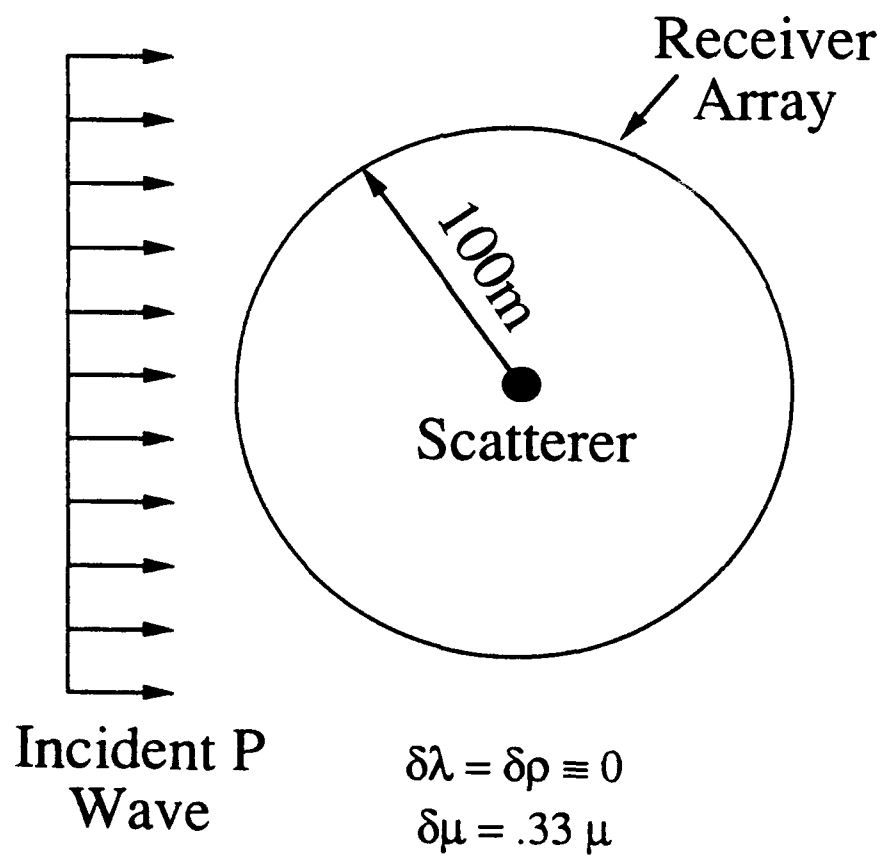


Figure 6: The source-receiver geometry used to validate the numerical single scattering solution.

Scattered P-wave (Point Diffractor)

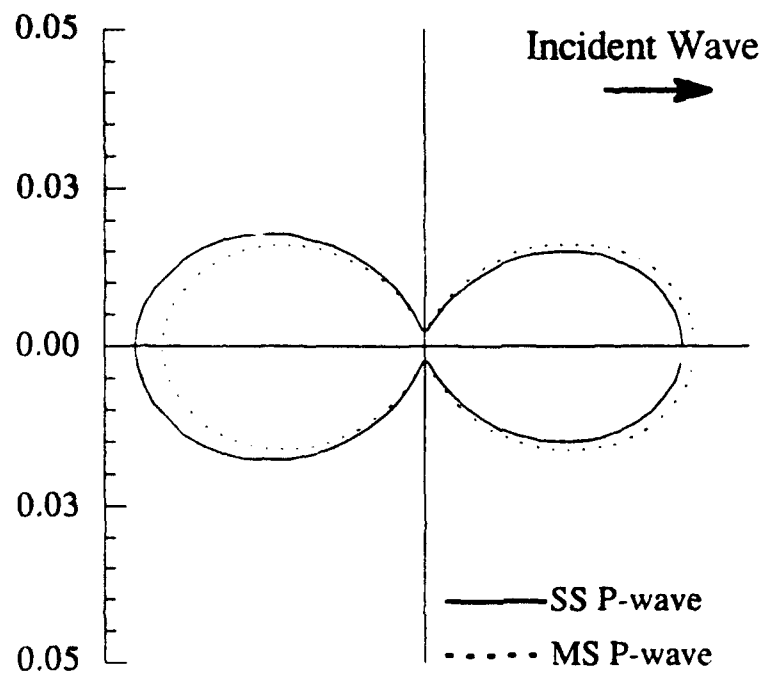


Figure 7: Comparison of the single and multiple scattering solutions for a plane P-wave incident on a point diffractor (33% variation in μ). Shown is the peak amplitude of the scattered P-wave as a function of angle.

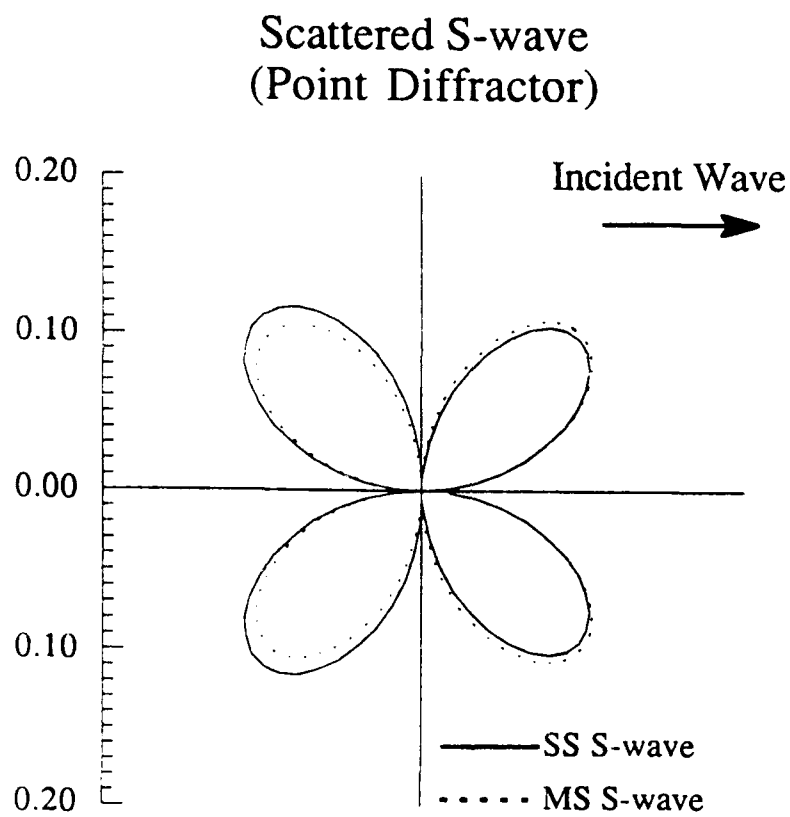


Figure 8: Comparison of the single and multiple scattering solutions for a plane P-wave incident on a point diffractor (33% variation in μ). Shown is the peak amplitude of the scattered S-wave as a function of angle.

The conventional finite difference technique (multiple scattering) uses a more accurate half-step finite difference. Second, errors in the finite differences arise due to the sharp gradients in the velocity model. These gradients cause the equivalent sources in the single scattering solution to be injected into the finite difference simulation without any spatial smoothing. The lack of smoothing introduced high wavenumbers into the displacement field, which are known to cause large errors in the solution (Appendix B). This problem could be minimized either by adopting a staggered finite difference formulation (Virieux, 1986), or by smoothing the velocity model slightly (Fornberg, 1987). The same general trends observed in the P-wave radiation are also visible in the S-wave radiation (Figure 8).

To isolate the errors caused by sharp gradients in the medium, the previous experiment was repeated for a slightly smoothed point diffractor. The smoothed point diffractor was constructed so that the velocity models had the shape of a two-dimensional Gaussian function ($\sigma^2=1$ grid spacing). The Gaussian shape was chosen because in wavenumber domain, the power spectrum is dominated by the low wavenumber components. As can be seen in Figures 9 and 10 the elimination of high wavenumbers in the model increased the accuracy of the solution. Notice that the overall shape of the radiation pattern is consistent with the previous point diffractor, but the amplitude of the scattered field is roughly three times greater. The increased amplitude is predicted from the analytical solutions, which shows that in the Rayleigh scattering regime the amplitude of the scattered field is proportional to the size of the scatterer (Appendix A).

This simple experiment demonstrates that there is sufficient agreement between the numerically calculated single and multiple scattering solution to warrant the use of our finite difference technique for calculating the single scattering solution. It was also shown that the accuracy of the single scattered solution is improved if the technique is limited to sufficiently smooth models. It is possible that adopting a staggered finite difference formulation would further improve the accuracy of the single scattering

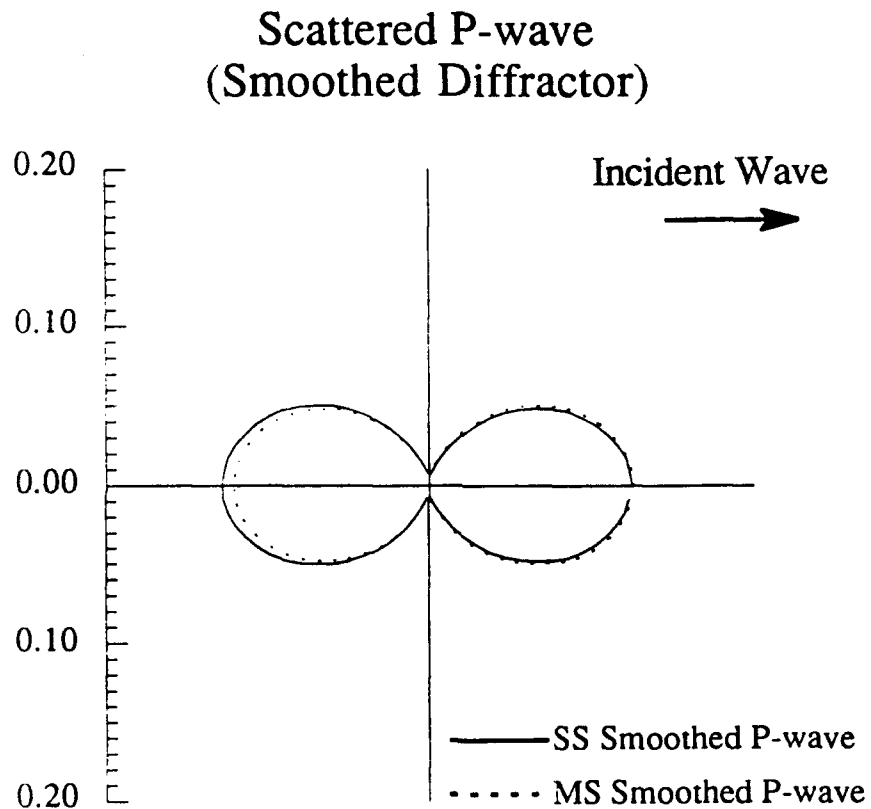


Figure 9: Same as Figure 7, but for the smoothed point diffractor. Notice the improvement in the equivalent source solution. The increase in size of the smoothed point diffractor is manifest in larger peak amplitude values in the scattered field (Appendix A).

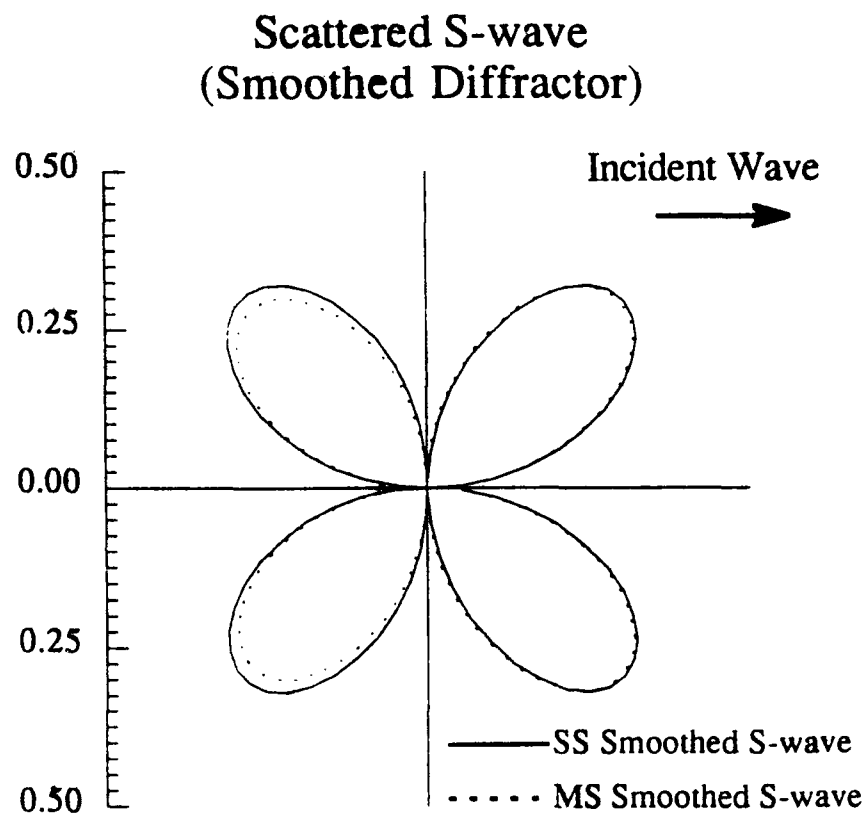


Figure 10: Same as Figure 8, but for the smoothed point diffractor. Notice the improvement in the equivalent source solution. The increase in size of the smoothed point diffractor is manifest in larger peak amplitude values in the scattered field (Appendix A).

solution, since that technique is more accurate in media with sharp discontinuities (e.g., Virieux, 1986; Stephen, 1988). For these reasons, the single scattering formulation will be used only on fairly smooth random media (such as those characterized by the Gaussian correlation function). Solutions for more textured random media (such as those characterized by the exponential or von Kármán correlation functions) will be postponed until the technique can be implemented using a staggered finite difference approach.

3.3 Single vs Multiple Scattering: A Case Study

Having established the validity and limitations of the finite difference technique for calculating the single scattering field, we can now compare the single scattering solution to the full, multiple scattering solution for two randomly heterogeneous media. Both velocity models (VEL and IMP) were generated from the same random realization for Lamé's parameter λ (Figure 11). The realization had Gaussian statistics with a mean of unity and 10% rms deviation. The spatial distribution of λ had a Gaussian correlation function, where the correlation length a of the medium was equivalent to the dominant wavelength of the source (29 m).

In one of the random media (VEL), the perturbations in the medium obeyed the following relationships,

$$\frac{\delta\lambda}{\lambda_0} = \frac{\delta\mu}{\mu_0} = -\frac{\delta\rho}{\rho_0}. \quad (3.15)$$

This combination of parameters produced random variations in both the shear and compressional wave velocities, but little variation in impedance (Figure 12). As a result, the majority of the scattering in this model is due to the velocity perturbations. In Appendix A this situation was referred to as velocity scattering and the scattered field from an isolated scatterer was shown to be dominated by forward scattering.

In the second model (IMP) the relationships between Lamé's parameters and

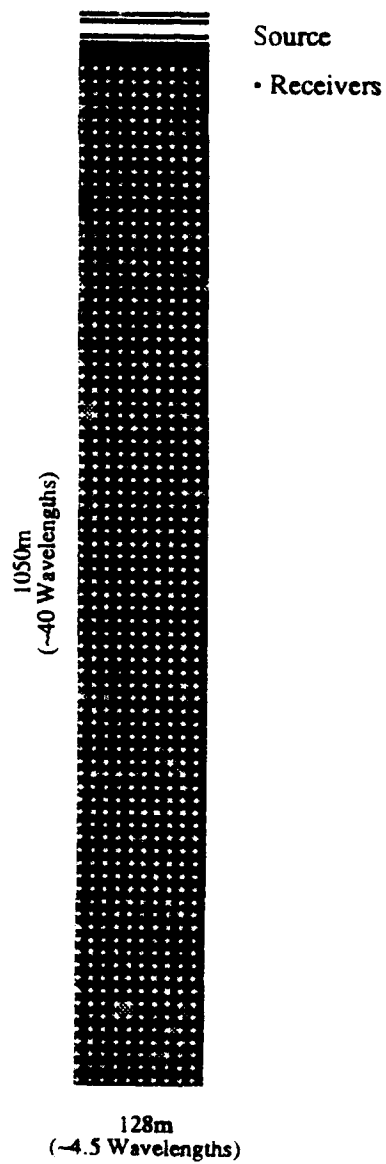


Figure 11: The realization of Lamé's parameter λ used to construct the two random media (VEL and IMP). The realization has Gaussian statistics, 10% rms deviation in λ and is characterized by a Gaussian correlation function with a correlation length of 29 m. The white dots are receiver positions.

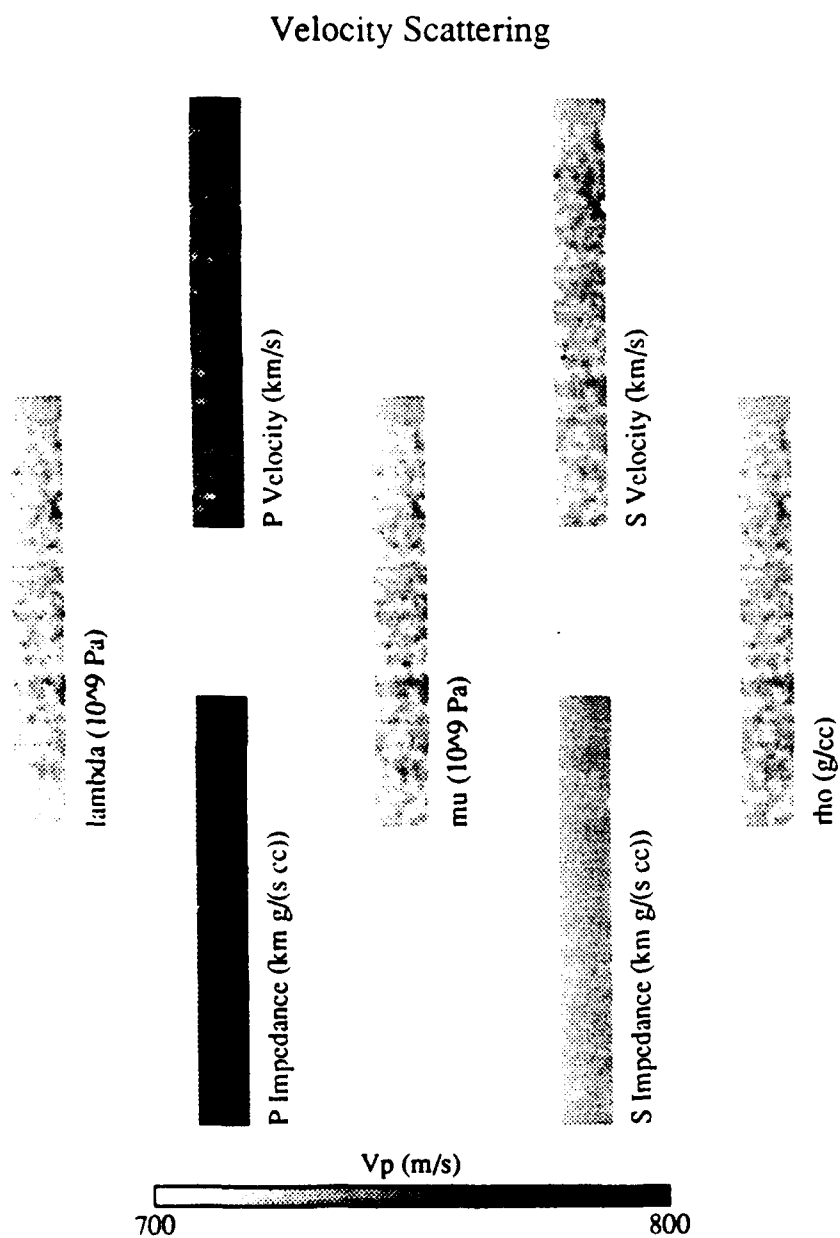


Figure 12: The P-wave and S-wave velocities, elastic moduli, density and P-wave ($\alpha\rho$) and S-wave ($\beta\rho$) impedances for the velocity scattering model.

density are given by,

$$\frac{\delta\lambda}{\lambda_0} = \frac{\delta\mu}{\mu_0} = \frac{\delta\rho}{\rho_0}. \quad (3.16)$$

A medium with this combination of parameters has no velocity variations, only impedance variations (Figure 13). In Appendix A it was shown that in these media P to P scattering is strongest in the backward direction. In addition, it was also shown that the magnitude of the backscattered field is inversely related to the size of the scattering body. Therefore, in this medium scattering should be strongest for low frequency waves.

In both media, the single scattering solution was obtained using the finite difference approach outlined above, and the multiple scattering solution was generated using a conventional finite difference formulation (Appendix B). The source was a plane P-wave which was introduced near the top of the grid. The source time function was a Ricker wavelet centered at 60 Hz, and the area around the source region was assumed to be homogeneous. In addition, the transition between the homogeneous and heterogeneous regions was smoothed to prevent reflections. To prevent contamination from the sides of the finite difference grid, the models were assumed to be horizontally periodic and absorbing boundary conditions were used on the top and bottom of the grids (Clayton and Engquist, 1977). Both models were 256 nodes wide and 2100 nodes long. The spatial grid spacing was $dx = 0.5\text{m}$ (60 points per wavelength (PPW) at 60 Hz). This resulted in a model which was 0.128 km (≈ 4.5 wavelengths) \times 1.05 km (≈ 40 wavelengths).

To compare the single and multiple scattering solutions, four separate simulations were made. The single scattering solution in the medium with velocity variations is denoted by SS_VEL, while that in the medium with only impedance variations is denoted by SS_IMP. Similarly, the multiple scattering solutions are labeled MS_VEL and MS_IMP. Synthetic seismograms (vertical component of the displacement vector) from the four simulations are shown in Figures 14 – 17. The individual seismograms within each plot have constant gain and since scattering in the impedance scattering

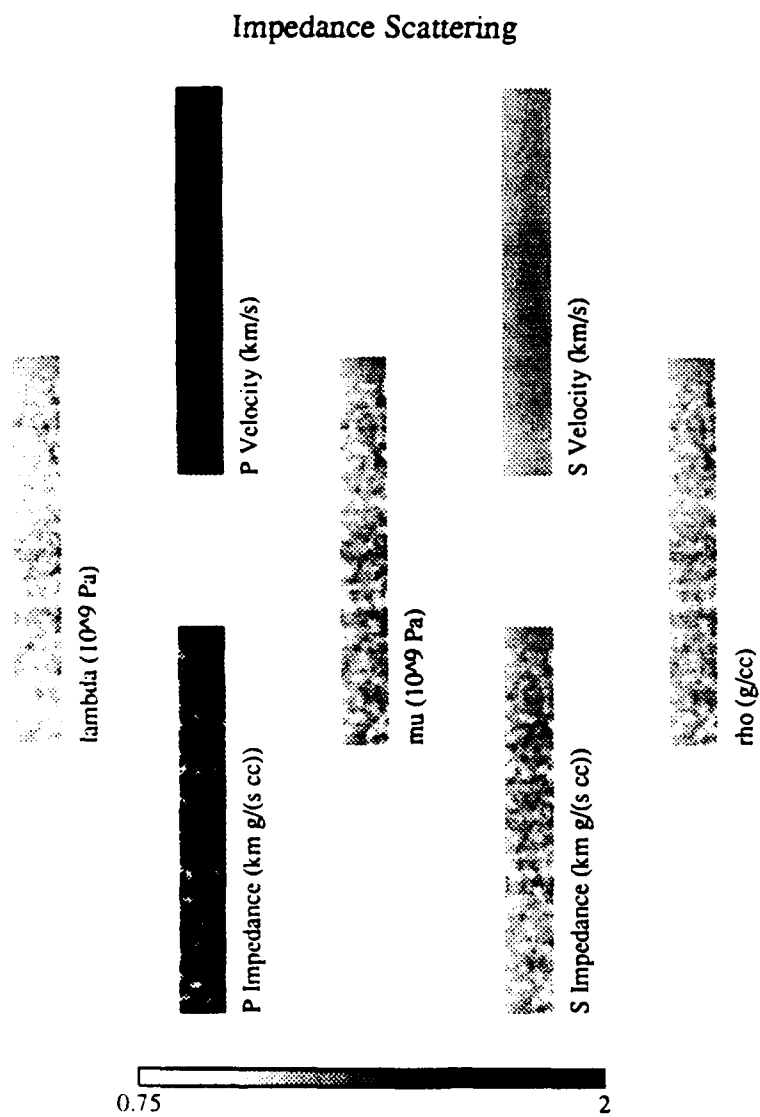


Figure 13: The P-wave and S-wave velocities, elastic moduli, density and P-wave ($\alpha\rho$) and S-wave ($\beta\rho$) impedances for the impedance scattering model.

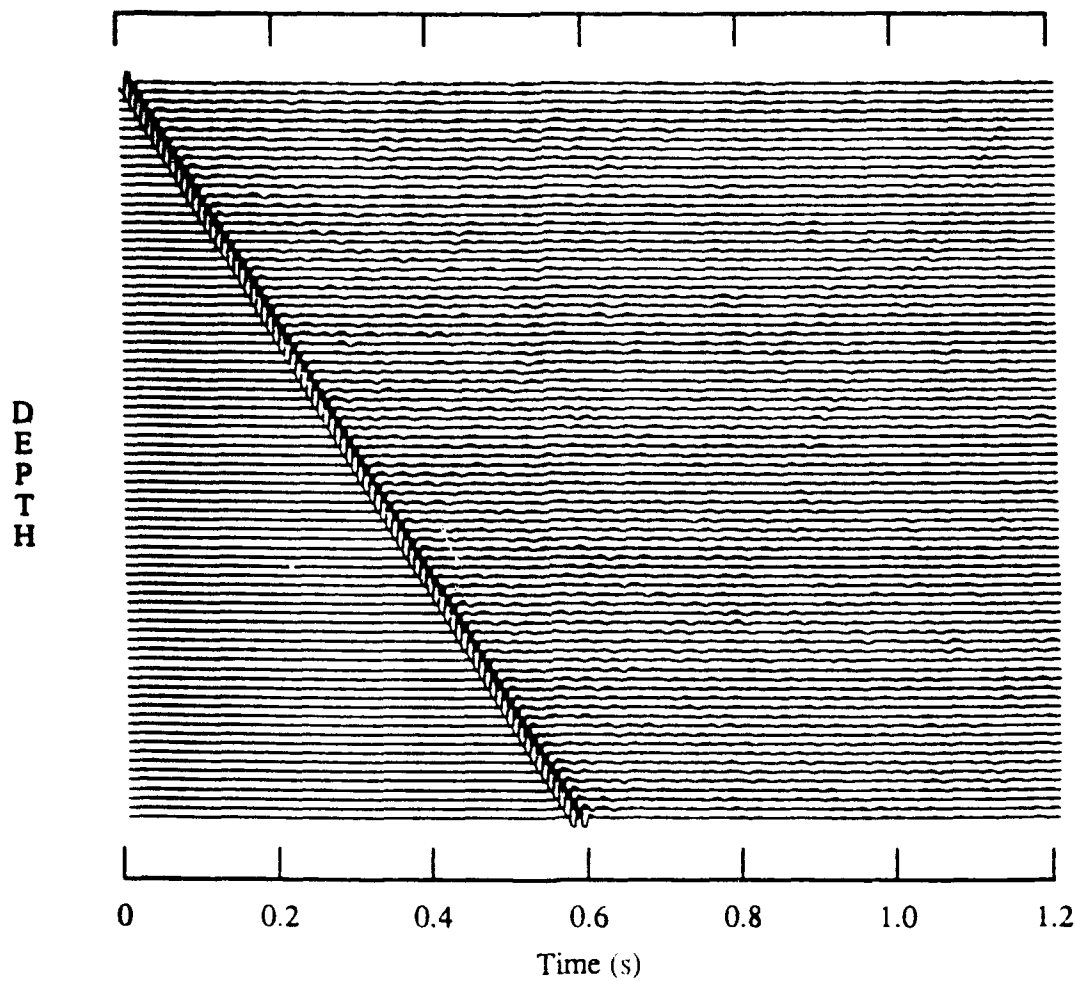


Figure 14: Synthetic seismograms from the multiple scattering solution in the impedance scattering medium. The distance between traces is 10% of the peak amplitude in the source. Scattering is small and seems to come from only relatively a few isolated scatterers.

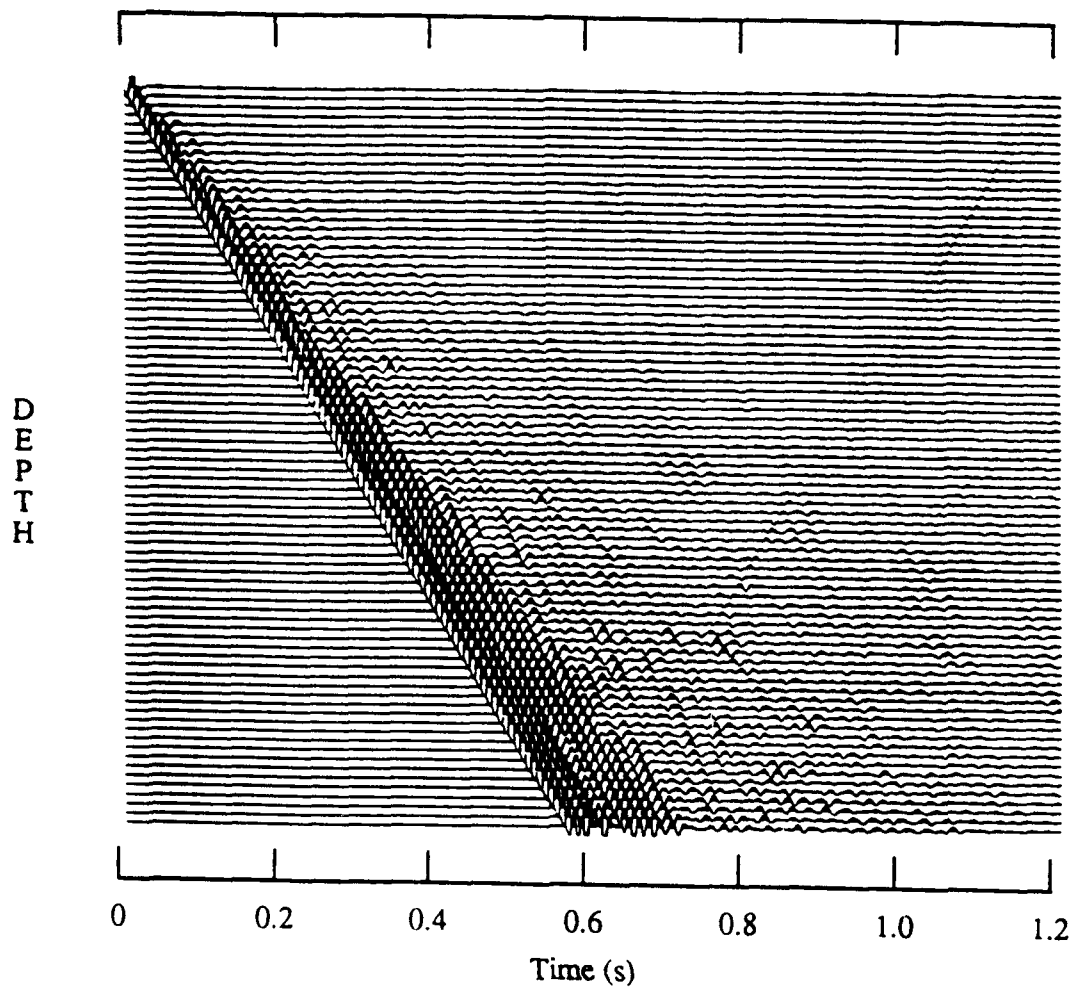


Figure 15: Synthetic seismograms from the single scattering solution in the impedance scattering medium. The scale is the same as Figure 14. Notice the similarity to the multiple scattering solution in the later arrivals, but the difference near the first arrival.

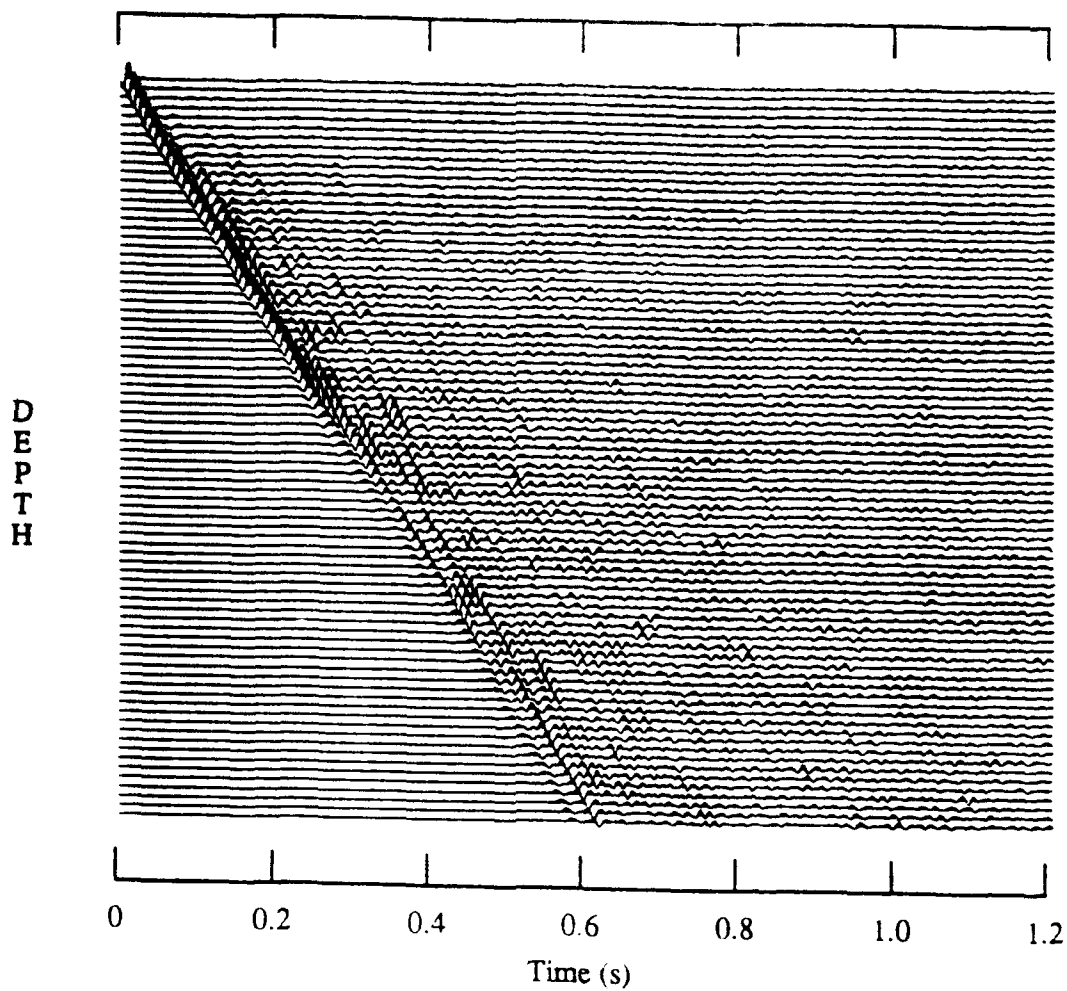


Figure 16: Synthetic seismograms from the multiple scattering solution in the velocity scattering medium. The scale is twice that in the previous figures to reflect the increase in scattering in the velocity scattering medium. Notice the lack of coherent arrivals in the coda and variations in amplitude and travel time in the first arrival.

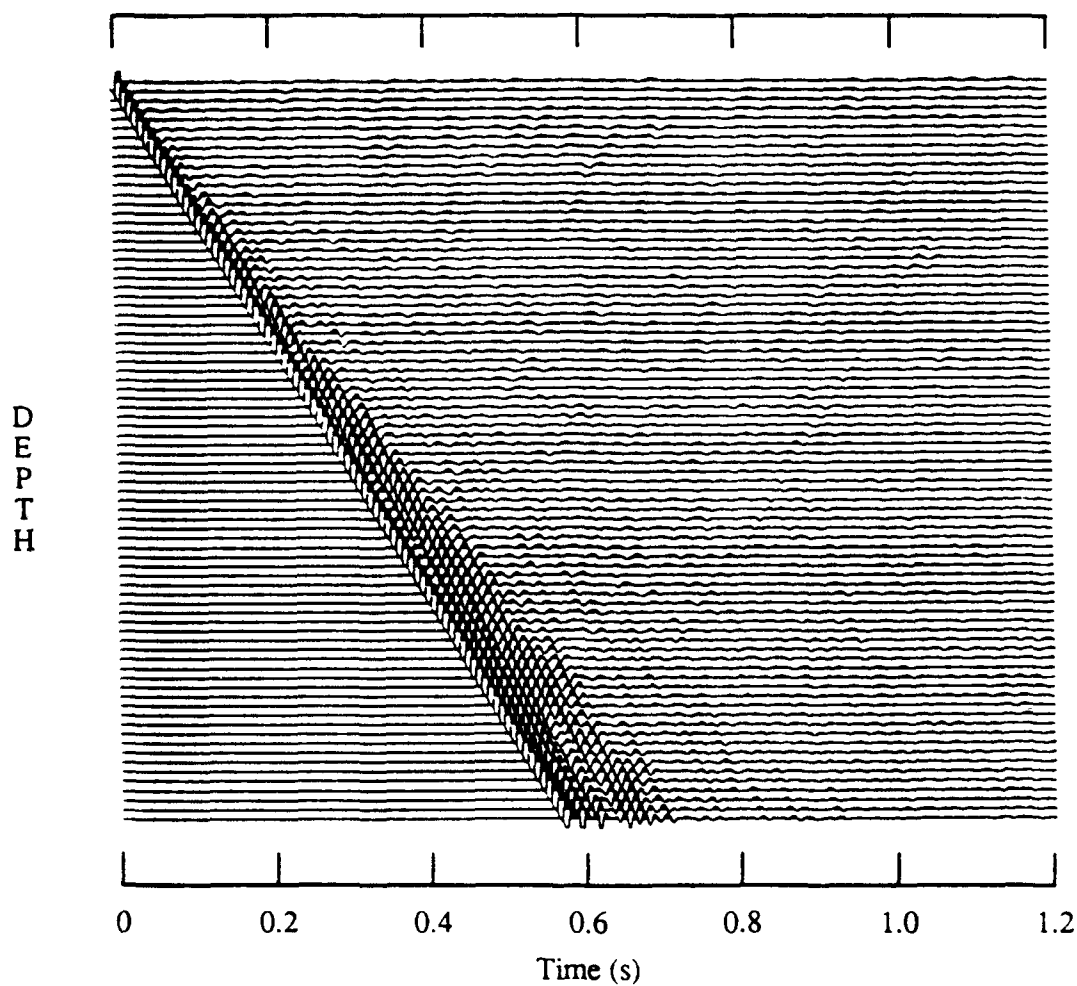


Figure 17: Synthetic seismograms from the single scattering solution in the velocity scattering medium. The scale is the same as that in Figure 16. Unlike the impedance scattering solutions, the single and multiple scattering solutions in the velocity scattering medium are quite different.

model was less than that in the velocity scattering model, seismograms from the impedance scattering model are shown at twice the scale. The detectable up-going wave in the seismograms from the impedance scattering models is a reflect from the bottom of the finite difference grid.

In the multiple scattering solution for the impedance scattering medium (MS_IMP), the most obvious feature is the relative lack of scattering. The incident wave travels through the medium with only minor fluctuations in amplitude and no travel time fluctuations (Figure 14). The amount of energy scattered from the incident wave is small and seems to emanate from only a few points in the medium. The scattered arrivals undergo little subsequent scattering and therefore appear as coherent arrivals across many neighboring receivers. Both from the particle motion (Figure 18) and from the moveout across the array, it is clear that the majority of the backscattered energy is P-wave energy.

The low magnitude of the scattered field is a consequence of the material parameters and the relatively large size and smoothness of the scatterers. The relationship between the perturbations favors backward scattering (Equation 3.16), but the size of the scatterers is large enough to effectively reduce backward scattering (Appendix A). With these two factors in mind, it is clear that low frequencies should dominate the scattered field. A plot of the power in the scattered field (where the scattered field is defined as the total multiple scattered field less the same incident wave traveling through a similar homogeneous medium) shows this to be the case (Figure 19a). When normalized to the power contained in the source pulse, this observation is made even more evident (Figure 19b).

Seismograms from the single scattering solution (Figure 15) look much like those from the multiple scattering, except for the concentration of energy around the first arrival. The excess energy is due to the accumulation of errors in the scattered field. These errors only affect the solution immediately following the incident wave and result because errors in the finite difference operator add in phase in the forward

Impedance Scattering Medium

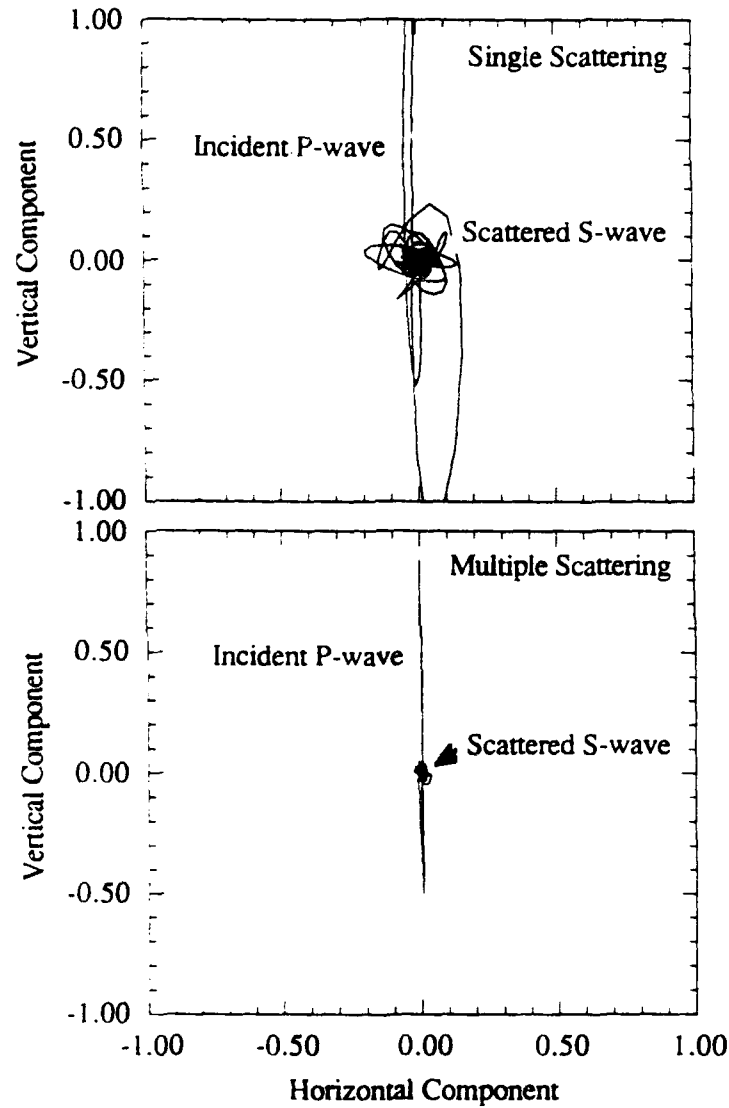


Figure 18: Hodogram (particle motion plots) from a receiver located at the center of the impedance scattering model. The hodogram is constructed from the multiple scattering solution and clearly demonstrates that the majority of the backscattered energy is due to P-wave to P-wave scattering.

Multiple Scattering Coda Wave Power (Impedance Scattering Model)

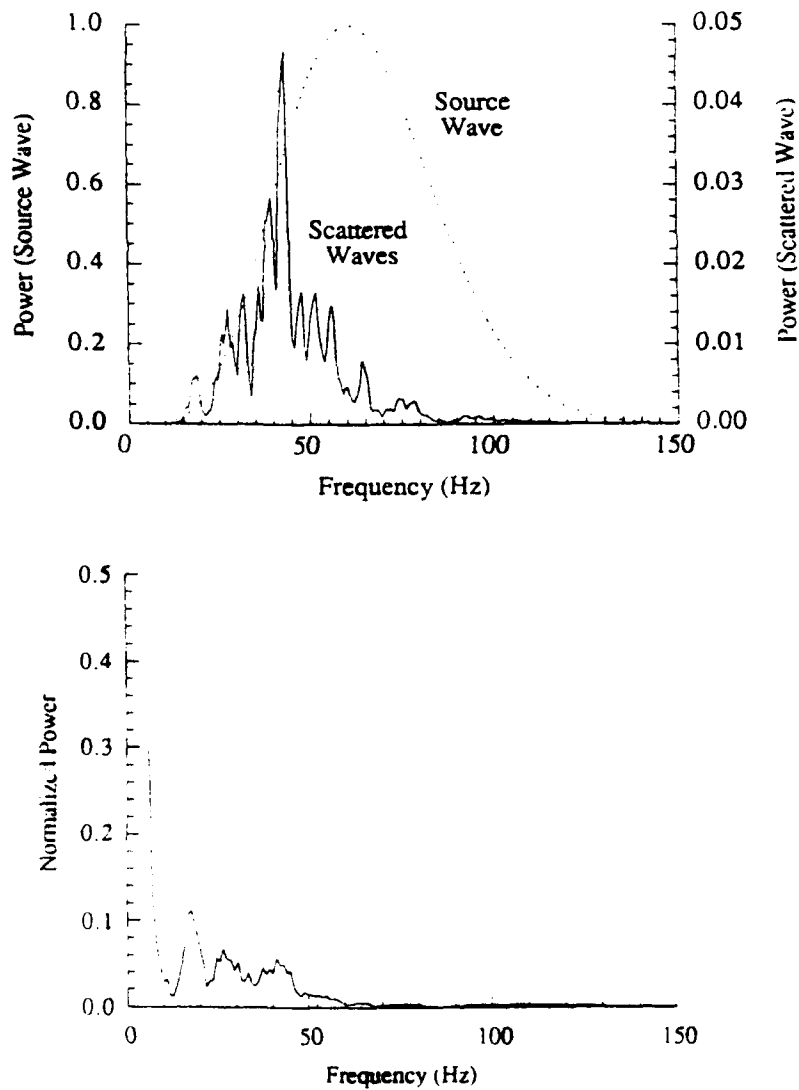


Figure 19: (Top) The power in the multiple scattered field from the impedance scattering model (magnified 20X) compared to that in the source pulse. (Bottom) The ratio of the power in the scattered wave to that in the source pulse. In this medium, the scattered field is dominated by low frequencies.

direction. It is important to stress however that these errors in no way affect the accuracy of the backscattered waves. Although the gain used in Figure 15 make the errors in the single scattering solution look extremely large, it should also be noted that even at the furthest offsets the amplitude of these errors are less than 10% of the amplitude of the incident wave. The latter part of the scattered field is generally overestimated under the Born approximation and the disparity between the single and multiple scattering solutions should be expected to increase with propagation distance. Enlarging and comparing some of the traces in Figures 14 and 15, it can be seen that except for the region around the first arrival, the two solutions agree very well (Figure 20). As expected, at far offsets the size of the scattered field is generally overestimated, but the general character of the late arrivals is still remarkably similar.

When the dominant form of scattering is velocity scattering, the difference between the multiple scattering and single scatter solutions is more obvious. Unlike the previous example, the multiple scattering solution to the velocity scattering model can contain significant travel time and amplitude variations in the first arrival, as well as significant amounts of energy late in the seismogram (Figure 16). Note the lack of coherent arrivals in the coda, as well as the frequency content of the coda. Compared to the impedance scattering medium, the coda has a wider frequency range (Figure 21), and it appears from these results that the maximum scattering in this medium occurs near the center frequency. These observations are consistent with earlier observations in both acoustic and elastic media (e.g., Chernov, 1960; Frankel and Clayton, 1986).

The most obvious difference between the single and multiple scattering solutions in the velocity scattering medium is the lack of late arrivals in the single scattering solution. This effect is most noticeable at near offsets (Figure 23). Also notice that in the single scattering solution, several scattered waves form coherent arrivals across neighboring receivers. This occurs because there is no secondary scattering of these waves. FK analysis of the coda reveals that most of the early arrivals result from

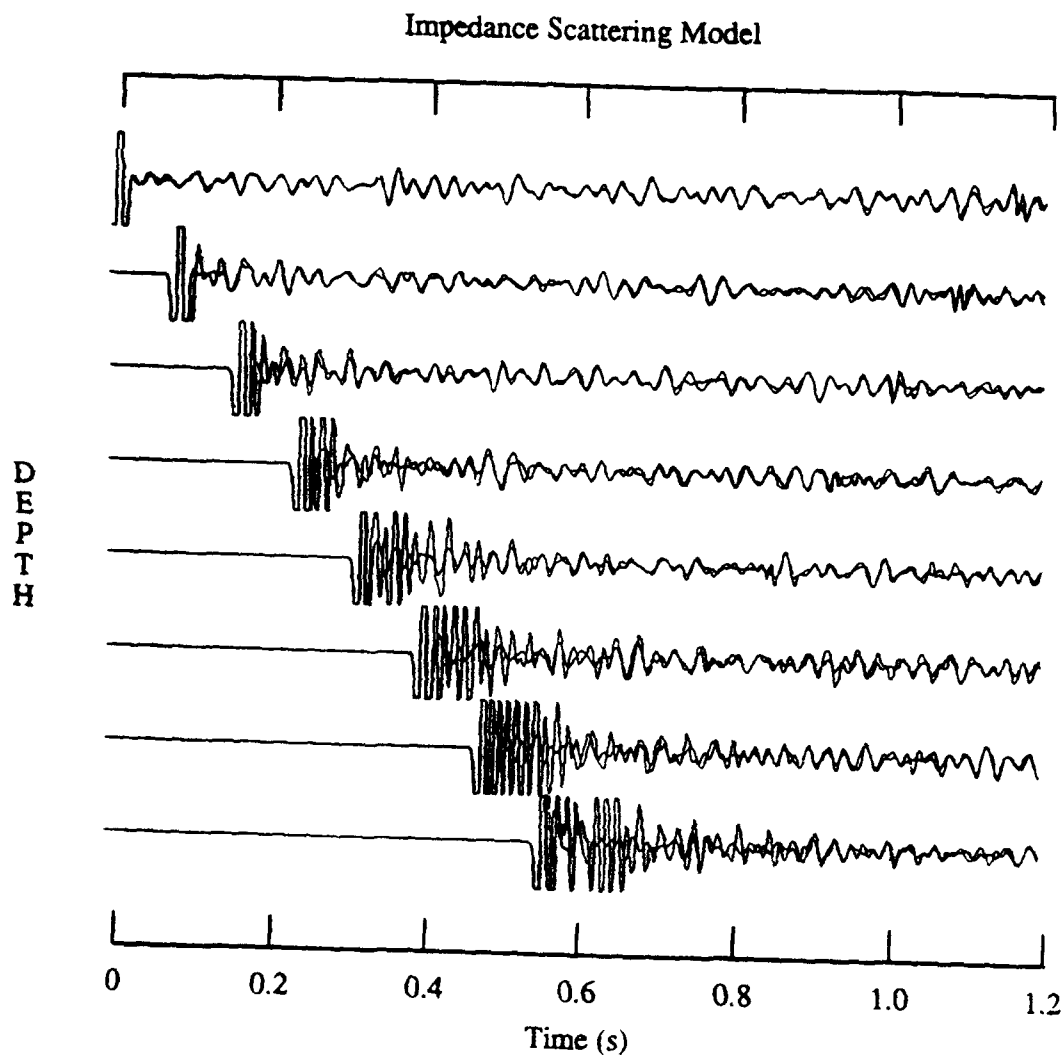


Figure 20: An overlay of the single and multiple scattering solutions from the impedance scattering medium show that the later arrivals agree very well. The disagreement near the first arrival is a consequence of the Born approximation.

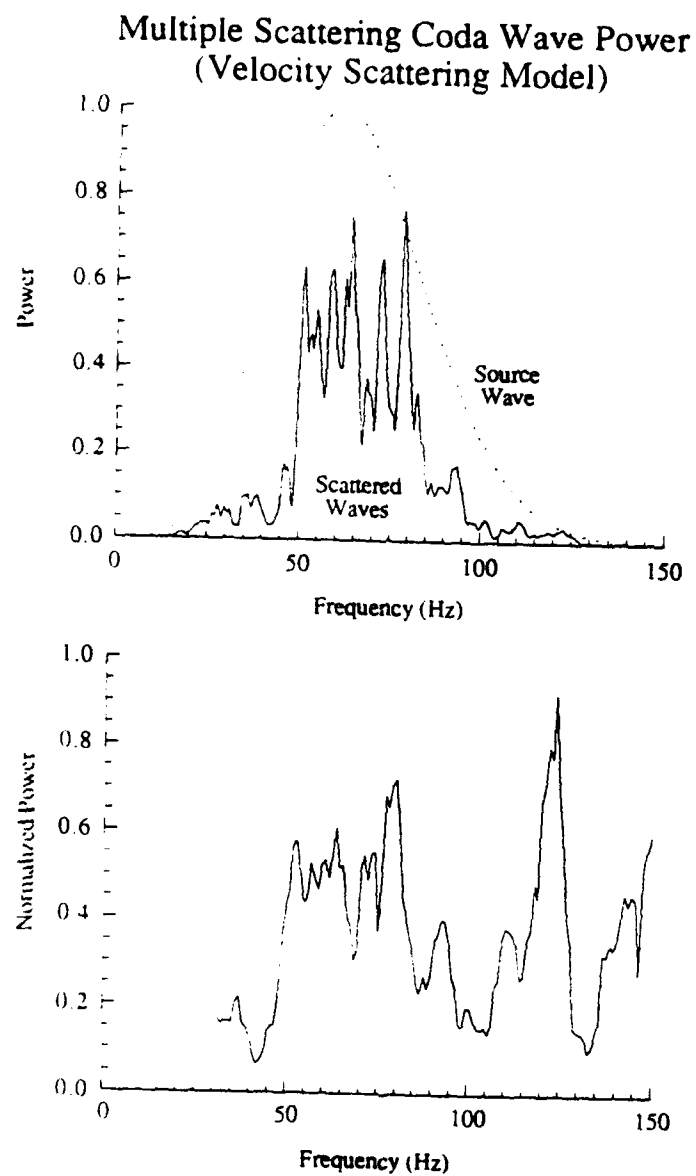


Figure 21: (Top) The power in the multiple scattered field from the velocity scattering model compared to that in the source pulse. (Bottom) The ratio of the power in the scattered wave to that in the source pulse. In this medium, there is significant power in the coda at all frequencies.

P to P scattering, while the later arrivals were dominated by P to S scattering. These observations were confirmed by particle motion analysis (Figure 22). Another important difference between the two solutions is the lack of travel time variations in the single scattering solution. This occurs because in the single scattering solution, the incident wave travels in the homogeneous background medium.

As was true for the previous random medium, the magnitude of the scattered wave increases with propagation distance in the single scattering solution, but decreases in the multiple scattering solution. Since the majority of the scattering in this medium is forward directed (Appendix A), there should be less frequency dependence in the coda. This is confirmed by Figure 21 which shows that there is little frequency dependence in the coda, except for possibly a slight peak near the center frequency. Plotting several of the seismograms in Figures 16 and 17 side by side shows that there is little agreement between the two solutions and highlights the lack of coda in the single scattering solution (Figure 17).

Power in the coda of the single scattering solution is significantly different than that in the multiple scattering solution (Figure 24a). Although there is power at low frequencies, the dominant feature in the data is the linear increase in power with frequency. When normalized to the source spectrum, it would appear that all of the high frequency energy in the source has been redistributed to the coda (Figure 24b). This is not a real effect, but an error due to the Born approximation. Beydoun and Tarantola (1988) found similar results for an acoustic medium and were able to show that the errors in amplitude of the transmitted wave increase linearly as a function of ωL , where ω is the angular frequency, and L is the propagation distance. Although the presentation here is based on forward modeling, the results are also consistent with Snieder (1990) who showed that inversion techniques based on the Born approximation are only capable of reconstructing the low wavenumber parts of the model. This occurs because upon inverse (Born) modeling, the wavefield is damped by a factor which is inversely proportional to frequency (or wavenumber).

Velocity Scattering Medium

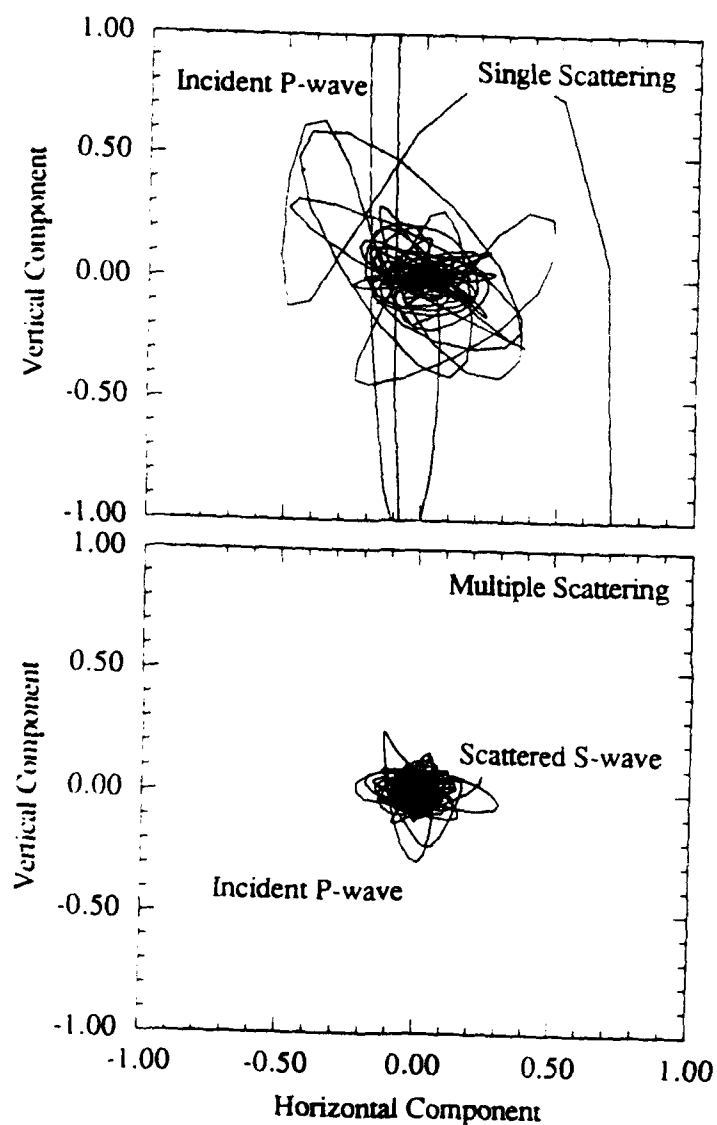


Figure 22: Hodogram (particle motion plots) from a receiver located at the center of the velocity scattering model. The hodogram is constructed from the multiple scattering solution. It was found from these hodograms that the early coda is dominated by P to P scattering and the later coda by P to S scattering.

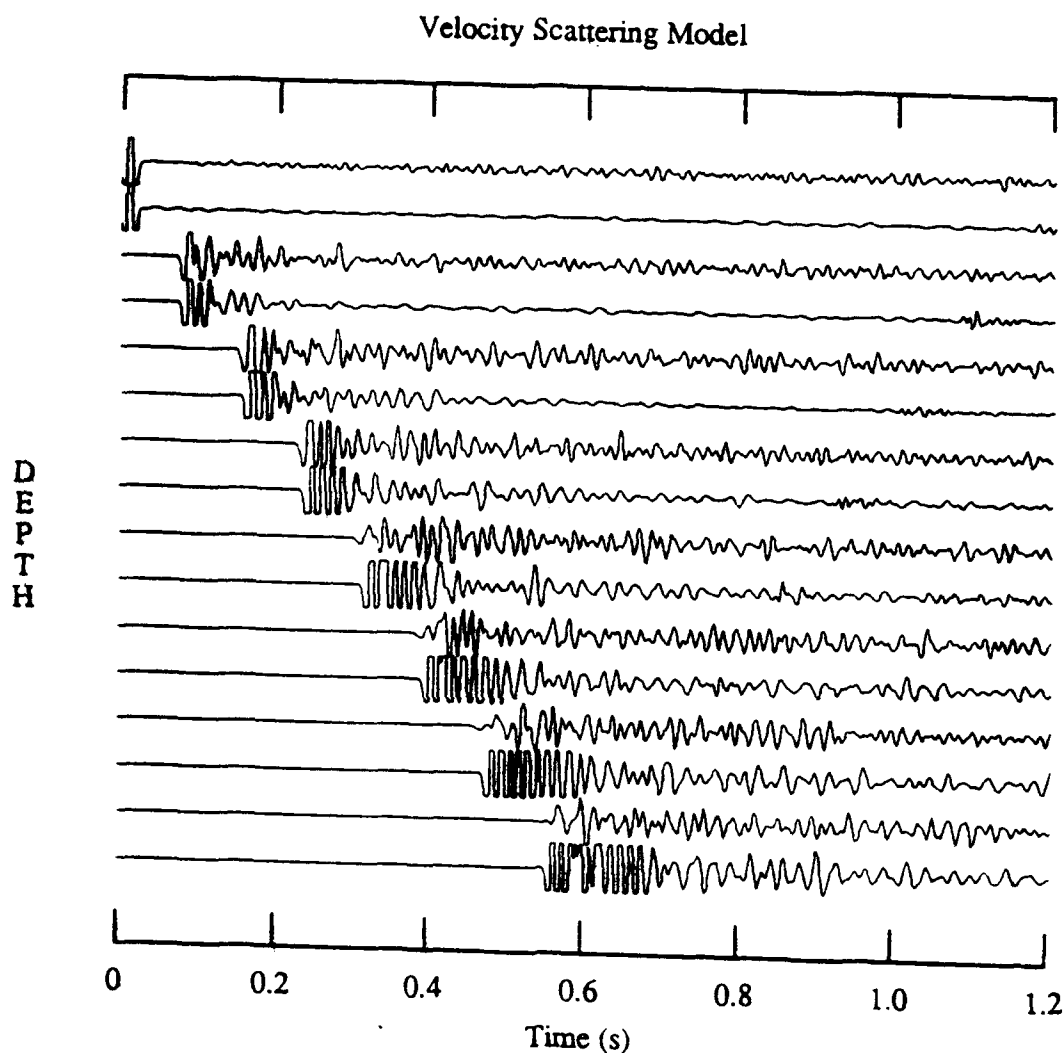


Figure 23: Seismograms from the multiple (top) and single (bottom) scattering solutions plotted side by side. Notice the lack of late arrivals at the near offsets in the single scattering solution. At far offsets, the single scattered field is dominated by P-waves near the first arrival and S-waves later in the coda.

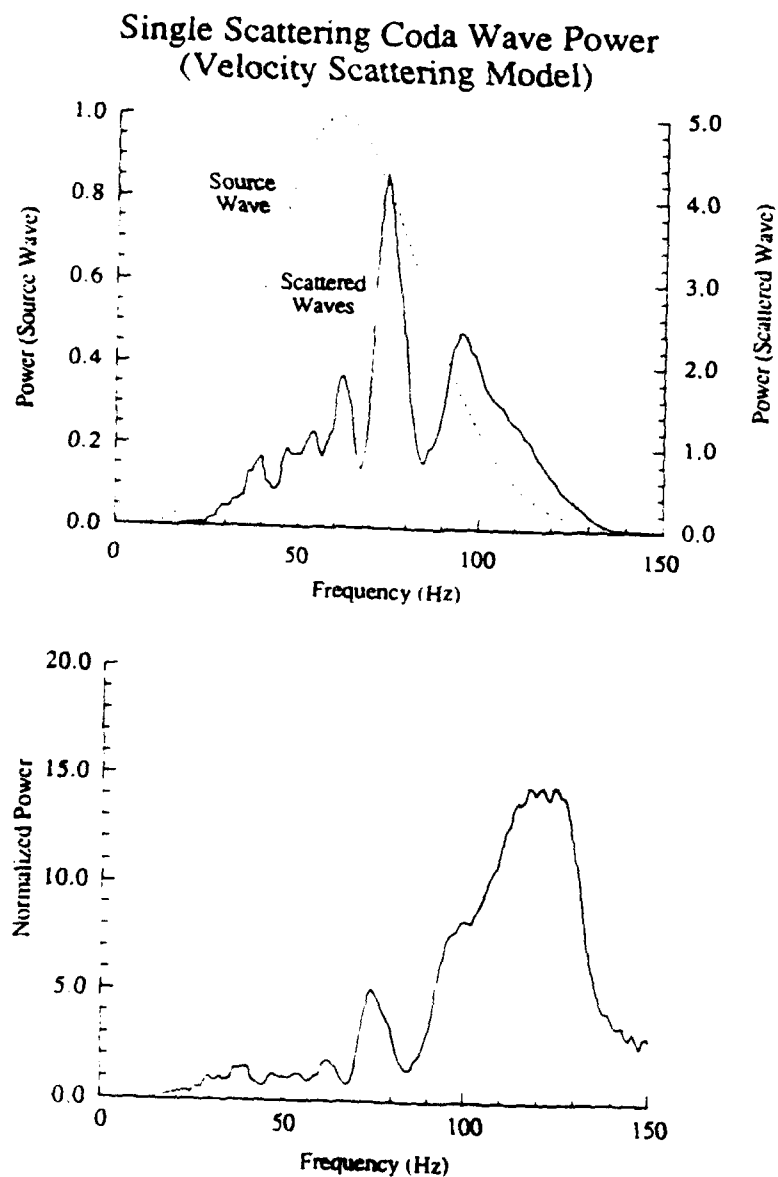


Figure 24: (Top) The power in the single scattered field from the velocity scattering model compared to that in the source pulse. (Bottom) The ratio of the power in the scattered wave to that in the source pulse. The power at high frequencies is largely due to errors introduced by the Born approximation.

3.3.1 Attenuation and Coda

One way to quantify the loss of energy due to scattering is through the dimensionless attenuation parameter Q . A variety of different techniques have been introduced to measure Q . One formulation relates the log decrement in amplitude of the transmitted wave to the propagation distance,

$$A(\omega, x) = A_0 e^{-\omega x / (2vQ_s)}, \quad (3.17)$$

where the incident wave is assumed to be a plane wave, A_0 is the initial amplitude of the transmitted pulse, ω is the angular frequency, x is distance, and v is velocity. This relation has been used to quantify the attenuation due to scattering (i.e. $Q = Q_s$) (e.g., Frankel and Clayton, 1986; Toksöz et al., 1988), as well as to describe the loss due to intrinsic attenuation (i.e. $Q = Q_i$) (e.g., Aki and Richards, 1980). As a result, this Q is often termed the scattering or transmission Q . The fact both processes can be explained by the same equation suggesting that it might be difficult to discriminate between attenuation due to scattering and intrinsic attenuation. This lead Aki (1980) to combine both type of attenuation when he studied scattering and attenuation of shear waves in the lithosphere.

Other measures of Q also exist. Aki (1969) suggested that seismic coda waves from local earthquakes are composed primarily of backscattered waves. He speculated the backscatter was caused by small-scale variations in the Earth's crust. Due to the large number and random distribution of these scatterers, he suggested treating the heterogeneities statistically. Aki and Chouet (1975) expanded on Aki's original work and presented a single scattering model in which the coda amplitude $A(\omega, t)$ is given by

$$A(\omega, t) \propto \left(\frac{\omega}{vQ_s} \right)^{1/2} t^{-a} e^{-\omega t / (2Q_c)}, \quad (3.18)$$

where v is velocity, a is a constant which depends on the geometrical spreading, Q_s is the "scattering Q " and Q_c is the "coda Q ". The term under the radical is often referred to as the turbidity of the medium and is proportional to the energy scattered

per unit distance traveled. Aki (1980) showed that in a medium without intrinsic attenuation the scattering Q is equivalent to the coda Q . Equation 3.18 was derived for either a point or line source, and thus not directly applicable for the geometry studied here.

Equations 3.18 and 3.17 represent two different measures for describing the rate energy is scattered by the medium. Q_c is derived from the coda of the seismogram, while Q_s is derived from the first arrival. Hudson and Heritage (1981) suggest that if the scattering region is strong, the Born approximation will be violated after some length of time because scattering from far away will be diminished by multiple scattering. They stress that the early scattering process is dominated by single scattering, but as the effective scattering region (i.e. the region between the source point and the incident wavefront) increases multiple scattering should become more important. This suggests that the rate of coda decay will be different between the two solutions at sufficiently long times.

To calculate the scattering Q , 955 seismograms from each of multiple scattering models were first bandpass filtered (± 5 Hz) around a series of frequencies (5, 15, 25, 35, 45, 55, 65, 75, 85, 95, 105, 115, 125, 135, 145, 155, 165 and 175 Hz), then enveloped. The natural log of the maximum value of the envelope was then plotted against distance and fit with a straight line (Figure 25). The slope of the line was then used to calculate Q_s as a function of frequency,

$$Q_s = \left[\frac{-\omega x}{2\alpha \ln [A(\omega, x)/A_0]} \right]. \quad (3.19)$$

This is the same procedure used by Frankel and Clayton (1986), except no correction for geometric spreading was necessary since the source was a plane wave. For all frequencies, the fall-off was roughly linear with distance. This suggests that the attenuation model presented in Equation 3.17 is capable of accurately explaining attenuation due to scattering in these media. Since this method uses the decrease in amplitude of the transmitted wave to calculate Q , it is not appropriate for the single scattering solutions, in which the amplitude of the total field increases with propa-

Multiple Scattering

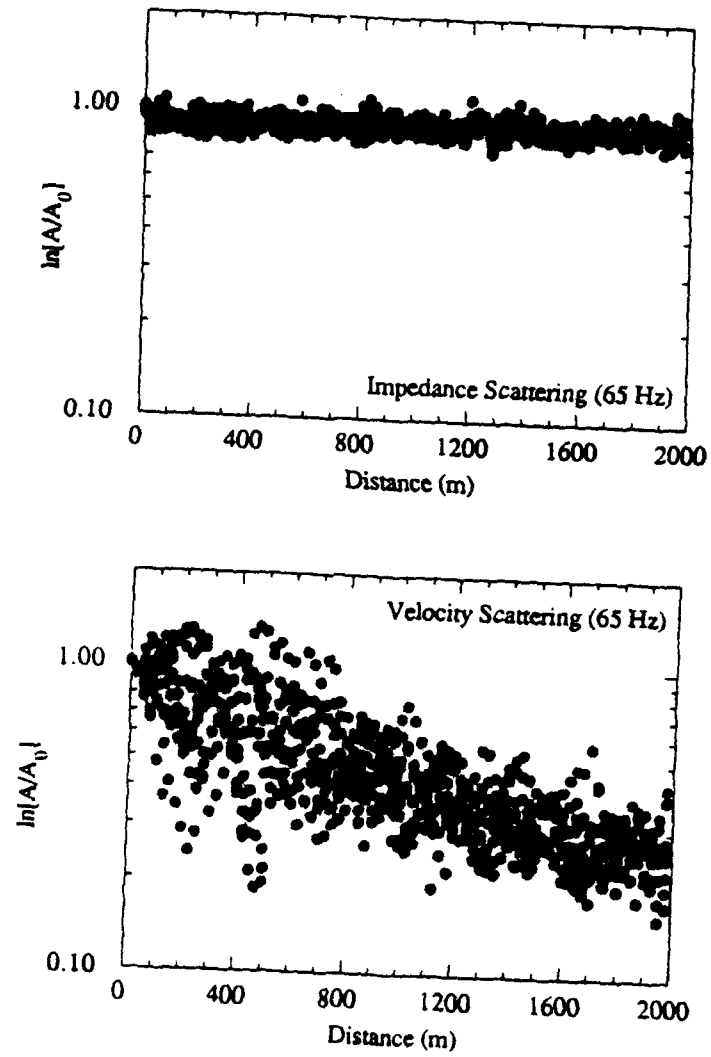


Figure 25: Logarithm of the peak amplitude after the data were bandpass filtered ($60 \pm 5 \text{ Hz}$), and enveloped. These are some of the data used to compute Q_t for the impedance (top) and velocity (bottom) multiple scattering media.

gation distance.

The calculated attenuation curves for the two models are shown in Figure 26. As expected, attenuation is greatest at low frequencies in the impedance scattering medium. At higher frequencies the attenuation curve falls off quickly, $\approx (ka)^{-4}$. The attenuation curve for the velocity scattering medium was clearly different. Attenuation increases with frequency until $ka \approx 1$, then at higher frequencies decreases slowly. This behavior has been observed in both elastic (Frankel and Clayton, 1986) and acoustic (Chernov, 1960) media which are characterized by the Gaussian correlation function. The attenuation curves confirm what was evident on the seismograms; the velocity scattering medium scatters more energy from the incident wave than the impedance scattering medium. Since the medium is assumed to be perfectly elastic, energy scattered from the primary wave must eventually be recorded as coda by another receiver. At low frequencies (25 Hz), the two media show comparable amounts of coda and similar coda decay rates (Figure 27). At higher frequencies, the velocity scattering medium has more coda, but still has roughly the same coda decay rate, indicating this coda decay rates by themselves cannot be used to distinguish between velocity and impedance scattering (Figures 28 – 29).

As was mentioned earlier, another measure of attenuation is the rate at which the code decays. Figures 27 – 29 show the rate of coda decay in the single and multiple scattering solutions for both random media. The data used in these figures are taken from the 40 second window shown in Figures 14 – 17. The raw time series was first bandpass filtered, enveloped, and then plotted in semi-log format. Several interesting features emerge from the data. At low frequencies (25 Hz), the coda in the impedance scattering medium is nearly flat and there is little difference between the single and multiple solutions (Figure 27). The agreement is not as good in the velocity scattering medium, but the rate of coda decay is still consistent between the two solutions. Near the center frequency (Figure 28), there is more slope to the coda curves and in both media the two solutions are no longer similar. The same trends persist at the

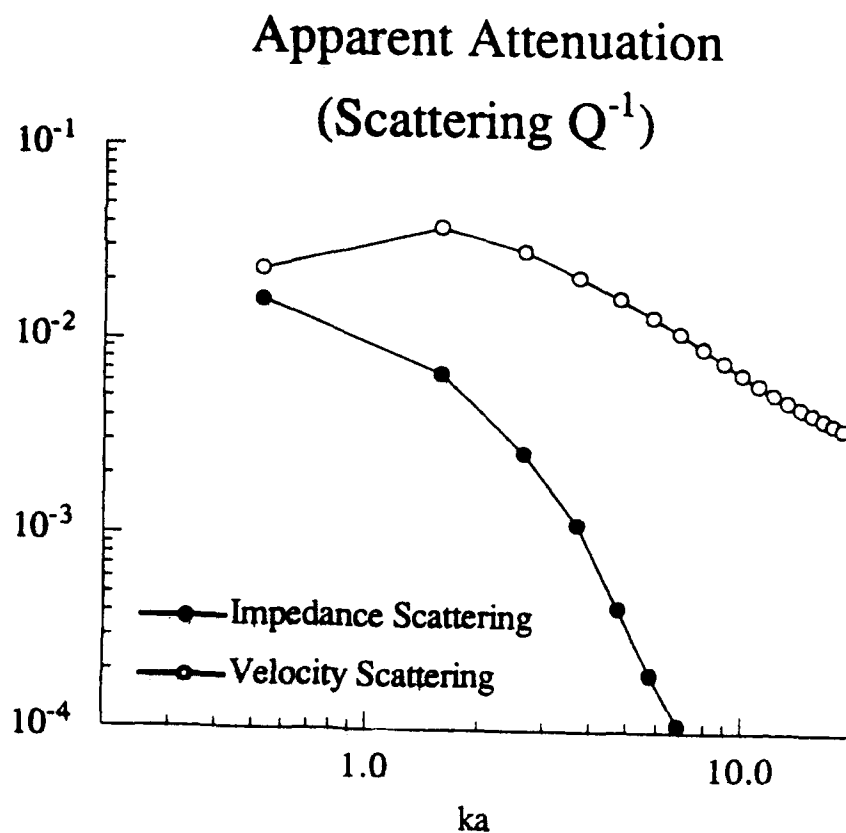


Figure 26: Attenuation as a function of normalized frequency ka for the two random media. In the velocity scattering medium, attenuation peaks near $ka=1$, while in the impedance scattering attenuation is greater for low frequencies.

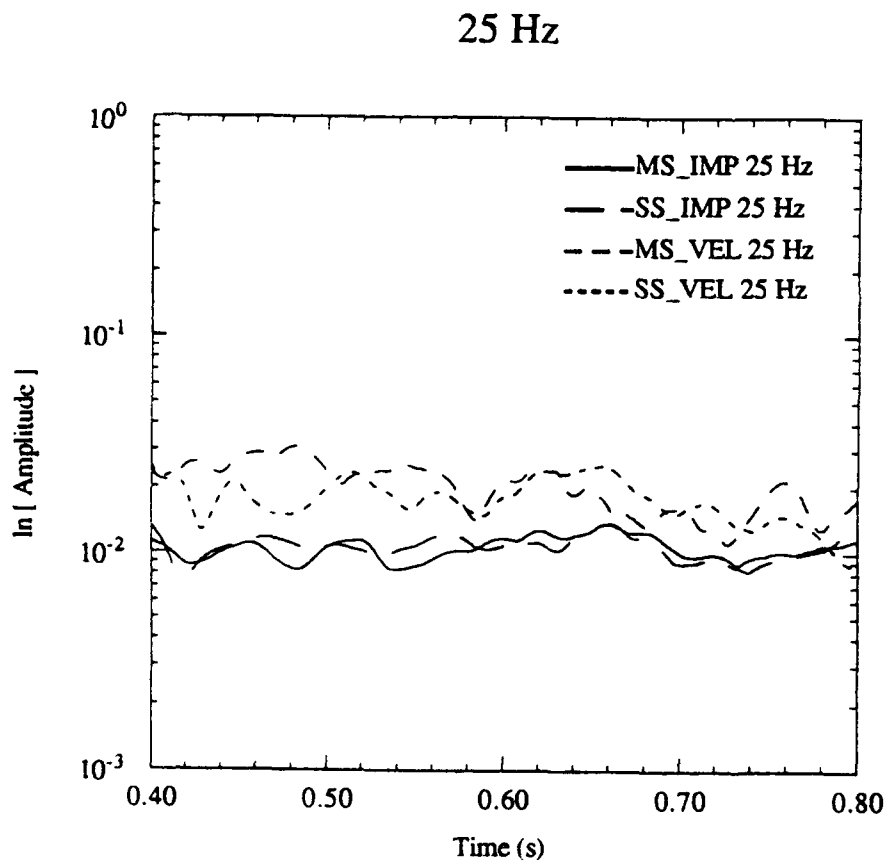


Figure 27: Coda decay rates at 25 Hz for the four models investigated here. Data were taken from the center of the models (Figures 14–17) and were windowed (.4–.8 sec), enveloped and plotted on semi-log axes.

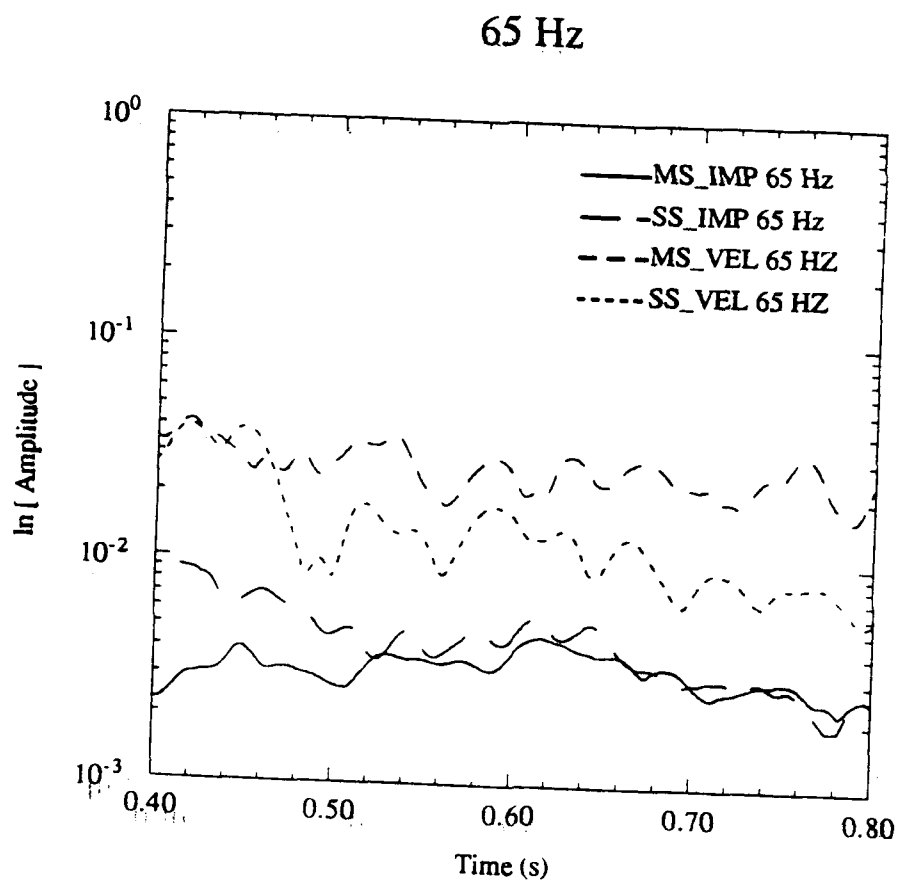


Figure 28: Same as Figure 27, but bandpass filtered around 65 Hz. At 65 Hz, the single and multiple scattering solutions begin to diverge.

105 Hz Coda

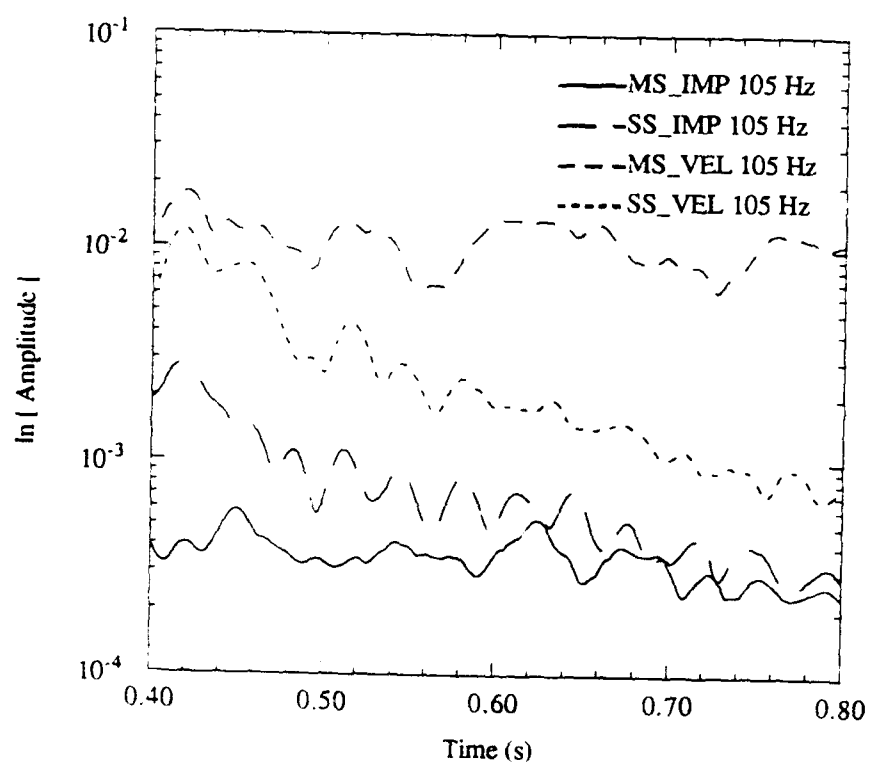


Figure 29: Same as Figure 28, but bandpass filtered around 105 Hz. Note the rate of decay in the single scattering solutions is faster than that in the multiple scattering solutions.

highest frequency (Figure 29), where the single scattering solution clearly decays faster than the multiple scattering solution. This is the most familiar distinction between the single and multiple scattering solutions. Reasoning along these lines, one must conclude that any attempt to use single scattering theory to estimate coda Q in a medium with significant multiple scattering will tend to underestimate the true Q of the medium.

3.4 Overview of the Scattering Process

In scattering studies, the divergence and curl of the displacement field are often calculated as a means of estimating the relative amounts of P-waves and S-waves. Strictly speaking this is only valid when the medium is homogeneous. If the medium contains perturbations, the gradient of the perturbations also contribute to the divergence and curl of the wavefield and as a result, the two modes (P-waves and S-waves) are not completely decoupled. With these limitations in mind, the divergence and curl of the displacement field are shown for the four simulations discussed above (Figures 30 – 33).

The divergence snapshots from the impedance scattering model show a clear difference between the multiple (Figure 30) and single (Figure 31) scattering solutions. Since there are no velocity variations, travel time variations in the direct P-wave are small for the multiple scattering solution. This is contrary to the single scattering solution, which contains both amplitude and travel time variations. These variations are due to transmission errors inherent in the Born approximation (Beydoun and Tarantola, 1988) and are even more pronounced in the velocity scattering model (Figure 33). The agreement between the single and multiple scattering solutions is much better in the curl snapshots (Figures 30 and 31). Here, the snapshots are nearly identical.

The wider range of frequencies in the scattered energy is clearly visible in the

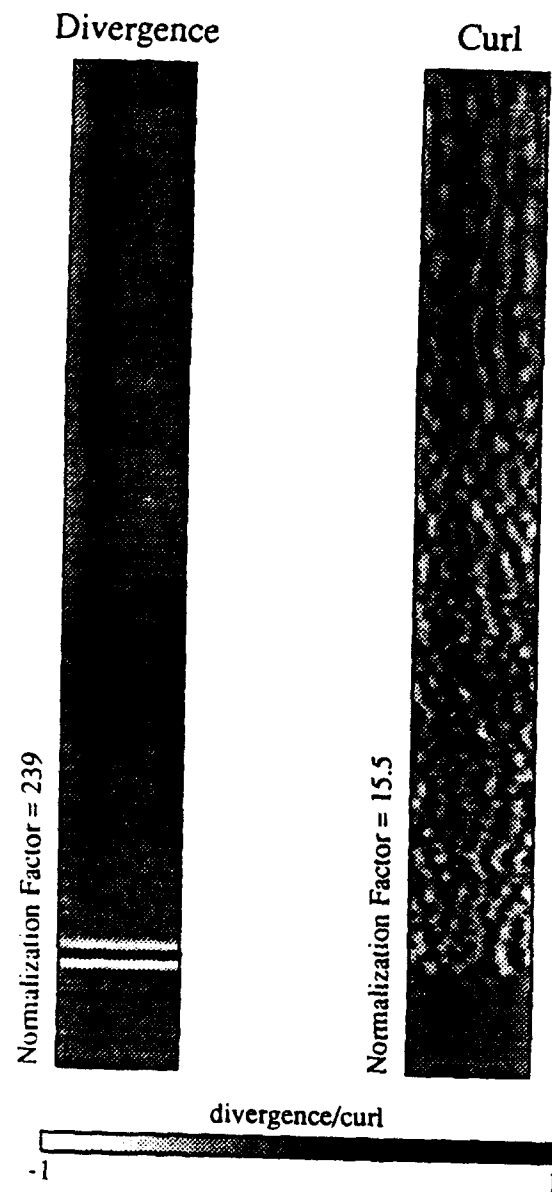


Figure 30: Snapshot picture of the divergence and curl of the displacement field at $t = .52$ s.
Shown here is the multiple scattering solution from the impedance scattering medium.

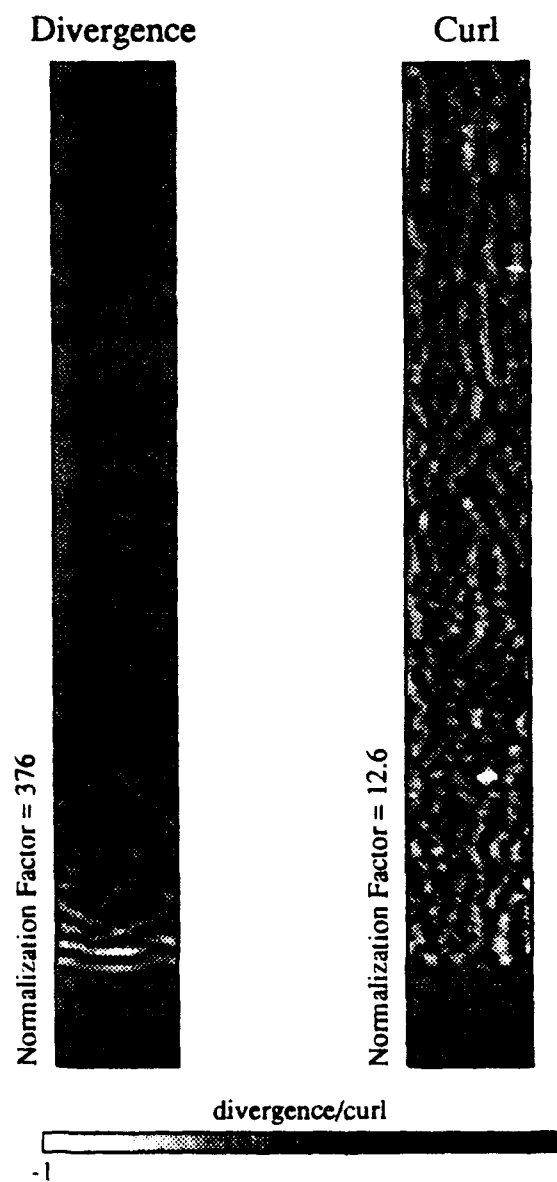


Figure 31: Same as Figure 30, but calculated using the single scattering technique.

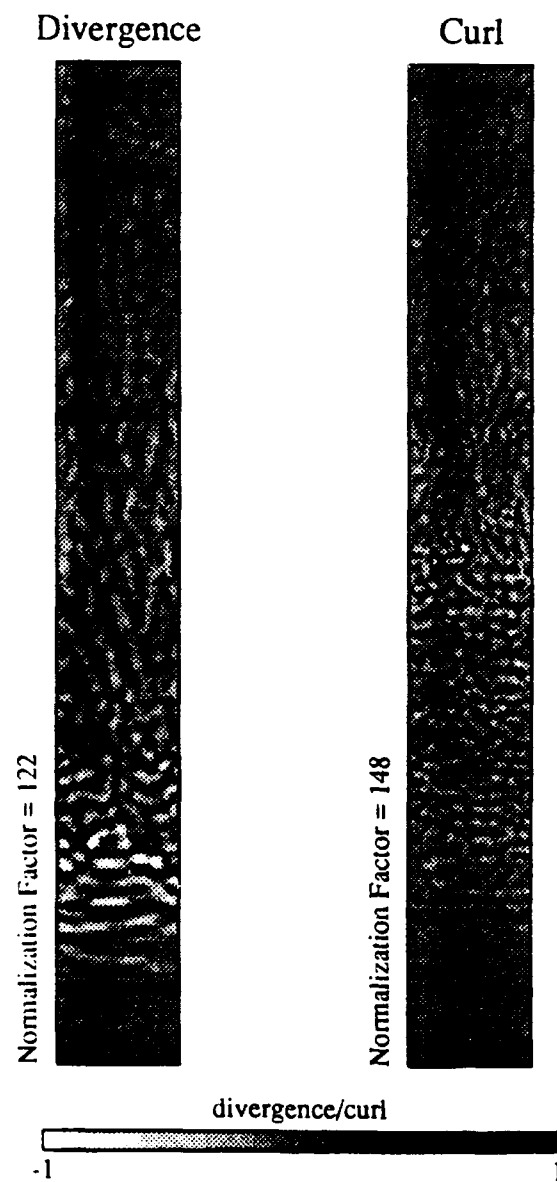


Figure 32: Snapshot picture of the divergence and curl of the displacement field at $t = 52$ s.
Shown here is the multiple scattering solution from the velocity scattering medium.

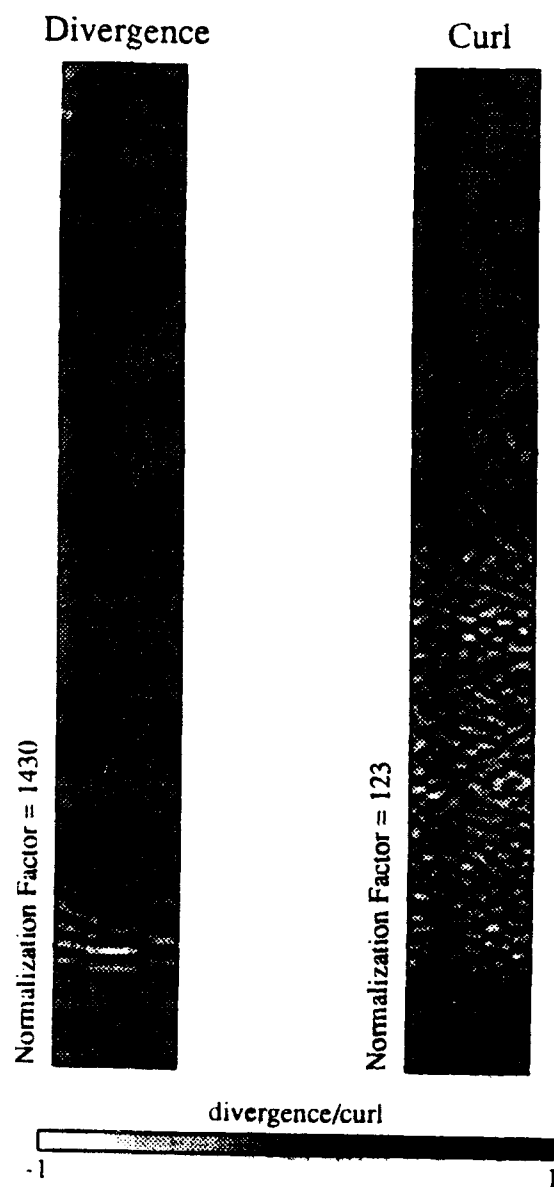


Figure 33: Same as Figure 32, but calculated using the single scattering technique.

results from the velocity scattering models (Figures 32 and 33). Note the complete loss of a coherent direct arrival in the multiple scattering solution. Also interesting, is the ratio in the peak divergence to peak curl. Note that unlike the previous example, the curl snapshot is quiescent near the first arrival and strongest late in the coda. This implies that multiple scattering may be important in the generation of S-waves.

The divergence snapshot from the velocity scattering medium (Figure 33) is very similar to that from the impedance scattering medium (Figure 31). The cause of this seems to be the accumulation of errors in the Born approximation. The curl of the single scattered field shows the importance of multiple scattering in this medium. Unlike the snapshot from the multiple scattering solution, there is evidence of significant P to S wave scattering near the first arrival. These arrivals are clearly visible across the model, were as in the multiple scattering solution they are not.

3.5 FK Analysis

One of the advantages of the finite difference technique is that seismograms can be calculated for the divergence and curl, as well as displacements. We use that ability in this section to Fourier transform those data and form frequency-wavenumber (F-K) plots of the the divergence (dominated by P-waves) and curl (dominated by S-waves). F-K analysis is a useful technique to illustrate the magnitude and direction of the scattered field.

The time window used for these analysis was the whole seismogram. Therefore, in the impedance scattering media the dominant feature in the F-K plots of the divergence is the direct P-wave (Figures 34 and 35). The P-wave in the multiple scattering solution shows no variation in propagation direction, while in the single scattering solution the P-wave is less well constrained. The S-wave plots show the S-wave is strongly side scattered and in the single scattering solution there is some backscattering of S-waves. Except for this backscattering, the F-K contours agree

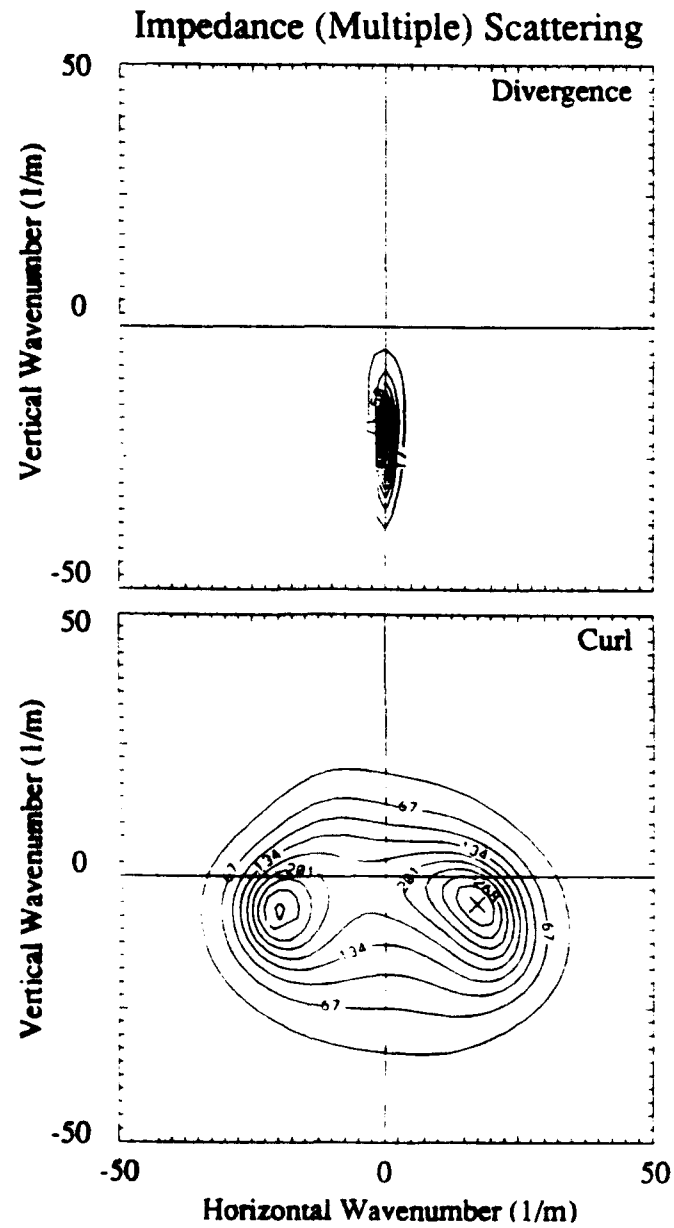


Figure 34: F-K plot of the divergence and curl of the (multiple scattering) wavefield in the impedance scattering medium shows clear separation between the two phases.

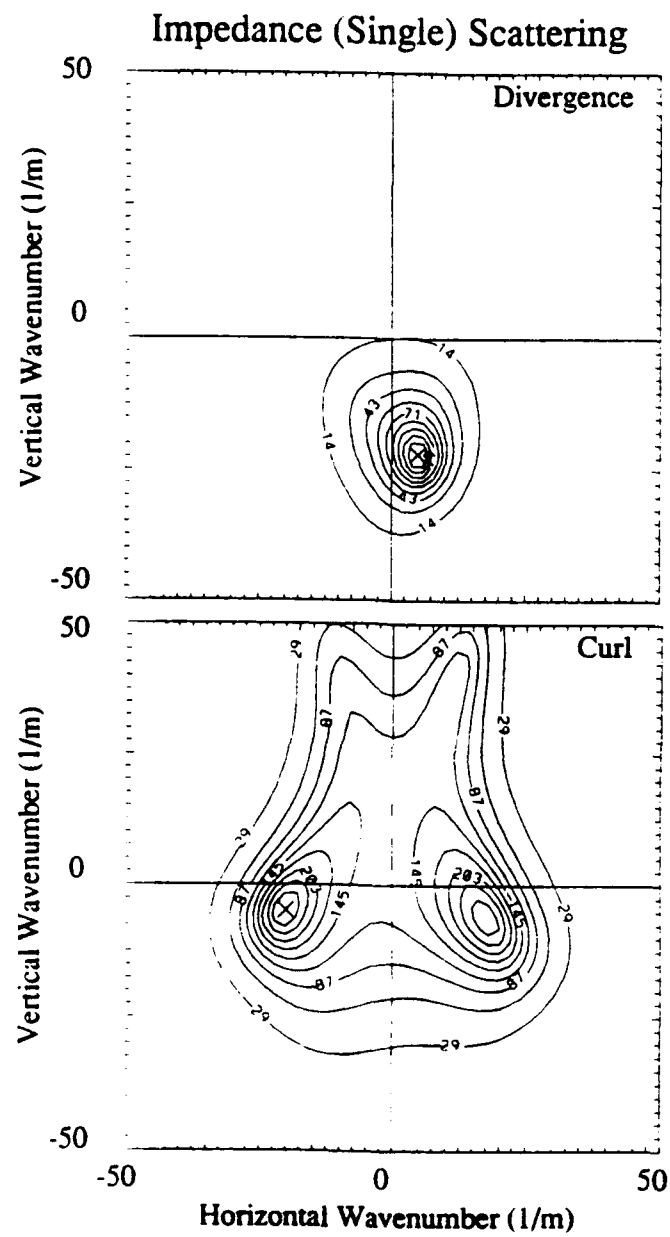


Figure 35: F-K plot of the divergence and curl of the (single scattering) wavefield in the impedance scattering medium shows clear separation between the two phases.

well for the S-waves.

Data from the velocity scattering media show that in the multiple scattering solution, both P and S waves are scattered over a broader range of angles (Figure 34). This is consistent with earlier findings that multiple scattering is important in this medium. The single scattering solution in this medium lacks the wide range of scattering angles observed in the multiple scattering solution (Figure 35). It is also interesting to note that the F-K plots for both the divergence and curl are nearly identical to those for the single scattering solution in the impedance scattering medium. The only difference is a slight forward shift in the S-wave energy and slightly more forward scattering of P-waves.

3.6 Conclusions

In this chapter, a new technique was developed which is capable of calculating the single scattering solution in an arbitrarily complex medium. First, the technique was validated by comparing the single and multiple scattering solutions for a simple isolated point scatterer. In the limit of an infinitely small scatterer, the two solutions should converge. The results obtained from this test showed some disagreement, but it appears that these errors are due to the choice of finite difference used here. Had a staggered grid formulation been used, the errors would most likely have been much smaller.

The bulk of the chapter was concerned with comparing the single and multiple scattering solutions for two randomly heterogeneous media. Both media were characterized by a Gaussian correlation function and had 10% rms deviation in λ , μ and ρ . In one of the models, the perturbations were chosen so that there were no velocity anomalies, only impedance anomalies. In the other, there were no impedance anomalies, only velocity anomalies. The former was shown to be dominated by low frequency backscattering, while in the latter scattering was forward directed over a

wide frequency band.

In the impedance scattering medium, the shape of the single and multiple scattering solutions were in good agreement away from the direct arrival. In general, the magnitude of the singly scattered arrivals was larger than the multiply scattered arrivals. This behavior can be directly traced to the fact that under the Born approximation, the direct arrival travels through the medium unaffected by the perturbations. The agreement between the two solutions in this medium suggests that single scattering theories should work well.

Agreement between the two solutions was much worse in the velocity scattering medium. The discrepancy arose because multiple scattering was important in this medium. This was confirmed by both the F-K analysis and the snapshot pictures of the divergence and curl. In this medium there were enough scatterers that significant amounts of energy was scattered from the incident wave. This causes attenuation due to scattering, and in the multiple scattering solutions diminishes the amplitude of the incident wave. This is not accounted for under the Born approximation and caused an accumulation of error which was proportional to the propagation length, the strength of the perturbations, and frequency.

Also important in the velocity scattering medium was the lack of late arrivals at near offsets in the single scattering solution. (Figure 23) and is indicative of the importance of multiple scattering in this medium. The lack of secondary scattering also tends to increase the coherency of scattered arrivals across neighboring receivers. This effect may be important and deserves further quantification.

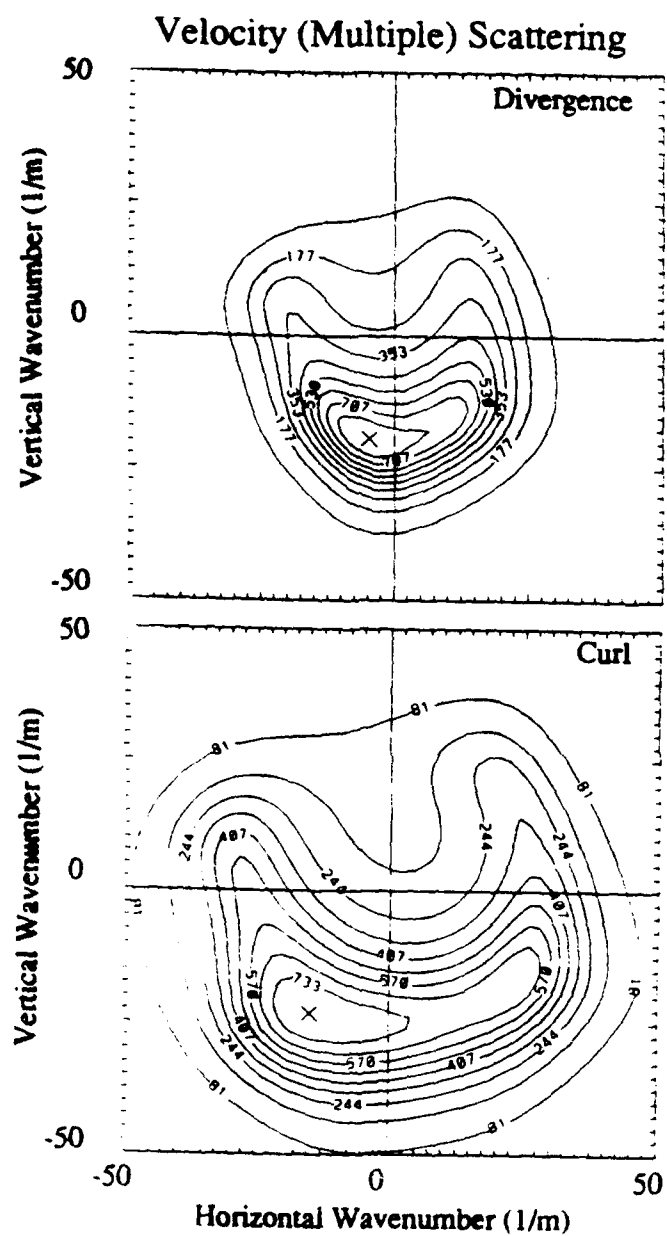


Figure 36: F-K plot of the divergence and curl of the (multiple scattering) wavefield in the velocity scattering medium.

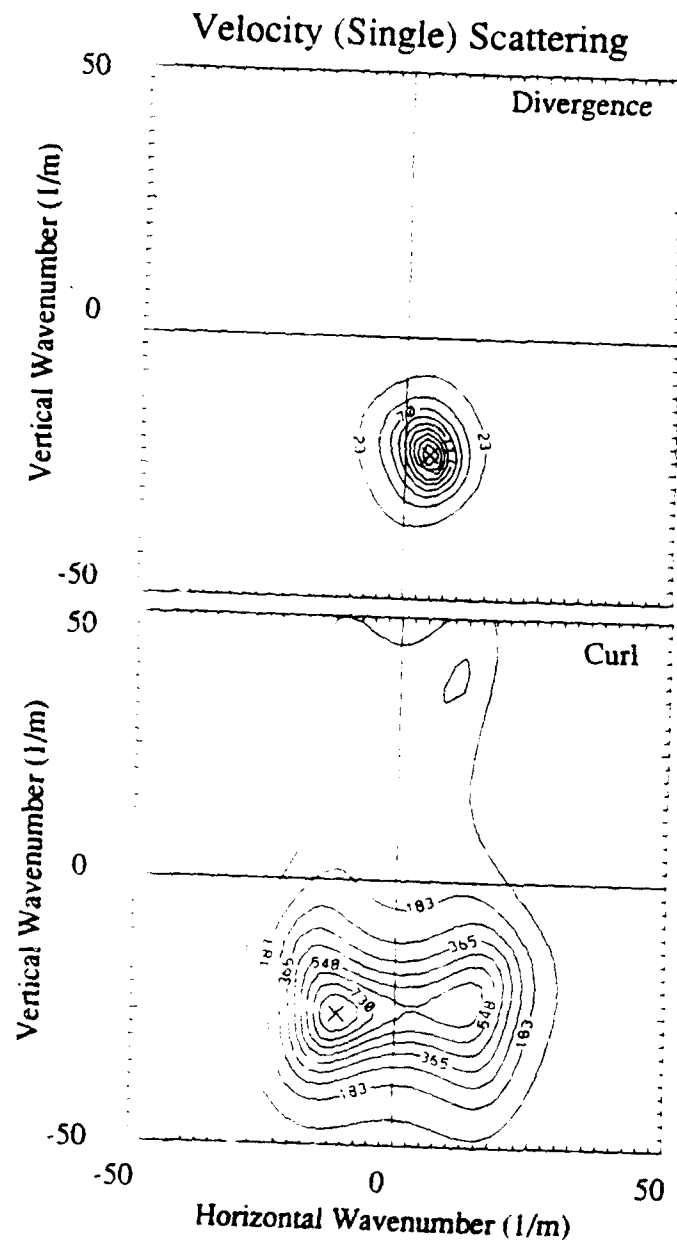


Figure 37: F-K plot of the divergence and curl of the (single scattering) wavefield in the velocity scattering medium. The importance of multiple scattering is reflected in the lesser range of wavenumbers present in the wavefield.

Chapter 4

Elastic Wave Scattering Below NORSAR

4.1 Introduction

Seismic data recorded at NORSAR show variations in amplitude and travel time which cannot be explained by a simple layered model. The magnitude and spatial variability of these features suggests that they are created by lateral heterogeneities in the crust and upper mantle. There is currently much debate as to what causes these variations, but they are likely to be due at least in part to changes in lithology, fracture density, fracture orientation, or temperature. Even with our limited understanding of the subsurface, it would seem likely that those anomalies in the near surface would tend to be dominated by ongoing geologic processes, and therefore regionally dependent. Similarly, variations in the lower crust may also reflect current geophysical processes, but in addition might contain remnant information from past geologic events. The motivation then is to understand the variations in crustal and lithospheric velocities so that we might be able to infer information concerning the geology of the region.

To accomplish this, we use full waveform data collected from the NORSAR and

NORESS arrays and forward modeling to propose a lithospheric model which is consistent with both the observed seismic data and current tectonic theories in Fennoscandia. We approach the problem from a deterministic point of view in that we investigate a series of specific realizations with known statistical properties. In order to construct a reasonable starting model, finite difference simulations are performed using several of the random lithospheric models proposed in the scattering literature. These simulations served to acquaint us with the sensitivity of the results to different models and to identify the influence of different types of heterogeneities. Once the starting model was chosen, a finite difference simulation was performed and the resulting seismograms compared to field data from the NORSAR and NORESS arrays. After examining the results, the model was updated and the process repeated. Throughout the process, each modification of the model was undertaken with full consideration of the known tectonic features of region.

The methodology pursued here is different than previous attempts to specify the lithospheric model below NORSAR. Early studies used Chernov (1960) scattering theory to relate the amplitude and phase fluctuations in the wavefield to slowness fluctuations in the medium (e.g., Aki, 1973; Berteussen et al., 1975a). These studies were shown to be accurate only for low frequencies ($f \leq 0.6$ Hz) (Aki, 1973) and completely neglected multiple scattering, as well as mode conversion. In addition, they required that the autocorrelation function of the medium is known *a priori* and easily manipulated mathematically. Flatté and Wu (1988) devised a less restrictive formalism which over came some of these limitations, though it too neglected mode conversion and multiple scattering and used only the arrival and log amplitude information from the recorded wavefield. In this chapter, we continue the work of Frankel and Clayton (1986) and use the finite difference technique to model elastic wave propagation in the crust. We then extract several important parameters from the synthetic data and compare these values to similar parameters taken from nuclear explosions recorded at NORSAR and NORESS. The field data then serves to

constrain subsequent finite difference models. The most important parameter used in this study is the coherency statistic. It is advantageous because it represents the average coherency (or similarity) of the wavefield and is therefore directly tied to ensemble average. The advantage of this study over earlier studies is that we use a realistic background earth model (to insure the correct wavelength scaling with depth), we consider the full elastic solution (to account for scattering due to mode conversion and multiple scattering) and we use the full waveform to compute the coherency statistics (as opposed to ensemble averages of the travel time and log amplitude measurements).

4.2 Scattering Beneath NORSAR

NORSAR is a large-aperture seismic array (≈ 125 km in diameter), located in Norway, which was designed to monitor teleseismic events. The array consists of 22 subarrays, each having as many as 6 short-period vertical component seismometers (Figure 38). In this study, we used only data from the 01A, 01B, 02B, 03C, 04C and 06C subarrays, which had a minimum and maximum receiver separation of approximately 3 km and 70 km respectively. This range of distances should allow us to identify the moderate wavelength velocity variations in the lithosphere. In addition, we also used short-period data from the NORESS array. The NORESS array is centered about the center element of the 06C subarray of NORSAR, but is a completely separate array in terms of its seismometers, electronics and transmission facilities. NORESS consists of 25 concentrically located receivers all within a 3 km circle (Figure 39). These data should help us to constrain the more rapidly varying fluctuations in the velocity field. NORESS was designed as an experimental array for regional monitoring. Like NORSAR, its receivers are deployed in vaults on piers set directly in crystalline bedrock, thus generate good quality data. It should be noted, however, that the data from NORESS generally have higher signal to noise ratios and contain more dynamic

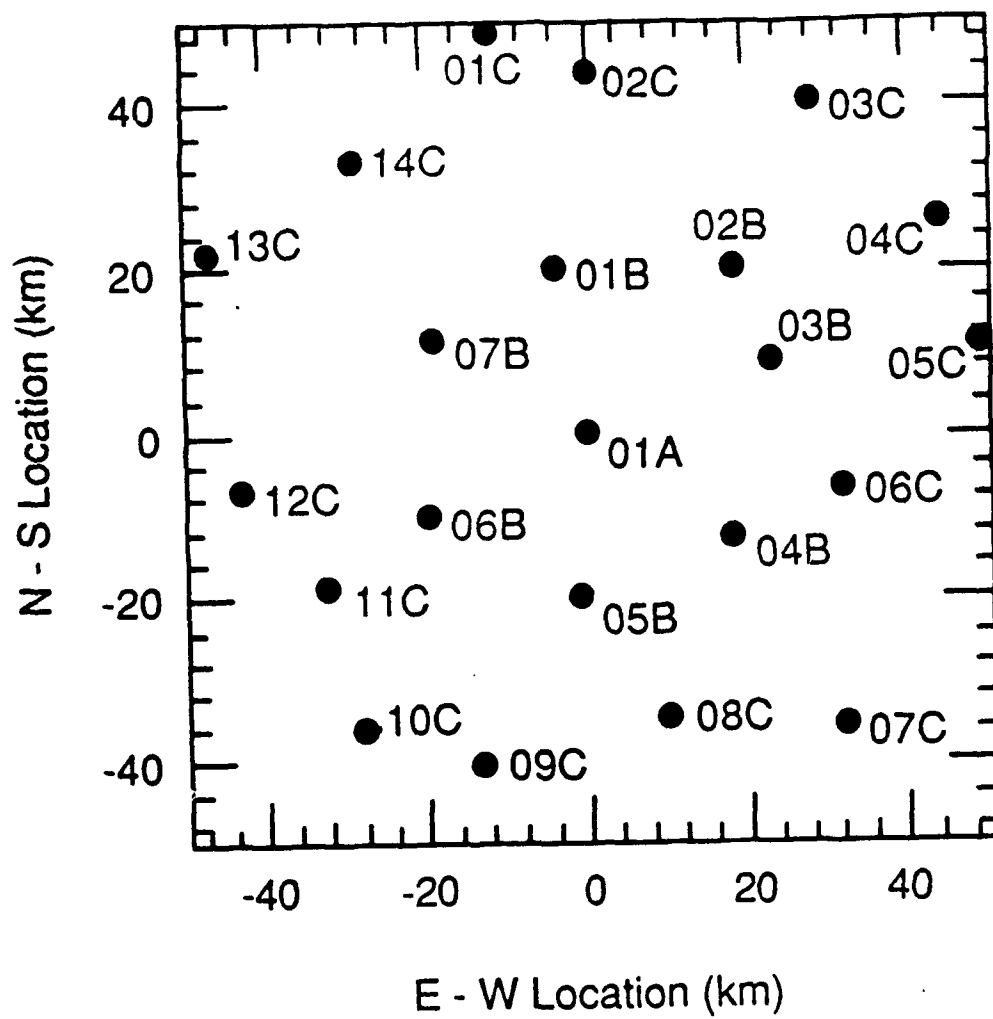


Figure 38: The NORSAR arrays. Only data from the 01A, 01B, 02B, 03C, 04C and 06C subarrays were used.

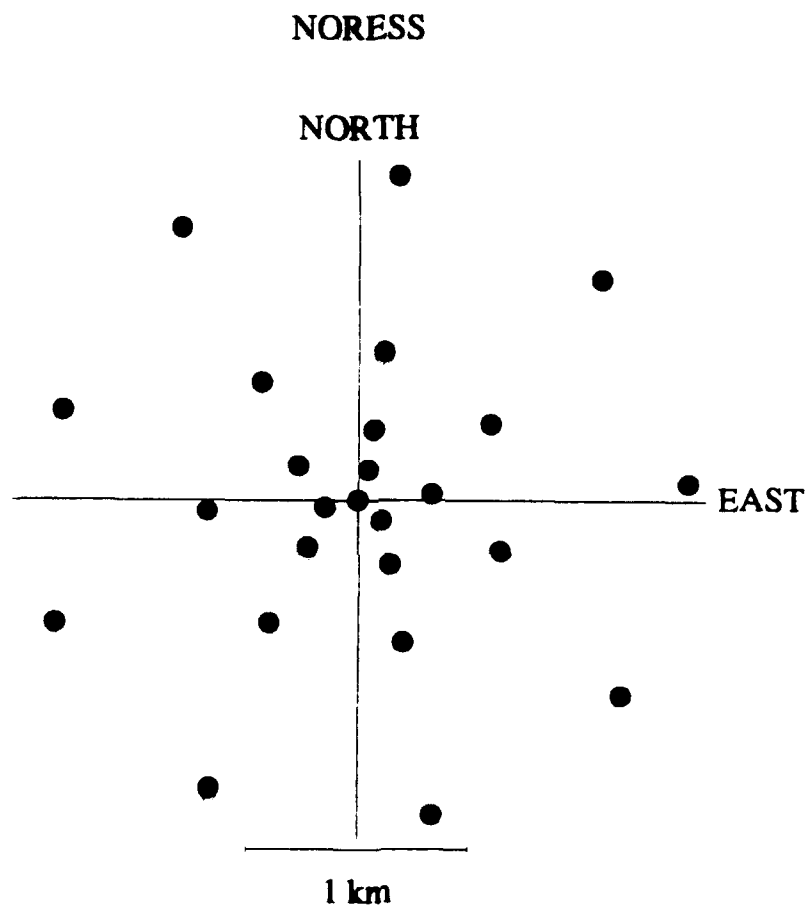


Figure 39: The NORESS array is located within the 06C subarray of NORSAR (Figure 38).

range.

The events investigated here are recordings from underground nuclear explosions at the Semipalatinsk test site (USSR) (49.93° N, 78.82° E). The larger of the two blasts ($m_b = 6.1$) occurred on December 4, 1987 and produced exceptionally clean recordings on the NORESS stations (Figure 40). Due to the limited dynamic range at NORSAR, this event was clipped on many of those stations. The smaller event ($m_b = 5.1$) which occurred on July 25, 1985 was well recorded at NORSAR (Figure 41). Data from nuclear blasts are often used to study scattering because the source function for these events is simple and well understood. In particular, data from the Semipalatinsk test area was preferred for this study because the source area is far enough from Norway ($\Delta = 38^{\circ} \approx 4200$ km) that the primary P-wave was nearly vertically incident (incidence angle $\approx 76^{\circ}$), and the curvature of the wavefront was small. These two factors allow the incident wave to be approximated by a plane wave.

4.2.1 Tectonic and Geophysical Setting

Large-scale Structure near NORSAR

The entire region surrounding NORSAR is part of the stable Baltic Shield, which is characterized by the predominance of Precambrian rocks (Sellevoll and Warrick, 1971). The Oslo graben, which is located slightly southeast of NORSAR, separates the Precambrian rocks into two parts. North of the graben, Precambrian rocks of southern Norway dip below the highly metamorphosed rocks of the Caledonian orogenic zone (Figure 42). The Scandinavian Caledonides consist of geosynclinal sedimentary and volcanic rock. An increasing degree of metamorphism with granitization and intrusions are evident from the Oslo graben to the northwest. It is in this region that the deep-seated orogenic processes have been especially active. This has resulted in the fusion of previous Precambrian basement and Cambrian-Silurian sedimentary rocks.

Much of the geology described above was mapped using seismic techniques. Knopoff

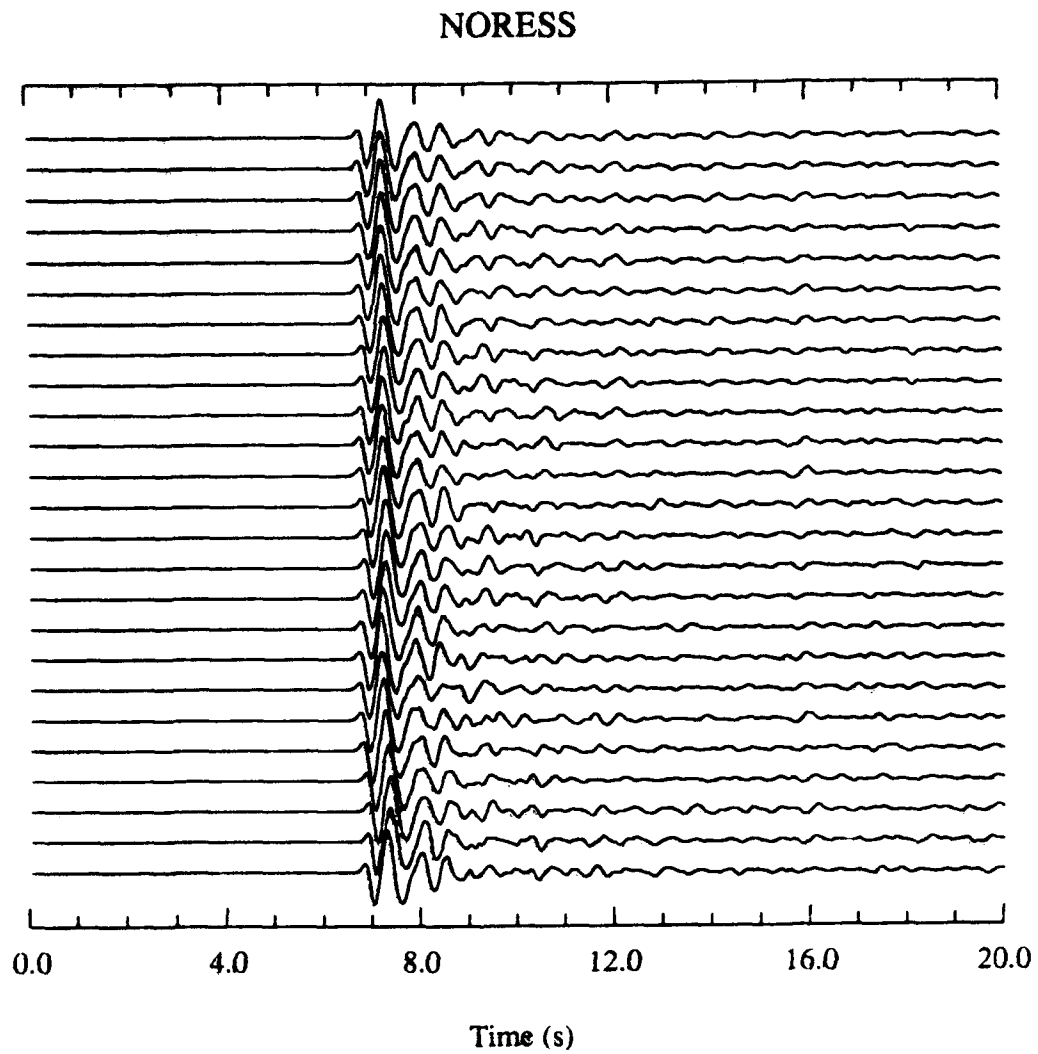


Figure 40: NORESS data (plotted at constant scale) from a nuclear explosion in *Eastern Kazakhstan*, USSR (December 12, 1987).

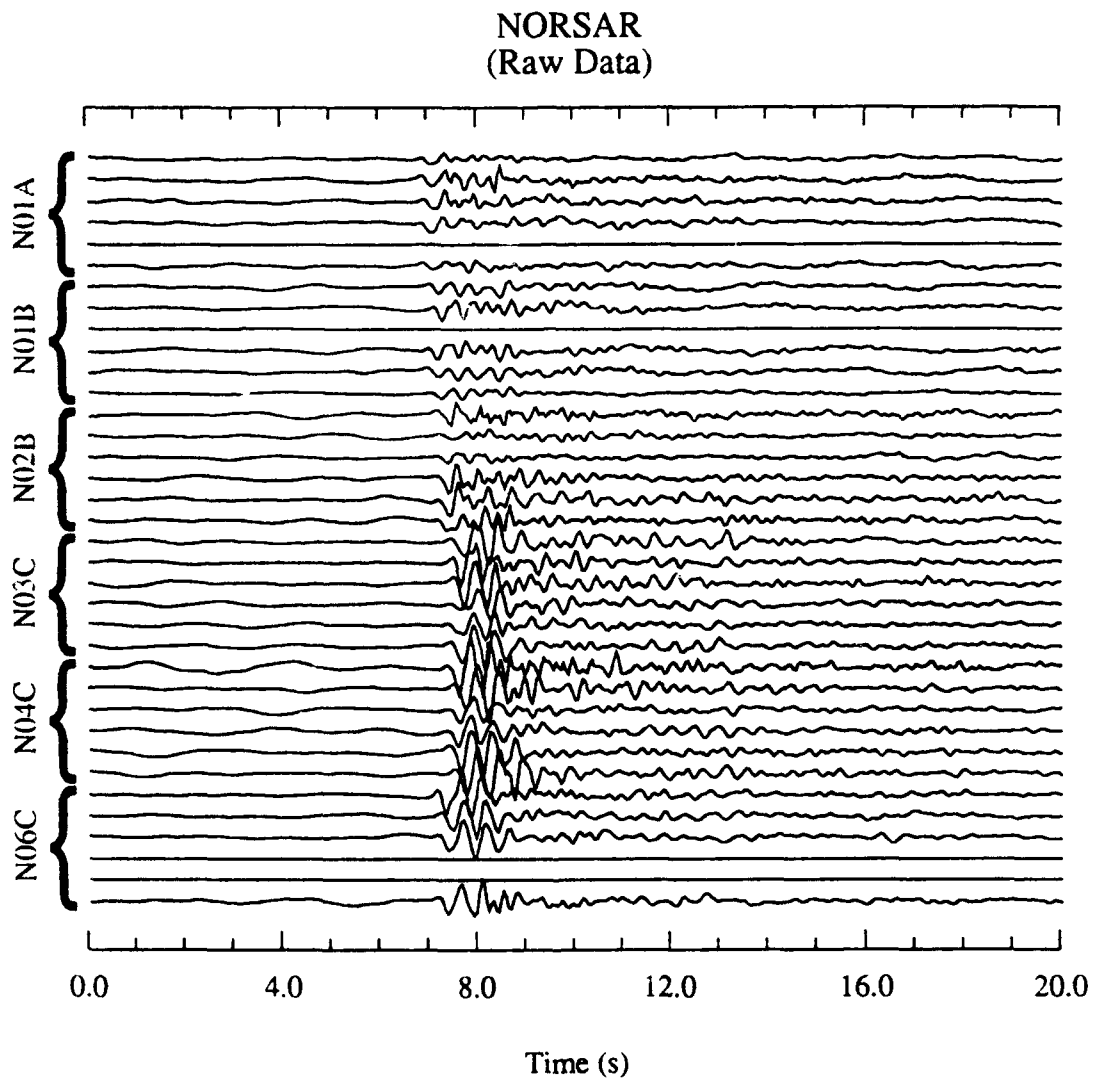


Figure 41: NORSAR data (plotted at constant scale) from a nuclear explosion in Eastern Kazakhstan, USSR (July 25, 1985).

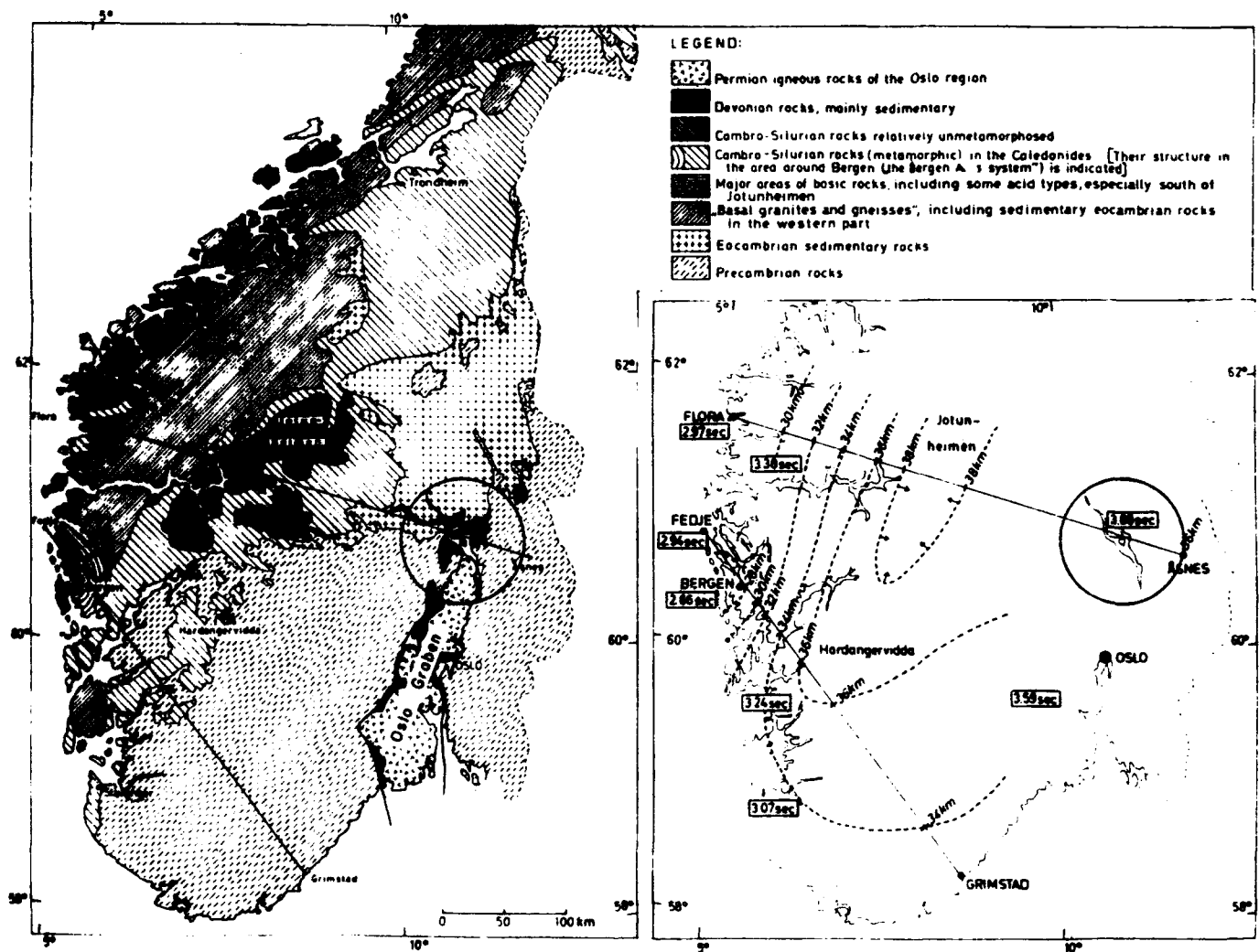


Figure 42: Simplified geologic map and preliminary contouring of the Moho in southern Norway (from Sellevoll and Warrick, 1971). The circle in each map corresponds to the aerial extent of the full NORSAR array (Figure 38).

(1983) and Tanimoto and Anderson (1985) used surface wave dispersion to mapped the large-scale velocity variations in the Fennoscandian lithosphere. The lateral extent of these features are too large to be resolved by our study and any effects would appear as constant travel time and amplitude shifts over our whole study area. For this reason, we look to more detailed studies which might identify features smaller than the width of our array (≈ 50 km). Tomographic imaging of the subsurface is capable of resolving features having dimensions on the order of 10 km and has been used extensively in Fennoscandia (e.g., Thomson and Gubbins, 1982; Husebye et al., 1986). This resolution has been sufficient to identify the seismic signature of most of the major tectonic provinces in southern Scandinavia, but smaller features such as the Oslo Rift have escaped detection. In an attempt to increase resolution, several reflection and refraction surveys have been performed near NORSAR (e.g., Sellevoll and Warrick, 1971; Mykkeltveit, 1980; Cassell et al., 1983). While most of these studies have concentrated on mapping the depth of the Moho and other discontinuities, several have suggested the existence of an alternating series of positive and negative velocity anomalies below the Moho. These studies suggest that the velocity anomalies are thin tabular features which have a lateral extent not greater than 100 km.

4.3 Scattering at NORSAR

4.3.1 Travel time and Amplitude Variations

The techniques described above are oriented towards identifying the long-wavelength variations in the velocity field. Synthetic data generated from these models may fit the average travel times observed at large aperture arrays, such as NORSAR, but cannot explain all the variations seen on the field data. The degree of mismatch is greater than expected from measurement errors (Berteussen, 1974) and usually attributed to heterogeneous structures in the Earth's crust and/or mantle. The purpose of this

section is to display the nature of these variations so that they can be compared to similar quantities measured from the synthetic models discussed below.

The data collected at NORSAR contained several dead traces (Figure 41) and significant amounts of low frequency noise (Figure 43). The low frequency noise was removed by highpass filtering above 1 Hz and the dead traces were removed before subsequent processing (Figure 44). After the preprocessing step, the data were bandpass filtered around 2 Hz, the peak frequency of the P-wave (Figure 43), so that reliable arrival times could be measured using a simple first break algorithm. These data were then fit (least squares criterion) with a plane, leaving the residuals as the travel time fluctuations. The same procedure was used to calculate the travel time fluctuations in the NORESS data, although the preprocessing step was unnecessary since that data contained very little background noise and no dead traces (Figure 45).

The linear regressions on the two datasets were consistent and yielded a backazimuth direction ≈ 8 north of east. Projecting the travel time residuals for the NORSAR data along the a line parallel to that direction (Figure 46) shows the residuals are generally on the order of .1 s and distributed evenly about zero. The total rms travel time variation observed for these data was about 0.06 s, considerably less than 0.2 s figure usually observed at large seismic arrays (e.g., Berteussen et al., 1975a; Powell and Meltzer, 1984). The reason for the discrepancy might be related to the fact that only data from six closely spaced subarrays was used in the calculations. Similarly, the travel time residuals for the NORESS data were calculated, but the rms variation in travel time was found to be less than the temporal sampling rate (1/40th s), which implies these variations are insignificant.

For both sets of data, the variations in log amplitude are considerably greater than the travel time variations. Log amplitude fluctuations in the NORSAR data showed as much as 0.75 rms variation across the array (Figure 47). The data show a definite linear trend; amplitudes are highest in the east. If these variations are due to changes in local surface geology, the effects can be adequately modeled by the finite difference modeling performed here. However, it is also possible that the dip of

NORSAR

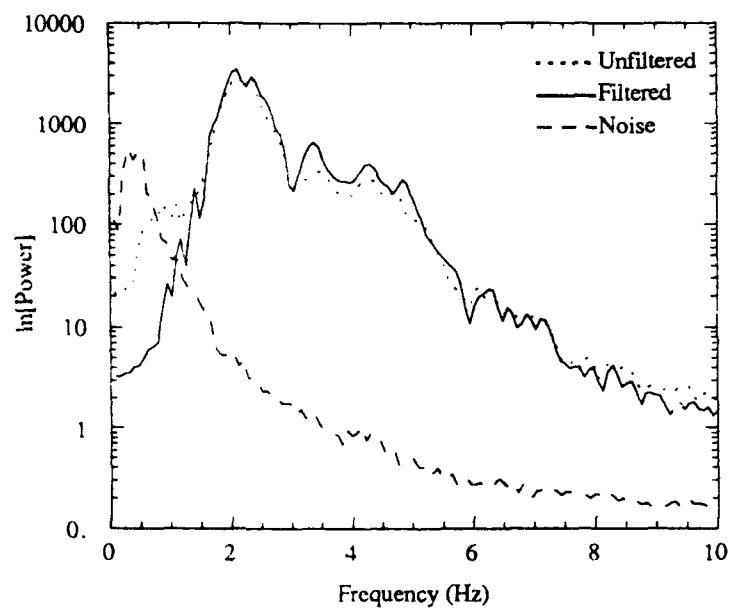


Figure 43: Average power spectra of the background noise (10 s preceding the first arrival), unfiltered traces, and bandpass filtered (1 – 10 Hz) traces at NORSAR.

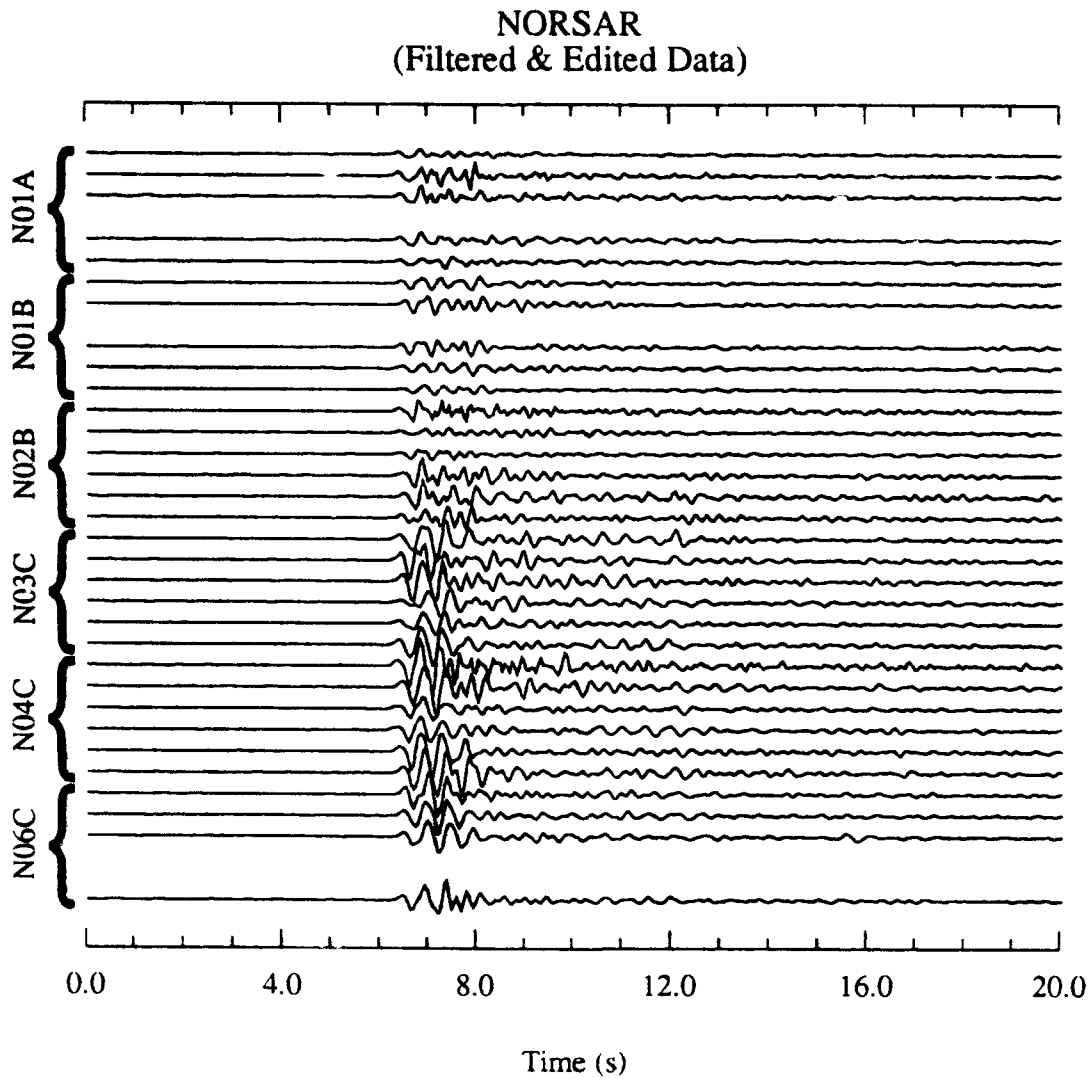


Figure 44: NORSAR data (plotted at constant scale) from a nuclear explosion in Eastern Kazakhstan, USSR (July 25, 1985). Traces have been bandpass filtered (1-10 Hz) and dead traces have been removed. These are the NORSAR data used in all subsequent calculations.

NORESS

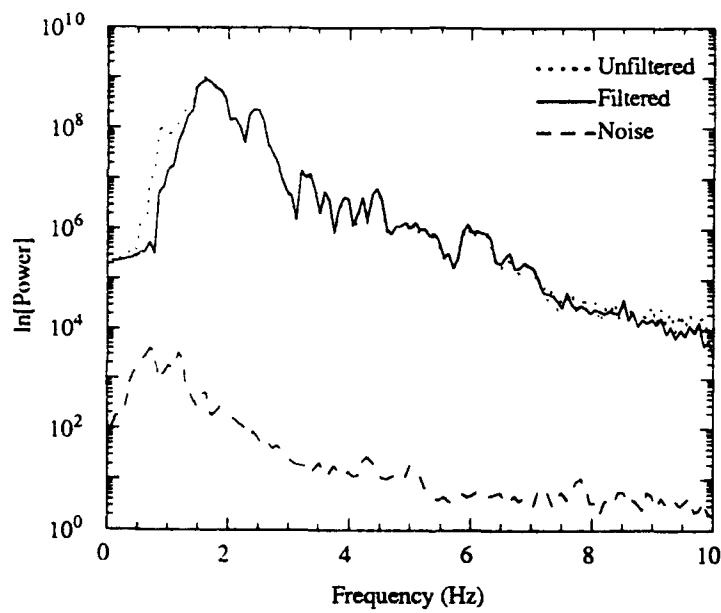


Figure 45: Average power spectra of the background noise (10 s preceding the first arrival), unfiltered traces, and bandpass filtered (1 – 10 Hz) traces at NORESS.

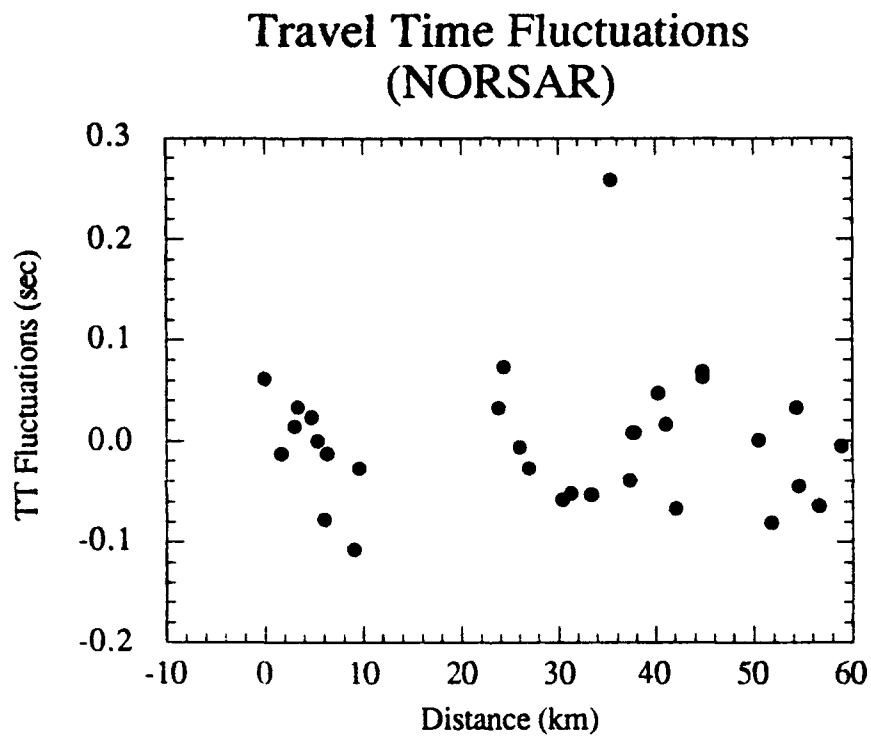


Figure 46: Travel time residuals projected along the great circle path between the source and the center of the NORSAR array. The rms deviation for these data was ≈ 0.07 s.

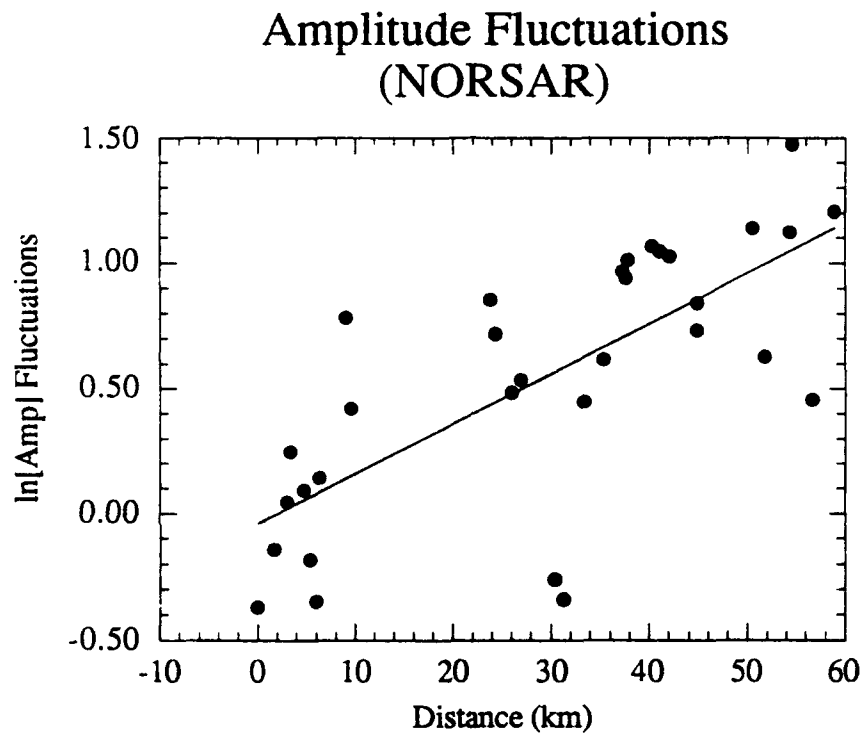


Figure 47: Fluctuations in log amplitude projected along the great circle path between the source and the center of the NORSAR array. The rms deviation for these data was 0.75 before removing the linear trend and 0.35 after removing the trend.

the Moho is also a factor. Figure 42 suggests that the depth to the Moho decreases steadily to the east, consistent with the trend in increased amplitude. Since all the modeling done in this study assumed a flat Moho, it is tempting to remove the linear trend before calculating the rms variation in amplitude. When this is done, the rms variation drops from 0.75 to 0.35. Similar findings were made for data from NORESS, but due to the lesser spatial extent of the array the rms variation in log amplitude was only 0.06 (Figure 48). The proximity of the receivers at NORESS allowed us to contour the amplitude fluctuations (Figure 49), something which was not possible with the NORSAR data. The contours are generally smooth, which is due in part to the contouring algorithm, but they also display variations as small as 200 m. The existence of these variations over distances as small as the width of NORESS is strong evidence for including a highly heterogeneous layer in the very near surface. In addition, by examining these features in the data, we have established one of the criteria which will help to constrain the lithospheric models which are presented below. Removal of the linear trend had little effect on the coherency calculations since that statistic is known to be affected only weakly by amplitude variations (Dainty and Toksöz, 1990).

4.3.2 Transverse Coherency (NORSAR)

For densely spaced receivers, the spatial trends in the amplitude and travel time may provide information about the scale-lengths of the scatterers. If the receiver coverage is too sparse, simple techniques such as contouring may be of little value. One measure which has proven useful in these circumstances is the transverse coherency function (Harichandran and Vanmarcke, 1984; Dainty and Toksöz, 1990; Menke et al., 1990). The coherency statistic has been used in both strong ground motion (Harichandran and Vanmarcke, 1984) and regional (Toksöz et al., 1990; Dainty and Toksöz, 1990) studies and is a frequency domain equivalent of the correlation function used by Bungum et al. (1985) and Ingate et al. (1985). The coherency function is useful in

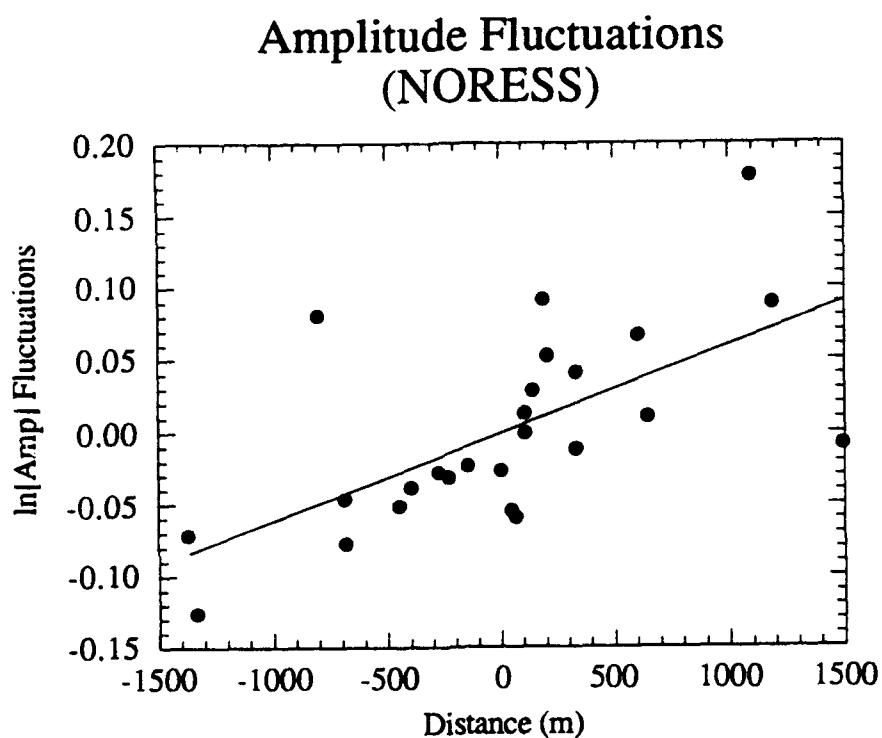


Figure 48: Fluctuations in log amplitude projected along the great circle path between the source and the center of the NORESS array. The rms deviation for these data was very small (0.06), even before removing the linear trend.

Log Amplitude Fluctuations at NORESS

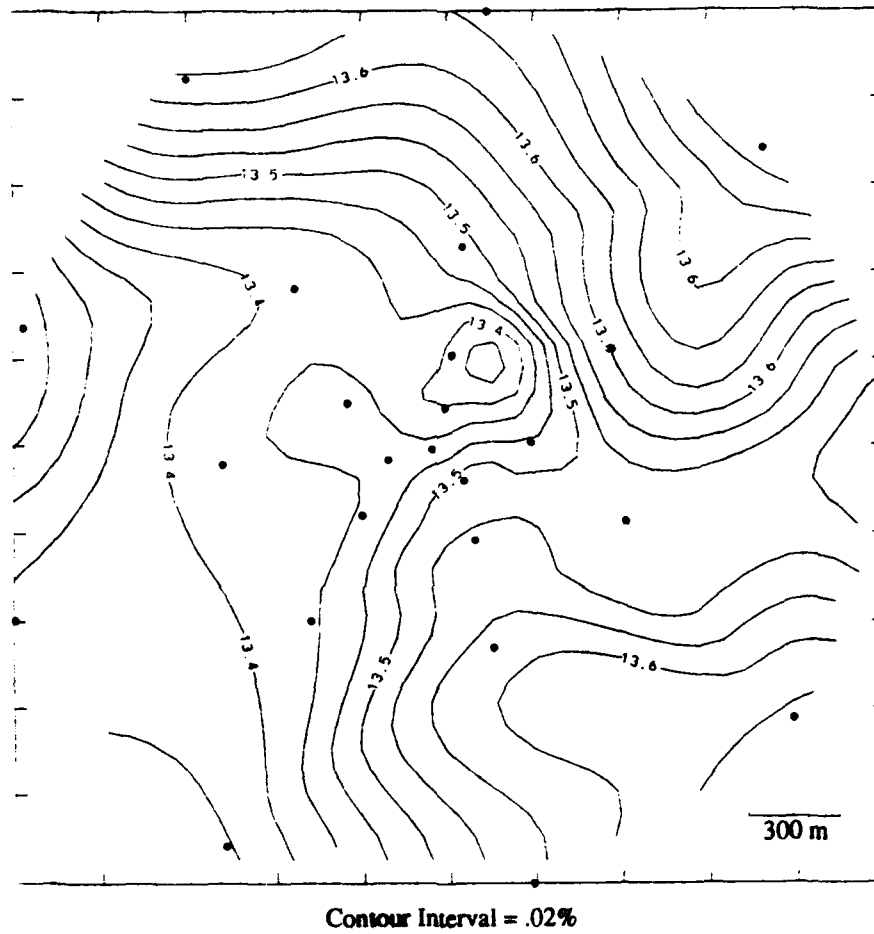


Figure 49: Contour of peak amplitude values observed at NORESS.

practice because it provides a dimensionless measure of similarity between two traces.

Before calculating the coherency, Jenkins and Watts (1968) and Harichandran and Vanmarcke (1984) suggest removing any gross travel time delays in the data. In the synthetic examples presented here, no time shifting was necessary since the source was normally incident on the receiver array. The field data was time shifted in the same manner as described above. After correcting for the normal moveout (which roughly aligns the traces), the seismograms were windowed and the crosscorrelation and autocorrelation between each receiver pair was calculated. These correlations were then further windowed with a Bartlett window. The purpose of the Bartlett window was to provide frequency smoothing of the correlation spectra and minimize bias at low coherencies (Jenkins and Watts, 1968). The smoothing makes the spectral estimates more reliable, but diminishes resolution. This problem is discussed in detail by Harichandran and Vanmarcke (1984). They show that to obtain optimal results, the width of the Bartlett window should be approximately 1/5 the width of the original data window. The coherency between each receiver pair can be calculated by

$$C(x, \omega) = \frac{S_{ij}(x, \omega)}{[S_{ii}(\omega)S_{jj}(\omega)]^{1/2}}, \quad (4.1)$$

where $x = |x_i - x_j|$ is the spatial separation between receivers i and j , ω is angular frequency, S_{ij} is the crosscorrelation spectrum between seismograms and S_{ii} and S_{jj} are the autocorrelation spectra.

Since the coherency values calculated from seismic data depend on the data window, they are only estimates of the true coherency. Better estimates can be obtained by averaging over the ensemble. This is accomplished by grouping the calculated coherencies into bins of approximately equal receiver distance and averaging. The magnitude of the coherency (here after called simply the coherency) is limited to the range between zero and one and the distribution of values is more log-normal than normal (Jenkins and Watts, 1968; Dainty and Toksöz, 1990). Accordingly, uncertainties in the coherency are found using the Fisher Z-transform. Errors associated with phase of the coherency function are not limited to any fixed range of values and seem

to be better described by the Gaussian distribution. Therefore, uncertainties in the phase values are estimated using the Gaussian normal distribution.

Coherency of Waveforms at NORSAR and NORESS

The coherency is one of the measures we will use to evaluate the similarity of the variations in the synthetic data to those in the field data. It is important then that we outline the key features in the coherency function which is observed at NORSAR and NORESS. Beginning with the NORSAR data, the coherency was calculated over a 4 s window which began ≈ 1 s before the onset of the direct arrival. The stacked (25 fold) power spectrum for this time window is shown in Figure 43. Note the strong peak at 2 Hz and the numerous notches in the spectrum. The lack of power at low frequencies is due to the high-pass filtering which was done prior to processing. The other depressions in the spectrum might be due to interference effects which arise because of scattering. Although the windowing of the correlation spectra helped to minimize the effects of these features, some care was necessary in order to calculate coherencies only for frequencies with good signal to noise ratios. After some experimentation, we found that we could get good coherency measurements at 1.5 Hz, 2.5 Hz and 3.5 Hz. The frequency separation between these frequencies is greater than the width of the smoothing window, thus yields independent results, and avoids the major notches in power spectrum.

Figures 50 – 52 show the spatial coherency and phase lag as a function of receiver separation for the NORSAR data. Each “x” on the coherency plots represents a single coherency measurement between two specific receivers. The darkened circles and associated error bars show the mean coherency value and its uncertainty as described above. Similarly, each “x” on the phase lag plots shows the relative time shift between a given pair of receivers. For the reasons described above, average phase lag values near zero are desirable. Lastly, the gap in the coherency data near 15 km is due to no receiver pairs having that spatial separation.

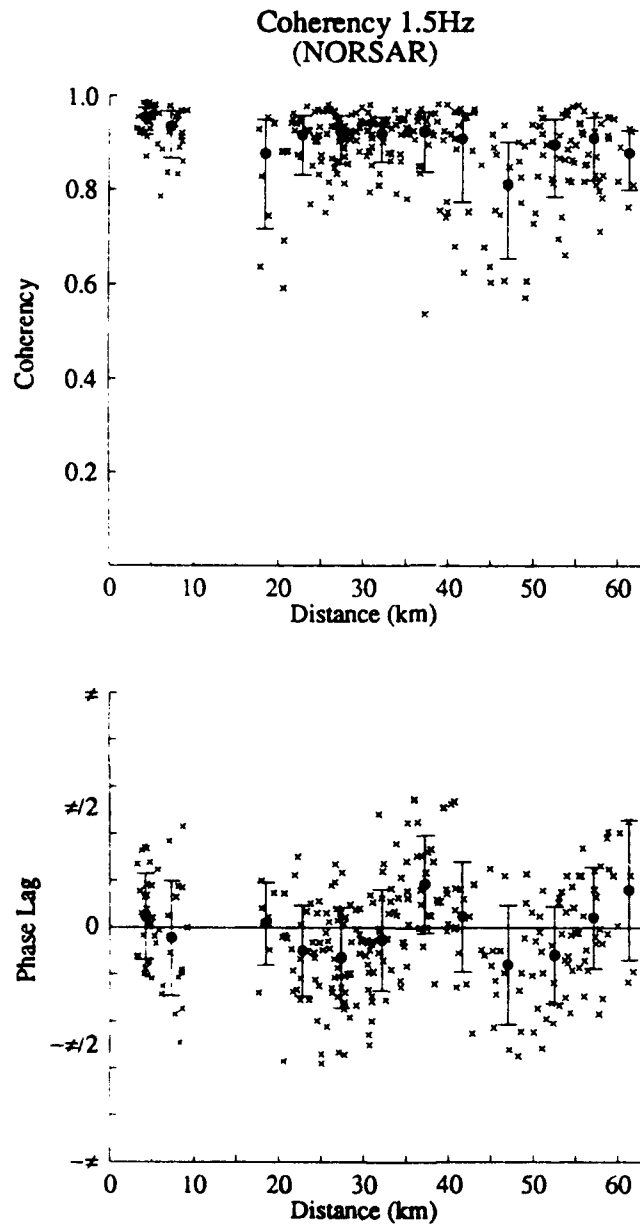


Figure 50: Coherency as a function of spatial separation for the direct arrival and early coda of the NORSAR data around 1.5 Hz. Each cross represents the coherency (top) or phase lag (bottom) estimate from one receiver pair. The filled circles and error bars are the mean values and their uncertainties.

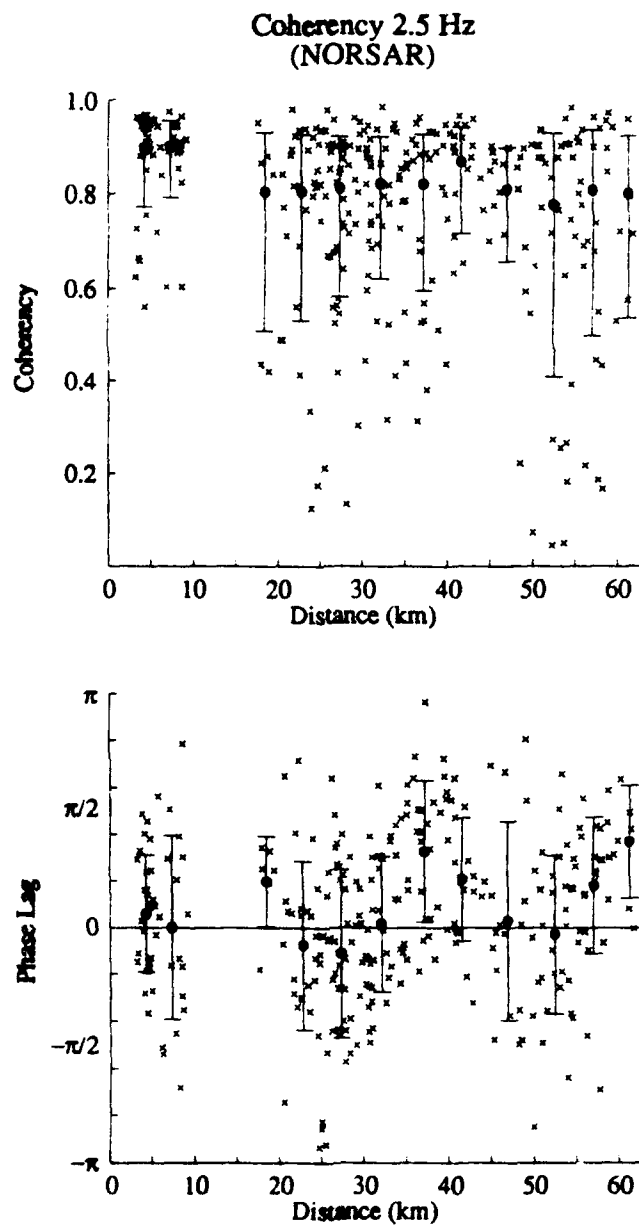


Figure 51: Coherency as a function of spatial separation for the direct arrival and early coda of the NORSAR data around 2.5 Hz. Each cross represents the coherency (top) or phase lag (bottom) estimate from one receiver pair. The filled circles and error bars are the mean values and their uncertainties.

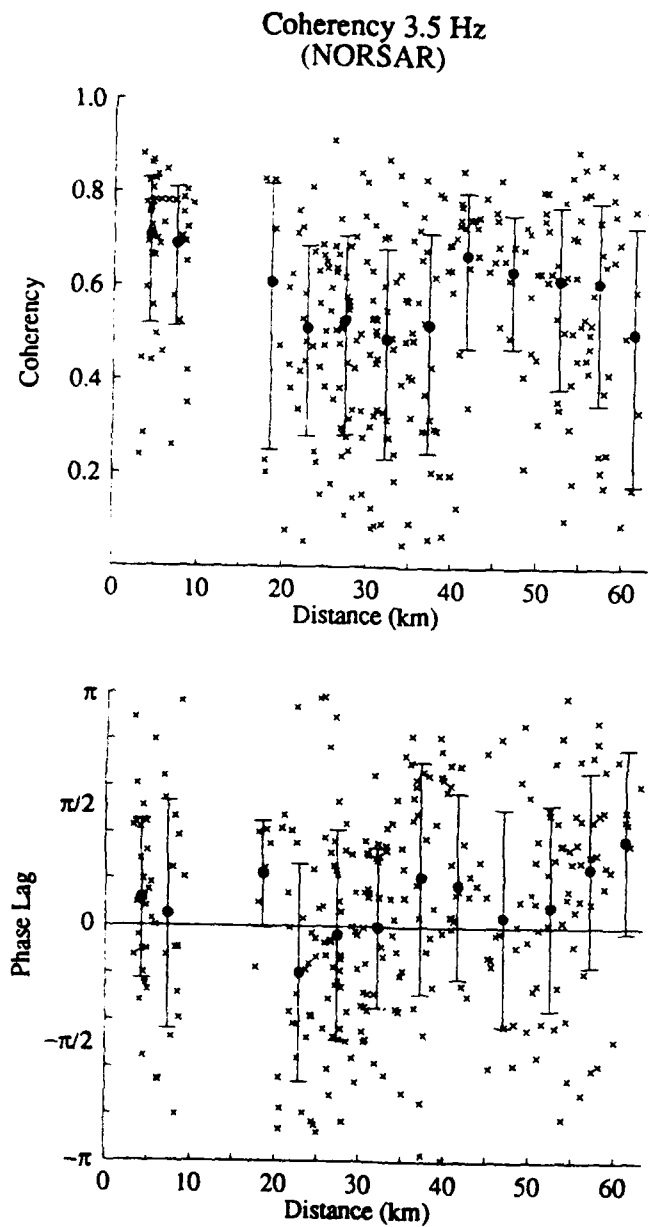


Figure 52: Coherency as a function of spatial separation for the direct arrival and early coda of the NORSAR data around 3.5 Hz. Each cross represents the coherency (top) or phase lag (bottom) estimate from one receiver pair. The filled circles and error bars are the mean values and their uncertainties.

The coherency of the NORSAR data at 1.5 Hz (Figure 50) shows very little falloff with distance out to the largest receiver separations (60 km). The significance of these values is supported by the relatively small variation in the individual coherency measurements and the small average phase lag values. The trend in the average coherency values at 2.5 Hz are similar to what was observed at 1.5 Hz, although in general the values are slightly lower. There is also more variation in individual coherency and phase lag measurements at this frequency. The coherency at 3.5 Hz is clearly different than was observed at the lower frequencies. There is considerable variation in both the individual coherency and phase lag values as well as a strong decrease in coherency with separation. It is tempting to explain the lower coherencies observed at this frequency on a decrease in the signal to noise ratio, however the power spectra (Figure 43) do not support this interpretation. An alternative explanation is that this frequency is simply more strongly scattered than the lower frequencies.

Due to the lack of closely spaced receivers in the NORSAR array, we turn to the NORESS data for insight into the small-scale crustal heterogeneities. Due to the distinct notches in the power spectra at 2 Hz and 3 Hz, the coherency was calculated at 1.5 Hz, 2.5 Hz and 3.5 Hz. All frequencies showed high coherency over the receiver separations at NORESS (3 km) and very little scatter in individual coherency and phase lag measurements, so data from the three frequencies were combined and displayed in Figure 53. The most important feature in these data is the existence of variations over distances as small as 3 km. The existence of these variations is especially interesting, given the lack of observable travel time anomalies. Charrette and Toksöz (1989) showed that highly heterogeneous media (such as those characterized by the von Kármán autocorrelation function) are capable of producing considerable waveform variations with little effect on travel times. One way to reconcile the observations at NORESS then is to include a highly heterogeneous near-surface layer.

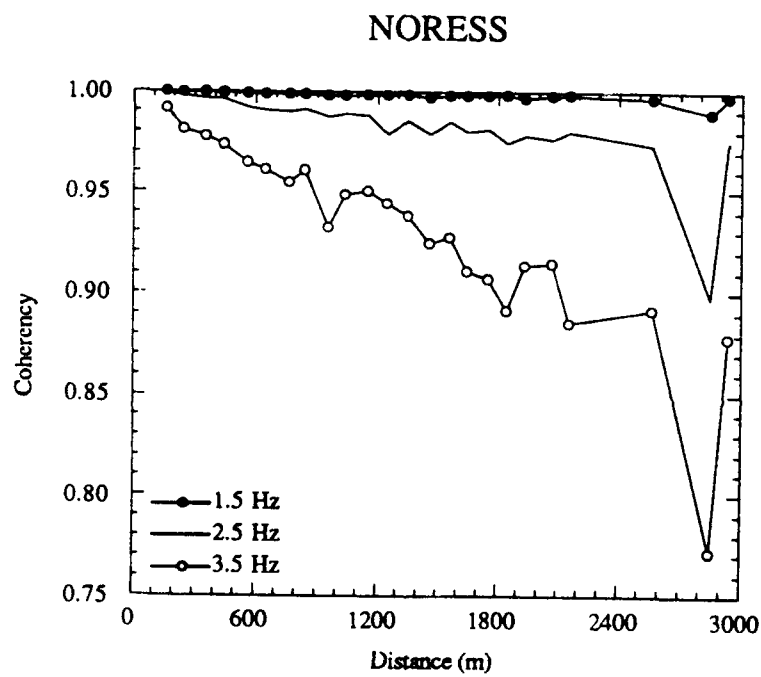


Figure 53: Uncertainties in the coherency measurements for the NORESS data were so small, the coherency curves for 1.5, 2.5, & 3.5 can all be shown together. The average phase lag for these data was zero for all distances.

4.4 The Coda

One of the most obvious features on high-frequency (≥ 1 Hz) teleseismic recordings is the coda that appears behind the direct P-wave and S-wave arrivals. Consider the NORSAR data used here; the source was a nuclear explosion which lasted only a fraction of a second yet the P-wave envelope stretches over several seconds. The same effect can be seen in data from local microearthquakes, which can have an S-wave coda lasting hundreds of seconds (Frankel and Wennerberg, 1987). Coda waves can be formed by a variety of mechanisms; reverberations in horizontally layered structure under the receiver (site response), reverberations in layered structure between the source and receiver, surface waves scattered by lateral heterogeneities, the conversion of body waves at depth or at the surface, and by anelastic effects. In this study, we assume that all the coda is produced by the scattering of body waves from velocity fluctuations in the lithosphere. Furthermore, when examining the synthetic data, we are limited by the modeling technique to two dimensional geometries and we can consider only scattering in the lithosphere under the receiver.

The significance of near source scattering can be measured by transforming the data to wavenumber domain. Each point in wavenumber domain maps to a plane wave, where the direction of the wavenumber vector is the backazimuth and the norm of the wavenumber vector is inversely proportional to the apparent velocity of the plane wave across the array. Figure 54 shows four FK plots, each over a 5 second window of the NORESS data (2 Hz). The first 5 second window is dominated by the incident P-wave, which is manifest as a well localized peak. In the second frame of Figure 54, the broadening of the peak indicate that energy is incident on the array from a wider range of angles. This is indicative of either P-wave scattering and/or S-wave scattering below the receiver array, or P-wave scattering below the source array. We favor the former explanation. In the third time window, the FK plot shows energy in both the first and third quadrants, indicating that some energy is being backscattered from the incident P-wave after it has reflected off the free surface.

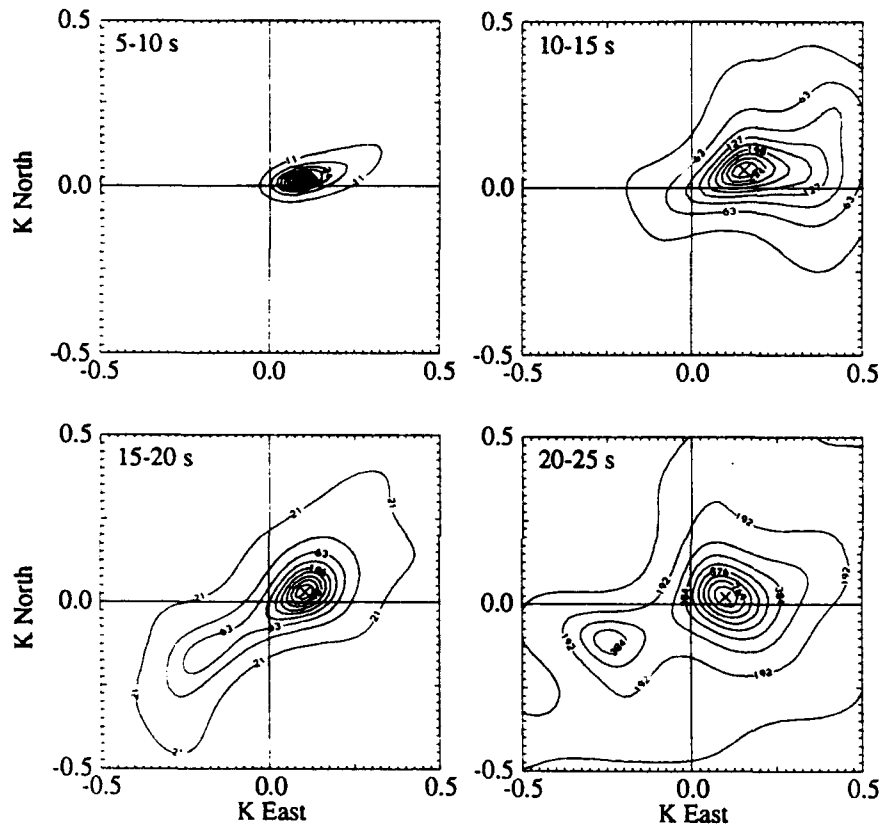


Figure 54: FK plots of four different time windows from the wavefield recorded at NORESS.
a) The 5 s after the first break, b) 5 – 10 s after the first break, c) 10 – 15 s after the first break and d) 15 – 20 s after the first break.

The apparent velocity of the backscattered energy suggests that this energy may be dominated by S-waves. The last time window, which begins ≈ 15 s after the first arrival, shows that a significant amount of the energy in this time window is due to backscattering. In summary then, the first few cycles of the incident wave appear to be dominated by energy coming directly from the source region. Later in the seismograms, the range of angles from which energy is incident on the array increases. Lastly, the existence of the secondary peak in the third and fourth quadrants suggest that backscattering is an important component of coda generation.

4.5 Forward Modeling in Random Media

Small-scale Structure in the Lithosphere

It is now well established that the amplitude and travel time anomalies observed at NORSAR and NORESS are due to small-scale velocity anomalies in the lithosphere (e.g., Aki, 1973; Frankel and Clayton, 1986; Flatté and Wu, 1988). Aki (1973) assumed the crust under LASA (an array similar in size to NORSAR) could be modeled as a random medium. Aki (1973) used Chernov (1960) scattering theory (based on the Born and Fresnel approximations) to relate amplitude and travel time variations to slowness fluctuations in the medium. If the slowness fluctuations in the medium were assumed to be Gaussian distributed and have a Gaussian autocorrelation, Aki (1973) found the crust could be modeled as a 60 km thick random medium with a correlation length of 10 km and 4% rms variation in velocity. An equally important finding in his study was that data up to 0.6 Hz were fit well by this model, but higher frequencies were not. The conclusion made in that study was the misfit occurred because the Born approximation had been violated. Capon (1974) used a slightly different implementation of the same theory (Chernov (1960) scattering theory) and found optimal results when the random heterogeneities extended to a depth of 136 km and the rms deviation in velocity was 1.9%. Like Aki (1973), it was assumed that

the random fluctuations had a Gaussian autocorrelation function. Berteussen et al. (1975a) gives an excellent review of Chernov scattering theory as applied to the earth and discusses several key issues, such as the lack of resolution between the rms deviation in slowness and the thickness of the random medium. They then investigate NORSAR data and found that 50 – 60% of the variance in amplitudes and travel times could be explained by the existence of a 50 km thick layer with random fluctuations having a Gaussian autocorrelation function. They found the best results with a correlation length of 15 km and 3% rms variation in slowness.

These studies are similar in that they are all restricted to the acoustic case and assume Chernov scattering, and therefore the Born approximation, is valid. As a result they neglect multiple scattering and mode conversion, both of which are important if the size of the scatterers is small compared to a wavelength. In addition, they all assume that the fluctuations in the lithosphere can be adequately described by the Gaussian autocorrelation function. Although, this function is desirable because it is easily manipulated mathematically, it is now generally believed that the earth's lithosphere contains more roughness (e.g., Wu and Aki, 1985a; Wu and Aki, 1985b). The studies are also limited in that they use only a very small portion wavefield, only the travel time residuals and the log amplitude of the P-wave. Lastly, all these studies assume a constant velocity background model, thus they neglect the effect of the background velocity on the wavelength of the incident wave.

Flatté and Wu (1988) used the acoustic parabolic approximation and weak scattering theory to derived the angular and transverse coherence functions in a general random medium. When they applied these techniques to data from NORSAR, they found the best-fitting lithospheric model was an overlapping two layered model. The top layer extended from the surface to a depth of 200 km and was characterized by a simple band-limited white spectrum. The second layer, superimposed on the first, extended from 15 km to 250 km and had fluctuations which obeyed a power spectrum of the form $W(\underline{k}) = A|\underline{k}|^{-4}$, where \underline{k} is the wavenumber vector and A is a

normalization constant. Although fairly simple, this is generally believed to be the best available random lithospheric model.

Frankel and Clayton (1986) overcame many of the problems inherent in the earlier scattering studies. They used the finite difference technique to model elastic wave propagation in random media and examined many aspects of the scattering problem. Based on the frequency dependence of the scattering Q in short-period data (15 – 30 Hz), they speculated that the crust (35 km thick) could be characterized by a random medium with a 0th order von Kármán autocorrelation function, a correlation length ≥ 10 km and standard deviation in velocity of 5%. They also neglected to include the effect of the background model as well as the effect of scattering below the source.

4.5.1 Finite Difference Simulations

To avoid many of the assumptions and limitations common to analytic scattering studies, we also chose to use the *finite difference technique to generate the scattered field*. Unlike earlier studies (e.g., McLaughlin et al., 1985; Frankel and Clayton, 1986) we include a realistic background earth model and use a full waveform method to compare synthetic seismograms to field data from NORSAR and NORESS. The finite difference scheme used in this thesis is a simple explicit second-order scheme to solve the elastic wave equation (Appendix B). Although computationally very expensive, we favor this technique because it is accurate for a wide range of wavelength to scatterer ratios, and it provides a complete solution to the elastodynamic equations of motion (e.g., Frankel and Clayton, 1984; McLaughlin et al., 1985; Frankel and Clayton, 1986). As a result, P-wave and S-wave mode conversions are accurately modeled for both forward and backward scattering. This is especially important because thus far most analytic scattering theories neglect shear waves completely and often consider only forward scattering (parabolic approximation). The trade-off for the increased accuracy is a significant increase in computational effort, which cur-

rently limits our study to only two-dimensional models. Frankel and Clayton (1986) also used two-dimensional finite difference modeling to investigate the effects of scattering. They suggested that the effect on travel time and amplitude variations would be very small. Furthermore, they also derived a two-dimensional equivalent to one of the analytical results presented by Chernov (1960) and showed that at low frequencies attenuation due to scattering was proportional to $(ka)^3$ in a three-dimensional medium and $(ka)^2$ in a two-dimensional medium. Using the same equation, they showed that in the high frequency limit the two solutions converged.

As was stated above, the synthetic models were made as realistic as possible by including the Parametric Earth Model (PEM) for continental structure (Dzienwonski et al., 1975), as the background velocity model. Inclusion of a realistic background model is necessary to account for the fact that the wavelength of the incident wave varies inversely with velocity, and therefore generally increases with depth. The models also included zero stress boundary conditions at the top of the finite difference grid and absorbing boundary conditions at the bottom. To avoid unwanted reflections from the sides of the grid, the model was assumed to be horizontally periodic. The simulation was carried out for 18000 time steps (thus producing 90 s of synthetic data) on a large finite difference grid (512 nodes by 2750 nodes) which simulated a 51.2 km by 275 km region of the lithosphere.

In all the simulations the incident wave was a plane P-wave, which entered the bottom of the grid as a Ricker wavelet centered at 1.65 Hz. Since the independent variable in the finite difference calculations was displacement, the resulting synthetic seismograms were differentiated with respect to time to produce seismograms of particle velocity, like those recorded at NORSAR and NORESS. Upon differentiation, the center frequency of data became 2 Hz, consistent with that of the field data (Figures 43 and 45).

The plane wave source used in this study is a good approximation of the true incident wave if the source is located far from the receiver array (as is the case with

the field data used here). Furthermore, it is likely that the incident wave would show little variation over a region the size studied here. This occurs because of the small range of takeoff angles (from the source) which constitute this portion of the wavefront. It is true however that we have neglected the effects of forward scattering (P-wave to P-wave scattering) in the source region, which would be constant across the spatial extent studied here. The effect of this type of scattering would be an overall increase in complexity and coda along the incident wave.

Since in the field data the source was located close to the surface, the wavefield observed at NORSAR traveled through the lithosphere twice; once beneath the source and once beneath the receiver array. Numerical limitations prevent us from modeling the full propagation path, so we must devise some way of estimating the coda produced in the source region. After investigating several different approaches, we chose an approximate technique based on a simple one-dimensional convolutional model (Dainty et al., 1973). The technique makes use of the fact that energy which has propagated through the lithosphere is the convolution of the transfer function of the lithosphere with the source wavelet. Since the source function is known for the synthetic data, it can be deconvolved from the synthetic seismograms, leaving only the transfer function. Convolving the transfer function with the seismogram results in a new seismogram which contains some of the features which would be observed in a seismogram of energy which had propagated through the medium twice. It must be pointed out that this is not an exact solution, but it does allow us a simple mechanism to include the first order effects of propagation through two lithospheric layers.

Simple Gaussian Models

As was mentioned above, it is generally believed that the lithosphere can not be adequately described by a Gaussian random medium like those presented in the early literature (e.g., Aki, 1973; Capon, 1974; Berteussen et al., 1975a). Still, it is worth investigating one such model so that these data can be compared to data from more

contemporary lithospheric models. For this purpose, we chose the model proposed by Aki (1973) (Table 1). Although the original analysis was based on the acoustic wave equation, we will extend the random velocity perturbations to the S-wave velocity field and include the PEM background velocity field to account for the change in wavelength with depth.

Before beginning a quantitative analysis of the data, it is often useful to observe the general trends in the scattered field. For this purpose snapshot pictures of the divergence and curl of the wavefield were output at 7 s increments and are shown in Figures 55 and 56. The medium is a two-dimensional realization of the lithospheric model proposed by Aki (1973). Snapshot pictures from any of the other simulations would contain many similar features. In an homogeneous medium, the divergence and curl exactly decompose the wavefield into its P-wave and S-wave components. This is not true in an heterogeneous medium, where the gradients of the material properties are not zero and therefore contribute to both the divergence and curl. Although if the medium is sufficiently smooth, the divergence is dominated by P-wave energy and the curl by S-wave energy.

The first snapshot picture of the divergence shows the incident P-wave shortly after it has entered the bottom of the heterogeneous zone (Figure 55). At this point, there is only a slight disturbance on the curl snapshot, which is due to the partial conversion of the P-wave to an S-wave as it enters the heterogeneous region (Figure 56). When the P-wave interacts with the free surface (the second frame), a strong S-wave is created, which is subsequently scattered as it travels downward behind the reflected P-wave. Note that in the subsequent frames the dominant scattering mechanism is common mode (P-wave to P-wave and S-wave to S-wave) forward scattering. This type of scattering tends to distort the incident wave and create strong diffractions with very little backscattering and little P-wave to S-wave scattering. As a result, the direct arrival is no longer a simple planar wavefront and distinct travel time and amplitude anomalies are visible along the wavefront.

Table 1. Proposed Crustal Models

	Autocorrelation		Correlation		rms		Thickness
	Function	Length	Length	Deviation	Deviation	Deviation	
Aki (1973)	Gaussian	10 km		4%			60 km
Capon (1974a)	Gaussian	12 km		1.9%			136 km
Berteussen (1975b)	Gaussian	15 km		3%			50 km
Frankel & Clayton (1986)	0th order von Kármán	≥ 10 km		5%			35 km
Flatte & Wu (1988)	Two layered model	k^n n=0,4	(0.9-2.2%)/(0.5-1.3%)	(0-200 km)/(15-250 km)			

Aki Model

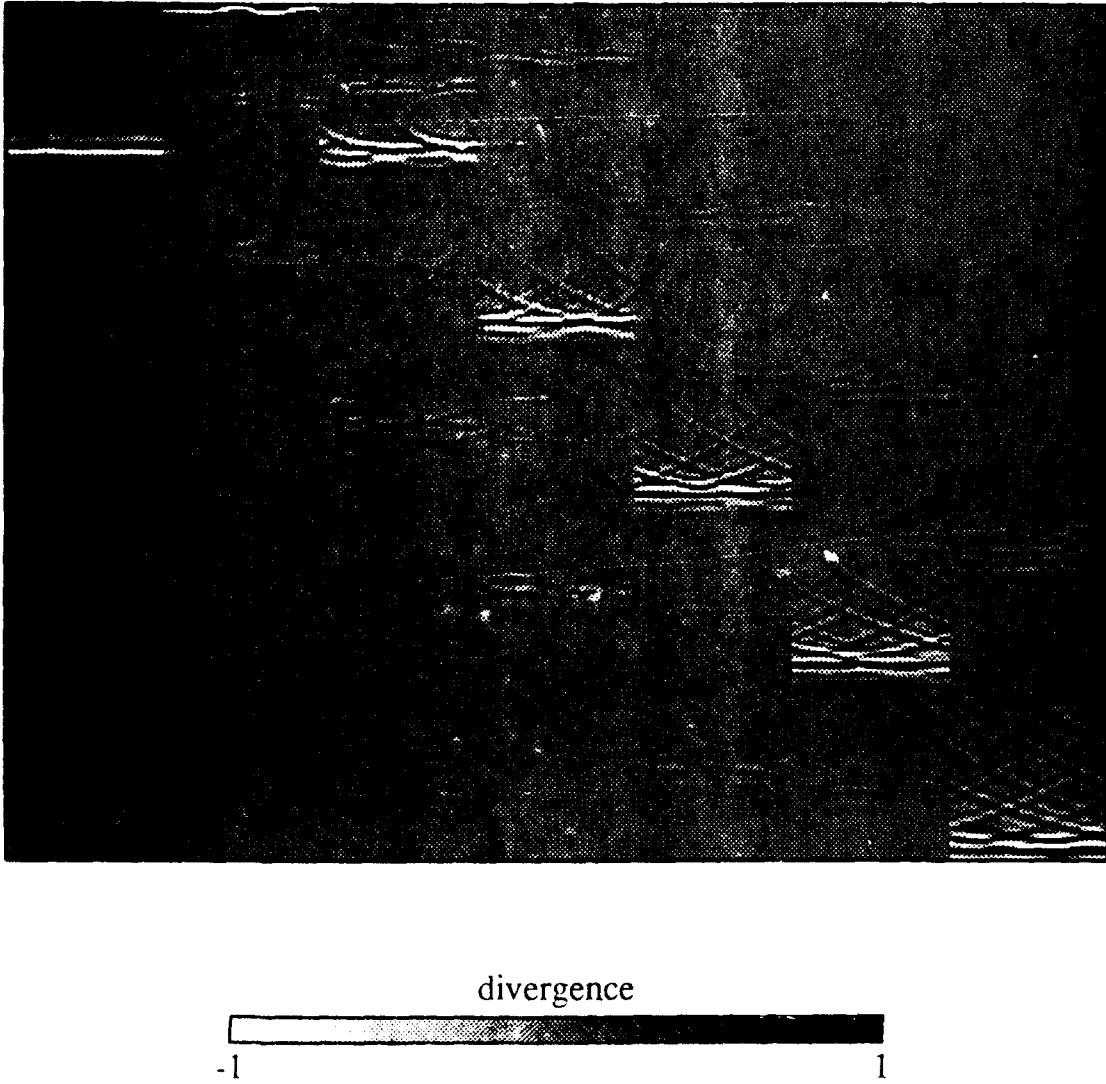


Figure 55: Snapshot pictures of the divergence of the wavefield at 7 s intervals. The random portion of the velocity model is like that proposed by Aki (1973), and the deterministic velocity structure is a simple reference earth model.

Aki Model

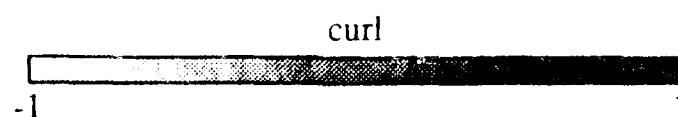


Figure 56: Same as Figure 55, but shows the curl of the wavefield.

Synthetic seismograms generated at 3.2 km intervals along the free surface are shown in Figure 57. The data have already been differentiated, to produce velocity data like that recorded at NORSAR, and only the time window between 25 s and 45 s is shown. The most striking feature in the data is the strong first arrival and lack of coda. The travel time fluctuations of the P-wave (Figure 58), show two large anomalies with a spatial separation of ≈ 25 km. Comparing Figures 58 and 59, note the correspondence between the amplitude and travel time fluctuations. The strong correlation between these two parameters is indicative of scattering in smoothly varying media dominated by large scatterers and was predicted by Chernov (1960) and Aki (1973). The periodicity in both these figures is a direct consequence of the periodicity in the velocity model and the source wave. Lastly, it should be pointed out that the discrete steps in the plot of the travel time variations (Figure 59) are due to the discrete sampling interval of the finite difference simulation. The large size of the simulation and the large number of timesteps, forced us to decimate the synthetic seismograms as they were computed. After decimation, the sampling interval was 0.05 s. The rms variation in travel time (0.08 s) and amplitude (0.46) in the data from this model were generally consistent with what was observed at NORSAR.

Another way to compare the synthetic data to field data is to calculate the coherency of the waveforms over distances similar to those at NORSAR and NORESS. This was done by first windowing the synthetic data over a 6 s window surrounding the first arrival. Then, the coherencies were calculated for two sets of 25 receivers. In the first set, the 25 receivers were each separated by .1 km, resulting in maximum and minimum separations of .1 km and 2.4 km; roughly equivalent to receiver separations at NORESS. Variations over these length scales will help to identify the prevalence of small-scale scatterers. In addition, a second set of receivers, each separated by 1 km, were investigated. The second data set spans distances more like that of NORSAR, and can therefore be compared to coherencies calculated for teleseismic arrays such as NORSAR. The latter data set will help to identify the large scale features in the

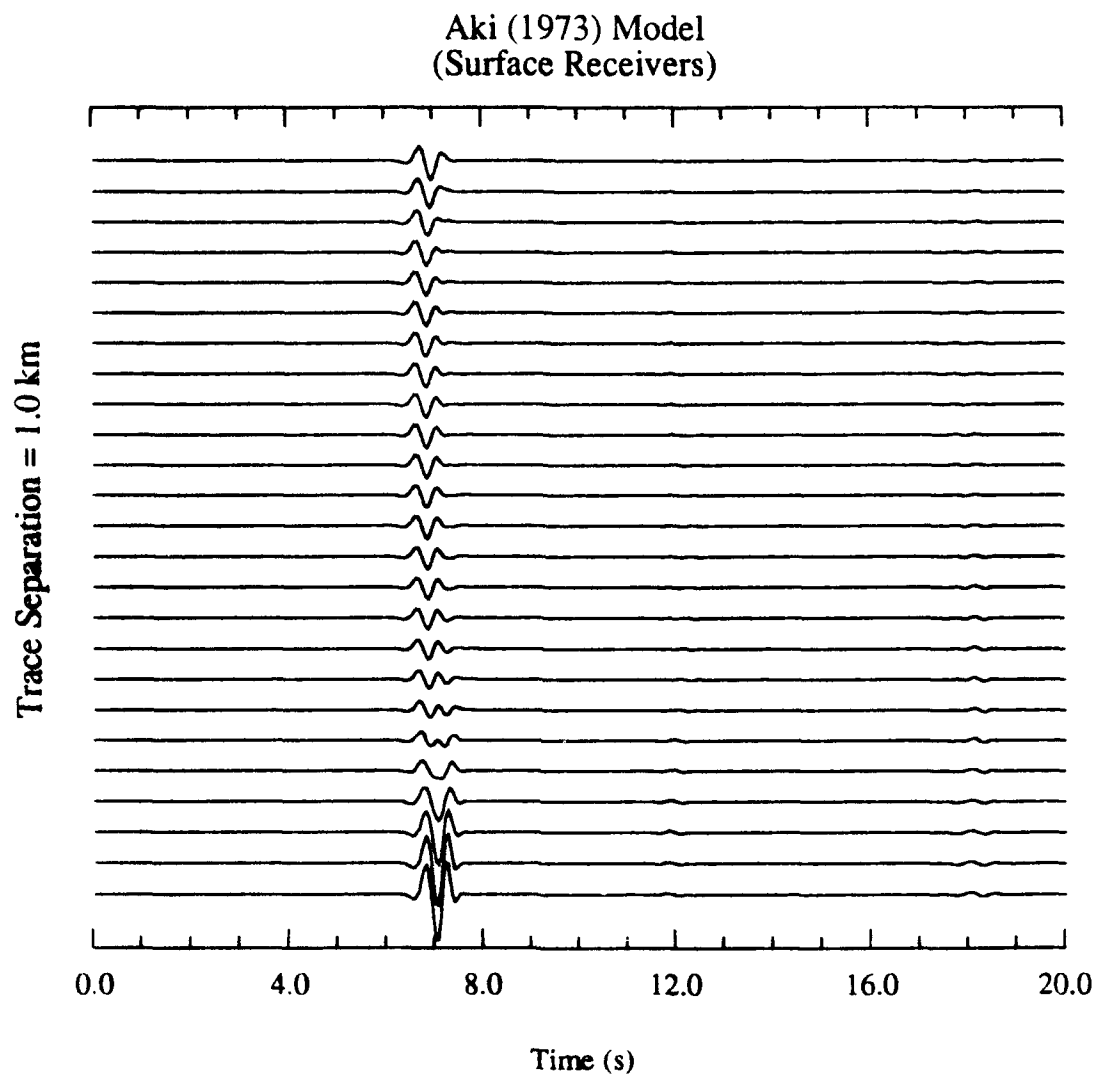


Figure 57: Synthetic seismograms resulting from the finite difference simulation of a plane wave propagating in a random medium like that proposed by Aki (1973).

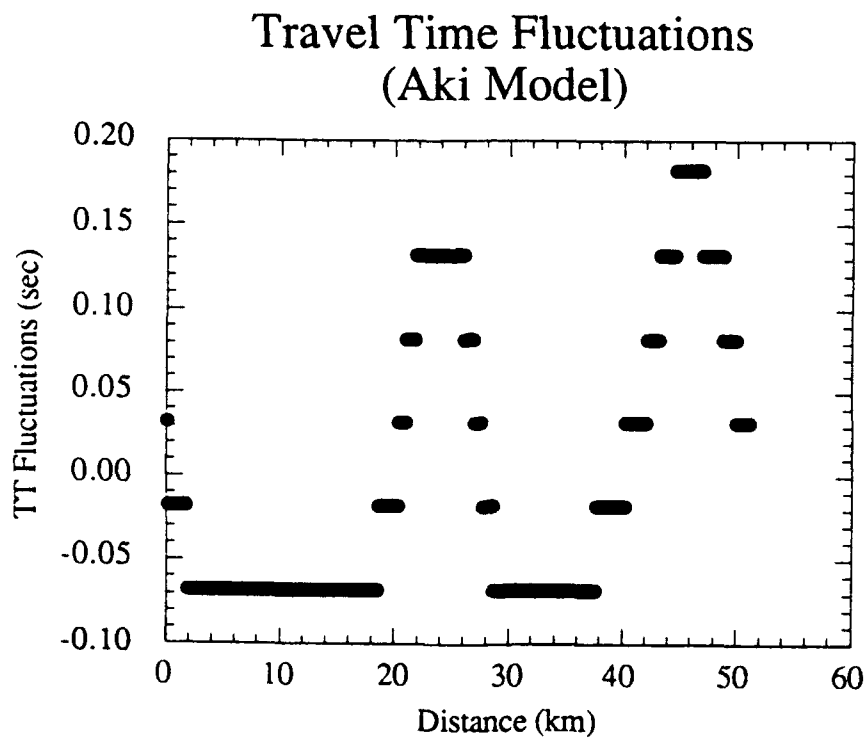


Figure 58: Travel time residuals which resulted from the Aki (1973) model. The rms variation for this parameter was ≈ 0.08 s.

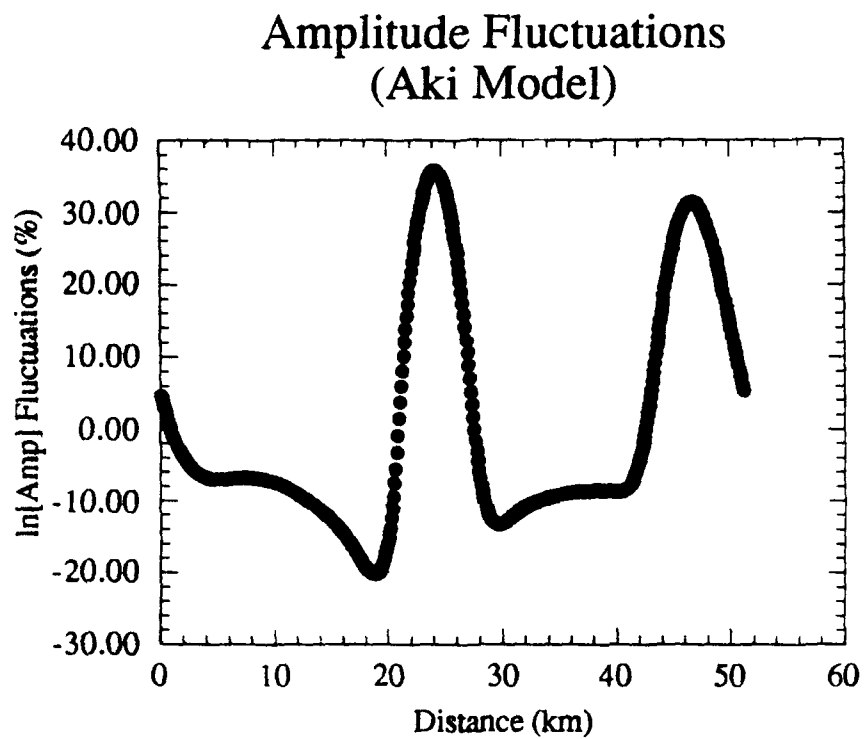


Figure 59: Fluctuations in log amplitude which resulted from the Aki (1973) model. The rms variation for this parameter was 0.459.

lithosphere.

Comparing the coherencies calculated from the synthetic data to that from the NORESS data highlights several important issues. At low frequencies (1 & 2 Hz), both data sets display high spatial coherency over the full range of distances (0 - 2.5 km). At higher frequencies (3 & 4 Hz), the fall-off rate of the coherency in the field data is considerably higher than that in the synthetic data. One explanation for this might be that the earth has more small (relative to the wavelength) scatterers, which would be consistent with the P-wave fluctuations discussed above. The difference between the two data sets becomes even more clear when the coherency is calculated for larger offsets. When measured over distances similar to those at NORSAR, the fall-off of the coherency with distance is far slower than is observed at NORSAR. Together, all the data suggests that this model is too smooth to represent the velocity fluctuations in the earth. The lack of roughness limits the amount of coda which is generated.

Simple single layer lithospheric models based on the Gaussian autocorrelation function have been proposed by several other authors (e.g., Capon, 1974; Berteussen et al., 1975a). All are similar to the one investigated above (Aki, 1973), although exact details concerning the thickness of the random layer, the intensity of the perturbations and the correlation length vary between studies (Table 1). Several of these models were investigated and each proved to have the same general characteristics described above. Namely, these models produced coherency measurements which were too large and they were not capable of reproducing the amount of coda generally observed at NORSAR and NORESS. It has been speculated that they all failed because they did not contain enough roughness. Frankel and Clayton (1986) recognized this and proposed modeling the lithosphere as a 35 km thick layer described by the 0th order von Kármán function. We investigated this model as well, and found it was desirable in that it produced more coda and therefore less coherent seismograms, however, the fall-off rate of the coherency as a function of distance was still significantly more than what is observed at NORSAR.

Multiple layered Models

Although the random models discussed above are capable of explaining some of the observed travel time and amplitude variations, they are probably too simple to describe the velocity field in the lithosphere. More realistic is the overlapping two layered model proposed by Flatté and Wu (1988). In that model, the heterogeneities obey a simple power law relation of the form,

$$W(\underline{k}) = A |\underline{k}|^{-p}, \quad (4.2)$$

where $W(\underline{k})$ is the power spectrum of the fluctuations, \underline{k} is the wavenumber vector, A is the normalization constant and p is the power law index. Flatté and Wu (1988) found the best agreement when the power law index was zero ($p = 0$) in the upper layer and four ($p = 4$) in the lower layer. In addition, to compensate for the limited aperture of the array and the frequency content of the source, the spectra were bandlimited so that there were no fluctuations with wavenumbers less than 0.05 km^{-1} and none greater than 1.1 km^{-1} (Figure 60). Flatté and Wu (1988) found best results when the rms deviation in velocity was .9 – 2.2% in the upper layer and .5 – 1.3% in the lower layer, although they acknowledge that resolution in this parameter is poor.

Snapshot pictures of the divergence of the wavefield are shown in Figure 61. By the time the incident wave has reached the depth shown in the first frame, it has already traversed the long wavelength heterogeneities near the bottom of the model and is about to enter the more heterogeneous crustal layer. The influence of these long wavelength features is to distort the incident wave and cause the numerous diffractions evident behind the incident wave. Although the dominant scattering mechanism is forward scattering, far more energy is side and back scattered relative to the Gaussian model described above. When the incident wave interacts with the free surface (second frame) it is partially converted to an S-wave (visible in the latter frames of Figure 62). The S-wave travels more slowly than the P-wave and therefore has a shorter wavelength.

Power Spectra for the Two Layer Lithospheric Model

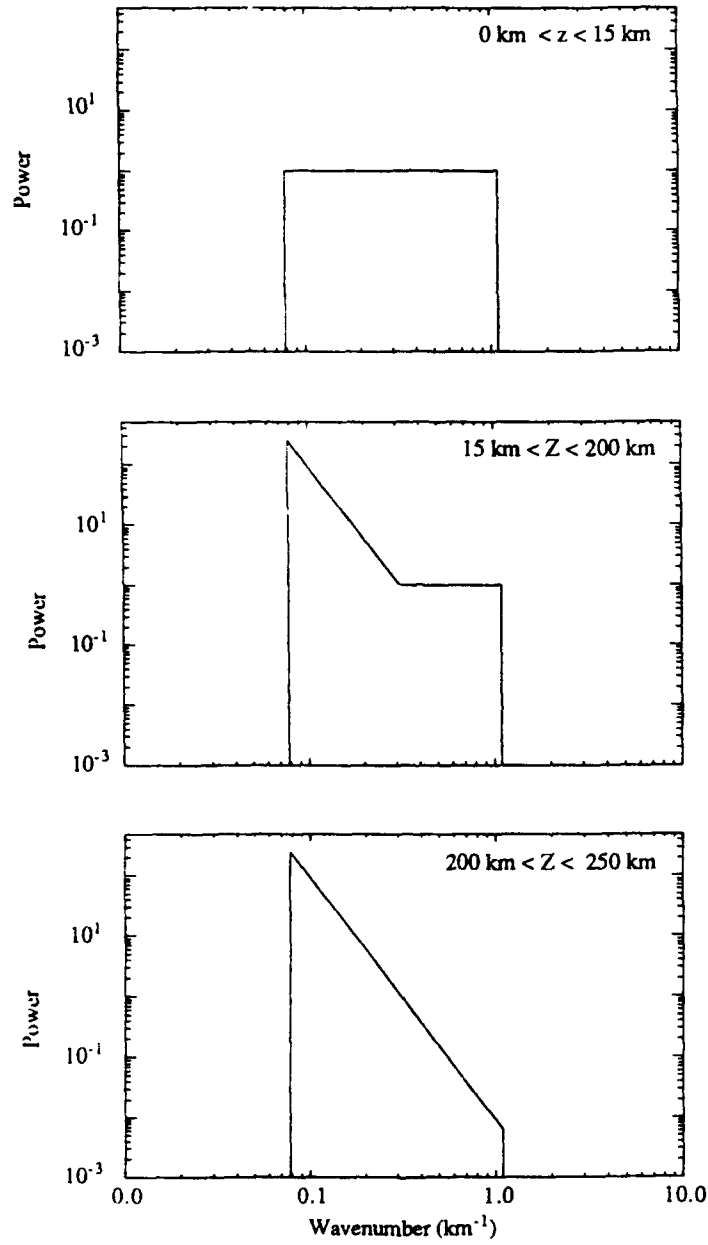


Figure 60: The lithospheric model proposed by Flatté and Wu (1988) was an overlapping two layer model. The upper layer had a bandlimited white spectrum and the lower a bandlimited power law spectrum which was proportional to k^4 .

Flatte & Wu Model

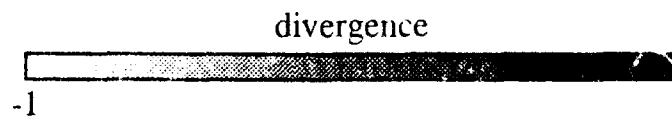
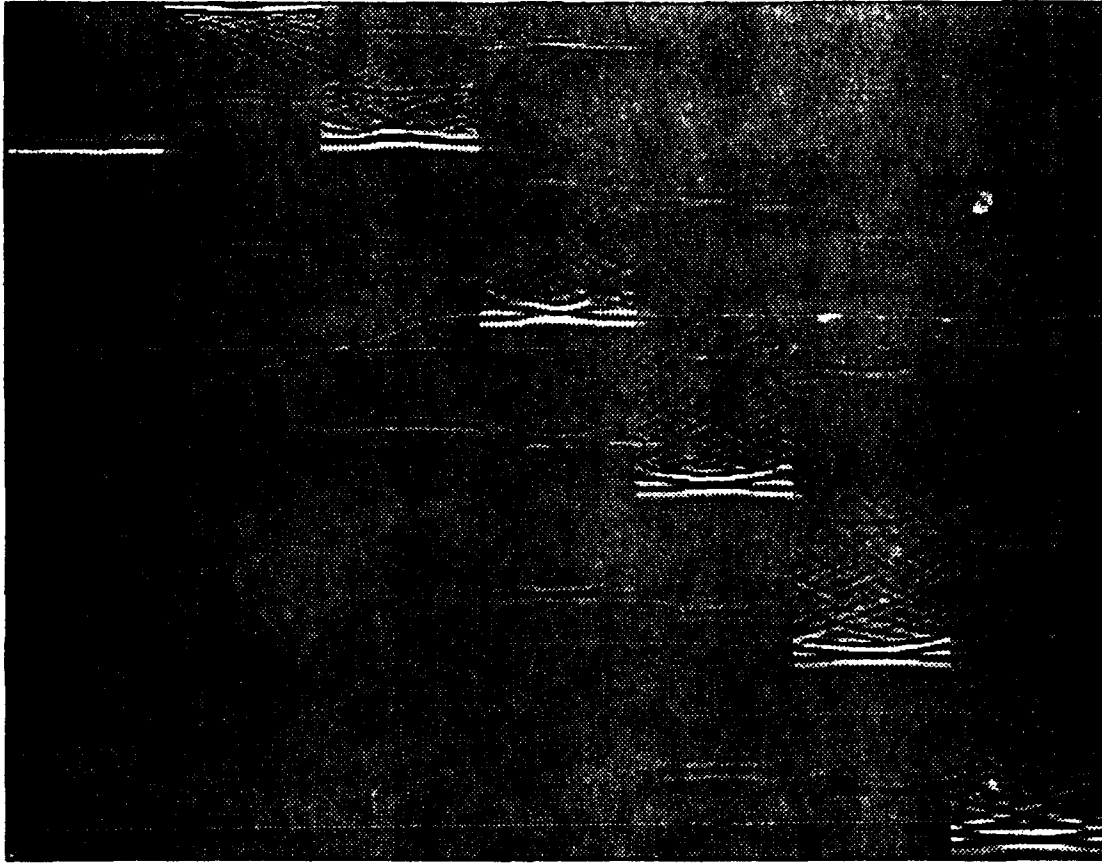


Figure 61: Snapshot pictures of the divergence of the wavefield at 7 s intervals. The random portion of the velocity model is like that proposed by Flatte and Wu (1988), and the deterministic velocity structure is a simple reference earth model.

Flatte & Wu Model

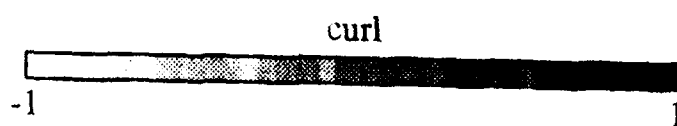
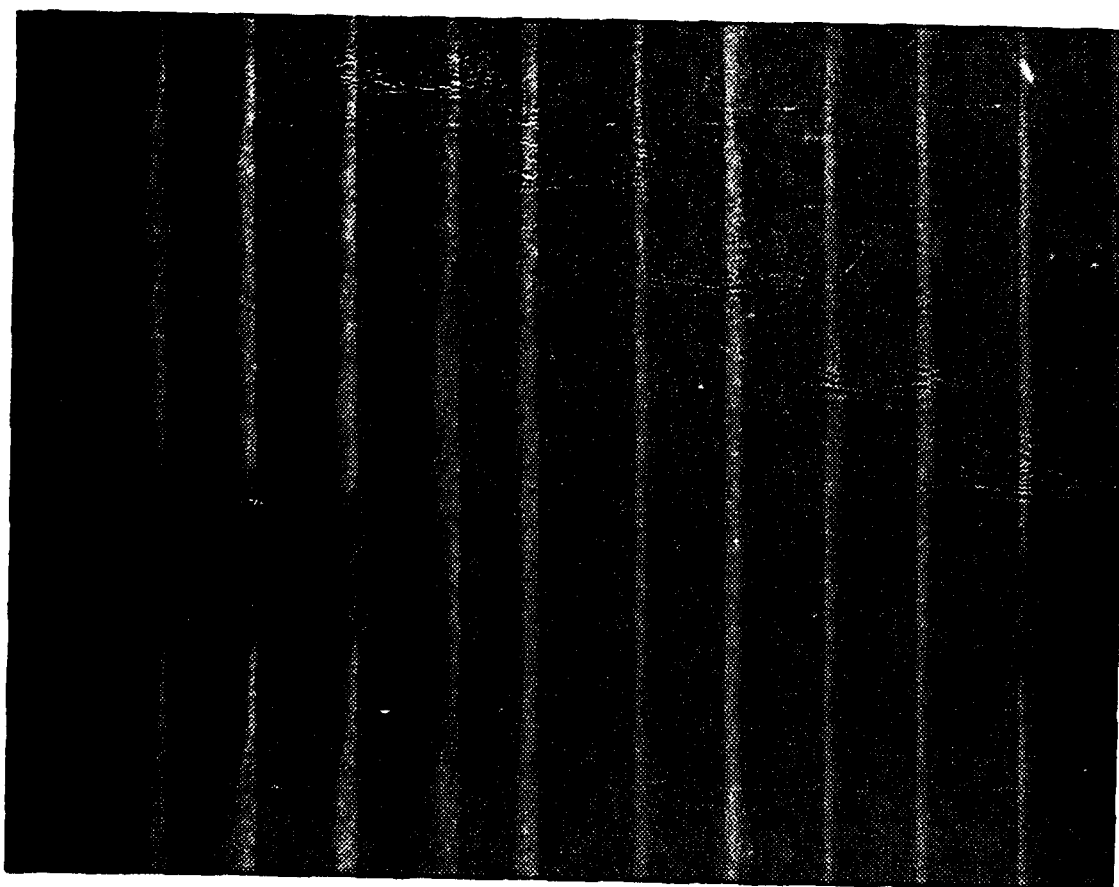


Figure 62: Same as Figure 61, but shows the curl of the wavefield.

Synthetic seismograms generated along the top of this model show considerable variation (Figure 63). Note the variability of the first arrival, as well as the variation in the strength of the multiply reflected arrivals at 12 s and 18 s. The general character of these waveforms is more consistent with the field, which suggests that this model may be more similar to the lithosphere than the smooth Gaussian model. The rms travel time residuals measured from this model were 0.06 s and the rms log amplitude fluctuations were 0.21198, both are consistent with what was observed at NORSAR, although the amount of amplitude variation might be slightly low. The variation in travel time (Figure 64) shows a single strong peak, corresponding to the longest wavelength anomaly which can be supported on the grid (51.2 km). This is further evidence that the long wavelength features have a large effect on travel times. The amplitude fluctuations (Figure 65) show more short wavelength variation than the travel time fluctuations, but still have a strong peak in the center of the model. The correspondence between the two type of fluctuations is not as striking as that observed in the Gaussian model, but it is still very evident.

In order to compare the variation in synthetic waveforms to the variation observed at NORSAR, the coherency was calculated from the data in Figure 63. Due to the periodicity in the velocity model, the aperture of the synthetic array was limited to the half-width of the grid. Thus, the maximum receiver separation in these coherency calculations is 25.6 km, approximately half the distance calculated for the NORSAR data. At the lowest frequency, 1.5 Hz, the coherency of the synthetic data (Figure 66) falls off slightly more slowly than is observed at NORSAR (Figure 50). There is also less scatter in the individual measurements, possibly suggesting that the lithosphere has more roughness than is present in this model. The same general trend is observed in the coherency of the higher frequencies (Figures 67 and 68).

It is interesting that although the model proposed by Flatté and Wu (1988) matches the observed travel time residuals and log amplitude fluctuations well, it does not match the falloff rates in the coherency function nor the general variability

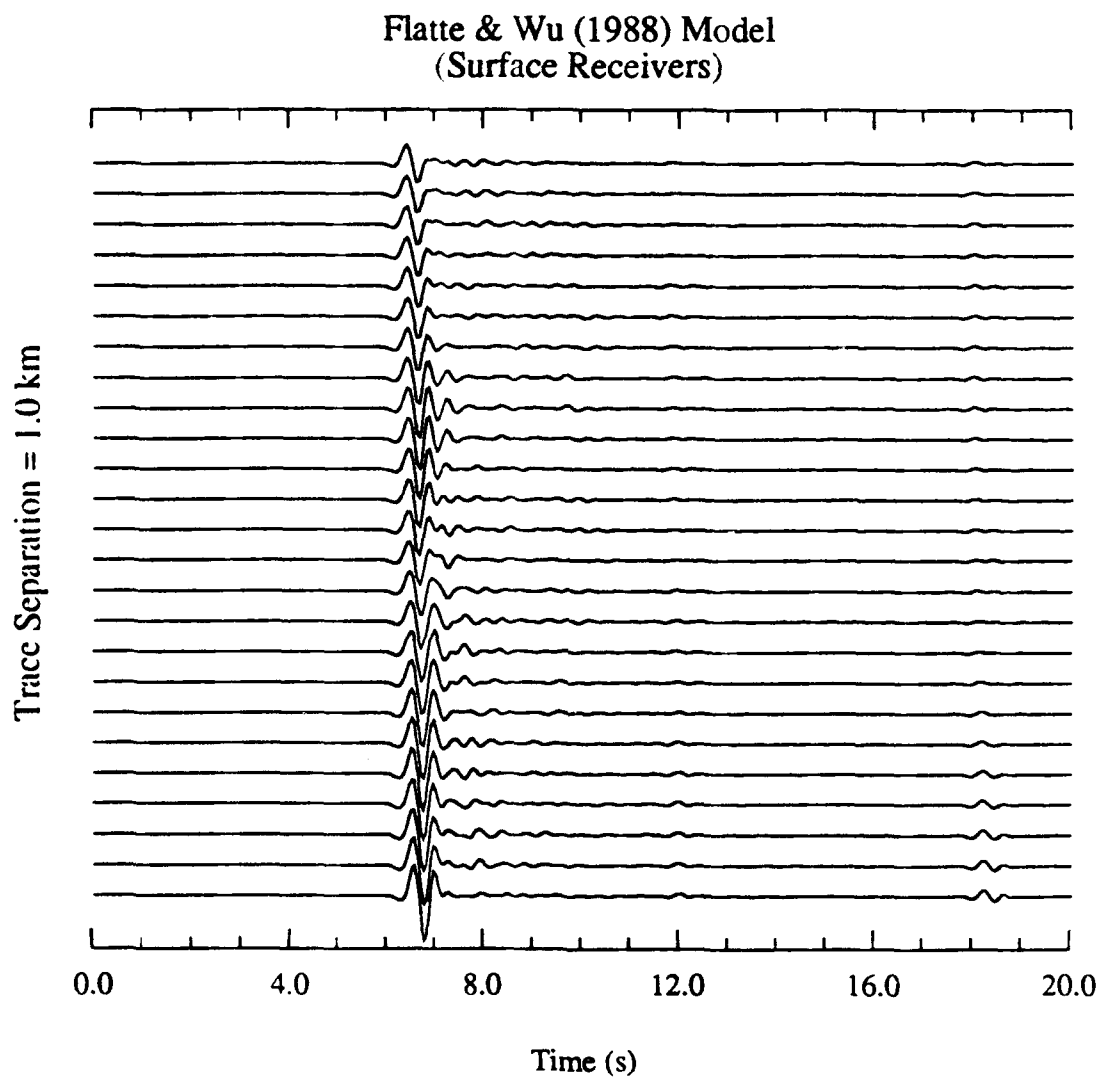


Figure 63: Synthetic data from a model like that proposed by Flatté and Wu (1988). The trace separation is 1 km.

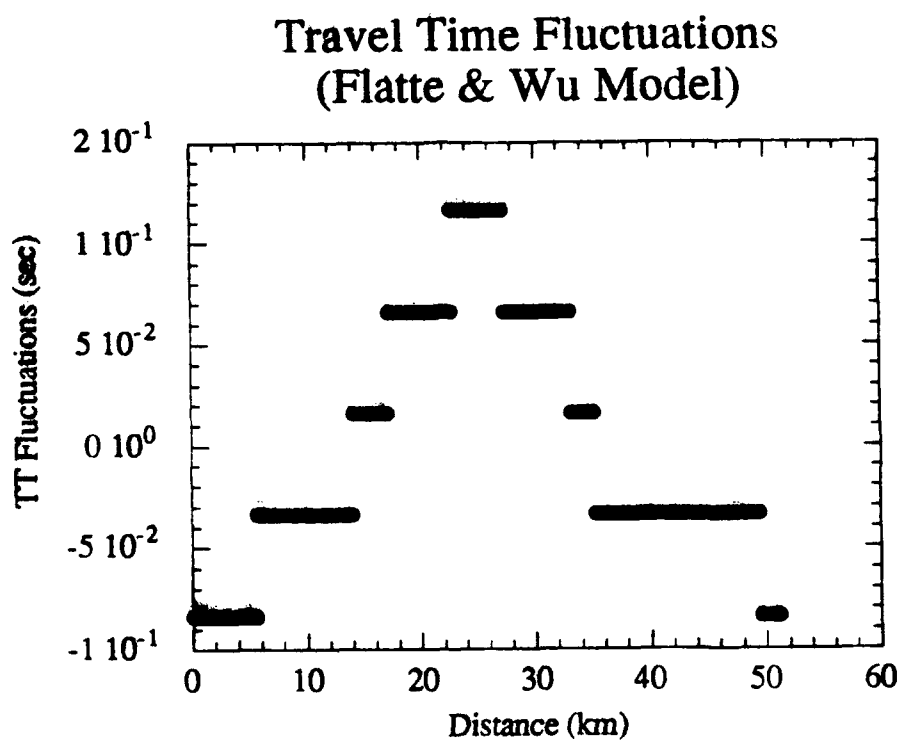


Figure 64: Travel time residuals which resulted from the Flatté and Wu (1988) model. The rms variation for this parameter was ≈ 0.06 s.

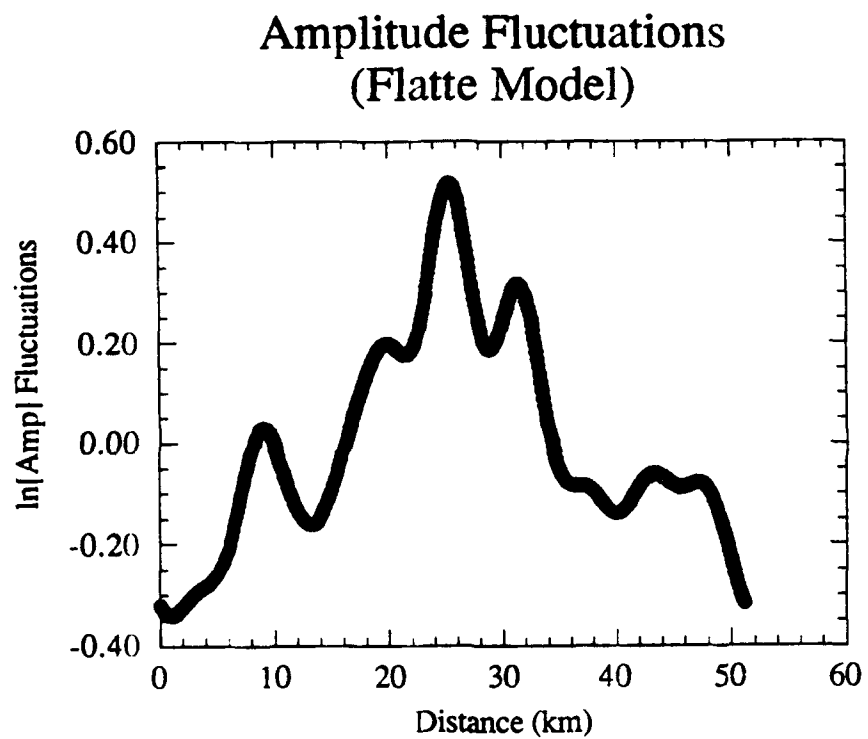


Figure 65: Fluctuations in log amplitude which resulted from the Flatté and Wu (1988) model. The rms variation for this parameter was 0.2.

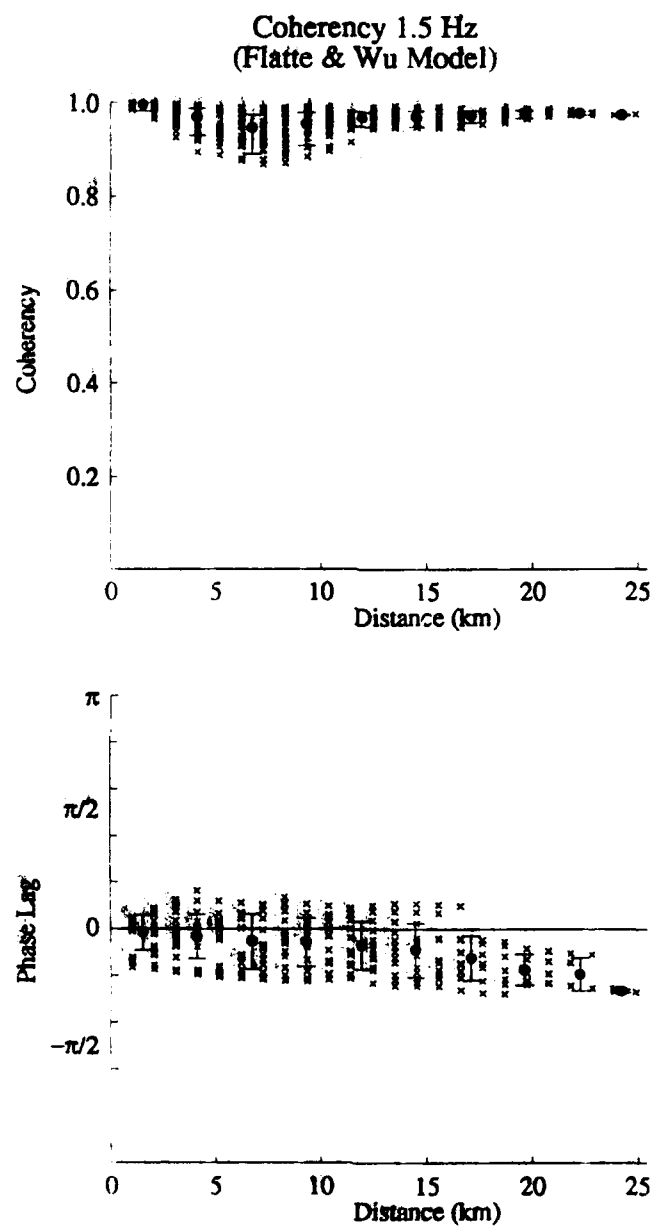


Figure 66: Coherency at 1.5 Hz as a function of spatial separation for the direct arrival and early coda of the data in Figure 63.

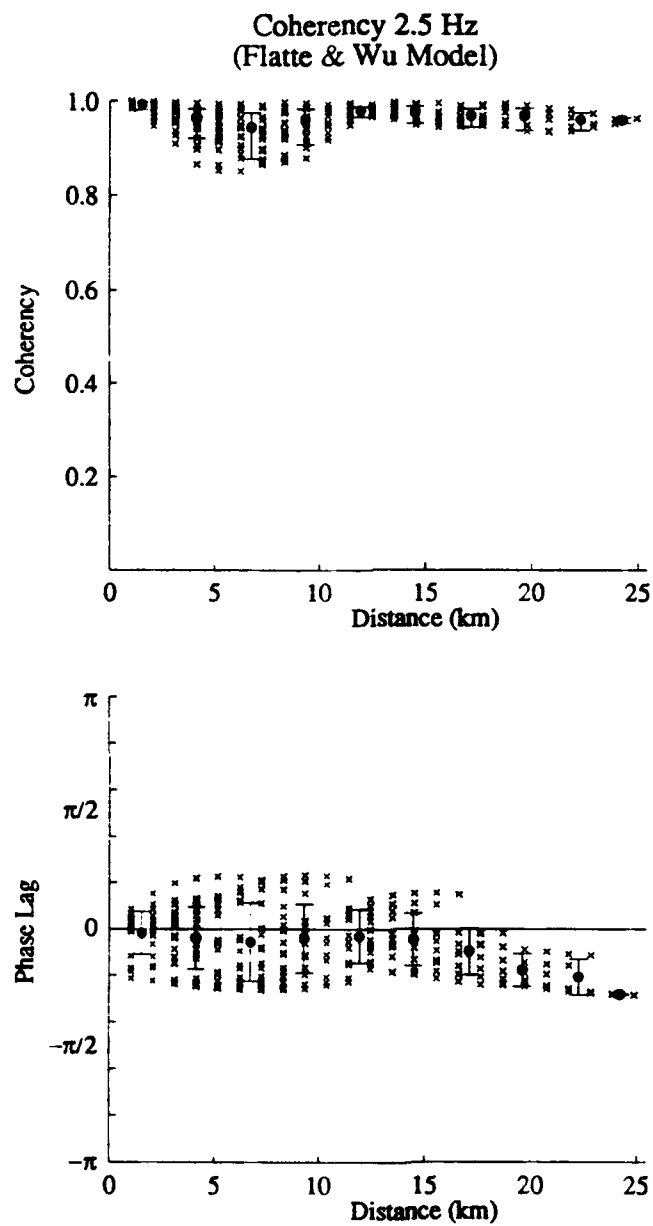


Figure 67: Coherency at 2.5 Hz as a function of spatial separation for the direct arrival and early coda of the data in Figure 63.

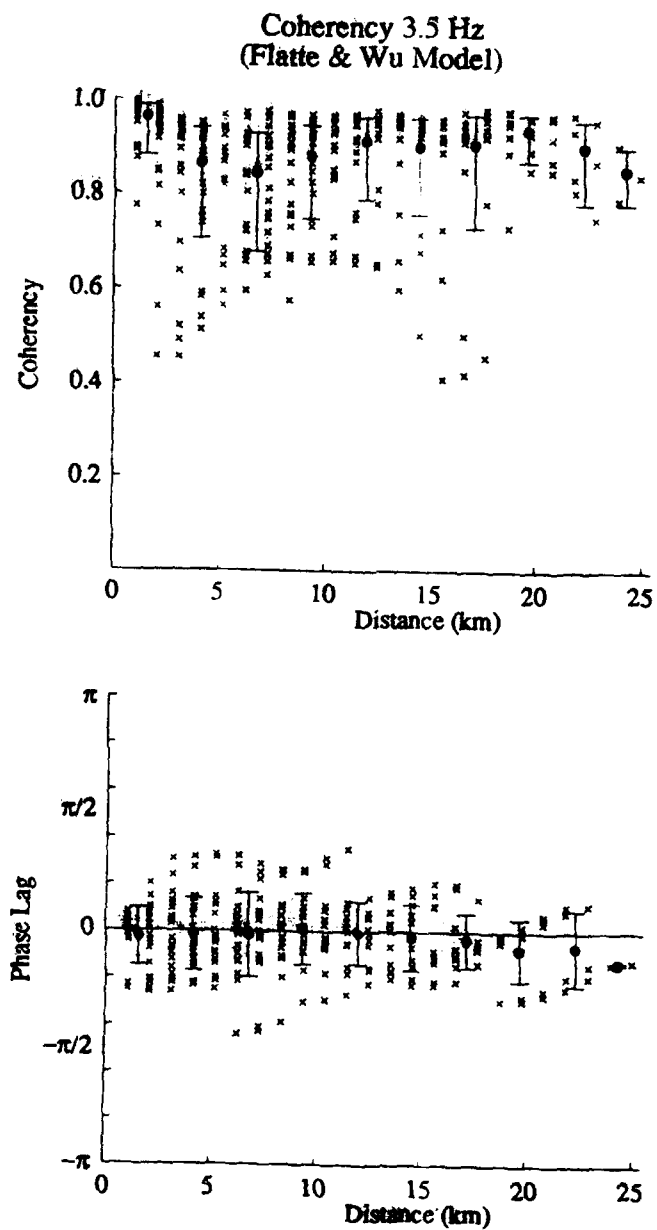


Figure 68: Coherency at 3.5 Hz as a function of spatial separation for the direct arrival and early coda of the data in Figure 63.

in these measurements. We attribute this to the lack of a highly variable near surface layer.

4.6 An Improved Random Lithospheric Model

None of the random models discussed above was capable of matching all of the trends observed in field data. The simple single layered models based on the Gaussian autocorrelation function appear to be too smooth and are not capable of exciting enough coda energy. The single layered model presented by Frankel and Clayton (1986) contain more short wavelength variation and therefore excite more coda. Still, the resulting waveforms from these model do not display a fall-off rate of the coherency function which is comparable to what is observed at NORSAR. Of the lithospheric models discussed above, the one proposed by Flatté and Wu (1988) is most consistent with the trends observed in the field data. It matches the total rms variation in travel time and log amplitude well, and coherencies calculated from these data match observed seismograms better than any of the previous models.

Working from the models presented above, we now propose a new crustal model which is consistent with reflection data from a nearby seismic experiment and better explains the travel time and amplitude fluctuations observed at NORSAR and NORESS. After running several simulations, we have found that a three layered model with varying degrees of roughness is appropriate. In our final model the uppermost layer extends from the surface to a depth of 3 km and is characterized by a bandlimited white spectrum. For reasons consistent with those presented by Flatté and Wu (1988), we chose the same wavenumber window for this layer. Below the highly heterogeneous near surface layer, we propose the remaining portion of the crust (down to 35 km) can be modeled as a 0th order von Kármán medium. This is consistent with the work presented by Frankel and Clayton (1986) and should generate an amount of coda consistent with that observed at NORSAR. Lastly, we model

the upper mantle as a random medium with an anisotropic Gaussian autocorrelation function. By anisotropic, we mean that the horizontal correlation length is different than the vertical correlation length. The correlation lengths which gave us the best results were 20 km in the horizontal direction and 5 km in the vertical direction. We obtained best results when the velocity perturbations in the upper and lower layers had 2% rms variation and those in the middle layer 3%.

The possibility of an anisotropic upper mantle is interesting and consistent with several studies based on the inversion of shear waves. Kennett and Nolet (1990) analyzed data from seismic arrays having apertures between 25 – 1000 km and suggested a heterogeneity model with a horizontal scale length of 300 – 400 km and a vertical scale length of 70 km in the uppermost mantle. They also speculated that the vertical scale length increased with depth. Based on the existence of partially coherent arrivals across the arrays and the extended coda it was also suggested there was substantial evidence for small-scale scatterers in the upper 200 km. Similar results were reported by Kennett and Bowman (1990), who used shear wave data and a coupled mode approach. The scale lengths reported in these studies are considerably larger than what was observed here. The explanation for this lies in the frequency of the input data. Those studies used 0.02 Hz surface wave data and 0.04 Hz body wave data, two orders of magnitude lower than was used here. The lower frequencies limit resolution to features larger than the width of NORSAR.

It is interesting to compare snapshot pictures of the divergence and curl in this model (Figures 69 and 70) to those from the simple one layer model proposed by Aki (1973) (Figures 55 and 56). Whereas the plane wave travels undisturbed up to the base of the crust in the model proposed by Aki (1973), in this model there are significant variations in the wavefront at that depth. The increased complexity in both the P-wave (divergence) and S-wave (curl) are clearly visible in the later snapshots. Note also the increased amount of side scattered energy in the model proposed here.

This Study

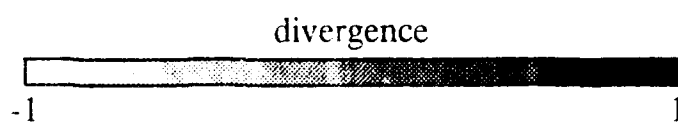
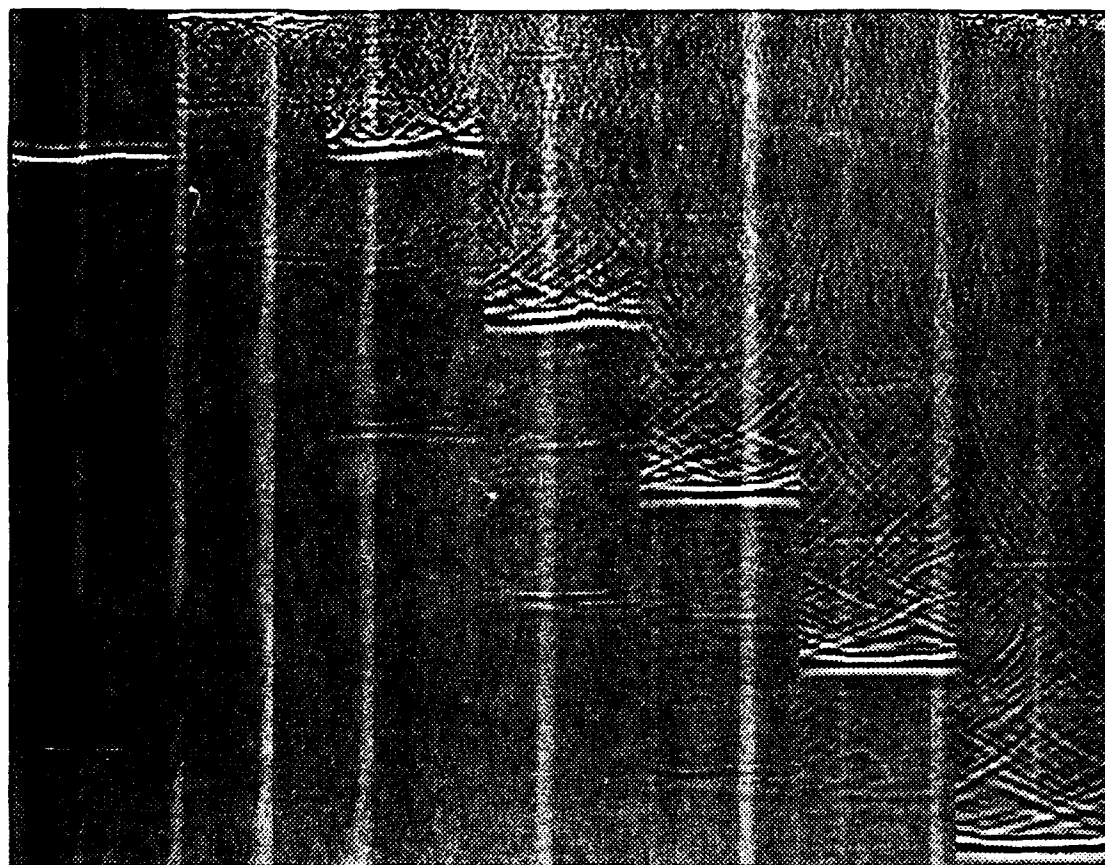


Figure 69: Snapshot pictures of the divergence of the wavefield at 7 s intervals. The velocity model is the three-layer model proposed here.

This Study

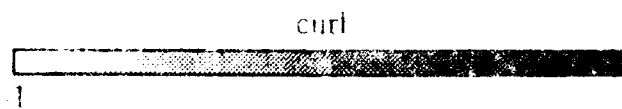
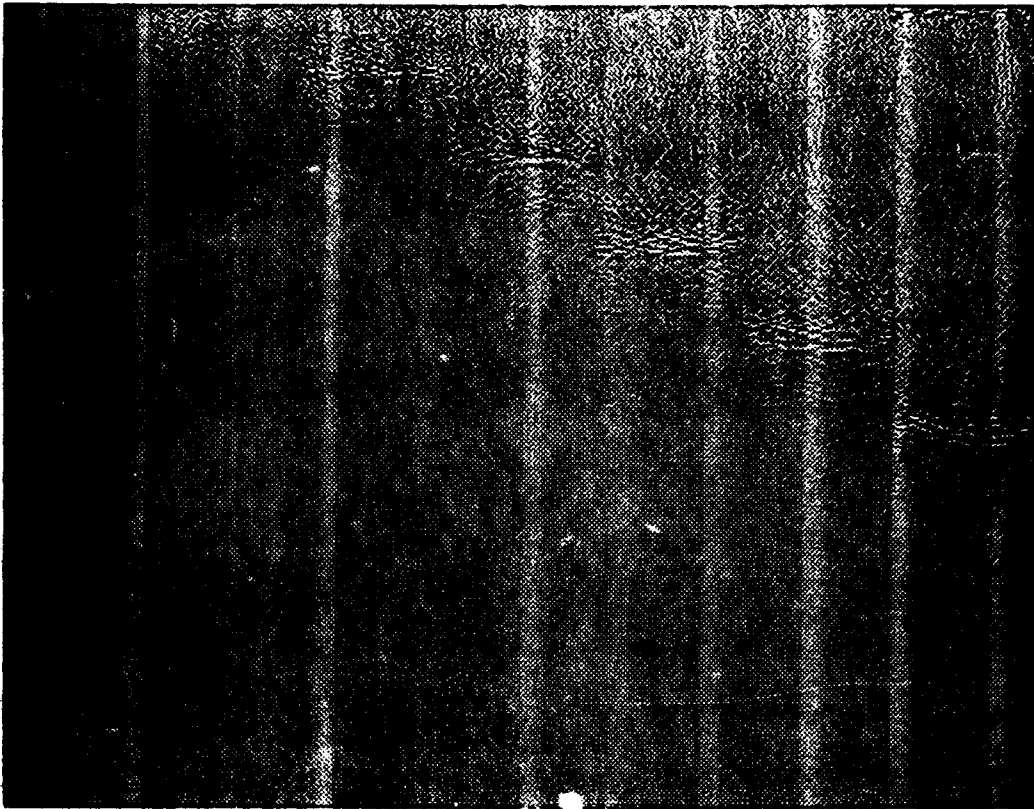


Figure 70: Same as Figure 69, but shows the curl of the wavefield.

Figure 71 shows 25 synthetic seismograms recorded along a 25 km section of the free surface. Note the variation of the seismograms with offset. The data have 0.08 s rms deviation in travel time (Figure 72), and 0.48 rms variation in log amplitude (Figure 73). These values are consistent to what was observed in the field data.

As compared to the field data, the synthetic data (Figure 71) appear to have less coda. This was to be expected and is discussed above. Therefore, to evaluate the ability of the model to match the coda observed at NORSAR, we should compare seismograms from the bottom of the random medium, where the incident wave has passed through the random medium twice (Figure 74). In terms of the energy behind the first arrival, these synthetic seismograms have amplitudes and coda signatures which compare favorably to the field data.

The coherency of the synthetic seismograms was calculated for both the small aperture (2.5 km) and large aperture (25 km) synthetic arrays, although only the large aperture results will be shown here. Using the same procedure outlined above, coherencies were calculated for the seismograms shown in Figure 71. Like the field data, the individual coherency values varied considerably between different receiver pairs (Figures 75 - 77). This was not true for most of the synthetic data discussed above and suggests that we are converging on the right type of variations our model. Also like the field data, the coherency is highest for the lower frequencies and diminishes with increasing frequency. The phase lags of the receiver pairs is also reminiscent of the field data, both in its average value and its variation. To insure that the periodic nature of the model was not biasing the coherency results, we performed a single simulated on a model eight times wider (≈ 400 km) than the previous models. The results were consistent, suggesting that the time window under study did not contain significant contamination due to periodicity of the velocity model.

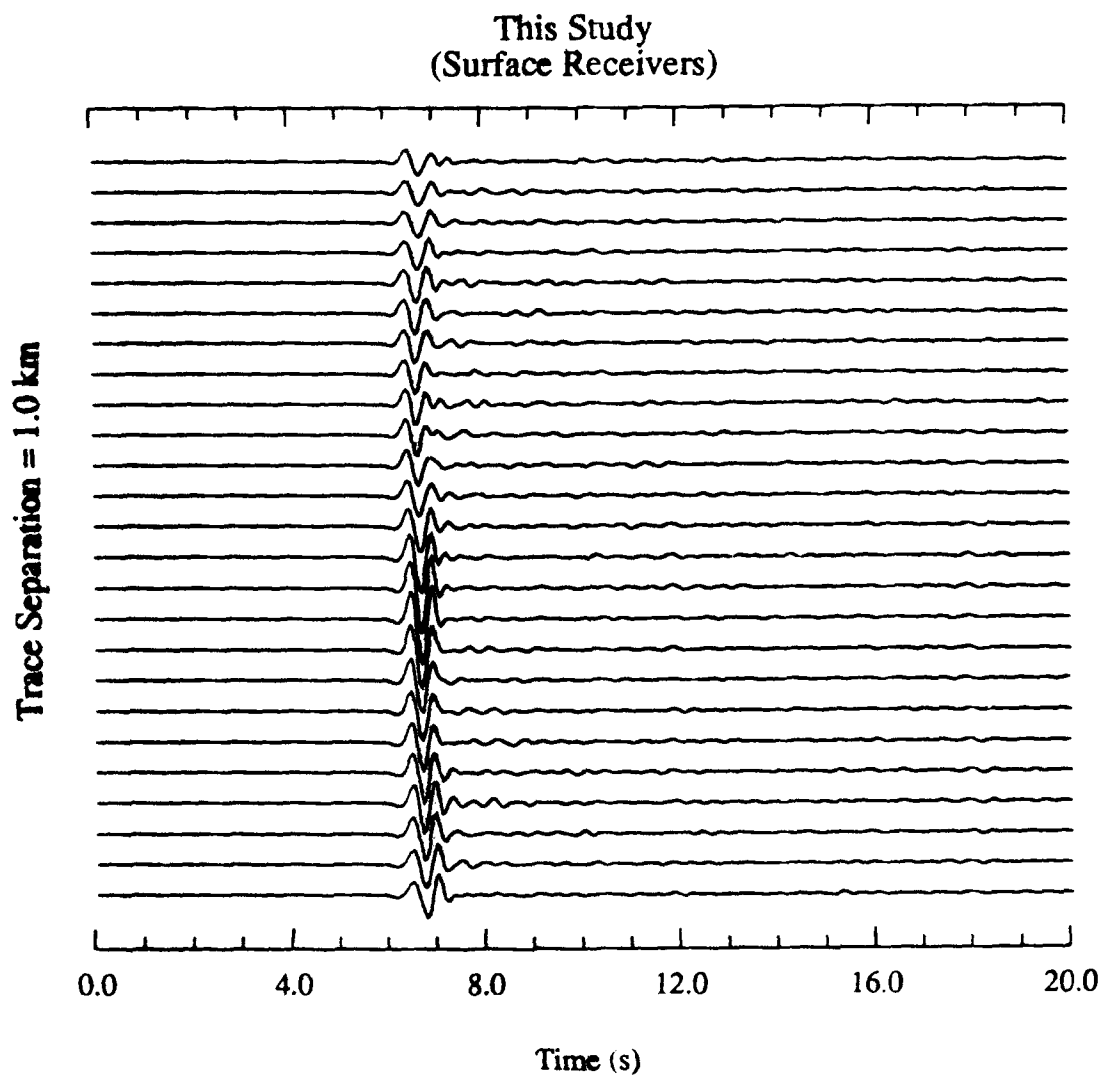


Figure 71: Synthetic data from the model proposed in this study. The trace separation is 1 km.

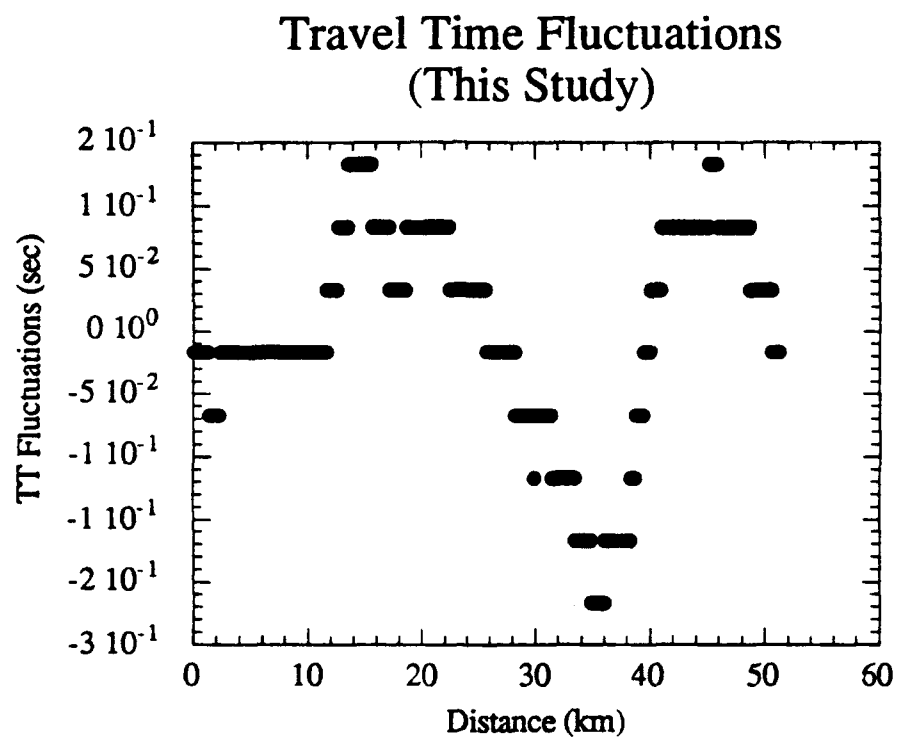


Figure 72: Travel time residuals which resulted from the three layered model proposed here.
The rms variation for this parameter was $\approx 0.08s$.

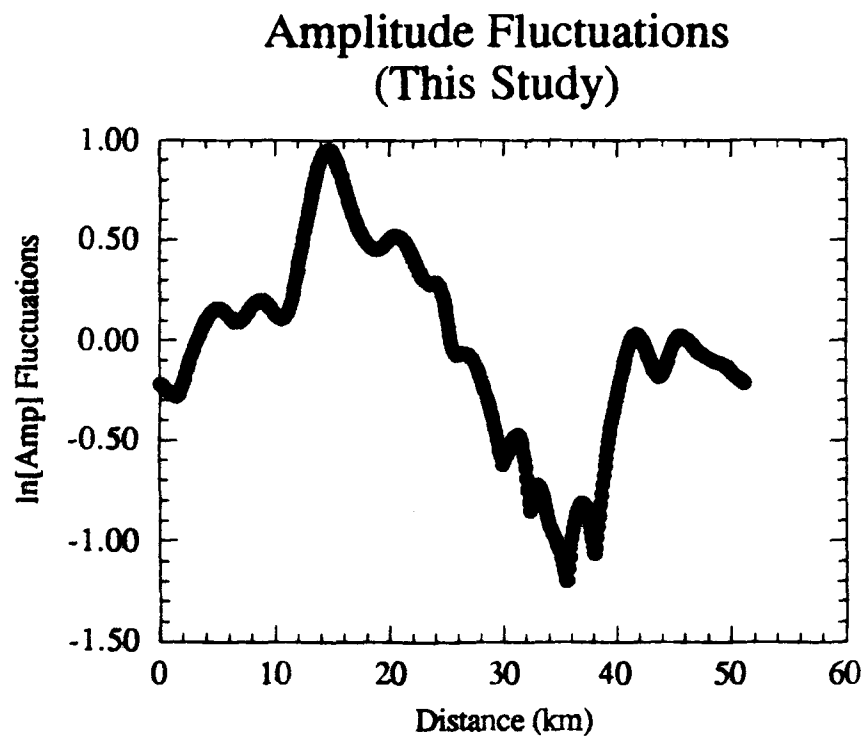


Figure 73: Fluctuations in log amplitude which resulted from the three layered model. The rms variation in this parameter is 0.48.

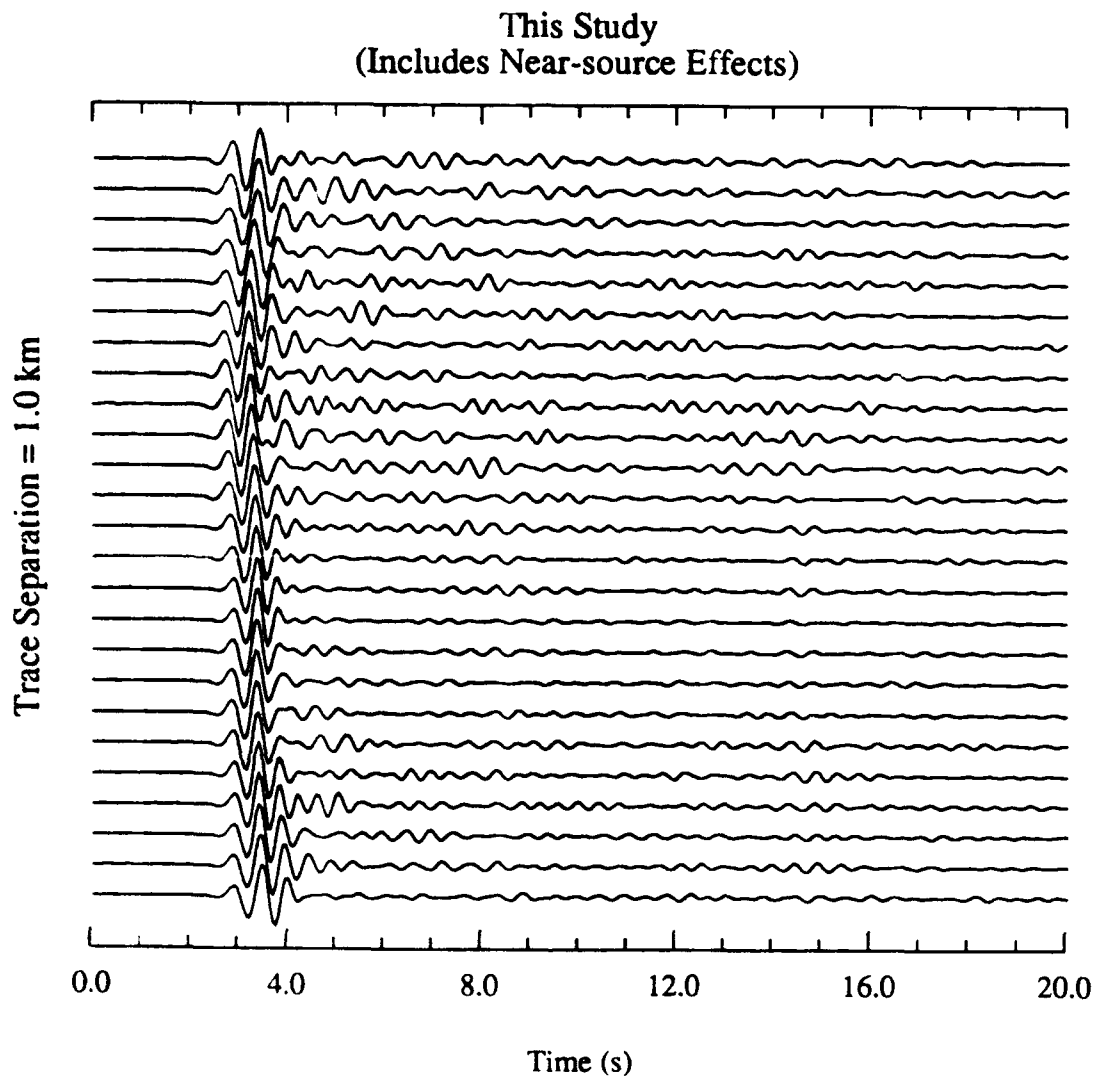


Figure 74: Synthetic data from the model proposed in this study. The trace separation is 1 km. What is shown are the traces in Figure 74 after they were convolved with the transfer function of the medium in an attempt to account for both lithospheric legs of the propagation path.

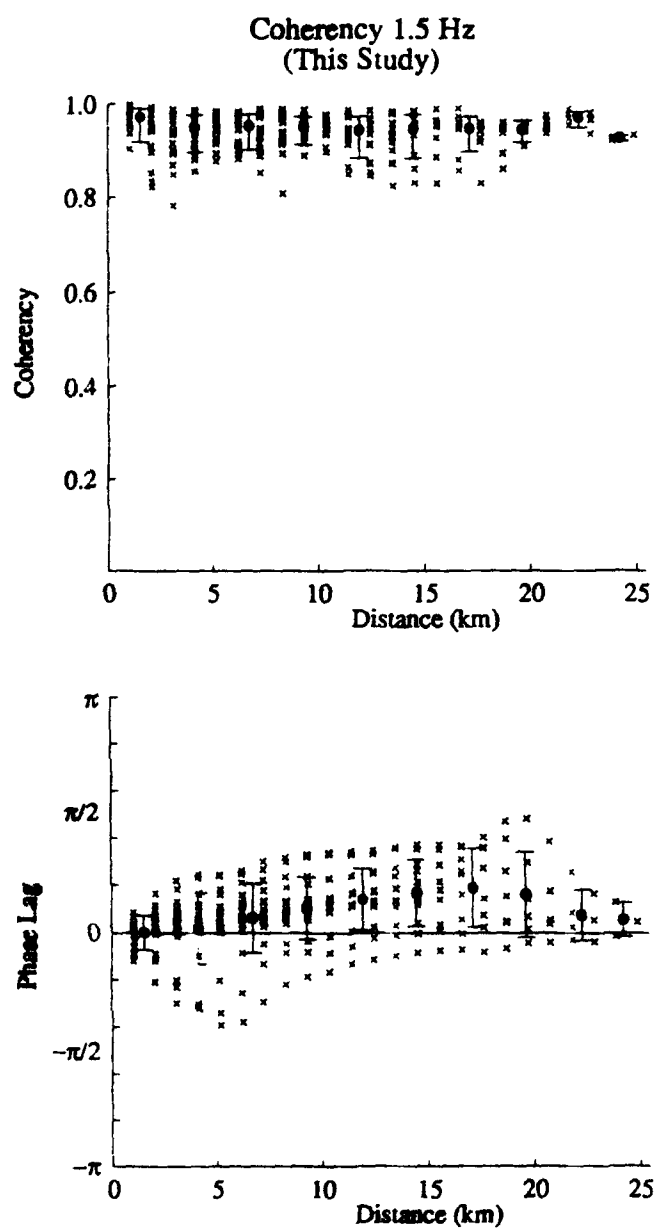


Figure 75: Coherency at 1.5 Hz as a function of spatial separation for the direct arrival and early coda of the data in Figure 71.

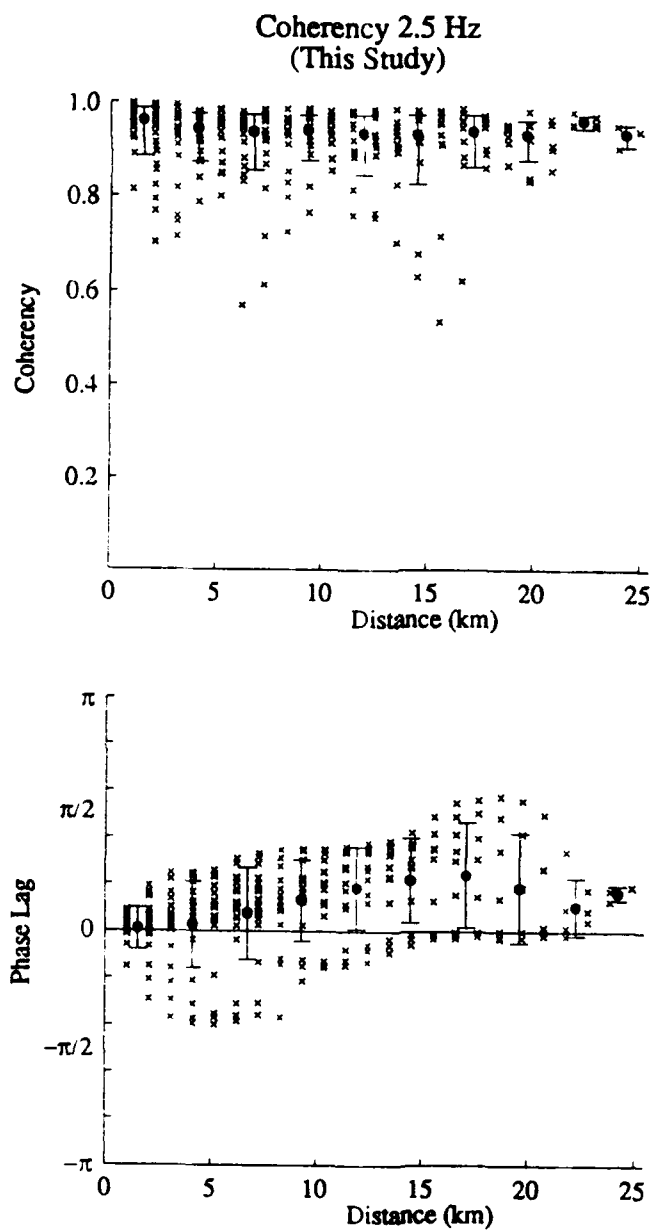


Figure 76: Coherency at 2.5 Hz as a function of spatial separation for the direct arrival and early coda of the data in Figure 71.

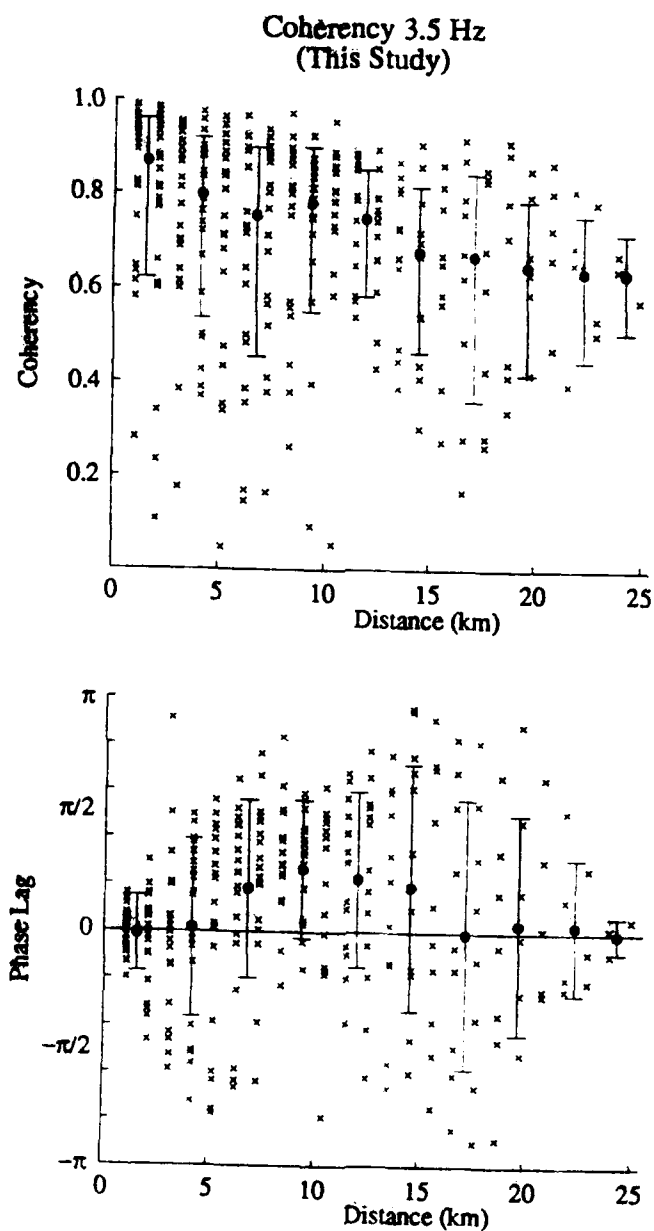


Figure 77: Coherency at 3.5 Hz as a function of spatial separation for the direct arrival and early coda of the data in Figure 71.

4.7 Conclusions

In this chapter we have shown that even in a the study of random media, a deterministic technique such as finite difference modeling can be useful. The main utility is that it allows one to study a particular aspect of the data in a controlled manner. This is often not possible in field studies where the earth, the source, and the receivers all introduce uncertainties into the investigation. Eventually, of course, the modeling must answer to the data. This is undertaken here by comparing several characteristics of the synthetic seismograms to field data from the NORSAR and NORESS arrays. The field data were from two nuclear blasts at the Semipalatinsk test site. The nuclear blasts are known to emit strong P-waves with a known source signature. With such strongly emergent data, we can be fairly sure all variations in the wavefield between receivers are due to heterogeneities below the receiver array. Furthermore, due to the large source-receiver distance, we can neglect the effect of scattering in the source region for all aspects of this study except coda generation. The reason for this lies in the observation that all energy arriving at the receiver emanated from a narrow range of take-off angles, implying the source effects are common to all energy arriving at the receiver.

After testing numerous random models, we found a three layered random model which both matched the observed travel time and amplitude variations observed at NORSAR and is consistent with seismic reflection data. The model, we propose has three random layers. The top layer is 3 km thick and described by a bandlimited white spectrum. The second layer extends from 3 km to the bottom of the crust (35 km) and can be described by the 0th order von Kármán autocorrelation function. Velocity fluctuations in this layer are fairly strong (3% rms variation), while in the top layer the fluctuations were only 2%. The third layer extends from the base of the crust to a depth of 250 km and was determined to have an anisotropic Gaussian correlation function. We found the best results when we specified the horizontal correlation length in the bottom layer to be 20 km and the vertical correlation length

to be 5 km.

The method used here has several important advantages over previous studies of scattering at NORSAR. First, it includes a realistic background model. This is important because in general velocity and therefore the wavelength of the incident wave, increases with depth. Secondly, we used several criteria to evaluate the suitability of each random lithospheric model. We used the total rms variation in travel time and log amplitude as first cut methods and the coherency statistic as the final discriminator. Unlike other studies which use only the P-wave travel time and amplitude to calculate the coherency (e.g., Flatté and Wu, 1988), we use full waveform data. By calculating the coherency between many pairs of receivers we are able to get the average properties of the wavefield from only a single event. Lastly, it should be noted that we included the effects of P-wave to S-wave scattering and multiple scattering in our analysis. These effects are often ignored in analytical studies, yet they proven to be important in the frequency range studied here (Aki, 1973).

Chapter 5

Summary and Conclusions

5.1 Overview

For the purpose of studying scattering, the velocity field in the earth can be divided into two parts. A deterministic background part, and a more variable "random" part. The background part of the velocity field represents the average or "bulk" properties of the medium, while the random fluctuations are the small-scale fluctuations away from the background value. A great deal of seismic research has been focused on delineating the background part of the velocity field. This seems natural, since chemical, thermal and structural boundaries are often continuous over large spatial extents and can produce strong coherent arrivals across neighboring seismometers. Knowledge gained from these studies is important and has led to highly successful models of the Earth's interior, both in exploration and whole earth seismology.

In this thesis, the goal is to understand the effects of the second type of velocity fluctuations; the random fluctuations. Since these fluctuations are too numerous to be identified uniquely, they are usually described statistically. The distribution of scatterers is commonly identified by some scale length, a correlation function and some measure of the magnitude of the average perturbation. In Chapter 2, these ideas are developed and the terminology used throughout the thesis is presented.

Perhaps the single most important feature in that chapter is the concept that a random medium can be characterized by its correlation function. The correlation function is a measure of the amount of variability in the medium. The three most commonly used correlation functions for earth studies are the Gaussian, exponential and von Kármán functions. The Gaussian correlation function is indicative of media which are very smooth, that is they have very little power at high wavenumbers. The exponential and von Kármán correlation functions typically characterize media which have more power at high wavenumber, and therefore have more rapid variations.

Most of the early studies which treated the lithosphere as a random medium made use of Chernov (1960) scattering theory. Although originally derived for acoustic media, Chernov scattering theory has been commonly used to study scattering in the earth. In this application, Chernov scattering theory suffers from four fundamental shortcomings. First, since the theories are based on the acoustic wave equation, they are only valid when P to S scattering is small (i.e. $ka \gg 1$). Second, the theories make no attempt to include the effects of multiple scattering, which may be important, especially in the upper lithosphere. Third, implicit in the assumption of stationarity is the limitation that the statistics of the random medium are constant along the entire propagation path. This assumption may not be valid since it is generally believed that the upper lithosphere is most heterogeneous region of the earth. Fourth, the theory assumes the analytic form of the autocorrelation function is known. Since the theory requires extensive manipulation of the autocorrelation function, most early researchers used well behaved functions such as the Gaussian or exponential functions.

Several studies (e.g., Frankel and Clayton, 1986; Flatté and Wu, 1988) as well as the work in this thesis suggest that the Gaussian correlation function is too smooth to adequately describe the velocity anomalies in the crust. Current research is directed toward media which exhibit a high degree of variability. Furthermore, it is anticipated that in the future more complex models like the overlapping two-layer model proposed

by Flatté and Wu (1988) or the three layer anisotropic model presented here will better explain the variation in waveforms observed at seismic arrays.

5.2 Summary

The purpose of this thesis was to study the effects of small-scale heterogeneities on the passage of seismic waves. To this end, a new technique was developed to obtain the single scattering solution in a particular random velocity model. The chief advantage of the technique is that it can be used on any arbitrarily complex velocity model. As a result, both the single and multiple scattering solutions can be obtained for the same velocity model. Comparing the synthetic seismograms for two representative random media allowed us to show several important conclusions.

When the medium is dominated by impedance scattering (i.e. the perturbations in Lamé's parameters and density are of the same sign and relative magnitude), there are no variations in velocity only variations in impedance. Then

- the Born approximation provides a reasonable estimate of the true scattered field. It is true that the amplitude of the single scattering solution is overestimated near the direct arrival and the error becomes larger with propagation distance, but the overall shape and arrival time of the scattered field agrees fairly well with the multiple scattering solution. As a result, coda decay rates for the single scattering solution are greater than corresponding rates for the multiple scattering solution.
- the scattered field is frequency dependent and dominated by backscattering. As predicted by analytical solutions, low frequency energy is more effectively backscattered than high frequency energy. This is a geometric effect which occurs because waves scattered from an elemental part of the scatterer add destructively in the backward direction, but constructively in the forward direction.

- As a result of the frequency dependent backscattering, the attenuation parameter Q^{-1} is peaked at low frequencies, then falls off quickly with frequency.

The implication of the work in Chapter 3 is that the single scattering theory is probably insufficient to accurately describe scattering in the earth. If this is true, it calls into question nearly all analytical studies of wave propagation in random earth models, since they generally rely on the single scattering approximation. In order to avoid any inaccuracies which might be introduced by the single scattering approximation, we make use of the finite difference technique for all the modeling done in Chapter 4. Finite difference modeling is particularly well suited to modeling wave propagation in heterogeneous media because it solves the full elastodynamic equation of motion directly.

The primary goal in Chapter 4 was to construct a random lithospheric model which was representative of the region below NORSAR. Several studies have suggested that the travel time and amplitude fluctuations observed at NORSAR are manifestations of scattering from small-scale structure beneath the array (e.g., Berteussen et al., 1975b; Aki, 1973; Flatté and Wu, 1988). It is generally agreed that the magnitude of the velocity anomalies are on the order of 1-4%, but there is no general consensus on the spatial correlation of the anomalies. Early studies suggested that the Gaussian correlation function was capable of explaining the observed amplitude and travel time fluctuations at LASA and NORSAR (Aki, 1973). Using a different statistical theory, Wu and Aki (1985a) modified that conclusion and suggested that there is probably more variability in the lithosphere and therefore a more textured model like the von Kármán function was in order. Evidence from forward modeling seems to corroborate this hypothesis (Frankel and Clayton, 1986). All of these studies assumed the lithosphere could be modeled by a randomly heterogeneous region which had constant statistical properties (i.e., the random medium was assumed to be stationary). Flatté and Wu (1988) developed a set of equations which allowed them to invert for the statistical properties of a non-stationary medium. Using this technique, they found that

the variability between waveforms observed at NORSAR could be explained by a two-layer random model.

In Chapter 4, we use finite difference modeling to test the suitability of several random models. As a result, we were able to produce a three layered lithospheric model which both matched the observed travel time and amplitude variations observed at NORSAR and is consistent with seismic reflection data. The model, we propose has three random layers. The top layer is 3 km thick and described by a bandlimited white spectrum. The second layer extends from 3 km to the bottom of the crust (35 km) and can be described by the 0th order von Kármán autocorrelation function. Velocity fluctuations in this layer are fairly strong (3% rms variation) and span a wide range of length scales. The third layer extends from the base of the crust to a depth of 250 km and was determined to have an anisotropic Gaussian correlation function. We found the best results when we specified the horizontal correlation length to be 20 km and the vertical correlation length to be 5 km. Best results were found when both the bottom and top layers had 2% velocity variations.

The white spectrum in the uppermost layer produced localized variations in the waveforms. During the course of this investigation, we found that the modeling was not very sensitive to the thickness of this layer, nor the magnitude of the velocity fluctuations in this layer. However without it, we could not explain the falloff in coherency which was observed at NORESS. The middle layer represents the bulk of the crust. After experimenting with several autocorrelation functions and numerous correlation lengths, we found the von Kármán function best suited to explain the variations in the crust. Media described by this function effectively generate coda, but have a relatively small effect on the time and amplitude of the incident wave Frankel and Clayton (1986). Together, these two layers generated reasonable amounts of coda and localized variations in the wavefield, but did not duplicate the travel time and amplitude variations observed at NORSAR. In order to explain these features, it was necessary to include a third layer which was capable of producing travel time and

amplitude fluctuations, but did not contribute greatly to the amount of coda in the wavefield. Numerous studies have shown that a Gaussian medium has these properties. After much experimenting, we found that a model with different correlation lengths in the horizontal and vertical directions was able to match the observed data well.

It is important to state that since this model is based on forward modeling only, we cannot guarantee its uniqueness. However, it fits the observed travel time and amplitude variations, waveform coherency and coda better than any previously published models. No formal attempt was made to determine the sensitivity of the modeling to slightly different velocity model. The reason for this was twofold. First, each different realization of the same random model produced some differences, thus complicating the notion of sensitivity. Second, for computational reasons, it was not possible to run and store the results from numerous simulations. We did however examine three different realizations of the final model to insure that the results were consistent.

References

- Aki, K., Analysis of seismic coda of local earthquakes as scattered waves, *J. Geophys. Res.*, **74**, 615-631, 1969.
- Aki, K., Scattering of P waves under the Montana IASA, *J. Geophys. Res.*, **78**, 1334-1346, 1973.
- Aki, K., Attenuation of shear waves in the lithosphere for frequencies from 0.05 to 25 Hz, *Phys. Earth Planet. Inter.*, **21**, 50-60, 1980.
- Aki, K. and B. Chouet, Origin of coda wave: Source, attenuation and scattering effects, *J. Geophys. Res.*, **80**, 3322-3342, 1975.
- Aki, K. and P. Richards, *Quantitative Seismology - Theory and Methods*, W. H. Freeman, San Francisco, 1980.
- Aki, K., A. Christofferson, and E. S. Husebye, Determination of the three-dimensional seismic structure of the lithosphere, *J. Geophys. Res.*, **82**, 277-296, 1977.
- Alford, R. M., K. R. Kelly, and D. M. Boore, Accuracy of finite-difference modeling of the acoustic wave equation, *Geophysics*, **39**, 834-842, 1974.
- Bataille, K., R. S. Wu, and S. M. Flatté, Inhomogeneities near the core-mantle boundary evidenced from seismic wave scattering-A review, *Pure Appl. Geophys.*, **132**, 151-174, 1990.
- Berteussen, K. A., *NORSAR location calibrations and time delay corrections*, NORSAR Sci Rep. 2-73/74, National Technical Information Service, Springfield, VA, 1974.
- Berteussen, K. A., A. Christofferson, E. S. Husebye, and A. Dahle, Wave scattering theory in analysis of P wave anomalies at NORSAR and LASA, *Geophys. J. R. astr. Soc.*, **42**, 403-417, 1975a.

- Berteussen, K. A., E. S. Husebye, R. F. Mereu, and A. Ram, Quantitative assessment of the crust-upper mantle heterogeneities beneath the Gauribidnaur seismic array in southern India, *Earth Planet. Sci. Lett.*, *37*, 326-332, 1975b.
- Beydoun, W. B. and A. Tarantola, First Born and Rytov approximations: Modeling and inversion conditions in a canonical example, *J. Acoust. Soc. Am.*, *83*, 1045-1055, 1988.
- Bickley, W. G., Formulae for numerical differentiation, *Math. Gaz.*, *25*, 19-27, 1941.
- Bracewell, R. N., *The Fourier Transform and its Applications*, McGraw-Hill, New York, 1978.
- Bungum, H., S. Mykkeltveit, and T. Kværna, Seismic noise in fennoscandia, with emphasis on high frequencies, *Bull. Seismol. Soc. Am.*, *75*, 1489-1513, 1985.
- Capon, J., Characterization of the crust and upper mantle structure under LASA as a random medium, *Bull. Seismol. Soc. Am.*, *64*, 235-266, 1974.
- Cassell, B. R. and K. Fuchs, Seismic investigations of the subcrustal lithosphere beneath Fennoscandia, *J. Geophys.*, *46*, 369-384, 1979.
- Cassell, B. R., Mykkeltveit, R. Kanestrom, and E. S. Husebye, A North Sea - southern Norway seismic crustal profile, *Geophys. J. R. astr. Soc.*, *72*, 733-753, 1983.
- Charrette, E. E. and M. N. Toksöz, Effects of stochastic heterogeneities on cross-well imaging, in *Expanded Abstracts of the 1989 SEG Meeting*, pp. 898-900, Soc. Explor. Geophys., 1989.
- Chernov, L. A., *Wave Propagation in a random medium*, McGraw-Hill, New York, 1960.
- Chouet, B., Effects of anelastic and scattering structures of the lithosphere on the shape of local earthquake coda, *Pure Appl. Geophys.*, *132*, 289-310, 1990.
- Claerbout, J. F., *Imaging the Earth's Interior*, Blackwell Scientific Publications, Boston, 1985.

- Clayton, R. and B. Engquist, Absorbing boundary conditions for acoustic and elastic wave equations, *Bull. Seismol. Soc. Am.*, *67*, 1529-1540, 1977.
- Dainty, A. M., A scattering model to explain seismic Q observations in the lithosphere, *Geophys. Res. Lett.*, *8*, 1126-1128, 1981.
- Dainty, A. M., High-frequency acoustic backscattering and seismic attenuation, *J. Geophys. Res.*, *89*, 3172-3176, 1984.
- Dainty, A. M. and M. N. Toksöz, Elastic wave propagation in highly scattering medium, a diffusion approach, *J. Geophys.*, *43*, 375-388, 1975.
- Dainty, A. M. and M. N. Toksöz, Array analysis of seismic scattering, *In press*, 1990.
- Dainty, A. M., M. N. Toksöz, K. R. Anderson, P. J. Pines, Y. Nakamura, and G. Latham, Seismic scattering and shallow structure of the moon in Oceanus Procellarum, *The Moon*, *9*, 11-29, 1973.
- Daudt, C. R., L. W. Braile, R. L. Nowack, and C. S. Chiang, A comparison of finite-difference methods, *Bull. Seismol. Soc. Am.*, *79*, 1210-1230, 1989.
- Dougherty, M. E. and R. A. Stephens, Seismic energy partitioning and scattering in laterally heterogeneous ocean crust, *Pure Appl. Geophys.*, *128*, 195-230, 1988.
- Dzienwonski, A. M., A. L. Hales, and E. R. Lapwood, Parametrically simple earth models consistent with geophysical data, *Phys. Earth Planet. Inter.*, *10*, 12, 1975.
- Eispruch, N. G., E. J. Witterholt, and R. Trull, Scattering of a plane transverse wave by a spherical obstacle in an elastic medium, *J. Appl. Phys.*, *31*, 806-818, 1960.
- Flatté, S. M. and F. D. Tappert, Calculation of the effect of internal waves on oceanic sound transmission, *J. Acoust. Soc. Am.*, *58*, 1151-1159, 1975.
- Flatté, S. M. and R. S. Wu, Small scale structure in the lithosphere and asthenosphere deduced from arrival time and amplitude fluctuations at NORSAR, *J. Geophys. Res.*, *93*, 6601-6614, 1988.

- Fornberg, B., The pseudospectral method: Comparisons with finite differences for the elastic wave equation, *Geophysics*, 52, 483-501, 1987.
- Frankel, A., A review of numerical experiments on seismic wave scattering, *Pure Appl. Geophys.*, 131, 639-685, 1989.
- Frankel, A. and R. Clayton, Finite difference simulations of wave propagation in two dimensional random media, *Bull. Seismol. Soc. Am.*, 74, 2167-2186, 1984.
- Frankel, A. and R. Clayton, Finite difference simulations of seismic scattering: implications for the propagation of short-period seismic waves in the crust and models of crustal heterogeneity, *J. Geophys. Res.*, 91, 6465-6489, 1986.
- Frankel, A. and L. Wennerberg, Energy-flux model of seismic coda: separation on scattering and intrinsic attenuation, *Bull. Seismol. Soc. Am.*, 77, 1223-1251, 1987.
- Gibson, B. S. and A. R. Levander, Modeling and processing of scattered waves in seismic reflection surveys, *Geophysics*, 53, 453-478, 1988.
- Goff, J. A. and T. H. Jordan, Stochastic modeling of seafloor morphology: inversion of sea beam data for second order statistics, *J. Geophys. Res.*, 93, 13589-13608, 1988.
- Greaves, R. J. and T. J. Fulp, Three dimensional seismic monitoring of an enhanced oil recovery process, *Geophysics*, 52, 175-187, 1987.
- Gubernatis, J. E., E. Domany, and J. A. Krumhansl, The Born approximation in the theory of scattering of elastic waves by flows, *J. Appl. Phys.*, 48, 2812-2819, 1977a.
- Gubernatis, J. E., E. Domany, and J. A. Krumhansl, Formal aspects of the theory of scattering of ultrasound by flows in elastic materials. *J. Appl. Phys.*, 48, 2804-2811, 1977b.

- Haddon, R. A. W. and J. R. Cleary, Evidence for scattering of seismic PKP waves near the mantle-core boundary, *Phys. Earth Planet. Inter.*, 8, 211-234, 1974.
- Harichandran, R. S. and E. H. Vanmarcke, *Space-time variation of earthquake ground motion*, Technical Report Res. Rept. R84-12, Dept. of Civil Engineering, Massachusetts Institute of Technology, Cambridge, MA, 1984.
- Herrmann, R. B., Q estimates using the coda of local earthquakes, *Bull. Seismol. Soc. Am.*, 70, 447-468, 1980.
- Hudson, J. A. and J. R. Heritage, The use of the Born approximation in seismic scattering problems, *Geophys. J. R. astr. Soc.*, 66, 221-240, 1981.
- Husebye, E. S., J. Hovland, A. Christoffersson, K. Åström, R. Slunga, and C. Lund, Tomographical mapping of the lithosphere and asthenosphere beneath southern Scandinavia and adjacent areas, *Tectonophys.*, 128, 229-250, 1986.
- Ingate, S. F., E. S. Husebye, and A. Christoffersson, Regional arrays and processing schemes, *Bull. Seismol. Soc. Am.*, 75, 1155-1177, 1985.
- Jenkins, G. M. and D. G. Watts, *Spectral Analysis and its Applications*, Holden-Day, Inc., San Francisco, 1968.
- Kelly, K. R., R. W. Ward, S. Treitel, and R. M. Alford, Synthetic seismograms: A finite-difference approach, *Geophysics*, 41, 2-27, 1976.
- Kennett, B. L. N., Seismic wave scattering by obstacles on interfaces, *Geophys. J. R. astr. Soc.*, 28, 249-266, 1972a.
- Kennett, B. L. N., Seismic waves in laterally inhomogeneous media, *Geophys. J. R. astr. Soc.*, 27, 301-336, 1972b.
- Kennett, B. L. N. and J. R. Bowman, The velocity structure and heterogeneity of the upper mantle, *Phys. Earth Planet. Inter.*, in press, 1990.
- Kennett, B. L. N. and G. Nolet, The interaction of the s-wavefield with upper mantle heterogeneities, *Geophys. J. R. astr. Soc.*, 101, 751-762, 1990.

- Knopoff, L., The thickness of the lithosphere from dispersion of surface waves, *Geophys. J. R. astr. Soc.*, *74*, 55-81, 1983.
- Macaskill, C. and T. E. Ewart, Computer simulation of two-dimensional random wave propagation, *IMA J. Appl. Math.*, *33*, 1-15, 1984.
- Mandelbrot, B. B., *Fractals*, W. H. Freeman, San Francisco, 1977.
- Mayne, W. H., Common reflection point horizontal data stacking techniques, *Geophysics*, *27*, 927-938, 1962.
- McLaughlin, K. L. and L. M. Anderson, Stochastic dispersion of short period P-waves due to scattering and multipathing, *Geophys. J. R. astr. Soc.*, *89*, 795-821, 1987.
- McLaughlin, K. L., L. M. Anderson, and Z. A. Der, Investigation of seismic waves using 2-dimensional finite difference calculations, in *Multiple scattering of waves in random media and random surfaces*, pp. 795-821, The Pennsylvania State University, 1985.
- Menke, W., A. L. Lerner-Lam, B. Dubendorff, and J. Pacheco, Polarization and coherence of 5 to 30 hz seismic wave fields at a hard-rock site and the relevance to velocity heterogeneities in the crust, *Bull. Seismol. Soc. Am.*, *80*, 430-449, 1990.
- Mereu, R. F. and S. B. Ojo, The scattering of seismic wave through a crust and upper mantle with random lateral and vertical inhomogeneities, *Phys. Earth Planet. Inter.*, *26*, 233-240, 1981.
- Miles, J. W., Scattering of elastic waves by small inhomogeneities, *Geophysics*, *25*, 642-648, 1960.
- Munasinghe, M. and G. W. Farnell, Finite difference analysis of Rayleigh wave scattering at vertical discontinuities, *J. Geophys. Res.*, *78*, 2454-2466, 1973.
- Mykkeltveit, S., A seismic profile in southern Norway, *Pure Appl. Geophys.*, *118*, 1310-1325, 1980.

- Nayfeh, A., *Perturbation Methods*, Wiley, New York, 1973.
- Ojo, S. B. and R. F. Mercu, The effect of random velocity functions on the travel times and amplitudes of seismic waves, *Geophys. J. R. astr. Soc.*, *84*, 607-618, 1986.
- Pao, Y. and C. Mow, *Diffraction of Elastic Waves and Dynamic Stress Concentration*, Crane, Russak & Co. Inc., New York, 1973.
- Powell, C. A. and A. S. Meltzer, Scattering of P-waves beneath SCARLET in southern California, *Geophys. Res. Lett.*, *11*, 481-484, 1984.
- Prange, M. D., *Seismic Wave Scattering from Rough Interfaces*, PhD thesis, Massachusetts Institute of Technology, Cambridge, MA, 1989.
- Rayleigh, J. W. S., On the light from the sky, *Phil Mag*, *41*, 107, 1871.
- Rayleigh, J. W. S., *The Theory of Sound*, V. II, Dover Publications, Inc, New York, 1896, (1945 edition).
- Ricker, N. H., *Transient Waves in Visco-elastic Media*, Elsevier Scientific Publishing Co., New York, 1977.
- Ringdal, F. and E. S. Husebye, Application of arrays in the detection, location, and identification of seismic events, *Bull. Seismol. Soc. Am.*, *72*, S201-S224, 1982.
- Robinson, E. A., Predictive decomposition of seismic traces, *Geophysics*, *22*, 767-778, 1957.
- Sato, H., Energy propagation including scattering effects. Single isotropic scattering approximation, *J. Phys. Earth*, *25*, 27-41, 1977a.
- Sato, H., Single isotropic scattering model including wave conversions. Scattering approximation, *J. Phys. Earth*, *25*, 163-176, 1977b.
- Sato, H., Coda wave excitation due to nonisotropic scattering and nonspherical source radiation, *J. Geophys. Res.*, *87*, 8665-8676, 1978.

- Scott, P. and D. V. Helmberger, Applications of the Kirchhoff-Helmholz integral to problems in seismology, *Geophys. J. R. astr. Soc.*, **72**, 747-768, 1983.
- Sellevoll, M. A. and R. E. Warrick, A refraction study of the crustal structure in southern Norway, *Bull. Seismol. Soc. Am.*, **61**, 457-471, 1971.
- Skolnik, M. I., *Radar Handbook*, McGraw-Hill Book Co., New York, 1970.
- Snieder, R., A perturbative analysis of non-linear inversion, *Geophys. J. Int.*, **101**, 545-556, 1990.
- Stephen, R. A., A review of finite difference methods for seismo-acoustics problems at the seafloor, *Review of Geophysics*, **26**, 445-458, 1988.
- Tanimoto, T. and D. L. Anderson, Lateral heterogeneity and azimuthal anisotropy of the upper mantle: Love and Rayleigh waves 100-250 s, *J. Geophys. Res.*, **90**, 1842-1858, 1985.
- Tatarski, V. I., *Wave Propagation in a Turbulent Medium*, McGraw-Hill, New York, 1961.
- Thomson, C. J. and D. Gubbins, Three-dimensional lithospheric modelling at NOR-SAR: linearity of the method and amplitude variations from the anomalies, *Geophys. J. R. astr. Soc.*, **71**, 1-36, 1982.
- Toksöz, M. N., A. M. Dainty, E. Reiter, and R. S. Wu, A model for attenuation in the earth's crust, *Pure Appl. Geophys.*, **128**, 81-100, 1988.
- Toksöz, M. N., A. M. Dainty, and E. E. Charrette, Spatial variation of ground motion due to lateral heterogeneity, *Structural Safety*, *In press*, 1990.
- Toksöz, M. N., A. M. Dainty, and E. E. Charrette, Coherency of ground motion at regional distances and scattering, *Phys. Earth Planet. Inter.*, **67**, 162-179, 1991.
- Trefethen, L. N., Group velocity in finite difference schemes, *SIAM Review*, **24**, 113-136, 1982.

- Červený, V., M. M. Popov, and I. Pšenčík, Computation of wave fields in inhomogeneous media-Gaussian beam approach, *Geophys. J. R. astr. Soc.*, **70**, 109-293, 1982.
- Vidale, J. E., Comment on "A comparison of finite-difference and Fourier method calculations of synthetic seismograms by C. R. Daudt *et al.*", *Bull. Seismol. Soc. Am.*, **80**, 493-495, 1990.
- Virieux, J., P-SV wave propagation in heterogeneous media: velocity-stress finite-difference method, *Geophysics*, **51**, 889-901, 1986.
- von Kármán, T., Progress in the statistical theory of turbulence, *J. Mar. Res.*, **7**, 252-264, 1948.
- Witte, D., *The Pseudospectral Method for Simulating Wave Propagation*, PhD thesis, Columbia University, Palisades, NY, 1989.
- Wu, R. S., Attenuation of short period seismic waves due to scattering, *Geophys. Res. Lett.*, **9**, 9-12, 1982a.
- Wu, R. S., Mean field attenuation and amplitude attenuation due to scattering, *Wave Motion*, **4**, 305-316, 1982b.
- Wu, R. S., Multiple scattering and energy transfer of seismic waves-Separation of scattering effect from intrinsic attenuation, *Geophys. J. R. astr. Soc.*, **82**, 57-80, 1985.
- Wu, R. S. and K. Aki, Elastic wave scattering by random medium and small scale inhomogeneities in the lithosphere, *J. Geophys. Res.*, **90**, 10261-10273, 1985a.
- Wu, R. S. and K. Aki, The fractal nature of the inhomogeneities in the lithosphere evidenced from seismic wave scattering, *Pure Appl. Geophys.*, **123**, 805-818, 1985b.
- Wu, R. S. and K. Aki, Scattering characteristics of elastic waves by an elastic heterogeneity, *Geophysics*, **50**, 582-595, 1985c.

- Wu, R. S. and K. Aki, The perturbation method in elastic wave scattering, *Pure Appl. Geophys.*, 131, 605-637, 1990.
- Yamakawa, N., Investigation of the disturbance produced by spherical obstacles on elastic waves (I), *Quart. Jour. Seismology*, 21, 1-12, 1956.
- Ying, C. F. and R. Truell, Scattering of a plane longitudinal wave by a spherical obstacle in an isotropic elastic solid, *J. Appl. Phys.*, 27, 1087-1097, 1956.

Appendix A

Born Scattering

A.1 Introduction

Rayleigh (1871) used dimensional analysis to show that when the size of a scatterer is small compared to a wavelength, the scattered field is proportional to $Vr^{-1}k^2$, where V is the volume of the scatterer, r is the distance to the observation point and $k(= 2\pi/\text{wavelength})$ is the wavenumber of the incident wave. He later solved the acoustical (longitudinal waves only) and optical (transverse waves only) problems exactly (Rayleigh, 1896). Through his analysis, Rayleigh was able to show that variations in compressibility act as simple isotropic point sources, while variations in density act as dipole sources. Central to Rayleigh's solution was the limitation that the amplitude and phase of the incident wave (i.e. the Green's function of the background wave) is constant over the entire extent of the scatterer. This is accurate only when the spatial extent of the scatterer is small compared to a wavelength (Skolnik, 1970). For larger scatterers, amplitude and phase variations in the incident wave cause the radiation pattern of the scattered waves to be more complex.

Several techniques have been introduced to solve the problem of scattering from a sphere which is similar in size to a wavelength. An exact solution has been presented for both the case of an incident P-wave (Ying and Truell, 1956; Yamakawa, 1956) and

an incident S-wave (Eispruch et al., 1960). The exact solution is obtained by formulating the problem in spherical coordinates and matching the boundary conditions at the surface of the sphere. Solutions derived by this technique are slowly converging infinite series which cannot be expressed simply, except in the low frequency limit (i.e. Rayleigh scattering limit). Besides giving extremely cumbersome results, the technique is limited to only spherical or cylindrical heterogeneities (Pao and Mow, 1973).

A second technique uses the elastodynamic equation of motion and the Born approximation to calculate the equivalent body force due to the heterogeneity. Once the body force is available, it can be convolved with the Green's function and integrated to obtain the scattered field. The same technique can be used to solve both the Rayleigh and Mie scattering problems, depending on the assumptions made concerning the incident field. In Rayleigh scattering the incident field is assumed to be constant across the scatterer, where as in Mie scattering that restriction is lifted. In this appendix, we will closely follow the work of Wu and Aki (1985c) which itself was based on the pioneering work of Miles (1960) and Gubernatis et al. (1977b). The goal then is to use this perturbative technique to obtain simple closed form solutions to the general Rayleigh scattering problem, as well as scattering from obstacles with Gaussian, and exponential distributions.

A.2 The Born Approximation and Single Scattering

It was shown in Chapter 3 that if the heterogeneities are weak, the scattered field obeys an inhomogeneous wave equation

$$\rho_0 \ddot{u}_i^1 - (\lambda_0 + \mu_0)(\nabla \cdot \underline{u}^1)_{,i} - \mu_0 \nabla^2 u_i^1 = Q_i, \quad (\text{A.1})$$

where

$$Q_i = -\delta\rho\ddot{u}_i^0 + (\delta\lambda + \delta\mu)(\nabla \cdot \underline{u}^0)_{,i} + \delta\mu\nabla^2 u_i^0 + (\delta\lambda)_{,i}\nabla \cdot \underline{u}^0 + (\delta\mu)_{,j}(u_{i,j}^0 + u_{j,i}^0). \quad (\text{A.2})$$

The far-field displacements due to the body force Q_i can be obtained by integrating the body force over its volume,

$$u_i^1(\underline{x}) = \int_V Q_j(\underline{\xi}) * G_{ij}(\underline{x}, \underline{\xi}) dV(\underline{\xi}). \quad (\text{A.3})$$

Here G is the homogeneous Green's function, \underline{x} is the receiver location, $\underline{\xi}$ is the position within the heterogeneity, and "*" is the convolutional operator. Substituting Equation A.2 into Equation A.3 and integrating by parts yields,

$$\begin{aligned} u_i^1(\underline{x}) = & - \int_V \delta\rho(\underline{\xi}) \ddot{u}_j^0(\underline{\xi}) * G_{ij}(\underline{x}, \underline{\xi}) dV(\underline{\xi}) \\ & - \int_V \left[\delta_{jk} \delta\lambda(\underline{\xi}) (\nabla \cdot \underline{u}^0(\underline{\xi})) + \delta\mu(\underline{\xi}) (u_{j,k}^0(\underline{\xi}) + u_{k,j}^0(\underline{\xi})) \right] \\ & * G_{ij,k}(\underline{x}, \underline{\xi}) dV(\underline{\xi}). \end{aligned} \quad (\text{A.4})$$

The first integrand is a simple point force convolved with the Green's function. The force is oriented in the particle motion direction of the incident wave and dependent on the the density perturbation of the medium. The second integrand is more complex, but can be shown to represent the equivalent force moment tensor for the the elementary volume $dV(\underline{\xi})$. Convolved with the Green's function, it represents the portion of the scattered field due to the perturbations in λ and μ . Thus, Equation A.4 is the integrated field due to the interaction of the incident wave with the heterogeneity.

If the volume V is sufficiently small, the incident wave and the Green's function can be considered constant across the scatterer. Ignoring the positional dependence on these parameters, the total uni-directional body force \underline{F} can be calculated by integrating the first term in Equation A.4. Assuming the incident field has a simple harmonic time dependence,

$$F_i = - \int_V \delta\rho(\underline{\xi}) \ddot{u}_j^0(\underline{\xi}) dV(\underline{\xi}) = \omega^2 u_i^0 \overline{\delta\rho} V, \quad (\text{A.5})$$

where $\overline{\delta\rho}$ is the average density perturbation over the heterogeneity. Similarly, the force moment tensor can be written as,

$$\begin{aligned} M_{ik} &= - \int_V [\delta_{jk} \delta\lambda(\underline{\xi})(\nabla \cdot \underline{u}^0(\underline{\xi})) + \delta\mu(\underline{\xi})(u_{j,k}^0(\underline{\xi}) + u_{k,j}^0(\underline{\xi}))] \\ &= -\delta_{ik} \overline{\delta\lambda} V (\nabla \cdot \underline{u}^0) - \overline{\delta\mu} V [u_{i,k}^0 + u_{i,k}^0]. \end{aligned} \quad (\text{A.6})$$

Then the far-field displacements are given by (Aki and Richards, 1980),

$$\begin{aligned} u_i^1 &= F_j * G_{ij} + M_{jk} * G_{ij,k} \\ &= \frac{1}{4\pi\rho_0\alpha_0^2 r} \gamma_i \gamma_j F_j(t - r/\alpha_0) \\ &\quad - \frac{1}{4\pi\rho_0\beta_0^2 r} (\gamma_i \gamma_j - \delta_{ij}) F_j(t - r/\beta_0) \\ &\quad + \frac{1}{4\pi\rho_0\alpha_0^3 r} \gamma_i \gamma_j \gamma_k \dot{M}_{jk}(t - r/\alpha_0) \\ &\quad + \frac{1}{4\pi\rho_0\beta_0^3 r} (\gamma_i \gamma_j - \delta_{ij}) \gamma_k \dot{M}_{jk}(t - r/\beta_0), \end{aligned} \quad (\text{A.7})$$

where r is the distance from the center of the scatterer, and γ_i are the directional cosines between the ray to the observer and the i axis. The first and third terms in Equation A.7 are the displacements arising from P-waves and the second and fourth terms are associated with S-waves.

The effects of the three anomalies $\overline{\delta\rho}$, $\overline{\delta\lambda}$, and $\overline{\delta\mu}$ are completely separated in Equations A.5 and A.6. The three orthogonal forces associated with perturbations in λ are of equal strength and affect only the diagonal elements of the force moment tensor, therefore this source can be interpreted as an isotropic point source. Perturbations in μ can produce both on and off diagonal elements in the force moment tensor. The on-diagonal elements correspond to on-line force couples and the off-diagonal pairs (which must be equal, due to the symmetry of the force moment tensor) correspond to double couple sources.

A.2.1 Plane P-Wave Source

In this section we will investigate the far-field displacements which are generated when a plane P-wave interacts with the heterogeneity in the medium. The displacements

due to a plane P-wave traveling in the $+x_1$ direction is written as,

$$u_i^0 = \delta_{i1} e^{-i\omega(t - x_1/\alpha_0)} \quad (\text{A.8})$$

The equivalent body force can be calculated by inserting Equation A.8 into Equation A.2,

$$Q_j = \left[\delta_{1j} (\bar{\delta}\rho\omega^2 - \frac{(\bar{\delta}\lambda + 2\bar{\delta}\mu)\omega^2}{\alpha_0^2} + 2i\frac{\omega}{\alpha_0}(\bar{\delta}\mu)_{,j} + i\frac{\omega}{\alpha_0}(\bar{\delta}\lambda)_{,j} \right] e^{-i\omega(t - x_1/\alpha_0)}. \quad (\text{A.9})$$

From Equations A.5 and A.6, the equivalent force and moments are given by,

$$F_i = \delta_{i1} \omega^2 \bar{\delta}\rho V e^{-i\omega t} \quad (\text{A.10})$$

$$M = \begin{vmatrix} \bar{\delta}\lambda + 2\bar{\delta}\mu & 0 & 0 \\ 0 & \bar{\delta}\lambda & 0 \\ 0 & 0 & \bar{\delta}\lambda \end{vmatrix} \frac{-i\omega V e^{-i\omega t}}{\alpha_0} \quad (\text{A.11})$$

and the far-field radiation pattern by,

$$u_i^1 = \left[\frac{\bar{\delta}\rho}{\rho_0} \gamma_i \gamma_1 - \frac{\bar{\delta}\lambda}{\lambda_0 + 2\mu_0} \gamma_i - \frac{2\bar{\delta}\mu}{\lambda_0 + 2\mu_0} \gamma_i \gamma_1^2 \right] \frac{\omega^2 V e^{-i\omega(t - r/\alpha_0)}}{4\pi r \alpha_0^2} + \left[\frac{\bar{\delta}\rho}{\rho_0} (\gamma_i \gamma_1 - \delta_{i1}) - \frac{2\beta_0 \bar{\delta}\mu}{\alpha_0 \mu_0} (\delta_{i1} \gamma_1 - \gamma_i \gamma_1^2) \right] \frac{\omega^2 V e^{-i\omega(t - r/\beta_0)}}{4\pi r \beta_0^2}. \quad (\text{A.12})$$

The far-field scattered waves depend on both the distance from the perturbation and the angular arc between the ray to the receiver and the particle motion direction of the incident wave. This suggests that Equation A.12 can be simplified by changing to polar coordinates. Choosing the coordinates such that the polar axis is in the particle motion direction of the incident wave (Figure A-1), and separating the P and S waves in Equation A.12 yields,

$$P_{u^P} = \hat{r} \left[\frac{\bar{\delta}\rho}{\rho_0} \cos \theta - \frac{\bar{\delta}\lambda}{\lambda_0 + 2\mu_0} - \frac{2\bar{\delta}\mu}{\lambda_0 + 2\mu_0} \cos^2 \theta \right] \frac{V \omega^2 e^{-i\omega(t - r/\alpha_0)}}{4\pi r \alpha_0^2} \quad (\text{A.13})$$

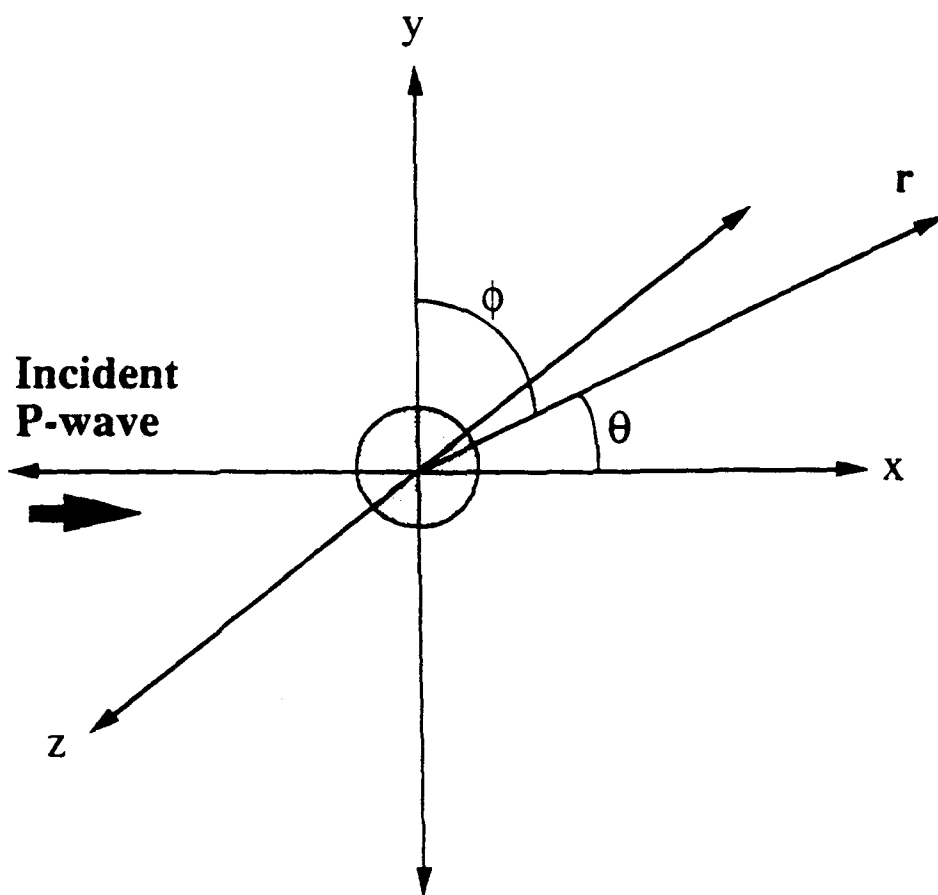


Figure A-1: The coordinate system used for an incident P-wave.

$$P_{u^S} = \hat{\theta} \left[-\frac{\overline{\delta\rho}}{\rho_0} \sin \theta - \frac{\beta_0 \overline{\delta\mu}}{\alpha_0 \mu_0} \sin 2\theta \right] \frac{V\omega^2 e^{-i\omega(t-r/\beta_0)}}{4\pi r \beta_0^2}, \quad (\text{A.14})$$

where P_{u^P} are the displacements due to P-wave to P-wave scattering and P_{u^S} are displacements due to P-wave to S-wave scattering. It is clear from these equations that regardless of the nature of the anomaly, the particle motion of the scattered P-wave is always in the radial direction, and that of the scattered S-wave is always in the $\hat{\theta}$ direction. Furthermore, the cosine dependence of the scattered P-wave indicates that P-wave scattering is most intense in the forward and backward directions, and is zero in the plane orthogonal to the incident particle motion direction. Conversely, the sine dependence in the S-wave terms indicates that the scattered S-wave is strongest in the plane perpendicular to the scattered P-wave lobes and is zero in the incident particle motion direction. It is interesting to note that for most materials (i.e., $\overline{\delta\lambda} \approx \overline{\delta\mu}$) the scattered S-wave is larger than the scattered P-wave.

The exact form of the total scattered field will depend on the magnitude and polarity of the various perturbations. We will discuss only a few of the infinite number of possibilities here.

When $\overline{\delta\lambda}$, $\overline{\delta\mu}$, and $\overline{\delta\rho}$ all have the same algebraic sign, (i.e. the inclusion is harder and heavier, or softer and lighter, than the background medium) P-wave scattering is greatest in the backwards direction. This occurs because at $\theta = \pi$ the three terms in Equation A.13 all have the same sign and therefore are in phase. As a special case, consider a heterogeneity in which

$$\frac{\overline{\delta\lambda}}{\lambda_0} = \frac{\overline{\delta\mu}}{\mu_0} = \frac{\overline{\delta\rho}}{\rho_0}. \quad (\text{A.15})$$

The velocity within the anomaly can be written as,

$$\alpha^2 = \frac{\lambda_0 + \delta\lambda + 2(\mu_0 + \delta\mu)}{\rho_0 + \delta\rho} = \frac{(\lambda_0 + 2\mu_0)(1 + \delta\rho/\rho_0)}{\rho_0(1 + \delta\rho/\rho_0)} = \alpha_0^2 \quad (\text{A.16})$$

and the impedance by,

$$\rho\alpha = (\rho_0 + \delta\rho)\alpha_0 \neq \rho_0\alpha_0. \quad (\text{A.17})$$

This combination of perturbations results in only an impedance contrast across the inclusion. Any scattering which takes place is then due to the impedance mismatch of the inclusion, hence the name "impedance scattering". The scattered field from the perturbations in λ , μ and ρ are shown individually in Figure A-2 and the total scattered field is shown in Figure A-3. Notice that for this particular choice of parameters, the total scattered P-wave is confined to the back-scattered direction. The scattered S-wave is considerably larger than the P-wave and is strongest in the side scattered direction. Notice, too, that no scattered S-wave is generated in the forward-backward direction and no P-wave is side-scattered.

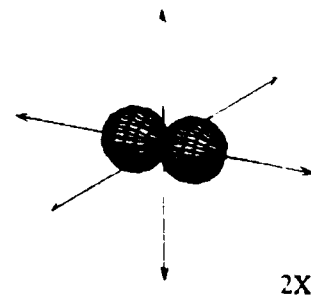
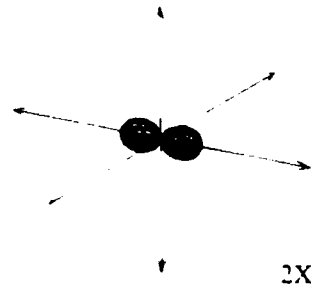
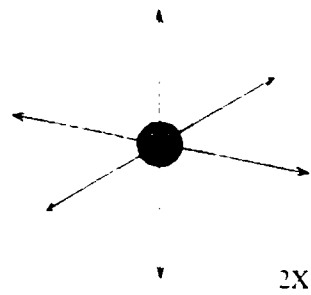
Also of interest is the case when the inclusion is lighter and harder or heavier and softer than the surrounding material. Consider the special case when

$$-\frac{\delta\lambda}{\lambda_0} = \frac{\delta\mu}{\mu_0} = \frac{\delta\rho}{\rho_0}. \quad (\text{A.18})$$

It is easy to show that there is no impedance change across the inclusion, only a velocity perturbation. This situation is often termed "velocity scattering". The radiation pattern due to velocity scattering is identical to that for impedance scattering, but rotated 180° (Figure A-4).

Velocity scattering is characterized by strong forward P-wave scattering, while impedance scattering gives rise to strong back-scattering of P-waves. In both cases, there is no scattered S-wave in either the forward or backward directions. The S-wave displacements are concentrated in the side-scattered directions, and are considerably larger than the scattered P-waves. The larger amplitude of the scattered S-wave should make it more visible/useful in some experiments, but its radiation pattern will make it difficult to observe in limited aperture transmission and reflection geometries. Similarly, the strong back-scattering characteristics of impedance scattering will make these anomalies difficult to quantify in most transmission experiments, and more easily quantified in reflection experiments.

P -> P Scattering



P -> S Scattering

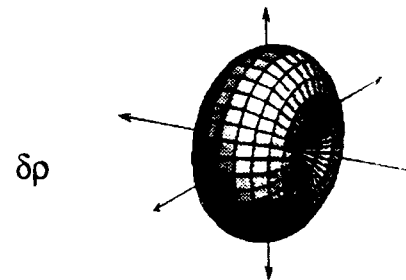
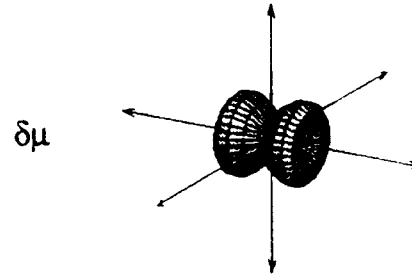
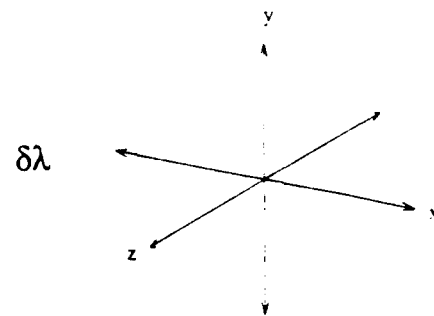
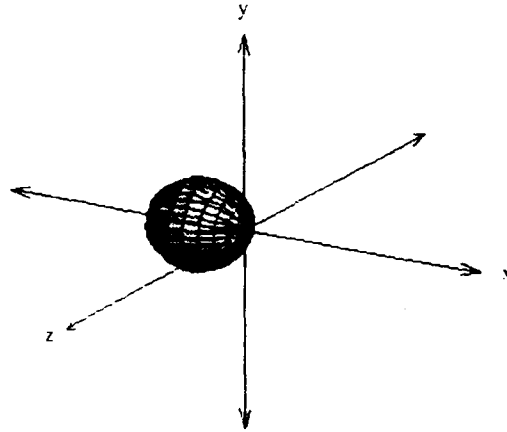


Figure A-2: Rayleigh impedance scattering due to variations in λ , μ and ρ . The incident wave was a P-wave traveling in the $+x$ direction and $\delta\lambda/\lambda_0 = \delta\mu/\mu_0 = \delta\rho/\rho_0$. Notice P-waves are displayed at $2X$ the S-waves.

P -> P Scattering



P -> S Scattering

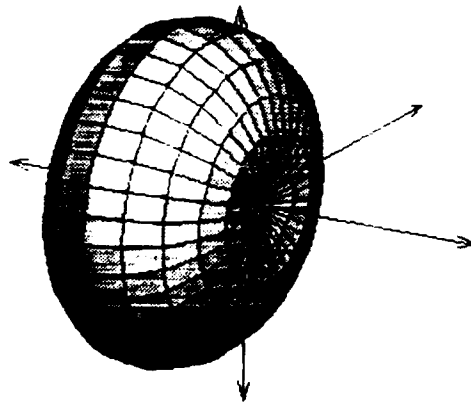
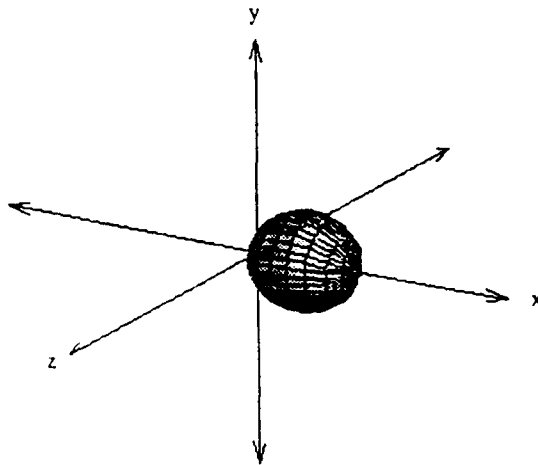


Figure A-3: The total scattered field from Figure A-2. In impedance scattering the P-wave is directed backwards, and the S-wave is strongest in the side-scattered direction.

P -> P Scattering



P -> S Scattering

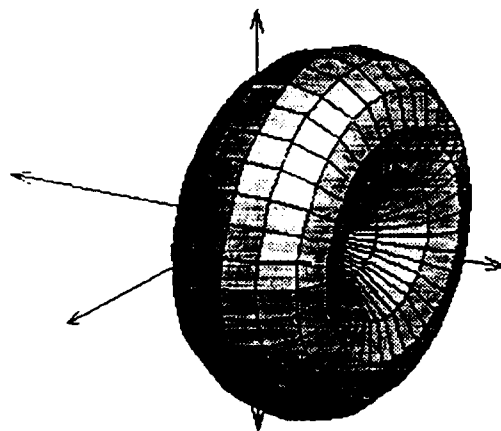


Figure A-4: Rayleigh velocity scattering of a P-wave results in a fore-scattered P-wave and a strong side-scattered S-wave. This scattering pattern is identical to Figure A-3, but rotated 180°.

A.2.2 Plane S-Wave Source

The same analysis can be applied for the case of an incident S-wave. Consider an S-wave propagating in the $+x_1$ direction, with particle motion in the x_2 direction,

$$u_i^0 = \delta_{2i} e^{-i\omega(t - x_1/\beta_0)}. \quad (\text{A.19})$$

Again, we can solve for the body force vector \underline{Q} by inserting Equation A.19 into Equation A.2,

$$Q_i = \left[\delta_{2i} (\bar{\delta}\rho\omega^2 - \bar{\delta}\mu \frac{\omega^2}{\beta_0^2} + \delta_{2i} \bar{\delta}\mu_{,1}) + \delta_{1i} i \frac{\omega}{\beta_0} \bar{\delta}\mu_{,2} \right] e^{-i\omega(t - x_1/\beta_0)}. \quad (\text{A.20})$$

Then the forces are,

$$F_i = \delta_{i2} \omega^2 \bar{\delta}\rho V e^{-i\omega t} \quad (\text{A.21})$$

$$M = \frac{-i\omega V}{\beta_0} \begin{vmatrix} 0 & \bar{\delta}\mu & 0 \\ \bar{\delta}\mu & 0 & 0 \\ 0 & 0 & 0 \end{vmatrix} e^{-i\omega t} \quad (\text{A.22})$$

and the far-field displacements are given by,

$$u_i = \frac{\omega^2 \bar{\delta}\rho V}{4\pi\rho_0 r} \left[\frac{\gamma_i \gamma_2}{\alpha_0^2} e^{-i\omega(t - r/\alpha_0)} - \frac{(\gamma_i \gamma_2 - \delta_{i2})}{\beta_0^2} e^{-i\omega(t - r/\beta_0)} \right] + \frac{\omega^2 \bar{\delta}\mu V}{\mu_0 4\pi r} \left[\frac{-2\gamma_i \gamma_1 \gamma_2}{\alpha_0^3} e^{-i\omega(t - r/\alpha_0)} + \frac{(2\gamma_i \gamma_1 \gamma_2 - \delta_{i1} \gamma_2 - \delta_{i2} 2\gamma_1)}{\beta_0^3} e^{-i\omega(t - r/\beta_0)} \right]. \quad (\text{A.23})$$

Switching to spherical coordinates (Figure A-5), with the polar axis pointing in the direction of the incident particle motion yields,

$$s_{u^P} = \hat{r} \frac{V\omega^2}{4\pi r \alpha_0^2} \left[\frac{\bar{\delta}\rho}{\rho_0} \cos \theta - \frac{\beta_0 \bar{\delta}\mu}{\alpha_0 \mu_0} \sin 2\theta \sin \phi \right] e^{-i\omega(t - r/\alpha_0)} \quad (\text{A.24})$$

$$s_{u^S} = \hat{\phi} \frac{V\omega^2}{4\pi r \beta_0^2} \left[\frac{\bar{\delta}\rho}{\rho_0} \sin \theta + \frac{\bar{\delta}\mu}{\mu_0} \cos 2\theta \sin \phi \right] e^{-i\omega(t - r/\beta_0)} - \hat{\theta} \frac{V\omega^2}{4\pi r \beta_0^2} \left[\frac{\bar{\delta}\mu}{\mu_0} \cos \theta \cos \phi \right] e^{-i\omega(t - r/\beta_0)} \quad (\text{A.25})$$

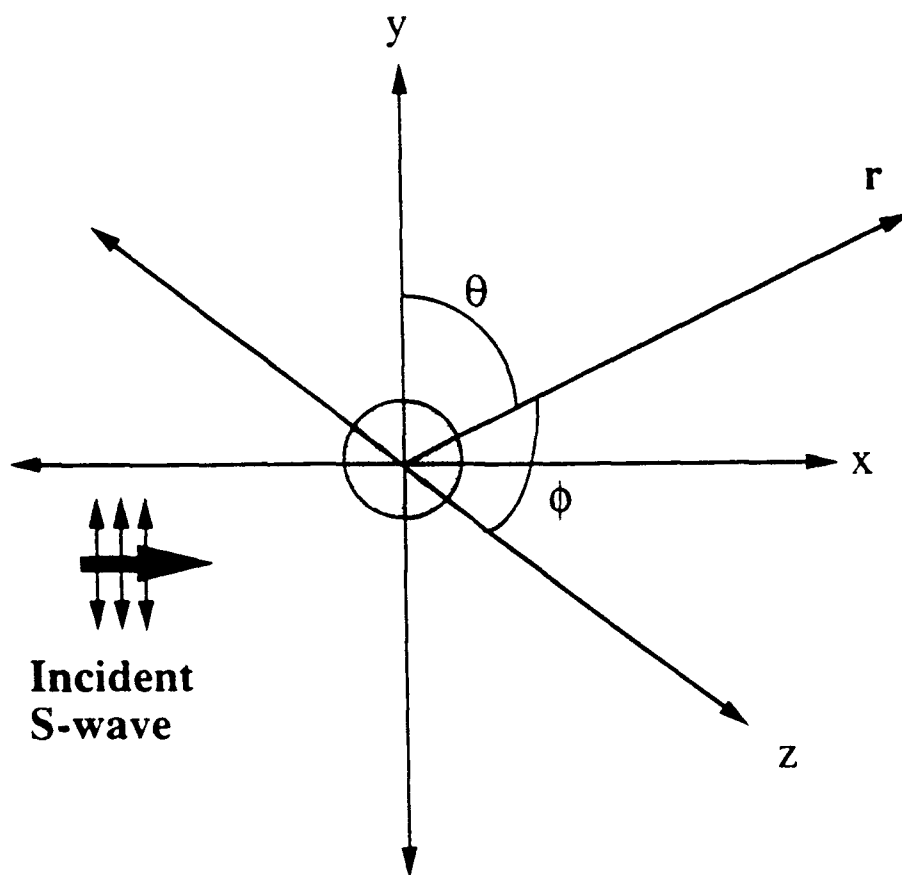


Figure A-5: The coordinate system used for an incident S-wave.

Interestingly, both the scattered P-wave and scattered S-wave are independent of perturbations in λ . The scattered P-wave results from variations in density and shear modulus. The equivalent force due to the variations in density point in the particle motion direction of the incident wave. This force creates a radiation pattern which has a simple cosine dependence for P-waves and sine dependence for S-waves.

The scattering pattern due to variations in μ are more complex. These perturbations create a double couple source in the x_1 - x_2 plane. The double couple source causes the S-wave to have displacements in two directions, θ and ϕ . The double couple force can be decomposed into two single couple forces by rotating the coordinate system, so that the polar axis is parallel to the force direction. Then, the S-wave displacements for each force couple can be calculated separately. Consider the displacements due to the element M_{12} . The displacements in the new coordinate system are given by,

$$s_{u_i}^S = -\frac{\omega^2 V}{4\pi r \rho_0 \beta_0^2} \left(\frac{\overline{\delta\mu}}{\mu_0} \right) (\gamma_i \gamma_1 - \delta_{i1}) \gamma_2 \quad (\text{A.26})$$

or in polar coordinates about the new polar axis by,

$$s_u^S = \hat{\theta}_{M_{12}} - \frac{\omega^2 V}{4\pi r \rho_0 \beta_0^2} \left(\frac{\overline{\delta\mu}}{\mu_0} \right) \sin^2 \theta \cos \phi. \quad (\text{A.27})$$

Similar results can be found for the other force couple M_{21} and the total scattered field from the variations in μ is given by the vector sum of the two single couple forces (Figure A-6).

The terminology introduced for P-wave scattering can also be used in S-wave scattering. When

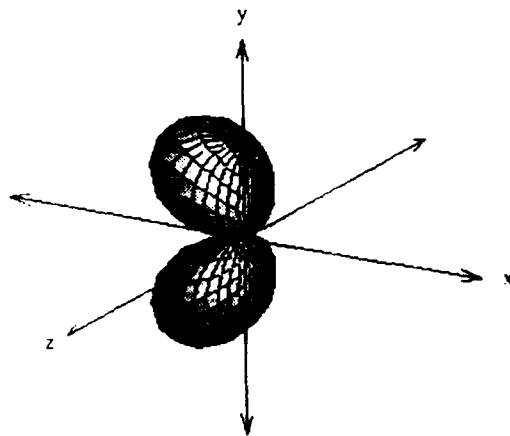
$$\frac{\overline{\delta\rho}}{\rho_0} = \frac{\overline{\delta\mu}}{\mu_0}, \quad (\text{A.28})$$

there is no discontinuity in velocity and only impedance scattering. In impedance scattering, S-wave to P-wave conversion is strongest in the back-scattered direction. S-wave to S-wave scattering is more complex and has three main lobes. The largest lobe is in the backward direction and the two smaller lobes are in the side-scattered direction (Figure A-7).

**THIS
PAGE
IS
MISSING
IN
ORIGINAL
DOCUMENT**

Pg. 185 - FIG A-6

S -> P Scattering



2X

S -> S Scattering

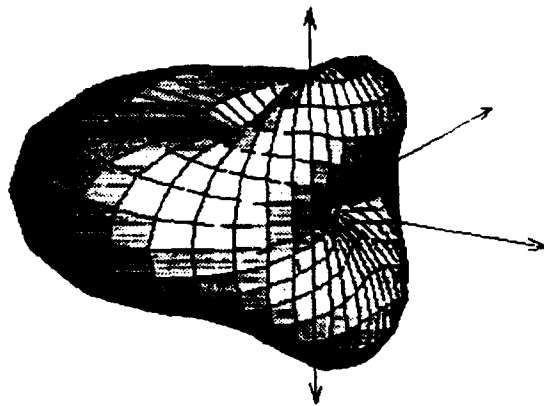


Figure A-7: The total scattered field from Figure A-6. Notice the strong back-scattered lobe which occurs for S-wave to S-wave scattering.

As was the case for P-wave scattering, the scattering pattern due to velocity scattering is opposite that for impedance scattering, Figure A-8. The large forward scattered S-wave suggests that these anomalies will be easiest to identify in transmission experiments, such as cross-well or VSP geometries.

A.3 Mie Scattering in a Weakly Heterogeneous Media

In the last section, a series of simple closed form solutions were obtained for elastic wave scattering from a small isolated heterogeneity. The metric used to define small was the wavelength. If the scatterer is small enough that the phase of the incident wave is nearly constant across the scatterer, the scattered field can be adequately described by Rayleigh scattering. However, when the size of the scatterer approaches that of a wavelength, the incident field will have significantly different phase at different points in the scatterer, resulting in a more complex scattering pattern.

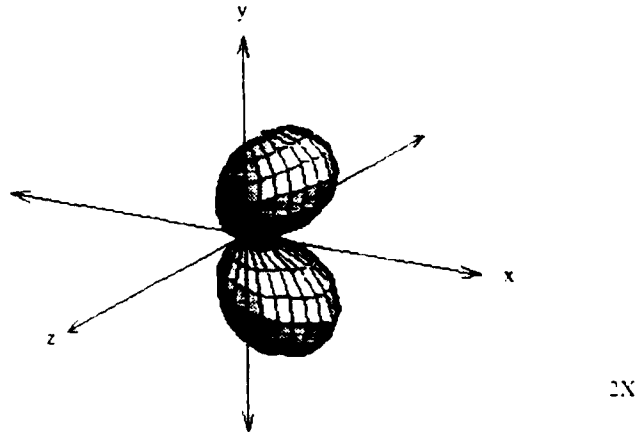
Using the results from the previous section, the Born approximation can be used to calculate the scattered field for a general elastic heterogeneity,

$$u_i(\underline{x}) = \int_V Q_j(\underline{\xi}) * G_{ij}(\underline{x}, \underline{\xi}) dV(\underline{\xi}). \quad (\text{A.29})$$

If the size of the scatterer is on the order of a wavelength, the incident wave and Green's function can no longer be considered constant about the scatterer. Equation A.29 can be solved approximately using the Fraunhofer approximation to the Green's function. Then,

$$\begin{aligned} u_i &= u_i^P + u_i^S \\ u_i^P(\underline{x}) &= \frac{\omega^2 e^{-i\omega(t-r/\alpha_0)}}{4\pi r \alpha_0^2} \int_V \left[\frac{\delta\rho(\underline{\xi})}{\rho_0} \gamma_i \gamma_j u_j^0(\underline{\xi}) \right. \\ &\quad \left. + \frac{i\alpha_0 \delta\lambda(\underline{\xi})}{\omega(\lambda_0 + 2\mu_0)} \gamma_i (\nabla \cdot \underline{u}^0(\underline{\xi})) + \frac{i\alpha_0 \delta\mu(\underline{\xi})}{\omega(\lambda_0 + 2\mu_0)} \gamma_i \gamma_j \gamma_k (u_{j,k}^0(\underline{\xi}) + u_{k,j}^0(\underline{\xi})) \right] \\ &\quad e^{-i\omega(\underline{\xi} \cdot \underline{x})/\alpha_0} dV(\underline{\xi}) \end{aligned} \quad (\text{A.30})$$

S -> P Scattering



S -> S Scattering

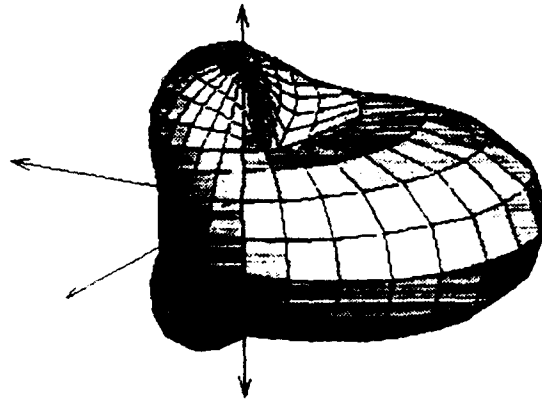


Figure A-8: Rayleigh velocity scattering of a S-wave results in a side-scattered P-wave and a strong fore-scattered S-wave. This scattering pattern is identical to Figure A-7, but rotated 180°.

$$u_i^S(\underline{x}) = \frac{\omega^2 e^{-i\omega(t-r/\beta_0)}}{4\pi r \beta_0^2} \int_V \left[\frac{\delta\rho(\underline{\xi})}{\rho_0} (\delta_{ij} - \gamma_i \gamma_j) u_j^0(\underline{\xi}) + \frac{i\beta_0 \delta\mu(\underline{\xi})}{\omega\mu_0} (\delta_{ij} - \gamma_i \gamma_j) \gamma_k (u_{j,k}^0(\underline{\xi}) + u_{k,j}^0(\underline{\xi})) \right] e^{-i\omega(\underline{\xi} \cdot \underline{x})/\beta_0} dV(\underline{\xi}). \quad (\text{A.31})$$

When the incident wave is a plane P-wave (Equation A.8), these equations can be simplified to,

$$P u_i^P = \frac{\omega^2 e^{-i\omega(t-r/\alpha_0)}}{4\pi r \alpha_0^2} \quad (\text{A.32})$$

$$\int_V \left[\frac{\delta\rho(\underline{\xi})}{\rho_0} \gamma_i \gamma_1 - \frac{\delta\lambda(\underline{\xi})}{\lambda_0 + 2\mu_0} \gamma_i - \frac{2\delta\mu(\underline{\xi})}{\lambda_0 + 2\mu_0} \gamma_i \gamma_1^2 \right] e^{i\omega(\xi_1 - \hat{x} \cdot \underline{\xi})/\alpha_0} dV(\underline{\xi})$$

$$P u_i^S = \frac{\omega^2 e^{-i\omega(t-r/\beta_0)}}{4\pi r \beta_0^2} \quad (\text{A.33})$$

$$\int_V \left[\frac{\delta\rho(\underline{\xi})}{\rho_0} (\delta_{i1} - \gamma_i \gamma_1) - \frac{\beta_0 2\delta\mu(\underline{\xi})}{\alpha_0 \mu_0} (\delta_{i1} - \gamma_i \gamma_1) \gamma_1 \right] e^{i\omega(\xi_1/\alpha_0 - (\hat{x} \cdot \underline{\xi})/\beta_0)} dV(\underline{\xi}).$$

For an incident S-wave,

$$S u_i^P = \frac{\omega^2 e^{-i\omega(t-r/\alpha_0)}}{4\pi r \alpha_0^2} \quad (\text{A.34})$$

$$\int_V \left[\frac{\delta\rho(\underline{\xi})}{\rho_0} \gamma_i \gamma_2 - \frac{\beta_0 2\delta\mu(\underline{\xi})}{\alpha_0 \mu_0} \gamma_i \gamma_1 \gamma_2 \right] e^{i\omega(\xi_1/\beta_0 - (\underline{x} \cdot \underline{\xi})/\alpha_0)} dV(\underline{\xi})$$

$$S u_i^S = \frac{\omega^2 e^{-i\omega(t-r/\beta_0)}}{4\pi r \beta_0^2} \quad (\text{A.35})$$

$$\int_V \left[\frac{\delta\rho}{\rho_0} (\delta_{i2} - \gamma_i \gamma_2) - \frac{\delta\mu}{\mu_0} (\delta_{i1} \gamma_2 + \delta_{i2} \gamma_1 - 2\gamma_i \gamma_1 \gamma_2) \right] e^{i\omega(\xi_1/\beta_0 - (\hat{x} \cdot \underline{\xi})/\beta_0)} dV(\underline{\xi}).$$

Now, suppose all three parameters λ , μ and ρ share the same parameter distribution function $P(\underline{\xi})$ such that,

$$\delta\lambda(\underline{\xi}) = \delta\lambda_0 P(\underline{\xi}) \quad (\text{A.36})$$

$$\delta\mu(\underline{\xi}) = \delta\mu_0 P(\underline{\xi}) \quad (\text{A.37})$$

$$\delta\rho(\underline{\xi}) = \delta\rho_0 P(\underline{\xi}), \quad (\text{A.38})$$

where $\delta\lambda_0$, $\delta\mu_0$, and $\delta\rho_0$ are the parameter values at the center of the inhomogeneity and

$$\delta\lambda_0 \int_V P(\underline{\xi}) dV(\underline{\xi}) = \overline{\delta\lambda} V \quad (\text{A.39})$$

$$\delta\mu_0 \int_V P(\underline{\xi}) dV(\underline{\xi}) = \overline{\delta\mu} V \quad (\text{A.40})$$

$$\delta\rho_0 \int_V P(\underline{\xi}) dV(\underline{\xi}) = \overline{\delta\rho} V. \quad (\text{A.41})$$

Using these definitions, the scattered field for an incident P-wave can be written as,

$$P_{u^P} = \hat{r} \left[\frac{\delta\rho_0}{\rho_0} \cos \theta - \frac{\delta\lambda_0}{\lambda_0 + 2\mu_0} - \frac{2\delta\mu_0}{\lambda_0 + 2\mu_0} \cos^2 \theta \right] \frac{\omega^2 e^{-i\omega(t-r/\alpha_0)}}{4\pi r \alpha_0^2} \int_V P(\underline{\xi}) e^{i\omega(\xi_1 - \hat{x} \cdot \underline{\xi})/\alpha_0} dV(\underline{\xi}) \quad (\text{A.42})$$

$$P_{u^S} = \hat{\theta} \left[-\frac{\delta\rho_0}{\rho_0} \sin \theta - \frac{\beta_0 \delta\mu_0}{\alpha_0 \mu_0} \sin 2\theta \right] \frac{\omega^2 e^{-i\omega(t-r/\beta_0)}}{4\pi r \beta_0^2} \int_V P(\underline{\xi}) e^{i\omega(\xi_1/\alpha_0 - (\hat{x} \cdot \underline{\xi})/\beta_0)} dV(\underline{\xi}) \quad (\text{A.43})$$

and those for an incident S-wave as,

$$S_{u^P} = \hat{r} \frac{\omega^2}{4\pi r \alpha_0^2} \left[\frac{\delta\rho_0}{\rho_0} \cos \theta - \frac{\beta_0 \delta\mu_0}{\alpha_0 \mu_0} \sin 2\theta \sin \phi \right] \int_V P(\underline{\xi}) e^{i\omega(\xi_1/\beta_0 - (\hat{x} \cdot \underline{\xi})/\alpha_0)} dV(\underline{\xi}) \quad (\text{A.44})$$

$$S_{u^S} = \frac{\omega^2}{4\pi r \beta_0^2} \left[\left[\hat{\phi} \frac{\delta\rho_0}{\rho_0} \sin \theta + \frac{\delta\mu_0}{\mu_0} \cos 2\theta \sin \phi \right] + \hat{\theta} \left[\frac{\overline{\delta\mu}}{\mu_0} \cos \theta \cos \phi \right] \right] e^{-i\omega(t-r/\beta_0)} \int_V P(\underline{\xi}) e^{i\omega(\xi_1 - (\hat{x} \cdot \underline{\xi}))/\beta_0} dV(\underline{\xi}) \quad (\text{A.45})$$

(A.46)

These equations are similar in form to the equations for Rayleigh scattering. The only difference is the volume V in those solutions has been replaced by a volume integral

of the form

$$\theta_n(\underline{x}) = \int_V P(\underline{\xi}) e^{-i\omega \underline{\xi} \cdot \underline{S}_n} dV(\underline{\xi}), \quad (\text{A.47})$$

This term has been identified as a shape (Gubernatis et al., 1977a), or volume (Wu and Aki, 1985c) factor. The volume factor modulates the Rayleigh solution. It accounts for the fact that the total scattered field is an integrated sum of scattered waves from all parts of the heterogeneity. Since the incident wave may not have constant phase across the heterogeneity, the total scattered field will be a superposition of waves which have different phase delays. As a result, this method of calculating the scattered field will always produce a smaller scattered wave than the Rayleigh solution (for similar sized scatterers). For common-mode scattering the volume factor is largest in the forward direction and smallest in the backward direction. This occurs because in common-mode scattering, the incident and scattered waves travel with the same slowness, and therefore always add constructively in the direction of propagation.

In Equation A.47, the term \underline{S}_n is the exchange slowness vector. From Equations A.42 - A.45 the slowness vectors are given by,

$$\underline{S}_1 = \frac{1}{\alpha_0} [\hat{x}_1 - \hat{x}] \quad (\text{A.48})$$

$$\underline{S}_2 = [\hat{x}_1/\alpha_0 - \hat{x}/\beta_0] \quad (\text{A.49})$$

$$\underline{S}_3 = [\hat{x}_1/\beta_0 - \hat{x}/\alpha_0] \quad (\text{A.50})$$

$$\underline{S}_4 = \frac{1}{\beta_0} [\hat{x}_1 - \hat{x}]. \quad (\text{A.51})$$

The form of Equation A.47 is similar to that of a spatial Fourier integral, where the wavenumber vector \underline{k} equals $\omega \underline{S}_n$. Then, for a specified scattering angle θ , the volume factor θ_n is equal to the spatial Fourier component of the parameter variation. When the spatial variation is spherically symmetric, the volume factor can be written in terms of a 1D Fourier transform,

$$\theta_n(\theta) = -\frac{2\pi}{\omega S_n} \frac{\partial}{\partial(\omega S_n)} \hat{P}(\omega S_n), \quad (\text{A.52})$$

where \hat{P} is the Fourier transform of the material perturbations and \underline{S}_n is the norm of the vector \underline{S}_n .

A.3.1 Mie Scattering from a Gaussian Inclusion

Several statistical models have been put forth to describe the statistical distribution of scatterers in the lithosphere, (Aki et al., 1977; Aki, 1980; Ringdal and Husebye, 1982; Wu, 1982a; Frankel and Clayton, 1984; Frankel and Clayton, 1986; Charrette and Toksöz, 1989; Toksöz et al., 1991). In crystalline rocks, the heterogeneities are probably broad smoothly varying features. It is speculated that these heterogeneities can be described by a Gaussian autocorrelation function. In sedimentary rocks, however, the heterogeneities might be more "rough" and better described by the exponential function. In this section we derive the volume factors for both the Gaussian and exponential functions and show their effects on the scattered waves.

A.3.2 Gaussian Parameter Function

For a spherical inclusion, the Gaussian parameter variation function is given by,

$$P(r) = e^{-r^2/a^2}, \quad (\text{A.53})$$

where a is the correlation length of the heterogeneity (Figure A-9). The one-dimensional Fourier transform of the parameter function is,

$$\hat{P}(k_r) = \sqrt{\pi} a e^{-k_r^2 a^2/4}. \quad (\text{A.54})$$

and the volume factors are given by,

$$\theta_n = (\sqrt{\pi} a)^3 e^{-(\omega S_n a)^2/4}. \quad (\text{A.55})$$

At low frequencies (i.e. when the wavelength is large compared to the size of the scatterer) the volume factor is nearly isotropic and the Mie solution is much like the Rayleigh solution (Figure A-10). As the frequency of the incident wave increases, the scattering pattern becomes more forward directed, until no energy is backscattered at all. The volume factor for an incident S-wave is similar to that for an incident P-wave (Figure A-11). In both cases, the volume factor has only one main lobe. The

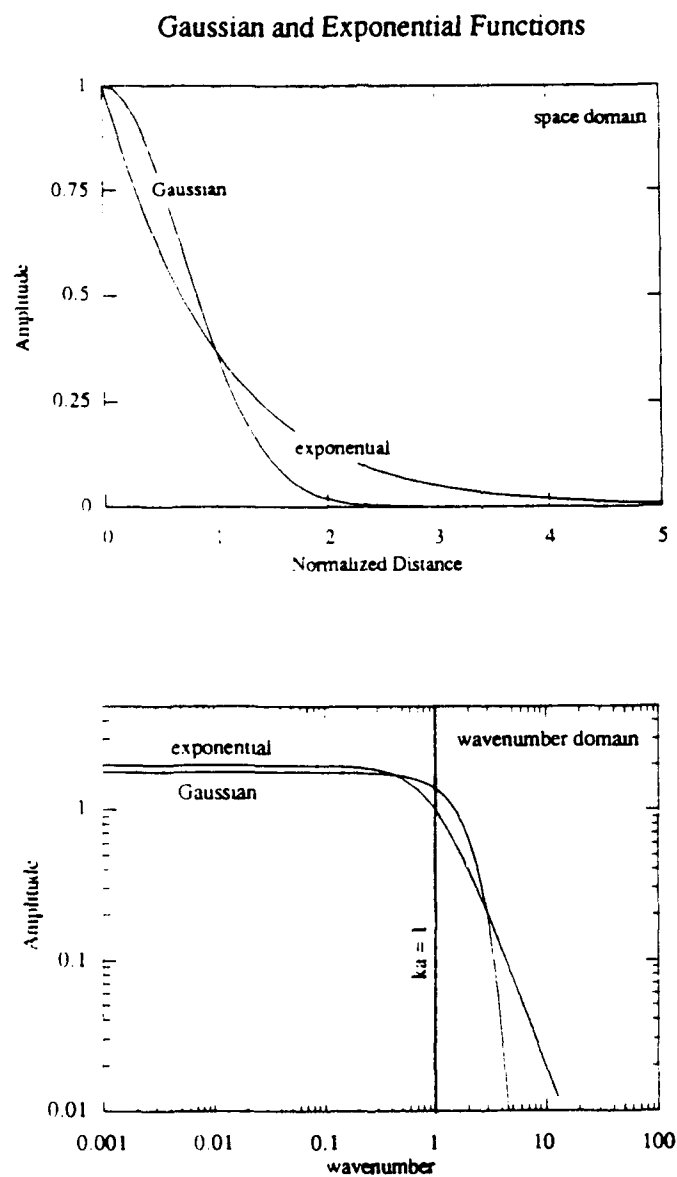


Figure A-9: Space and wavenumber domain representations of the Gaussian and exponential functions.

Incident P-Wave

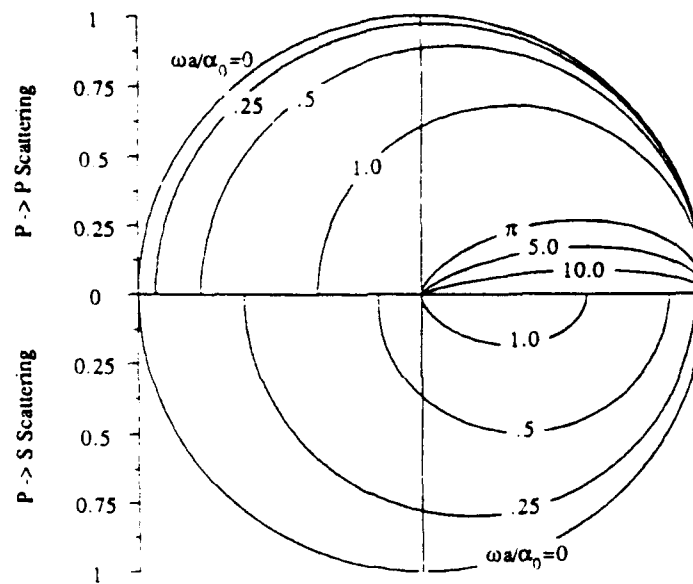


Figure A-10: The volume factors for a P-wave incident on a spherical inclusion with a Gaussian parameter function. The upper half of the diagram is for P to P scattering and the forward scattering direction is to the right. The volume factor varies smoothly with angle and strongly favors forward scattering of both P and S waves.

Incident S-Wave

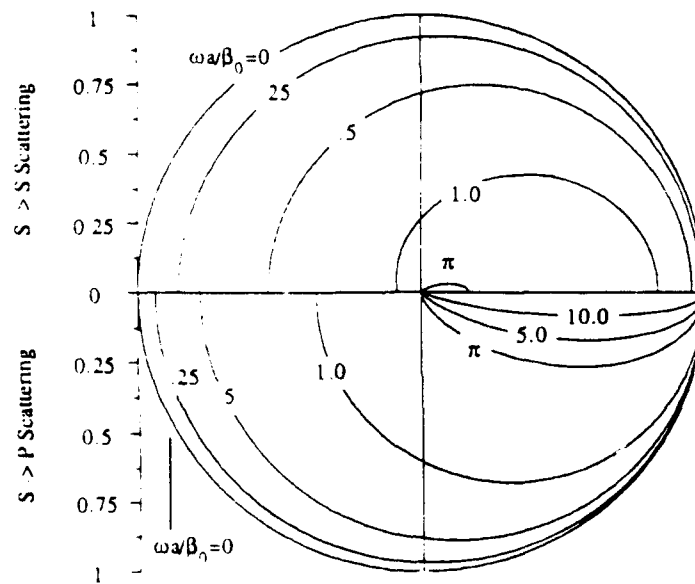


Figure A-11: The volume factors for an S-wave incident on a spherical inclusion with a Gaussian parameter function. The upper half of the diagram is for S to S scattering and the forward scattering direction is to the right. As for an incident P-wave, the volume factor varies smoothly with angle and strongly favors forward scattering of both P and S waves.

main lobe is oriented in the forward scattered direction and varies smoothly with scattering angle. Other parameter functions, especially those with sharper space domain features (e.g., a spherical boxcar function) have been shown to produce much more complex volume factors (Gubernatis et al., 1977a; Wu and Aki, 1985c).

In the back-scattered direction, the volume factor decreases as the size of the heterogeneity increases (Figure A-10). This has the effect of severely reducing the amplitude of both the scattered P (Figure A-12) and scattered S waves, (Figure A-13).

The effect of the volume factor on velocity scattering is similar for S-waves (Figure A-15), but quite different for P-waves (Figure A-14). Since in velocity scattering the P-wave is strongly forward scattered the effect of the volume factor is small. In both impedance and velocity scattering the Mie solution approaches the Rayleigh solution as the size of the scatterer decreases.

A.3.3 Exponential Parameter Function

The exponential function,

$$P(r) = e^{-r/a}, \quad (\text{A.56})$$

is similar to the Gaussian, but is not as well localized in the space (or wavenumber) domain (Figure A-9). The one-dimensional Fourier transform of the exponential is,

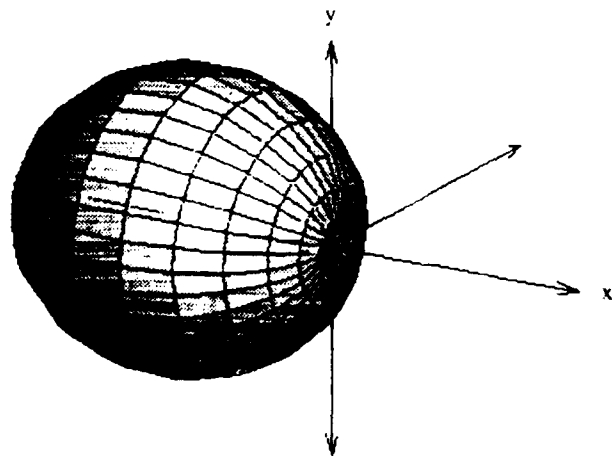
$$\hat{P}(k_r) = 2a/(1 + k_r^2 a^2), \quad (\text{A.57})$$

and the volume factors are given by,

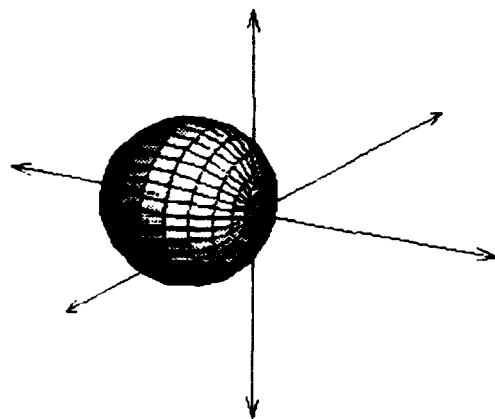
$$\theta_n = \frac{8\pi a^3}{[1 + \omega^2 S_n^2 a^2]^2}. \quad (\text{A.58})$$

The volume factors for incident P and S waves are shown graphically in Figure A-16 and Figure A-17 respectively. The scattering patterns from an inclusion with an exponential parameter function (Figures A-18-A-21), are much like those from an inclusion with a Gaussian parameter function. For velocity scattering, the scattered P-wave is noticeably more forward directed, but otherwise it is very similar to the Gaussian case.

P -> P Scattering



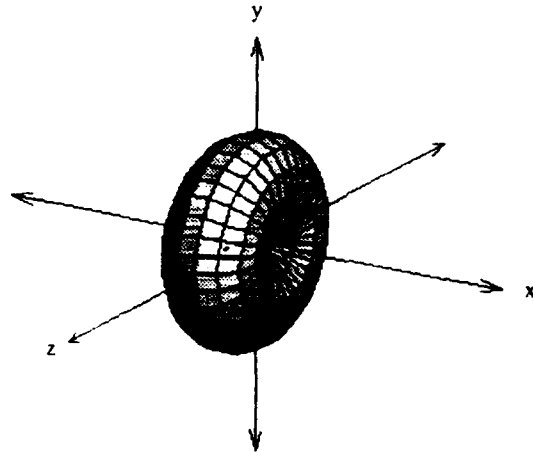
$$a\omega/\alpha = 0.5$$



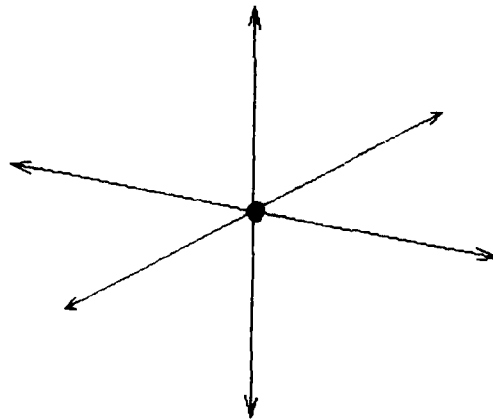
$$a\omega/\alpha = 1.0$$

Figure A-12: Mie scattering includes the effects due to the finite shape of the scatterer. Shown are P to P impedance scattering patterns (magnified 4X) which result from two different sized inclusions with Gaussian parameter functions. Note the strong reduction is the amount of back-scattered energy as the size of the inclusion is increased. For infinitely long wavelengths, this solution reduces to Figure A-3.

P -> S Scattering



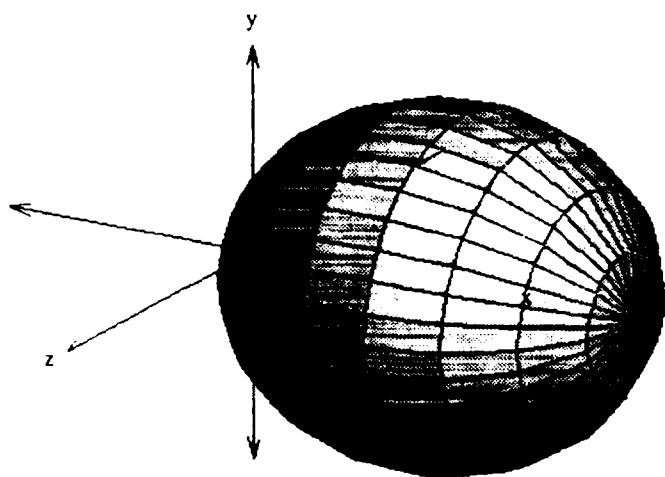
$$a\omega/\alpha = 0.5$$



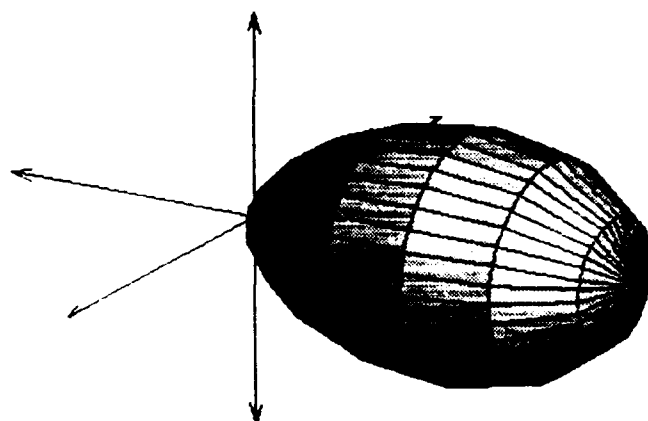
$$a\omega/\alpha = 1.0$$

Figure A-13: P to S impedance (Mie) scattering patterns (magnified 2X) which result from two different sized inclusions with Gaussian parameter functions. Note the near extinction of the scattered S-wave when the size of the inclusion is larger than 1/6 of a wavelength. For infinitely long wavelengths, this solution reduces to Figure A-3.

P -> P Scattering



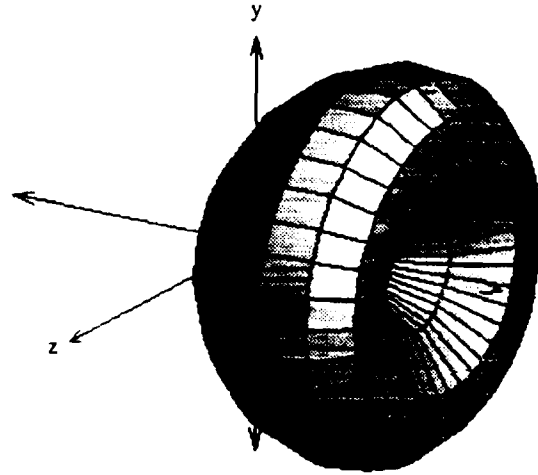
$$a\omega/\alpha = 0.5$$



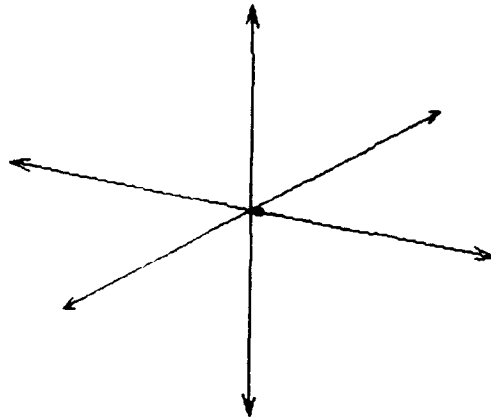
$$a\omega/\alpha = 1.0$$

Figure A-14: P to P velocity (Mie) scattering patterns (magnified 4X) which result from two different sized inclusions with Gaussian parameter functions. Unlike the impedance scattering case, the size of the scattered wave is not greatly affected by the size of the scatterer. For infinitely long wavelengths, this solution reduces to Figure A-4.

P -> S Scattering



$$a\omega/\alpha = 0.5$$



$$a\omega/\alpha = 1.0$$

Figure A-15: P to S velocity (Mie) scattering patterns (magnified 2X) which result from two different sized inclusions with Gaussian parameter functions. Again, note the near extinction of the scattered S-wave when the size of the inclusion is larger than 1/6 of a wavelength. For infinitely long wavelengths, this solution reduces to Figure A-4.

Incident P-Wave

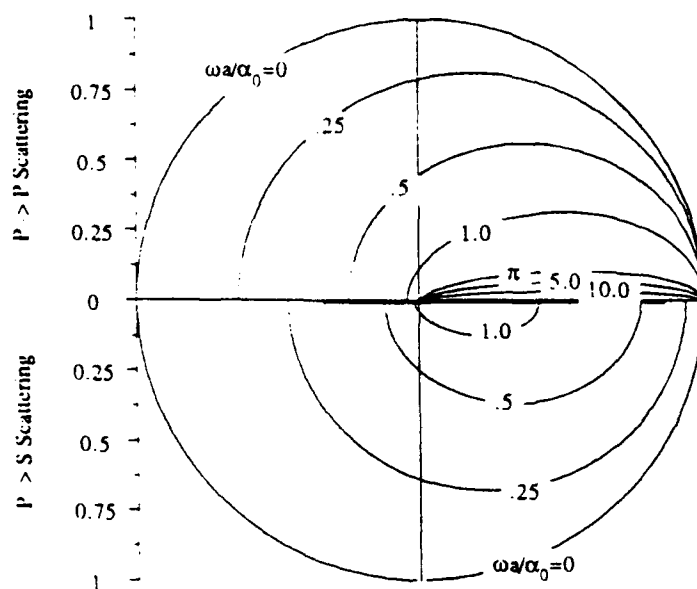


Figure A-16: The volume factors for a P-wave incident on a spherical inclusion with an exponential parameter function. The upper half of the diagram is for P to P scattering and the forward scattering direction is to the right. The volume factor varies smoothly with angle and strongly favors forward scattering of both P and S waves.

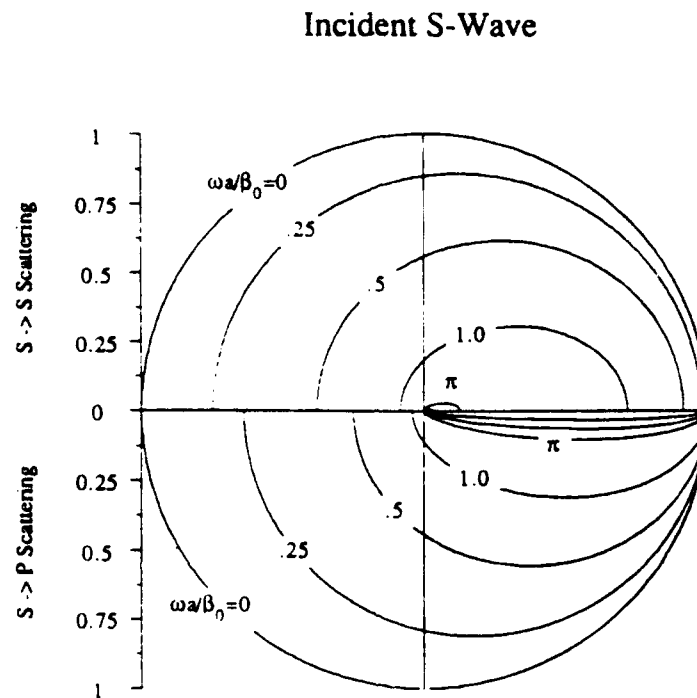
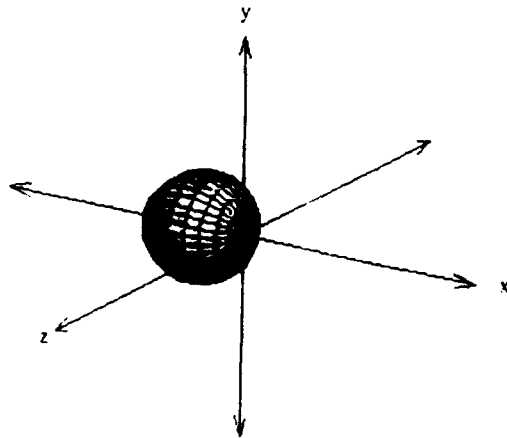
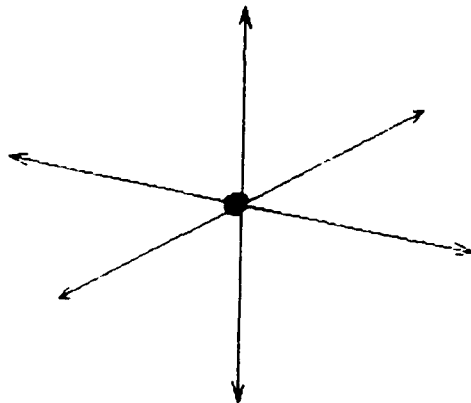


Figure A-17: The volume factors for an S-wave incident on a spherical inclusion with an exponential parameter function. The upper half of the diagram is for S to S scattering and the forward scattering direction is to the right. As for an incident P-wave, the volume factor varies smoothly with angle and strongly favors forward scattering of both P and S waves.

P -> P Scattering



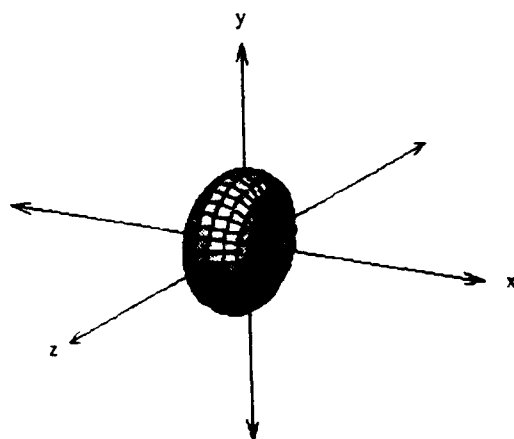
$$a\omega/\alpha = 0.5$$



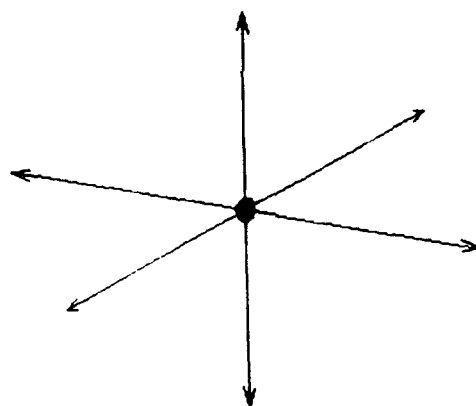
$$a\omega/\alpha = 1.0$$

Figure A-18: P to P impedance (Mie) scattering patterns (magnified 4X) which result from two different sized inclusions with exponential parameter functions. Note the strong reduction in the amount of back-scattered energy as the size of the inclusion is increased. The scattering pattern is similar to Figure A-12.

P -> S Scattering



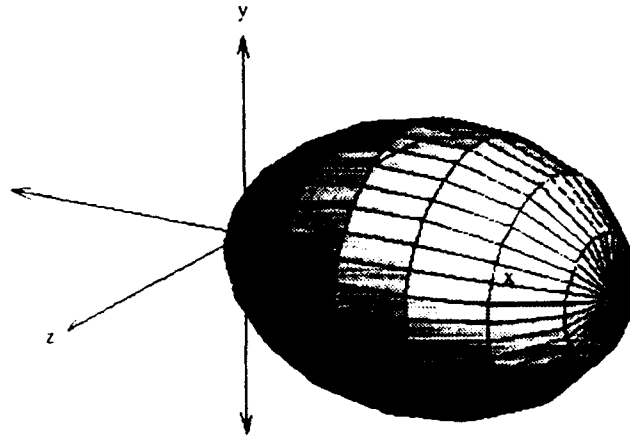
$$a\omega/\alpha = 0.5$$



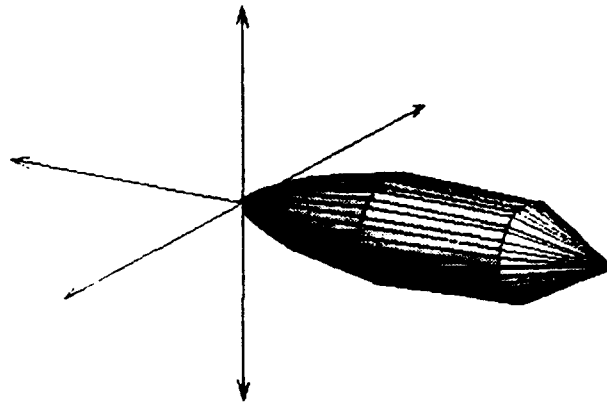
$$a\omega/\alpha = 1.0$$

Figure A-19: P to S impedance (Mie) scattering patterns (magnified 2X) which result from two different sized inclusions with exponential parameter functions. Note the near extinction of the scattered S-wave when the size of the inclusion is larger than 1/6 of a wavelength. The scattering pattern is similar to Figure A-13.

P -> P Scattering



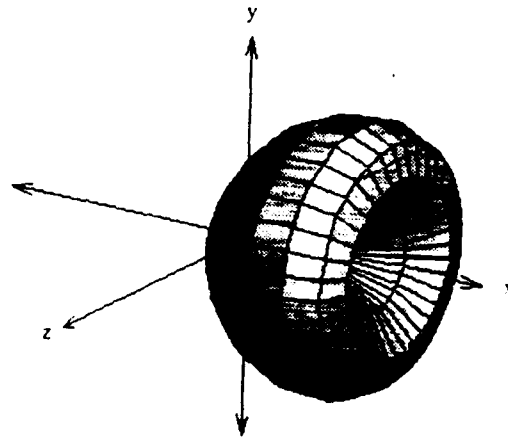
$$a\omega/\alpha = 0.5$$



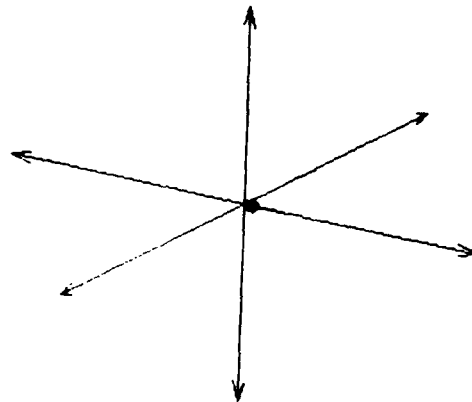
$$a\omega/\alpha = 2.0$$

Figure A-20: P to P velocity (Mie) scattering patterns (magnified 4X) which result from two different sized inclusions with exponential parameter functions. Unlike the impedance scattering case, the size of the scattered wave is not greatly affected by the size of the scatterer. The scattering pattern is similar to Figure A-12, but slightly more concentrated in the forward direction.

P -> S Scattering



$$a\omega/\alpha = 0.5$$



$$a\omega/\alpha = 2.0$$

Figure A-21: P to S velocity (Mie) scattering patterns (magnified 2X) which result from two different sized inclusions with exponential parameter functions. Again, note the near extinction of the scattered S-wave when the size of the inclusion is larger than 1/6 of a wavelength.

Appendix B

Finite Difference Modeling

B.1 Introduction

Finite difference modeling has proven to be an effective technique for numerically simulating wave propagation in the earth. The popularity of the technique stems from its ability to generate a complete solution to the elastic wave equation. Thus direct, reflected, diffracted, and guided modes are all accurately modeled. The technique is also easy to implement and accurate over a wide range of wavelength to scatterer ratios. The latter is not true of high frequency techniques, such as raytracing. The chief disadvantage of the finite difference technique is its computational intensity. As a result, large scale three dimensional simulations can be done only on state of the art supercomputers and require prohibitive amounts of CPU time.

A great number of finite difference schemes have been introduced in the literature. These schemes are generally divided into two broad classes; explicit schemes and implicit schemes. Both iteratively solve the wave equation, but in explicit schemes it is possible to calculate displacements at a later time from only earlier displacement values. This leads to easier implementation and may explain their widespread use in geophysical problems. Implicit schemes use both future and past time steps to provide unconditional stability. However, seismic wave simulation is bound by dispersion

error, not by stability, so the increased complexity of implicit schemes has not been justified.

Finite difference schemes can be further categorized by their order of accuracy. Since the value of a continuous function sampled on a discrete grid is known only at the node points, the usual method of deriving finite difference operators is to assume an interpolating function then exactly differentiate that function. The most commonly used interpolant is the Lagrange polynomial. Bickley (1941) gives the general form of the differentiated Lagrange polynomial as

$$\frac{d^k f(x)}{dx^k} \Big|_{x=x_j} = \frac{k!}{m!h^k} \sum_{i=0}^m A_i f(x_i) + E \left(h^{m+1} \frac{d^{k+1} f(x)}{dx^{k+1}} \right), \quad (B.1)$$

where k is the order of differentiation, m is the order of accuracy, and h is the sample spacing. It is clear from Equation B.1 that the size of the error term E decreases as the order of the interpolant increases. It is also clear that as the order of the interpolant increases, the number of computations increases.

All forward modeling presented in this thesis made use of an explicit second-order finite difference technique on a non-staggered grid. This approach allows both components of the displacement vector to be specified at the same point in space, making the implementation of boundary conditions and subsequent processing considerably easier. The cost of this simplification is a slight loss in accuracy, especially in areas with sharp spatial gradients in material properties (Virieux, 1986). A second reason for choosing this formulation is that both absorbing and free surface boundary conditions are far easier to incorporate into low order finite difference schemes. Lastly, in order to accurately describe some of the random media, it was necessary to sample the medium at a very high spatial sampling rate. In light of the high sampling rate, low order schemes were more efficient than high order schemes.

Other schemes are also commonly used in seismic applications. Currently, the most popular schemes seem to be fourth-order explicit schemes (e.g., Frankel and Clayton, 1984; Frankel and Clayton, 1986; Gibson and Levander, 1988). The popularity of these schemes stems from the fact that they provide sufficient accuracy with

a larger step size. The pseudo-spectral method, the high order end member in the family of finite difference schemes, has also generated some interest in the seismic literature (e.g., Fornberg, 1987; Witte, 1989). This method uses a Fourier series as the interpolation function. The Fourier transform is efficiently calculated using the Fast Fourier transform. The derivative of the interpolant is simply its Fourier spectrum times ik , where k is the wavenumber. The pseudo-spectral technique has the advantage that it exactly differences any spatial frequency which is not aliased, but it has the disadvantage that it implicitly assumes periodicity, thus making free surface and absorbing boundaries difficult to implement.

The trade-off between high and low order finite difference schemes has been investigated in the seismic literature (Fornberg, 1987; Daudt et al., 1989; Vidale, 1990) but it appears the optimal choice for the order of accuracy may be application as well as machine dependent. The latter point has important implications for three-dimensional finite difference work, where parallel computers will likely dominate. On most parallel computers, individual nodes can perform local calculations orders of magnitudes faster than they can access data from neighboring processors. In light of this, it seems low order finite difference schemes might be more efficient on these machines. Conversely, machines with high speed vector processors and fast RAM (memory) can compute and access memory at high speed and may favor higher order schemes.

B.2 2-D Finite Difference Modeling

The wave equation for a linearly elastic, isotropic, heterogeneous medium can be written as (Aki and Richards, 1980)

$$\rho \ddot{\mathbf{u}}_i - (\lambda \nabla \cdot \mathbf{u})_{,i} - [\mu(u_{i,j} + u_{j,i})]_{,j} = 0, \quad (\text{B.2})$$

where $\mathbf{u} = \mathbf{u}(\mathbf{x}, t)$ is the displacement vector, λ and μ are the Lamé's parameters, and ρ is density.

Most features in the Earth's crust are fully three dimensional in nature. However, due to computational limitations we were only able to model two-dimensional geometries. We have chosen to use the two-dimensional plane stress equations in a Cartesian coordinate system. All stresses are assumed to be invariant in the y direction. It should be noted that the Green's function for a two-dimensional system is scaled by $1/\sqrt{r}$, as opposed to $1/r$ for a three-dimensional medium. As a result, some care must be exercised when comparing synthetic 2-D results to actual field data.

We follow the coordinate system commonly used in seismology; x is the horizontal offset and z is depth. Expanding Equation B.2 and setting displacements and stresses in the y direction equal to zero gives

$$\rho \partial_{tt} u = \partial_x [(\lambda + 2\mu) \partial_x u + \lambda \partial_z w] + \partial_z [\mu (\partial_z u + \partial_x w)] \quad (\text{B.3})$$

$$\rho \partial_{tt} w = \partial_z [(\lambda + 2\mu) \partial_z w + \lambda \partial_x u] + \partial_x [\mu (\partial_z u + \partial_x w)],$$

where u and w are the horizontal and vertical components of the displacement vector. These equations fully describe the motion of compressional (P) and vertically polarized shear (SV) waves within the medium. There is no need to consider the horizontally polarized shear (SH) waves since that motion is completely decoupled in two-dimensional systems and will not be excited by our source.

All finite difference modeling in Cartesian coordinates was done using the explicit second order scheme introduced by Kelly et al. (1976). In that scheme, displacements, stresses, and the material properties are all specified on the same grid. The scheme uses midpoint finite difference operators to approximate second order partial derivatives with only one independent variable,

$$\partial_x \lambda(x, z) \partial_x u(x, z, t) \approx D_x \lambda(x, z) D_x u(x, z, t) \quad (\text{B.4})$$

$$\begin{aligned} &\approx \frac{1}{dx^2} [\lambda(x + dx/2, z)(u(x + dx, z, t) - u(x, z, t)) \\ &- \lambda(x - dx/2, z)(u(x, z, t) - u(x - dx, z, t))], \end{aligned} \quad (\text{B.5})$$

but a less accurate full step stencil to approximate mixed derivatives

$$\partial_x \mu(x, z) \partial_z u(x, z, t) \approx D_x \mu(x, z) D_z u(x, z, t) \quad (\text{B.6})$$

$$\approx \frac{1}{4dxdz} [\mu(x+dx, z)(u(x+dx, z+dz, t) - u(x+dx, z-dz, t)) - \mu(x-dx, z)(u(x-dx, z+dz, t) - u(x-dx, z-dz, t))] . \quad (B.7)$$

Inserting the finite differences into Equation B.3 yields

$$\begin{aligned} \rho D_{tt}u &= [D_x(\lambda + 2\mu)D_xu + D_x\lambda D_zw \\ &+ D_z\mu D_zu + D_z\mu D_xw] \end{aligned} \quad (B.8)$$

$$\begin{aligned} \rho D_{tt}w &= [D_z(\lambda + 2\mu)D_zw + D_z\lambda D_xu \\ &+ D_x\mu D_xw + D_x\mu D_zu] \end{aligned} \quad (B.9)$$

B.2.1 Numerical Dispersion

Trefethen (1982) showed that finite difference approximations to the elastic equation of motion produce a medium which is both dispersive and anisotropic. That analysis was presented for the acoustic wave equation, but used a finite difference scheme similar to that used here. Prange (1989) followed that procedure and obtained simple closed form expressions for both the phase and group velocity of elastic waves traveling on a staggered finite difference grid. He was able to obtain simple closed form expressions because the second differences in his equations were obtained by recursively applying the first difference equations. The finite difference scheme used here does not have that property, thus its dispersion relation is more complex.

Numerical analysis of the dispersion equation for the inhomogeneous wave equation is extremely complex. Therefore, most studies concentrate on the homogeneous form of the isotropic elastic wave equation

$$\partial_{tt} \begin{bmatrix} u \\ w \end{bmatrix} = \begin{bmatrix} \alpha^2 \partial_{xx} + \beta^2 \partial_{zz} & (\alpha^2 - \beta^2) \partial_{xz} \\ (\alpha^2 - \beta^2) \partial_{xz} & \alpha^2 \partial_{zz} + \beta^2 \partial_{xx} \end{bmatrix} \begin{bmatrix} u \\ w \end{bmatrix} \quad (B.10)$$

The dispersion relation for the homogeneous elastic wave equation can be found by inserting a trial solution of the form $e^{i(kx \pm \omega t)}$ into Equation B.10. After simplification,

it can be shown that the eigenvalues are given by

$$\omega^2 = -\alpha^2(\underline{k} \cdot \underline{k}) \quad (\text{B.11})$$

$$\omega^2 = -\beta^2(\underline{k} \cdot \underline{k}) \quad (\text{B.12})$$

where ω is the angular frequency and \underline{k} is the wavenumber vector. Notice that in a purely elastic medium, the phase velocity is independent of frequency and therefore equivalent to the group velocity. Also notice that the dispersion curve is a circle, indicating the medium is isotropic. Since Equation B.10 is Hermitian, its eigenvectors are orthogonal. The first eigenvector points in the direction of \underline{k} (i.e. P-wave motion is longitudinal) and the second is orthogonal to \underline{k} (i.e. S-wave motion is transverse).

The eigenvalues for the finite difference equations can be found by inserting the finite difference approximations (Equations B.4 and B.6) into Equation B.10. Taking the limit as $\Delta t \rightarrow 0$ and using the same trial solution results in extremely complicated analytic forms for the eigenvalues and eigenvectors. Due to the complexity of those equations, the error in phase velocities for the compressional and shear modes are displayed graphically in Figures B-1 and B-2. The phase velocities of the medium depend on the eigenvalues, and are given by $C(\underline{k}) = \omega/|\underline{k}|$. In the analytic form of the elastic wave equation, the phase velocities are constant. Figures B-1 and B-2 show this is not the case for the finite difference wave equation. In the wavenumber domain, the error in phase velocities is shown to be a function of the finite difference grid spacing. At small spacings, the error in phase velocity is small for both P and S waves. At larger step sizes, the error contours for the compressional phase velocity slowly become less circular. This is numerically induced anisotropy. The shear phase velocity is even more anisotropic. Along the axes of the grid, the shear wave can be seen to travel too slowly, while at 45° to the axes, the shear wave velocity is too fast.

The group velocity vector is defined as

$$\underline{U}(k) = \nabla_{\underline{k}} \omega. \quad (\text{B.13})$$

For an elastic, homogeneous, isotropic medium, the group velocity vector is inde-

Error in Phase Velocity (Compressional Waves)

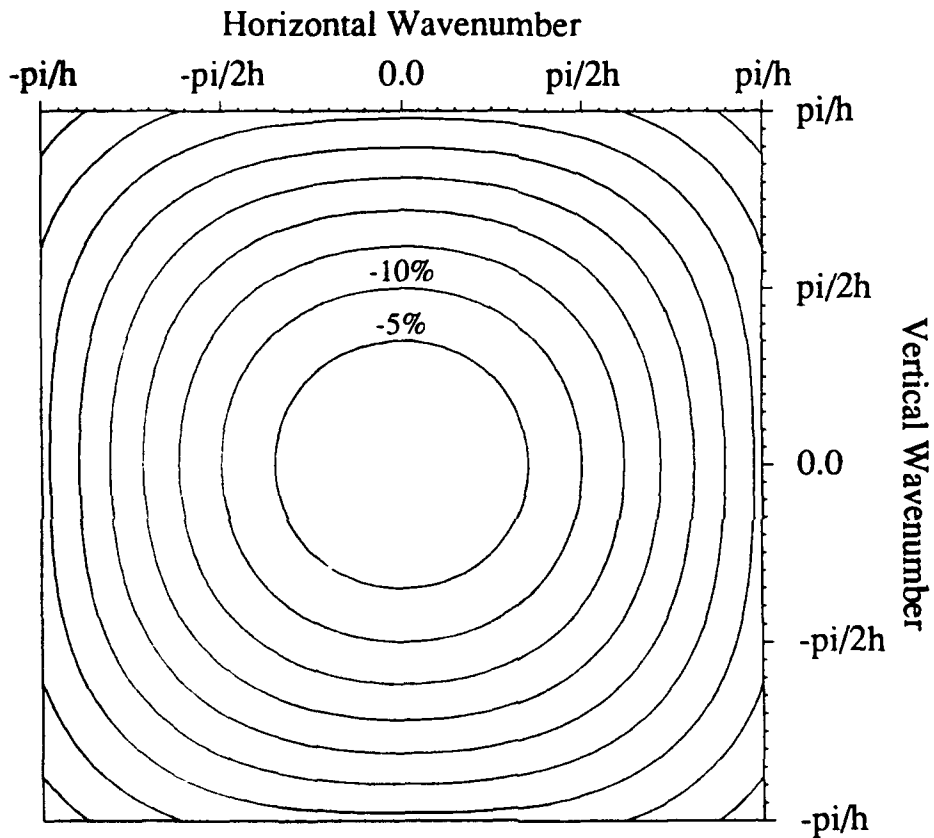


Figure B-1: In wavenumber space, the dispersive and anisotropic nature of the finite difference grid is clear. This plot contours the errors in compressional phase velocity as a function of wavenumber. In all modeling the spatial step size h was chosen so that no frequencies had phase velocity errors greater than 1%.

Error in Phase Velocity (Shear Waves)

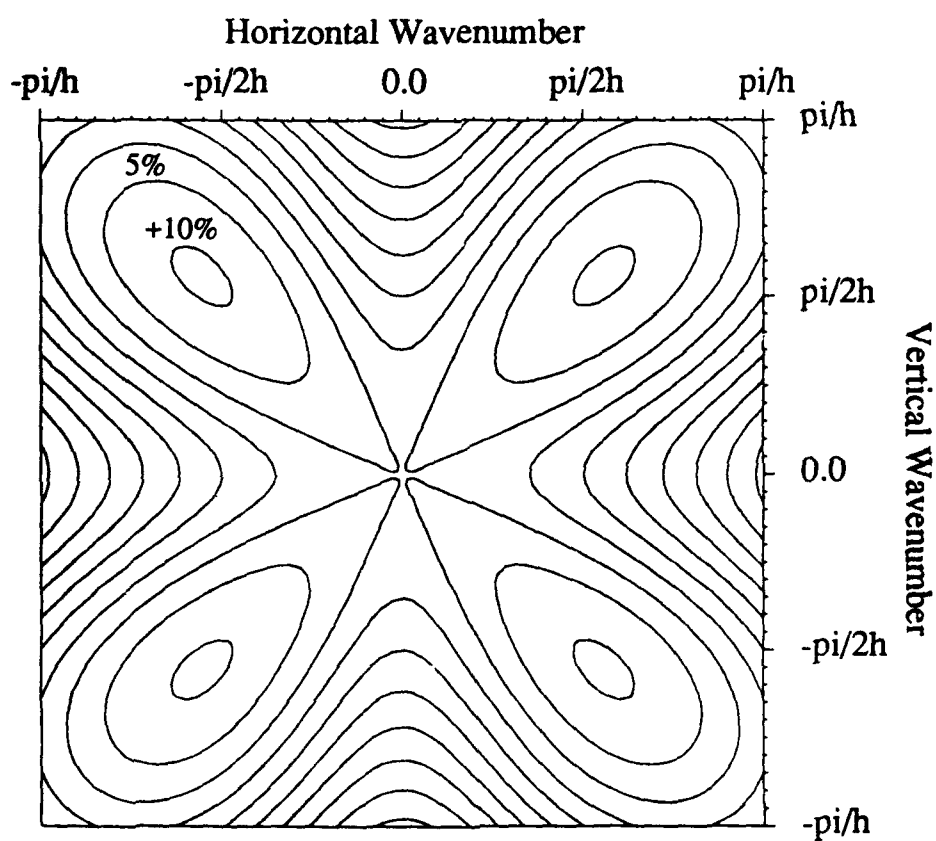


Figure B-2: Similar to Figure B-1, but for the shear wave. Notice the highly anisotropic nature of the finite difference grid. Also notice that shear waves tend to travel fastest at 45° and slowest along the axes of the grid.

pendent of frequency and direction. These properties are only observed in the finite difference equations when the spatial step size is very small (Figures B-3 and B-4). At larger step sizes, the magnitude of the group velocity vector is generally underestimated for both P and S waves. These errors are shown graphically in Figures B-5 and B-6. In addition, there is a consistent error in the direction of the group velocity vector. Only in a few directions (0° , 45° , and 90°) are the group velocity vectors oriented correctly. Energy traveling in other directions will tend to be focused towards the diagonals of the grid. As a result, there may be too much energy traveling in these directions

Both these errors can be minimized by maintaining a sufficiently high sampling rate. Throughout this thesis, we sustained a sampling rate of at least 10 points per wavelength (PPW) for the shortest wavelengths on the grid (i.e. $k = \pi/5$). For P-waves, this resulted in phase velocity errors of less than 1.5% and group velocity errors of less than 5.0% (Figures B-1 and B-6). Errors were much smaller at the center frequency of the source wavelet.

B.2.2 Sources and Boundary Conditions

Energy can be introduced into a finite difference simulation in two ways, either by specifying the initial conditions (i.e. the displacement and the time derivative of displacement) over the whole grid, or driving one or more nodes with a time varying displacement function. In general, we use the first technique when modeling phenomena in which the source is a plane wave. The second technique is reserved for situations when the desired source is a line source (2-D equivalent of a point source). The source function most commonly used is the Ricker wavelet (Ricker, 1977), since it is well localized in both the spatial and Fourier domains (Figure B-7).

To minimize computational time and storage, artificial boundaries must be introduced along the "edges" of the grid. Throughout this thesis we use a second-order paraxial elastic wave equation at all boundaries from which we desire no reflections

Group Velocity Vector (Compressional Waves)

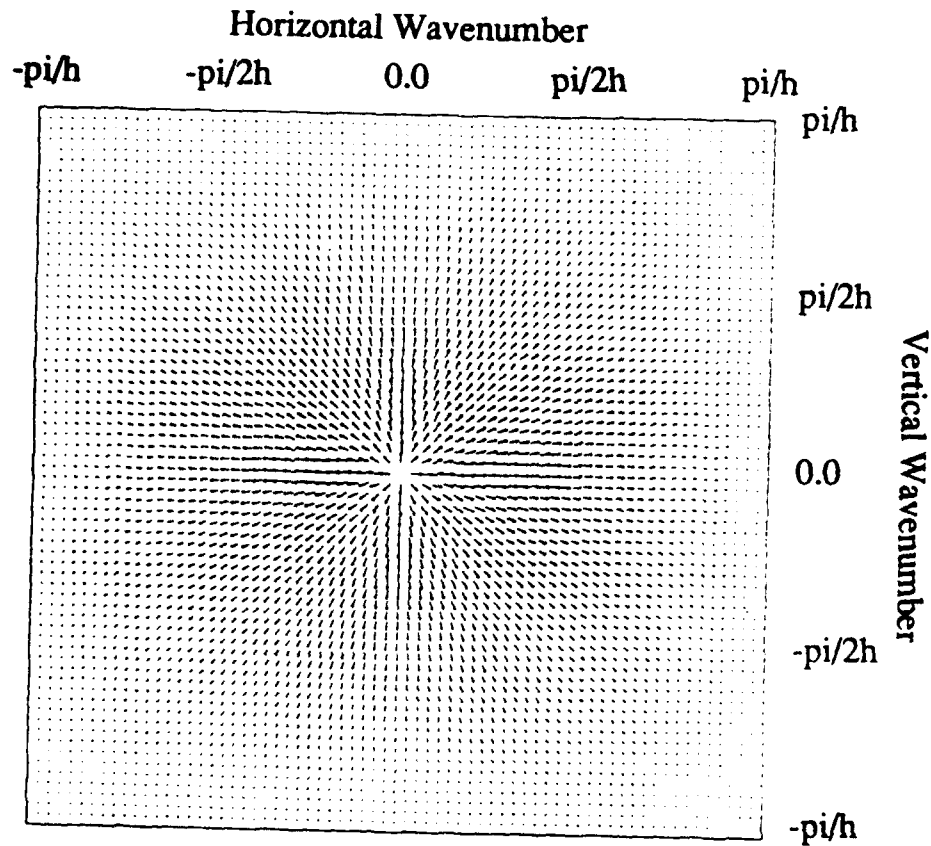


Figure B-3: For an isotropic medium, the magnitude of the group velocity vector is independent of frequency and points radially away from the origin. Here, only at 0° , 45° , and 90° do the group velocity vectors point in the radial directions. Along all other propagation directions, the group velocity vectors are biased towards 45° .

Group Velocity Vector (Shear Waves)

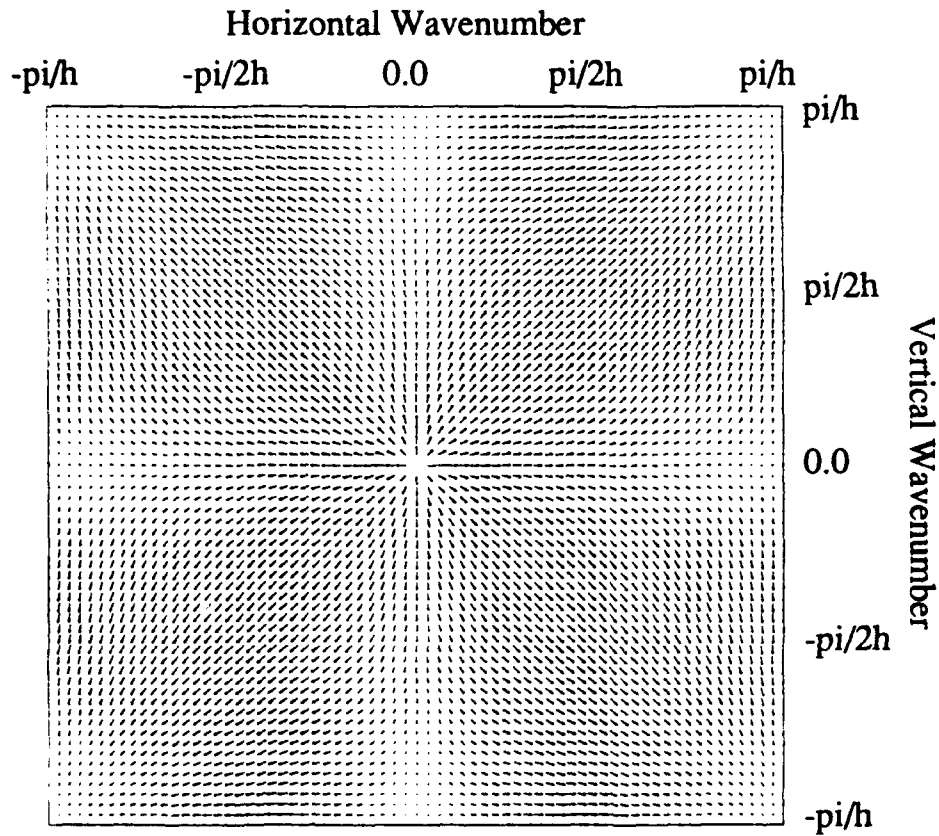


Figure B-4: For a non-dispersive isotropic medium, the shear wave group velocity vector points radially away from the origin and has constant length. Note that only at 0° , 45° , and 90° do the group velocity vectors point in the radial direction. Along all other propagation directions, the group velocity vectors are biased towards 45° .

Error in Group Velocity (Compressional Waves)

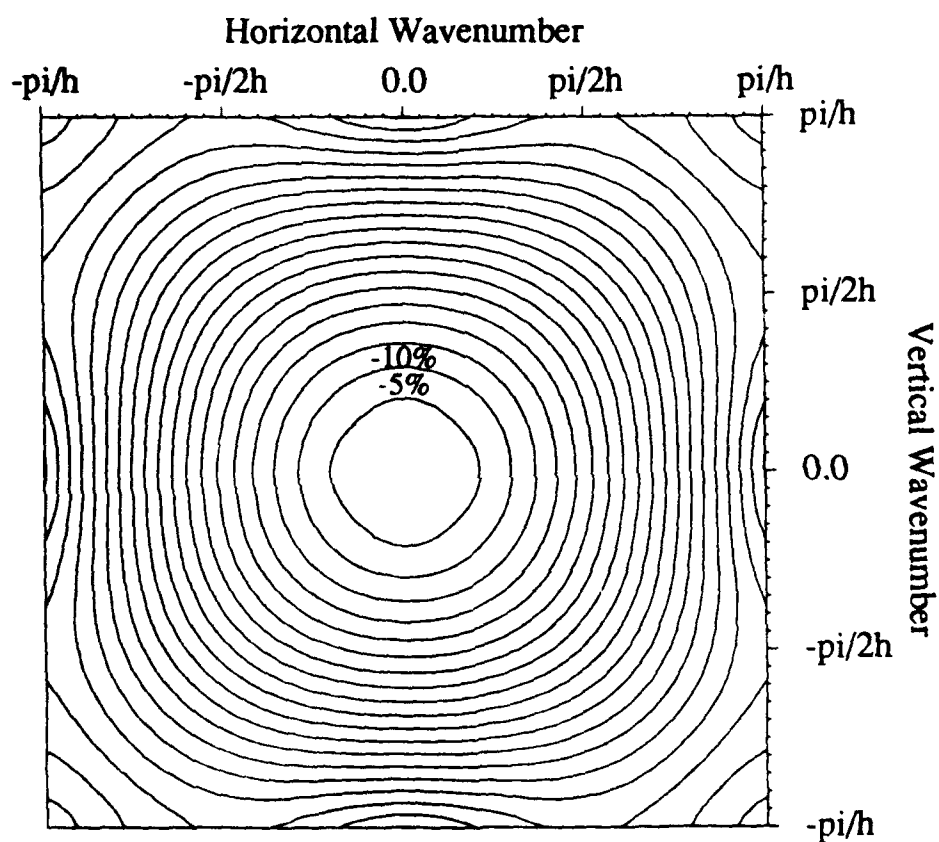


Figure B-5: The errors in group velocity are frequency and azimuthally dependent. In general, errors are largest for P-waves traveling along the axes of the grid and smallest for those traveling at 45° .

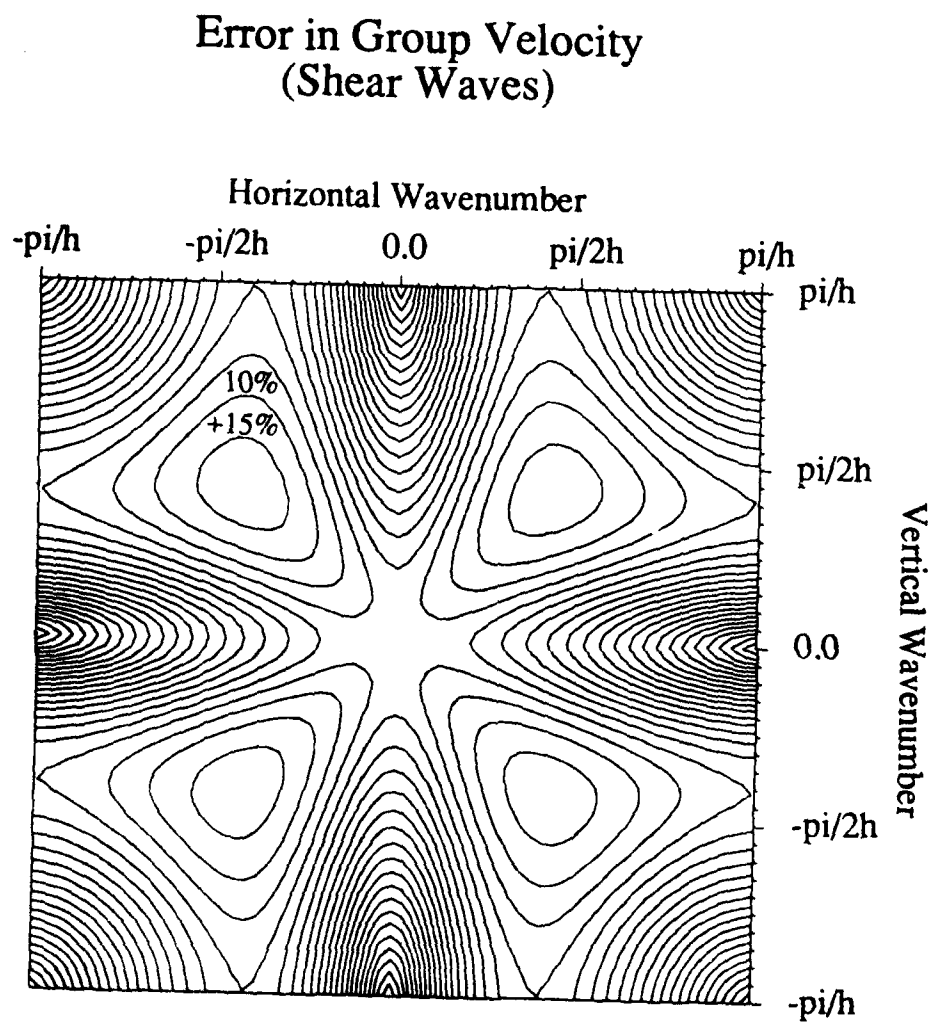


Figure B-6: Same as Figure B-5, but for shear waves. Notice that largest errors in shear wave group velocity occurs at 45°.

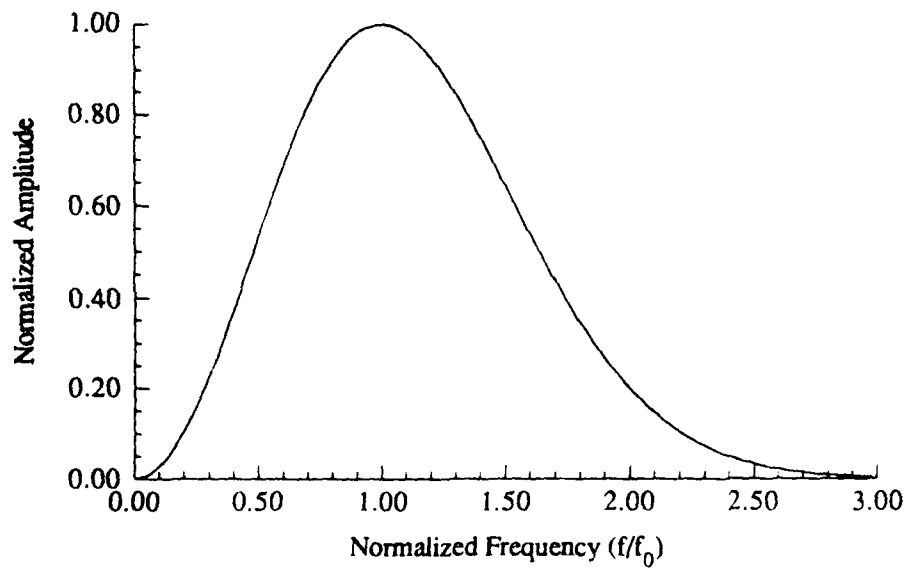
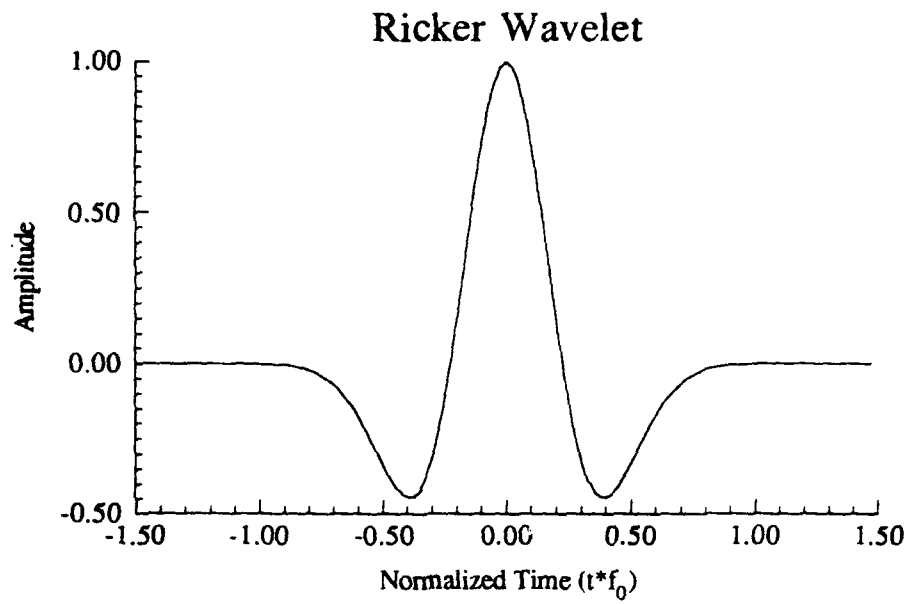


Figure B-7: The Ricker wavelet in time and frequency domains.

(Clayton and Engquist, 1977). To mimic a free surface, we make use of a row of pseudo-nodes above the grid and solve the zero stress equations,

$$0 = \partial_z u + \partial_x w \quad (\text{B.14})$$

$$0 = \lambda \partial_x u + (\lambda + 2\mu) \partial_z w, \quad (\text{B.15})$$

at the free surface (Munasinghe and Farnell, 1973).

B.3 A Point Diffractor

To investigate the accuracy of the finite difference technique a series of simulations were made to study the scattering from a point diffractor. Sharp contrasts are known to lead to inaccuracies in most finite difference algorithms. These errors are due to spatial aliasing of the high wavenumbers, which are folded into the low wavenumber components (Witte, 1989). A point diffractor on a discrete grid is an extreme example of this phenomenon, since in the Fourier domain the spectrum of the medium is constant out to the spatial Nyquist frequency.

In all three simulations a plane P-wave was incident on a point diffractor which had no perturbation in λ or ρ , but a 33% perturbation in μ . The source-time function of the P-wave was a Ricker wavelet (Figure B-7) which was sampled at 25, 50 or 100 points per wavelength (PPW) at the center frequency. Figures B-8 and B-9 show the radiation patterns for P-P and P-S scattering. At coarse sampling rates, the solutions differ considerably from the analytical solutions. Note the large errors at 45° in the S-wave solution. These secondary lobes occur because the higher frequencies in the S-wave were under-sampled. For these frequencies, the group velocity vector is biased away from the axes of the grid. As the sampling rate is increased, the solution is seen to converge towards the analytic solution.

Scattered P-wave (Finite Difference Method)

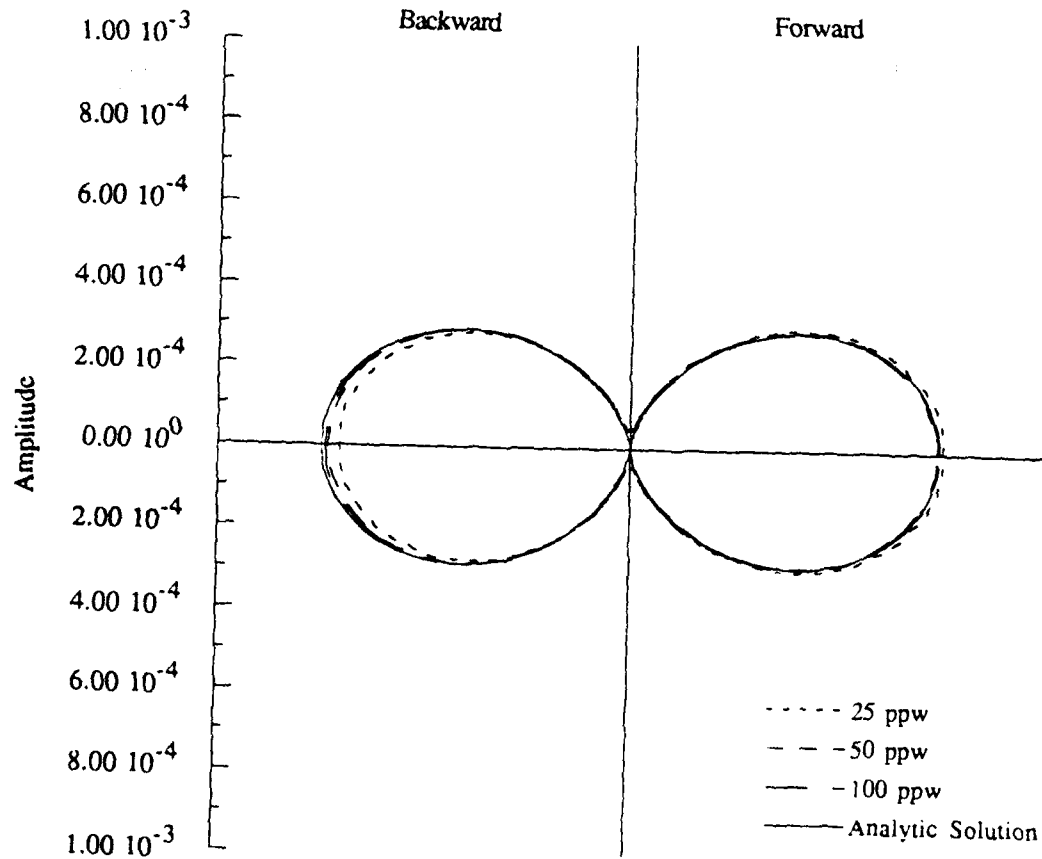


Figure B-8: Comparison of the finite difference solutions at 3 different grid spacings, 25 PPW, 50 PPW, and 100 PPW. Shown is the scattered field resulting from a plane P-wave incident on a point diffractor (33% variation in μ). The scattered field was generated by subtracting the incident field from the total scattered field.

Scattered S-wave (Finite Difference Method)

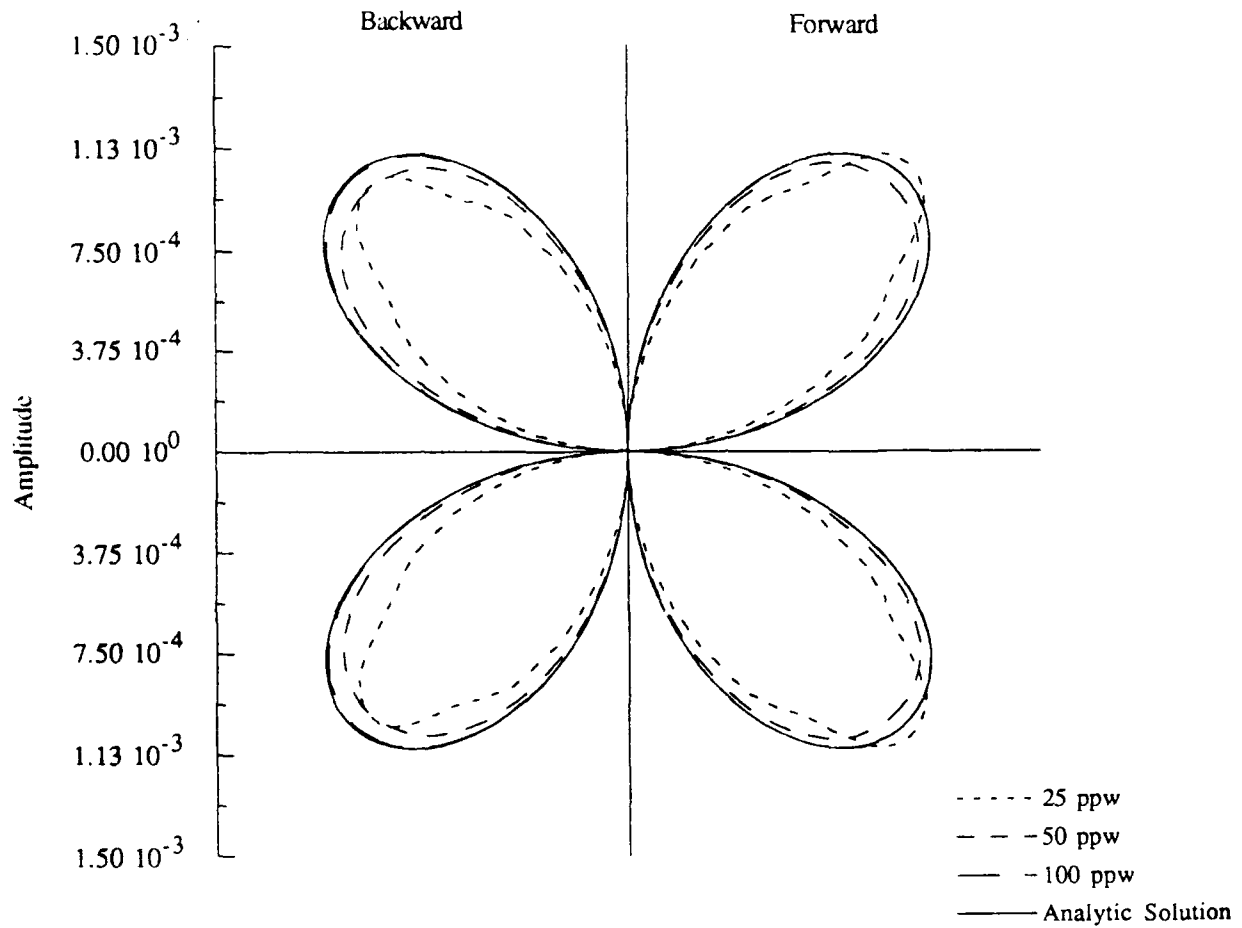


Figure B-9: The scattered S-wave for a plane P-wave incident on a point diffractor (33% variation in μ). The scattered field was generated by subtracting the incident field from the total scattered field.

EFFECTS OF AN EXPLOSIVE SOURCE IN AN ANISOTROPIC MEDIUM

Batakrishna Mandal and M. Nafi Toksoz

Earth Resources Laboratory, Department of Earth, Atmospheric, and Planetary Sciences, Massachusetts Institute of Technology,
Cambridge, Massachusetts 02139

Abstract. Numerical experiments have been conducted to study the effects of anisotropy for a seismic source in an anisotropic medium. An algorithm has been developed to compute complete seismic waveforms in general anisotropic media [Mandal and Toksoz, 1990]. Using this tool, we have shown that placing the source in an anisotropic medium affects the seismic waveforms significantly. An explosive source in an anisotropic medium produces an azimuthally dependent radiation pattern, for P, SV, and Rayleigh waves, and also generates SH waves. In some cases of anisotropy, the radiation pattern may be similar to those of earthquakes.

Introduction

The azimuthal dependence of radiation patterns of P, SV, and Rayleigh waves and the generation of SH and Love waves by underground nuclear explosions have been studied extensively [e.g., Kisslinger et al., 1961; Press and Archambeau, 1962; Toksoz et al., 1964; Archambeau and Sammis, 1970; Toksoz and Kehler, 1972; Massé, 1981; Wallace et al., 1983; Gupta and Blandford, 1983; Lynnes and Lay, 1988; Johnson, 1988; Priestley et al., 1990]. Various mechanisms, including tectonic strain energy release by relaxation of the medium around the exploration-generated cavity, triggering of an earthquake, dislocation across cracks, spallation and "slapdown," and scattering from heterogeneities, have been proposed and found to explain some of the data. No single mechanism has been identified that could satisfactorily explain all of the data [Massé, 1981; Gupta and Blandford, 1983; Johnson, 1988].

The complexity of the explosion-source phenomenon in heterogeneous and pre-stressed media was reviewed at the March, 1989, Lake Tahoe Symposium [Patton and Taylor, 1989]. There is some consensus that at long periods the non-uniform radiation pattern of Rayleigh waves and the generation of Love waves for explosions, such as Boxcar, Benham, Greeley, etc., are due to tectonic strain release, and can be modeled as a combination of an explosion plus a double-couple source that may be due to fault slip [Toksoz and Kehler, 1972; Wallace et al., 1983, 1985; Massé, 1981; Burger et al., 1986; Johnson, 1988]. At short periods there is azimuthal dependence of body wave amplitudes of explosions, such as Greeley, that may fit the tectonic strain release pattern [Lay et al., 1984]. The structure under the NTS is complex and scattering due to heterogeneities near the source that can produce an azimuthal variation of amplitudes [Lynnes and Lay, 1988; Taylor, 1983]. Although the scattering by heterogeneities near the source can complicate the radiation pattern, the transverse (SH) waves produced are generally much smaller than the radial component [McLaughlin et al., 1987; McLaughlin and Jih,

1988; Charrette and Toksoz, 1989]. Furthermore, since cavity collapses that accompany some explosions do not produce Love waves, while explosions do, SH waves cannot be attributed to scattering alone. The tectonic strain release by explosions seems to be controlled by the local state of stress. The strain energy released due to an explosion-created cavity [Press and Archambeau, 1962] contribute to the radiation of SH waves but it is not clear if this mechanism alone can account for all the long-period Love waves.

An important mechanism that can be responsible for non-uniform radiation patterns of P, SV, and Rayleigh waves, and the generation of SH waves from explosions is seismic anisotropy of the medium in which the explosion takes place. Recent observational studies show that most crustal rocks have some degree of seismic anisotropy due to randomly distributed aligned fractures [e.g., Stephen, 1981, 1985; Crampin, 1984; Lo et al., 1986; Thomsen, 1986; Winterstein, 1986; Martin, 1990]. Several major factors contribute to seismic anisotropy: (1) preferred orientation of the minerals due to deposition or metamorphism; (2) geometric effects, such as alternating high-and low-velocity thin beds (e.g., shales, carbonates); and (3) tectonic stress-induced preferred orientation of micro- and macro-fractures in shallow crust. For example, the Topopah Spring Member Tuff from Nevada has a velocity anisotropy of 8% and differences in linear compressibilities in two directions of 18% [Martin, 1990]. In the presence of local or regional tectonic stress, most hard rocks will have significant anisotropy. An explosion detonated in an anisotropic medium will have a non-isotropic radiation pattern due to the directional dependence of the compliance of the material around it.

The complexity of seismic radiation patterns and the generation of transversely polarized waves from explosions were investigated for transversely isotropic media with vertical axis of symmetry by Mandal and Mitchell [1986] and by Ben-Menahem and Sena [1990], and for general anisotropic media by Mandal and Toksoz [1989, 1990]. Mandal and Toksoz [1990] calculated synthetic seismograms for sources embedded in the anisotropic medium. The radiation patterns are different from those of isotropic space. An explosion source in an anisotropic full space can generate a significant amount of shear wave energy where none would be generated in an isotropic medium [Mandal and Toksoz, 1989; Ben-Menahem and Sena, 1990; Mandal and Toksoz, 1990]. These studies also show that the radiation pattern of P waves from an explosion in an azimuthally isotropic medium is not spherical. Mandal and Toksoz [1990] showed that the radiation patterns vary azimuthally and a significant transverse component is generated when an explosive source is in an azimuthal anisotropic medium.

Interest in seismic anisotropy increased rapidly among both solid-earth and exploration seismologists in the past decade. We suggest to new readers two articles by Crampin [1989] and Winterstein [1990] of various anisotropic terminology. These articles will help to understand general idea of wave propagation in anisotropic media.

Explosion Source Phenomenology
Geophysical Monograph 65
Copyright 1991 American Geophysical Union

Computation of Complete Waveforms in Anisotropic Media

The theoretical developments of wave motion in anisotropic media for the last 10 years were reviewed by Crampin [1977, 1981] and Pao [1983]. The following articles describe the computation of synthetic waveforms in layered anisotropic media: (1) for surface waves [Crampin, 1970]; (2) body waves [Keith and Crampin, 1977a,b,c]; (3) point source solutions for wave propagation only in the sagittal plane [Booth and Crampin, 1983a,b]; (4) scheme of synthetic waveforms in layered anisotropic media [Fryer and Frazer, 1984]; (5) complete waveforms in transversely isotropic layered media with vertical axis of symmetry [Mandal and Mitchell, 1986], and (6) complete synthetic seismograms for general anisotropic media where the source can also be placed inside the anisotropic medium [Mandal and Toksoz, 1990].

In general, wave propagation in anisotropic media is a three-dimensional problem. For an isotropic or transversely isotropic medium with a vertical axis of symmetry, the energy propagating from the source to receiver is restricted to the sagittal plane (propagation plane). In these cases, the computation is straightforward and the mathematics of wave motion have been established for the last few decades. However, in azimuthal anisotropic media, the energy generally propagates out of the sagittal plane, causing the transverse component of the wavenumber vector to be non-zero [e.g., Auld, 1973]. This phenomenon complicates the computational problem of wave propagation in anisotropic media.

The details of the numerical procedure of computing complete synthetic seismograms is described in detail in our earlier paper [Mandal and Toksoz, 1990]. Our algorithm for computing complete synthetic seismograms has been implemented for general anisotropic layered media using extended reflectivity theory [Kennett, 1983] and numerical wavenumber integration [Bouchon and Aki, 1977]. The displacement stress vectors are calculated for different wave numbers and frequencies. The final solutions in the time domain are computed by double integrations in the wavenumber and frequency domains. These integrations may be carried out by: (1) contour integration in the complex plane; (2) Fourier transform; and (3) numerical wavenumber summation. The numerical wavenumber summation is a common method for computing complete waveforms where all possible waves (e.g., body waves, surface waves, interface waves, multiples, etc.) are included in the computations. In summary, our computational algorithm is divided into three steps. First, the steady-state wave field radiation produced by a seismic source is represented as a superposition of waves propagating with discrete phase velocities. In this way a single source is replaced by a periodic array of sources. The effect of secondary sources is removed by introducing both a small constant imaginary part of the frequency and proper wavenumber step size. Second, each phase velocity component of the wavefield is propagated through a stack of layers using the reflection and transmission properties of individual interfaces by a recursion scheme with scatterer operators and scatterer products [e.g., Saastamoinen, 1980; Kennett, 1983; Fryer and Frazer, 1984]. The resulting contributions are summed for each wavenumber to transform them from the wavenumber domain to the space domain. Third, the solution is Fourier-transformed to the time domain, and the unwanted effects of source periodicity and the imaginary part of frequency are removed. This final solution yields the complete wavefield within the medium for the particular source considered. This procedure is common for isotropic and anisotropic media except for the computation of the eigensolutions. In an isotropic medium or transversely isotropic medium with a vertical axis of symmetry, this computation of eigensolutions can be performed analytically [e.g., Mandal and Mitchell, 1986]. In a general anisotropic medium, the elastodynamic solutions are computed from a Christoffel equation of a six-order polynomial form [Fedorov, 1968; Musgrave, 1970; Auld, 1973; Fryer and Frazer, 1987]. This procedure needs a high degree of numerical precision. To avoid these problems Mandal and Toksoz [1990] derived the system matrix \mathbf{A} (function of medium parameters and phase slownesses) of the

differential system of a displacement-stress vector in a special form. They calculated the elastodynamic solutions by computing the eigenvalues and eigenvectors of the system matrix \mathbf{A} using the QR algorithm [Golub and Van Loan, 1983]. This method is very stable. The eigenvalues and eigenvectors are computed simultaneously. These eigensolutions are used to propagate a wavefield from source to receiver by a recursion scheme with scatterer operators and scatterer products.

The problem of wave propagation in general anisotropic media is conveniently addressed in Cartesian coordinates. This coordinate system is useful to introduce a point source in an anisotropic medium as discussed by Fryer and Frazer [1984]. For each wavenumber and frequency, an equivalent wave vector discontinuity can be established through a displacement-stress discontinuity at the source depth. The displacement-stress discontinuity is represented by a point force and a moment tensor with a body force equivalent, given by Burridge and Knopoff [1964]. In this way a point force can be introduced within a stratified anisotropic medium for each wavenumber and frequency. The point force response of a source is evaluated when all possible wavenumbers and frequencies are included in the computations. An asymptotic analytic solution of a point source in a transversely isotropic medium with a vertical axis of symmetry has recently been established [Ben-Menahem and Sena, 1990]. However, this method has not been extended to general anisotropy. For a general anisotropic medium, a point source analytical solution has not yet been developed for possible computer implementation.

Synthetic Waveforms Due to an Explosive Source in an Anisotropic Medium

This shows theoretical examples of synthetic seismograms due to an explosion source in an anisotropic medium. In this paper we show examples only for explosive sources. Three anisotropic models are used for the theoretical examples. The first two examples demonstrate the source radiation pattern in an infinite anisotropic medium. The third example is a layered anisotropic medium where the effect of anisotropy can be investigated both on body waves as well as on guided waves such as Lg. We have chosen anisotropic media having hexagonal symmetry with two symmetry axes. One axis is vertical known as *azimuthal isotropy* or *transverse isotropy* with vertical axis of symmetry. In this case, the medium is an anisotropic medium where no variation of properties with azimuth in the horizontal plane. This type of anisotropy

Azimuthal isotropic medium

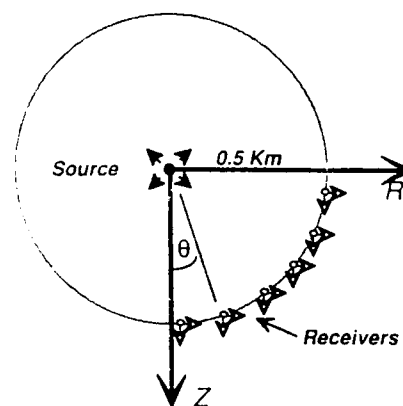


Fig. 1. Source and receiver geometry in a transversely isotropic medium. The Z axis is the symmetry axis.

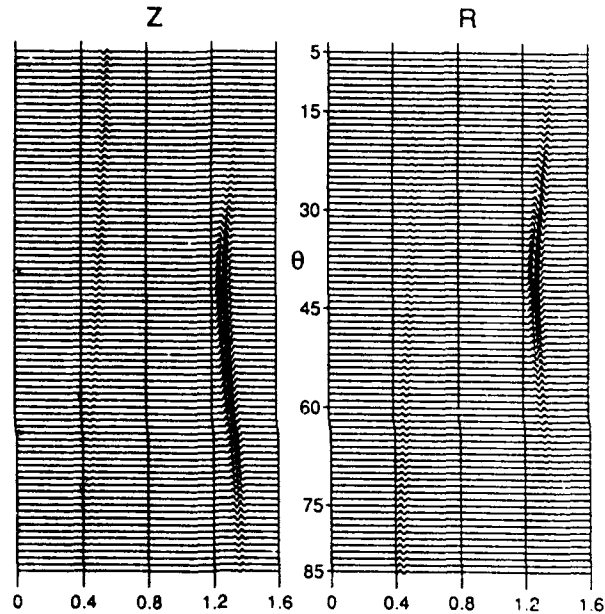


Fig. 2 Synthetic seismograms at the receivers on an arc of radius 0.5 km from an explosion source (Figure 1). The 0-50 Hz responses are convolved with a Ricker wavelet of 20 Hz center frequency.

could be found due to presence of fine or periodic thin layers in the crust, specially in sedimentary basins [e.g., Postma, 1955], and in the upper mantle [e.g., Anderson and Regan, 1983]. The other axis is horizontal which displays (azimuthal anisotropy). This type of anisotropy could be present in the crust where fluid-filled cracks, microcracks, or pore spaces are expected to align vertically perpendicular to the minimum horizontal stress [e.g., Crampin, 1984].

1. Azimuthal Isotropy

For the azimuthal isotropic model, we use medium parameters measured in the field at relatively shallow depths in the Eocene Wills Point formation at Sulphur Springs, Texas [Robertson and Corrigan, 1983]. The medium is a soft shale containing minor amounts of silt and sand. Robertson and Corrigan calculated the five elastic constants. The density normalized elastic constants are:

$C_{ij}/\rho \text{ (km}^2\text{s}^{-2}\text{)} =$					
1.96	1.50	1.13	0	0	0
	1.96	1.13	0	0	0
		1.12	0	0	0
			0.15	0	0
				0.15	0
					0.23

To study the radiation pattern from an explosion source in this medium, we computed synthetic seismograms for receivers distributed on a vertical plane at a radial distance of 0.5 km. The source-receiver in the vertical plane is shown in Figure 1. The frequency responses are calculated from 0-50 Hz. To calculate the synthetic seismograms a source wavelet with a center frequency of 20 Hz is convolved with the medium response. The vertical and radial components of the seismograms are shown in Figure 2

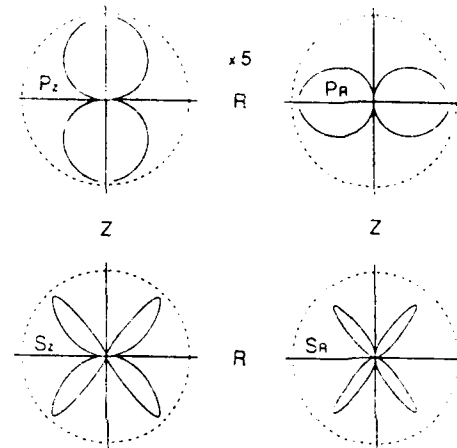


Fig. 3. Amplitude radiation patterns of P- and S-waves in vertical plane. Subscripts Z and R stand for vertical and radial components, respectively. Dashed circles are for reference. In an isotropic medium, the P-wave radiation pattern would be circular and there would be no S-waves. Note that P-wave amplitudes are magnified by a factor of five in the plot.

for the range from 5° to 85° in one quadrant. Because of symmetry, the responses in the other quadrants are the same. The arrival times for both P and S waves vary as a function of angle θ , as do the amplitudes. The P- and S-wave amplitude radiation patterns for both vertical and radial components are shown in Figure 3. They are measured from peak amplitudes in P- (2-0.7 S) and S-wave windows (1-1.6 S) of the seismograms shown in Figure 2. The P-wave radiation patterns do not differ significantly from the isotropic case. The S-wave radiation patterns are similar to those of a double-couple source. (Note that if the medium were isotropic there would be no S waves at all.) Ben-Menahem and Sena [1990] found similar results with their asymptotic analytical solutions for a source in an azimuthally isotropic medium.

Azimuthal anisotropic medium

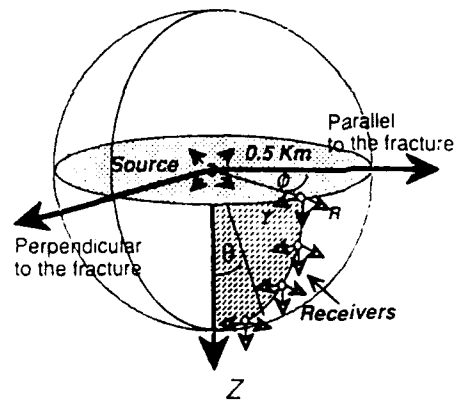


Fig. 4. Source and receivers arrangement for azimuthal anisotropic medium. This case represents a horizontal maximum principal stress with microcracks aligned vertically and parallel to this stress axis.

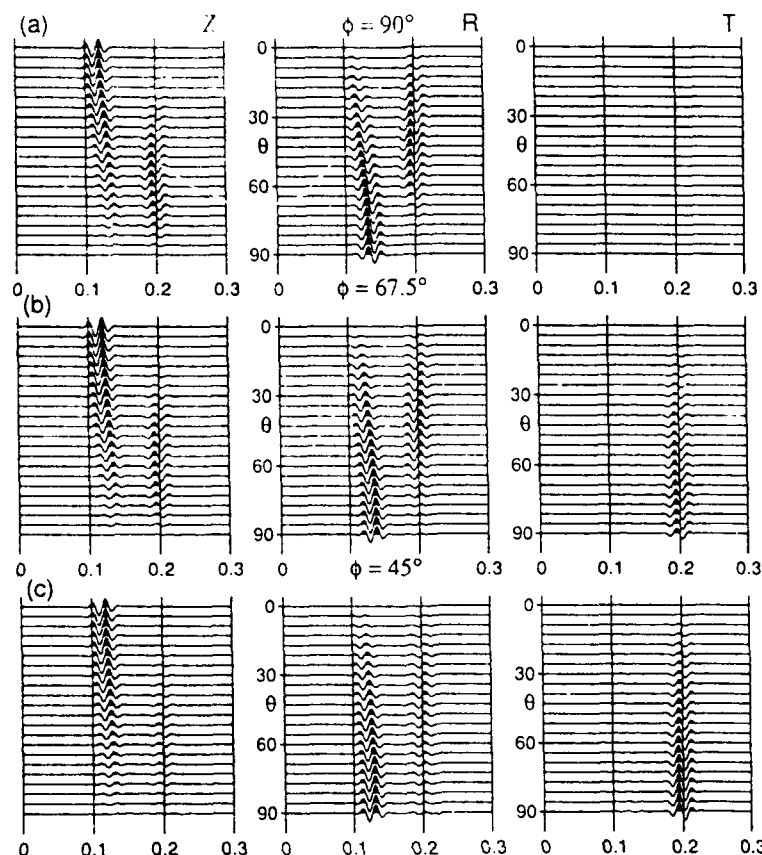


Fig. 5. Three-component synthetic seismograms at three different vertical planes: (a) $\phi = 90^\circ$, (b) $\phi = 67.5^\circ$, and (c) $\phi = 45^\circ$ from the crack plane (Figure 4). The source center frequency is 50 Hz, chosen to clearly separate the phases at the short (0.5 km) source-receiver distance.

II. Azimuthal Anisotropy

In this case, we focus on the problem of an anisotropic medium with a horizontal symmetry axis. Such a medium might be appropriate for models where there are tectonic stresses in the medium and the maximum stress is horizontal. This type of anisotropy can be explained by five elastic constants at its symmetry axis direction. The anisotropic constants are derived from the theory developed by Hudson [1980,1981] using a "cracked solid" approximation. It is assumed that anisotropy is due to vertical cracks and microcracks oriented preferentially by the horizontal principal stress. This approach provides a convenient way to calculate the elastic constants. The actual mechanism producing the anisotropy could be vertical dikes or any other geologic process. We assume the host rock matrix is isotropic with parameters $V_p = 6.132$ km/s, $V_s = 3.266$ km/s, and $\rho = 2.7$ gm/cc. To introduce anisotropy we assume the crack density and aspect ratio to be 0.1 and 0.001, respectively. The density normalized elastic constants are:

$$C_{ij}/\rho \text{ (km}^2\text{s}^{-2}\text{)} = \begin{matrix} & 22.1 & 9.56 & 9.56 & 0 & 0 & 0 \\ & 34.7 & 13.37 & 0 & 0 & 0 & 0 \\ & & 34.7 & 0 & 0 & 0 & 0 \\ & & & 10.66 & 0 & 0 & 0 \\ & & & & 8.57 & 0 & 8.57 \end{matrix}$$

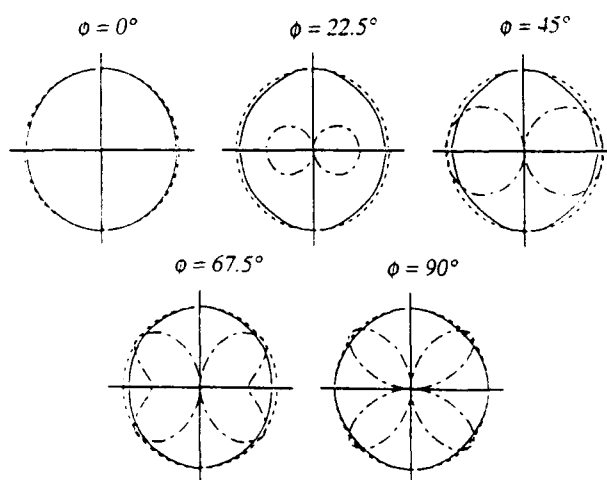


Fig. 6. Amplitude radiation patterns at five different azimuthal vertical planes (Figure 4). Solid lines are the P-wave radiation patterns. Long dash lines represent the S-wave radiation patterns. Small dash lines represent the reference circle.

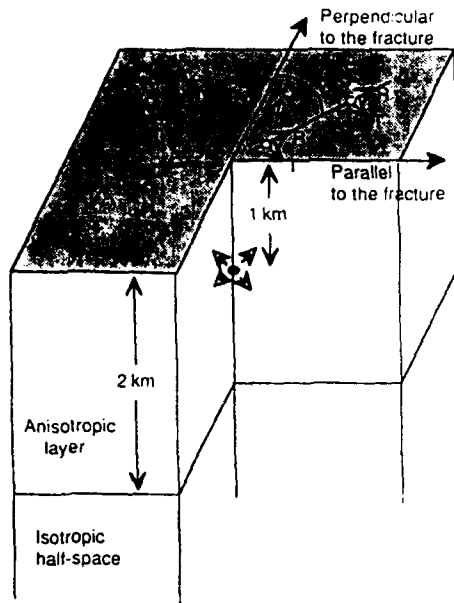


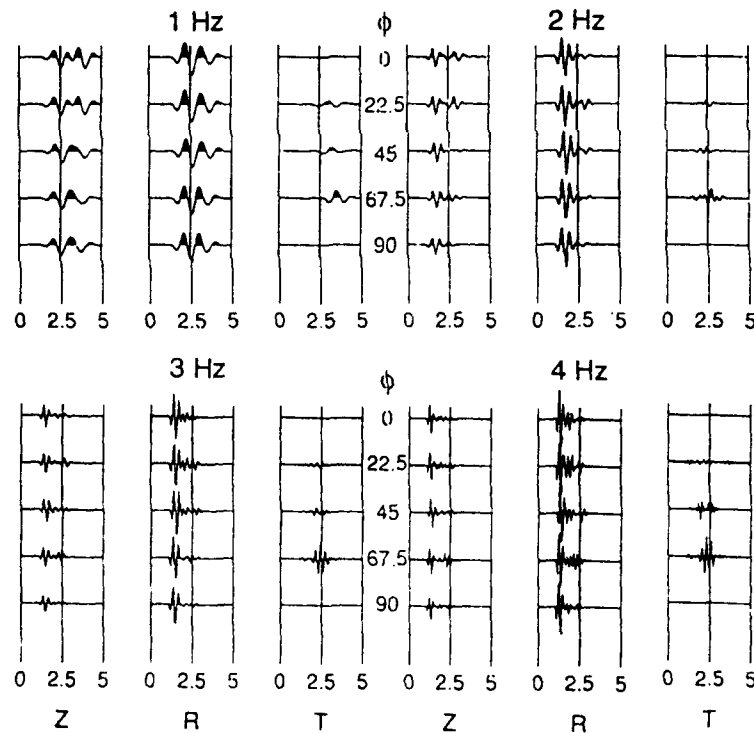
Fig. 7. Schematic diagram of an anisotropic layer over an isotropic half-space.

The source and receiver geometry used in this case to study the radiation pattern are shown in Figure 4. We calculate synthetic seismograms at five different vertical planes, $\phi = 0, 22.5^\circ, 45^\circ, 67.5^\circ$ and 90° . There are 22 receivers placed at equal angular spacing in each quadrant of each azimuthal vertical plane. The receivers are placed on an arc of radius 0.5 km. The impulse response is calculated for 0–140 Hz frequency range, and these are convolved with a Ricker wavelet-type source time function with 50 Hz center frequency. Three-component seismograms are shown in Figures 5a–c for three different azimuthal planes. The azimuth $\phi = 90^\circ$ represents the plane of propagation perpendicular to the crack orientation. In this plane (Figure 5a), the transverse component is zero. The vertical and radial components show shear wave arrivals which would not be present in an isotropic medium. Travel times depend on the direction for both P and S waves. For the plane $\phi = 67.5^\circ$ (Figure 5b), there are significant transverse components for S waves. These are due to the anisotropy of the medium. Similar results are also observed at the plane $\phi = 45^\circ$ (Figure 5c).

Figure 6 shows the radiation patterns of rms amplitude of P- and S-

waves $A = \sqrt{A_Z^2 + A_R^2 + A_T^2}$, where A is the total rms amplitude

and suffixes Z,R,T are z-, r-, t- component responses at five different azimuthal vertical planes. The P- and S-wave amplitudes have been measured in different azimuthal planes from the time domain responses of the complete waveforms (Figure 5). The time windows for P- and S-waves are (.08–.16 S) and (.16–.28 S) respectively. Diagnostic features



Dist = 5 Km, Layer over Half-space, 20% crack density

Fig. 8. Three-component synthetic seismograms for the layers over half-space model of Figure 7 at 5 km epicentral distance, for five azimuths and at frequencies of 1, 2, 3, and 4 Hz. Note the presence of significant transverse shear waves at $\phi = 67.5^\circ$ azimuth.

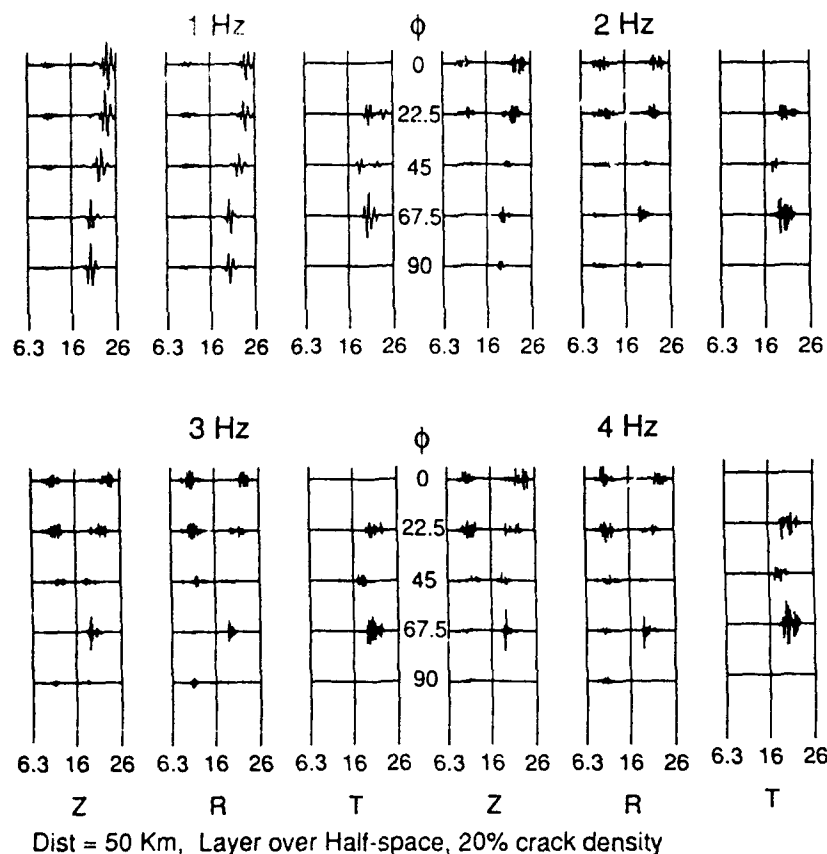


Fig. 9. Three-component synthetic seismograms for the layer over half-space model of Figure 7 at 50 km epicentral distance, for five azimuths and at frequencies of 1, 2, 3, and 4 Hz. The transverse (SH) component of Lg waves are especially dominant at $\phi = 57.5^\circ$ and $\phi = 22.5^\circ$ azimuths.

are as follows:

- (1) At the crack plane ($\phi = 0^\circ$) there are no shear waves, i.e., behavior is the same as the isotropic medium.
- (2) The radiation patterns of P-waves do not differ significantly between the planes.
- (3) The shear wave radiation pattern changes with the plane of propagation.
- (4) The shear wave radiation pattern changes from none (at $\phi = 0^\circ$) to monopole ($\phi = 22.5^\circ$), to intermediate ($\phi = 67.5^\circ$), to dipole ($\phi = 90^\circ$) type of source.

These features of source radiation patterns in anisotropic media, combined with the anisotropic interface effects (free surface, isotropy-anisotropy, and anisotropy-anisotropy) and propagation effects in anisotropic media, will complicate the total responses at the receivers. Some of these features are discussed in Mandal and Toksoz [1989,1990] and Mandal [1991].

III. Anisotropic Layer Over an Isotropic Half-Space

To understand the effects of anisotropy (source radiation and propagation including interface effects) on seismic waves from an explosive source, we present an example of theoretical seismograms from an explosive source in a layered, azimuthally anisotropic medium. The

model consists of a 2-km-thick azimuthally anisotropic layer over an isotropic half-space. Such a model may represent an anisotropic tuff over an isotropic basement, or a shallow layer with open microfractures oriented preferentially due to tectonic stresses. At greater depths the microfractures close due to overburden pressures and the medium becomes isotropic. The source is an explosion at 1 km depth in the anisotropic layer of 2 km thickness, as shown in Figure 7. The anisotropic layer parameters are calculated using a model of aligned, vertical, fluid-filled fractures (aspect ratio of 0.001 and fracture density 20 per cent). The density normalized elastic constants of the top layer are:

$C_{ij}/\rho \text{ (km}^2\text{s}^{-2}\text{)} =$					
28.7	11.6	11.6	0	0	0
	30.0	12.0	0	0	0
		30.0	0	0	0
			9.0	0	0
				5.86	0
					5.86

The isotropic half-space has P- and S-wave velocities of 6.2 km/s and 3.5 km/s respectively, and the density of 2.8 gm/cc.

In the geometry considered the fracture planes are parallel to the east-west direction as shown in Figure 7, and the north-south is normal to the

fracture planes. We calculate seismograms for five different azimuths ($N0^\circ$, $N22.5^\circ E$, $N45^\circ E$, $N67.5^\circ E$ and $N90^\circ E$) with stations at two distances, 5 and 50 km from the epicenter. After the responses are calculated by wavenumber and frequency integration in the 0–10 Hz frequency band, the synthetic seismograms are generated by convolving these with a Ricker wavelet-type pulse centered at 1 Hz, 2 Hz, 3 Hz, and 4 Hz.

The seismograms are shown in Figures 8 and 9 at distances 5 km and 50 km, respectively. The transverse motion due to anisotropy is prominently illustrated in both figures. At 50 km distance, the seismograms are more complex due to the presence of multiple reflections and Lg modes. The complexity of waveforms due to anisotropy stands out at the higher frequencies. Multiple arrivals of quasi-shear waves are observed because of shear wave splitting and the presence of a cusp (e.g., Shearer and Chapman, 1989) of the slowness surface in the anisotropic medium. However, the generation of transverse components, and non-uniform radiation patterns of P, quasi-shear and Lg waves observed on vertical and radial components, are primarily due to anisotropy at the source. An explosion in an anisotropic medium has a non-uniform radiation pattern and generates significant transverse motion at certain azimuths because: (1) a spherical explosion in an anisotropic medium becomes non-spherical due to the directional dependence of elastic compliance; and (2) the reflection (especially at the free surface) and conversion of seismic waves propagating in an anisotropic medium further complicates the seismograms and their frequency dependence. These examples show that anisotropy may be a significant factor in contributing to the azimuthal variations of amplitudes of P, qS, Lg, and Rg waves and the generation of transverse waves by explosions.

Conclusions

In this study we have shown the effects of medium anisotropy on the generation and the radiation patterns of seismic waves from an explosion source using synthetic seismogram calculations. We used three models, starting from a simple homogeneous, but anisotropic full-space, to a more representative layered model to demonstrate the effect of anisotropy. The source radiation pattern in an anisotropic medium is different than the source in an isotropic medium. A spherical explosion in an anisotropic medium has a non-spherical radiation pattern due to the directional dependence of elastic compliance. Also, anisotropy may be a significant factor contributing to the generation of transverse waves by explosions.

Our examples demonstrate that anisotropy contributes to non-uniform radiation patterns and to the generation of SH waves by the explosions. Before we can determine whether anisotropy is a major cause of complexities of a radiation pattern, more work needs to be done. If the medium is tectonically stressed, it would be anisotropic. In such a case both source radiation patterns in an anisotropic medium as well as tectonic strain release would contribute to the complexity of the radiation patterns. To evaluate the relative contribution of these two effects, we need to look at all waves, at all frequencies. For example, anisotropy produces a transverse component for P-waves as well as characteristic radiation patterns. Conventional tectonic strain release, on the other hand, does not produce transverse P-waves.

Another important question is the effect of heterogeneities near the source. Large heterogeneities could produce cos 2θ -type amplitude variation of primary phases (Lynnes and Lay, 1988), as does anisotropy. The transverse components of phases and radiation patterns in an anisotropic medium are, however, different from those produced by heterogeneity. These differences also depend on frequency.

To separate the relative importance of different mechanisms contributing to non-uniform radiation patterns by explosions, additional theoretical/numerical modeling and more detailed analysis of actual data are required.

Acknowledgments Partial support was provided by the Defense Advanced Research Projects Agency through contract F19628-89-K-0020 administered by the Air Force Geophysics Laboratory.

References

- Anderson, D. L., and J. Regan, Upper mantle anisotropy and the oceanic lithosphere, *Geophys. Res. Lett.*, 10, 841–844, 1983.
- Archambeau, C. G., and C. Sammis, Seismic radiation from explosions in prestressed media and the measurement of tectonic stress in the Earth, *Rev. Geophys.*, 6, 241–288, 1970.
- Auld, B. A., *Acoustic Fields and Wave in Solids*, Vol. 1, Wiley, New York, 1973.
- Ben-Menahem, A., and A. G. Sena, Seismic Source Theory in Stratified Anisotropic Media, *J. Geophys. Res.*, 95, 15,395–15,427, 1990.
- Booth, D. C., and S. Crampin, The anisotropic reflectivity technique: theory, *Geophys. J. R. astr. Soc.*, 72, 755–766, 1983a.
- Booth, D. C., and S. Crampin, The anisotropic reflectivity technique: anomalous reflected arrivals from an anisotropic upper mantle, *Geophys. J. R. astr. Soc.*, 72, 767–782, 1983b.
- Bouchon, M., and K. Aki, Discrete wavenumber representation of seismic source wave fields, *Bull. Seism. Soc. Am.*, 67, 259–277, 1977.
- Burger, R., T. Lay, T. Wallace, and L. Burdick, Evidence of tectonic release in long-period S-waves from underground explosions at Novaya Zemlya Test Sites, *Bull. Seism. Soc. Am.*, 76, 733–755, 1986.
- Burridge, R. and L. Knopoff, Body force equivalents for seismic dislocations, *Bull. Seism. Soc. Am.*, 54, 1875–1888, 1964.
- Charrette, E. E., and M. N. Toksoz, Effects of stochastic heterogeneities on cross-well imaging, *Expanded Abstracts of the 1989 SEG Meeting*, 898–900, 1989.
- Crampin, S., The dispersion of surface waves in multilayered anisotropic media, *Geophys. J. R. astr. Soc.*, 21, 387–402, 1970.
- Crampin, S., A review of the effects of anisotropic layering on the propagation of surface waves, *Geophys. J. R. astr. Soc.*, 49, 9–27, 1977.
- Crampin, S., A review of wave motion in anisotropic and cracked elastic-media, *Wave Motion*, 3, 343–391, 1981.
- Crampin, S., Effective elastic constants for wave propagation through cracked solids, *Geophys. J. R. astr. Soc.*, 78, 691–710, 1984.
- Crampin, S., Suggestions for a consistent notation for seismic anisotropy, *Geophys. Prosp.*, 37, 753–770, 1989.
- Fedorov, F. I., *Theory of Elastic Waves in Crystals*, Plenum Press, New York, 1968.
- Fryer, L. N., and L. N. Frazer, Seismic waves in stratified anisotropic media, *Geophys. J. R. astr. Soc.*, 78, 691–710, 1984.
- Fryer, L. N., and L. N. Frazer, Seismic waves in stratified anisotropic media—II: Elastodynamic eigensolutions for some anisotropic systems, *Geophys. J. R. astr. Soc.*, 81, 73–101, 1987.
- Golub, G. H., and C. F. Van Loan, *Matrix Computations*, The John Hopkins University Press, Baltimore, 1983.
- Gupta, I. N., and R. R. Blandford, A mechanism for generation of short-period transverse motion from explosions, *Bull. Seism. Soc. Am.*, 73, 571–591, 1983.
- Hudson, J. A., Overall properties of a cracked solid, *Math. Proc. Camb. phil. Soc.*, 88, 371–384, 1980.
- Hudson, J. A., Wave speeds and attenuation of elastic waves in material containing cracks, *Geophys. J. Roy. astr. Soc.*, 64, 133–150, 1981.
- Johnson, L. R., Source characteristics of two underground nuclear explosions, *Geophys. J.*, 95, 15–30, 1988.
- Keith, C. M. and S. Crampin, Seismic body waves in anisotropic media: reflection and refraction at a plane interface, *Geophys. J. R. astr. Soc.*, 49, 181–208, 1977a.
- Keith, C. M., and S. Crampin, Seismic body waves in anisotropic media

- propagation through layer, *Geophys. J. R. astr. Soc.*, 49, 239–243, 1977b.
- Keith, C. M. and S. Crampin, Seismic body waves in anisotropic media: synthetic seismogram, *Geophys. J. R. astr. Soc.*, 49, 225–243, 1977c.
- Kennett, B. L. N., *Seismic Wave Propagation in Stratified Media*, Cambridge University Press, 1983.
- Kisslinger, C., E. J. Mateker, Jr., and T. V. McEvilly, SH motion from explosions in soil, *J. Geophys. Res.*, 66, 3487–3496, 1961.
- Lay, T., T. Wallace, and D. Helmberger, The effects of tectonic release on short-period P waves from NTS explosion, *Bull. Seism. Soc. Am.*, 74, 819–847, 1984.
- Lo, T. W., K. B. Coyner and M. N. Toksoz, Experimental determination of elastic anisotropy of Berea sandstone, Chicopee shale and Chelmsford granite, *Geophysics*, 51, 164–171, 1986.
- Lynnes, C. S. and T. Lay, Analysis of amplitude and travel-time anomalies for short-period P-waves from NTS explosions, *Geophys. J.*, 92, 431–443, 1988.
- Mandal, B., Reflection and transmission properties of elastic waves on a plane interface for general anisotropic media, *J. Acoust. Soc. Am.*, 90, 1106–1118, 1991.
- Mandal, B., and B. Mitchell, Complete seismogram synthesis for transversely isotropic media, *J. Geophys.*, 59, 149–156, 1986.
- Mandal, B., and M. N. Toksoz, Radiation patterns from explosions in anisotropic media, *Proceedings of the DOE/LLNL Symposium on Explosion-Source Phenomenology*, 215–230, 1989.
- Mandal, B., and M. N. Toksoz, Computation of complete waveforms in general anisotropic media—Results from an explosion source in anisotropic medium, *Geophys. J. Int.*, 103, 33–45, 1990.
- Martin, R. M., Anisotropy of Topopah Spring Member Tuff, *NER Report*, 1990.
- Massé, B. P., Review of seismic source models for underground nuclear explosions, *Bull. Seism. Soc. Am.*, 71, 1249–1268, 1981.
- McLaughlin, K. L., L. M. Anderson, and A. C. Lees, Effect of local geologic structure on Yucca Flats, Nevada Test Site, explosion waveforms: two-dimensional linear finite-difference simulations, *Bull. Seism. Soc. Am.*, 77, 1211–1222, 1987.
- McLaughlin, K. L. and R. S. Jih, Scattering from near-source topography teleseismic observation and numerical simulations, *Bull. Seism. Soc. Am.*, 78, 1319–1414, 1988.
- Musgrave, M. J. P., *Crystal Acoustics*, Holden-Day, San Francisco, 1970.
- Pao, Y., Elastic waves in solids, *J. Appl. Mech.*, 50, 1152–1164, 1983.
- Patton, H. J., and S. R. Taylor (eds.), *Proceedings of the DOE/LLNL Symposium on Explosion-Source Phenomenology*, Lake Tahoe, CA, March 14–16, 1989, 251 p., 1989.
- Postma, G. W., Wave propagation in a stratified medium, *Geophysics*, 20, 780–806, 1955.
- Press, F., and C. Archambeau, Release of tectonic strain by underground nuclear explosions, *J. Geophys. Res.*, 68, 5777–5787, 1962.
- Priestley, K. F., W. R. Walter, V. Martynov, and M. V. Rozhkov, Regional seismic recordings of the Soviet nuclear explosion of the joint verification experiment, *Geophys. Res. Lett.*, 17, No. 2, 179–182, 1990.
- Robertson, J. D., and D. Corrigan, Radiation patterns of a shear-wave vibrator in near-surface shale, *Geophysics*, 48, 19–26, 1983.
- Saastamoinen, P. R., On propagators and scatterers in wave problems of layered elastic media: a spectral approach, *Bull. Seism. Soc. Am.*, 70, 571–590, 1980.
- Shearer, P. M., and C. H. Chapman, Ray tracing in azimuthally anisotropic media—I. Results for models of aligned cracks in the upper crust, *Geophys. J.*, 96, 51–64, 1989.
- Stephen, R. A., Seismic anisotropy observed in upper oceanic crust, *Geophys. Res. Lett.*, 8, 865–868, 1981.
- Stephen, R. A., Seismic anisotropy in the upper oceanic crust, *J. Geophys. Res.*, 90, 11383–11396, 1985.
- Taylor, S. R., Three-Dimensional Crust and Upper Mantle Structure at the Nevada Test Site, *J. Geophys. Res.*, 88, 2220–2232, 1983.
- Thomsen, L., Weak elastic anisotropy, *Geophysics*, 51, 1954–1966, 1986.
- Toksoz, M. N., A. Ben-Menahem, and D. G. Harkrider, Determination of source parameters of explosions and earthquakes by amplitude equalization of seismic surface waves, *J. Geophys. Res.*, 69, 4355–4366, 1964.
- Toksoz, M. N. and H. H. Kehr, Tectonic strain release by underground nuclear explosions and its effect on seismic discrimination, *Geophys. J. R. astr. Soc.*, 31, 141–161, 1972.
- Wallace, T. C., D. V. Helmberger, and G. R. Engen, Evidence of tectonic release from underground nuclear explosions in long-period P waves, *Bull. Seism. Soc. Am.*, 73, 593–613, 1983.
- Wallace, T. C., D. V. Helmberger, and G. R. Engen, Evidence of tectonic release from underground nuclear explosions in long-period S waves, *Bull. Seism. Soc. Am.*, 75, 157–174, 1985.
- Winterstein, D. F., Anisotropy effects in P-wave and SH-wave stacking velocities contain information on lithology, *Geophysics*, 51, 661–672, 1986.
- Winterstein, D. F., Velocity anisotropy terminology for geophysicists, *Geophysics*, 55, 1070–1088, 1990.

AN ANALYSIS OF THE NATURE AND ATTENUATION OF Lg WAVES

by

Ningya Cheng and M. Nafi Toksöz

Earth Resources Laboratory

Department of Earth, Atmospheric, and Planetary Sciences

Massachusetts Institute of Technology

Cambridge, MA 02139

ABSTRACT

On short-period seismograms of regional seismic events, Lg is the most dominant phase. Lg waves can be interpreted as a superposition of higher mode surface waves, or equivalently, as an interference of multiply reflected S waves in the crust. Lg waves are widely used to evaluate the mean value of attenuation (Q^{-1}) of S waves in the crust as a function of frequency. They are also used to determine earthquake magnitudes (m_{bLg}). Several observations indicate that lateral structure variations have major effects on Lg wave propagation and attenuation. The exact mechanisms responsible for this attenuation are not well understood and have not been modeled adequately.

In this paper we use the mode summation approach to model the Lg waves. Using the flat-layered model with frequency dependent Q , the synthetic seismogram of Lg and Rg are calculated. These are in good agreement with observed data recorded at Fenoscandian array FINESA. We found that, in these data, modes 1 to 14 make up most of the Lg waves.

For laterally heterogeneous crustal models, the coupled mode method is used to synthesize the vertical component of Lg waves. This is applied to propagation across a sedimentary basin in a flat-layered reference structure. There is substantial attenuation of the Lg phase across the basin. The attenuation of the Lg phase across the central graben of the North Sea is studied by modeling Lg propagation across the laterally varying structure. The Lg attenuation can be explained by the effects of sedimentary layer thickening and Moho surface uplift associated with the graben.

Key words: Lg waves, coupled mode method, mode summation, the North Sea.

Abbreviated title: Nature and attenuation of Lg waves.

INTRODUCTION

On the short-period seismograms of local and regional seismic events, the Lg phase usually has the largest amplitude. Press and Ewing (1952) first identified the Lg phase associated with continental structure. Based on a number of theoretical studies, the Lg phase has been explained as a combination of higher mode surface waves (Oliver and Ewing, 1957, 1958; Knopoff *et al.*, 1973; Panza and Calcagnile, 1975). Using the multi-mode analysis method, Cara *et al.* (1981) showed that Lg waves, recorded in California networks (SCARLET and CALNET), propagate with a group velocity of 3.2 to 3.5 km/s, can be identified as higher mode surface waves. Herrmann and Kijko (1983) simulated some empirical vertical component Lg relations observed in eastern North America with the higher mode surface wave theory. Synthetic seismograms of the crustal phases at a regional distances calculated by the discrete wavenumber method are in very good agreement with data from the French seismic network, especially the Lg phase (Bouchon, 1982). Lg waves are viewed as guided waves made up of S waves incident on the Moho at angles more grazing than the critical incidence and multiply reflected within the crust (Bouchon, 1982; Olson *et al.*, 1983). Also the method of ray diagrams applied to the Lg waves propagation in 2-D and 3-D structures provide a graphic representation of the nature of Lg waves travelling within a heterogeneous medium (Kennett, 1986; Bostock and Kennett, 1990).

Because the Lg phase propagates efficiently over long distances and samples the whole crust, its amplitude analysis is widely used to evaluate the mean quality factor (Q) of S waves

in the stable continental crust. This analysis can be done either in the time domain or in the frequency domain. These studies are carried out in areas such as North America (Street, 1976; Jones *et al.*, 1977; Bollinger, 1979; Mitchell, 1980; Dwyer *et al.*, 1983; Hasegawa, 1985; Chavez and Priestley, 1986, Toksöz *et al.*, 1990), Western Europe (Nicolas *et al.*, 1982; Campillo *et al.*, 1985), and Asia (Nuttli, 1980, 1981). The most common feature of these studies is the quality factor Q dependent on frequency is in the form $Q = Q_0 f^\xi$, where ξ is around 0.5.

On the other hand, observations showed that over some regions Lg waves are strongly attenuated. It has been difficult to determine whether this Lg attenuation is due to structure change or a very low Q zone. These observations motivated studies on Lg propagation in laterally heterogeneous crust. Current models have been limited to the 2-D SH case (Kennett and Mykkeltveit (1984). Kennett and Mykkeltveit applied the coupled mode method to the Lg phase across the central graben of the North Sea and showed a very poor mode transmission at 1 Hz for Love modes. Campillo (1987) synthesized the SH seismogram with a combination of the discrete wavenumber method and the boundary integral equation approach for the uprise of the Moho and the basin model in a 0-1 Hz frequency band.

In this paper the mode summation (higher mode surface wave) is used to to synthesize Lg wave seismograms for the P-SV case. In the first part of the paper, the flat-layered crust model is considered. Synthetics are compared with the observations at the FINESA array. The mode analysis of Lg waves is provided. Then the coupled mode method is applied to

the Lg phase in the laterally varying crust. The synthetic vertical component of the Lg seismogram and mode transmission matrix is obtained. The basin model and the North Sea case are considered.

Lg WAVES IN FLAT-LAYERED CRUST

In this section the flat-layered crust model is used to synthesize seismograms of Lg waves by mode summation. Green's function of Rayleigh wave term is given. Synthetic seismograms of Lg and Rg are compared with the observations. The mode composition of the Lg phase is analyzed.

Green's Function of the Rayleigh Wave Term

Green's function for the Rayleigh wave term in a homogeneous elastic layered medium has a closed form in the frequency domain (Aki and Richards, 1980).

$$G_{ij}(\vec{r}, \vec{r}_s, \omega) = \sum_{n=0}^N p_i^n(z, \phi) p_j^n(z_s, \phi) \frac{1}{8cU I_1} \sqrt{\frac{2}{\pi k_n D}} e^{i(k_n D + \frac{\pi}{4})} \quad (1)$$

where the source is at \vec{r}_s with depth z_s and the receiver is at \vec{r} with depth z , and

$$p^n(z, \phi) = \begin{pmatrix} r_1^n(z) \cos \phi \\ r_1^n(z) \sin \phi \\ i r_2^n(z) \end{pmatrix}. \quad (2)$$

ϕ and D are the azimuth angle and the horizontal distance between the source and the receiver. Index n refers to the mode number with total N modes at frequency ω . $r_1^n(z)$ and $r_2^n(z)$ are the radial and vertical displacement eigenfunctions of the Rayleigh wave. c and U are the phase and the group velocity of the Rayleigh wave. Integral I_1 is defined by

$$I_1 = \frac{1}{2} \int_0^\infty \rho(z) [(r_1^n(z))^2 + (r_2^n(z))^2] dz. \quad (3)$$

The displacement field excited due to different types of sources can be obtained from the Green's function. For a point explosion source, where the moment tensor is a diagonal matrix with equal elements $M_{xx} = M_{yy} = M_{zz} = M$, the vertical displacement in the frequency domain is given by:

$$u_z(\vec{r}, \omega) = \sum_{n=0}^N \frac{r_2(z)}{8cUI_1} \sqrt{\frac{2}{\pi k_n D}} M(\omega) e^{i(k_n D + \frac{\pi}{4})} [k_n r_1(z_s) + \frac{dr_2}{dz} |_{z_s}]. \quad (4)$$

The summation is taken from $n = 0$ to N to get both the Rg and Lg waves. The fundamental mode ($n = 0$) corresponds to the Rg wave part and $n = 1, 2, \dots, N$ make up the Lg waves. The Green's function provides a fast way to synthesize the Lg and Rg waves if eigenfunctions of the surface wave are known.

Mode Analysis of the Lg Phase

To determine which modes contribute most strongly to Lg waves we use Lg seismograms from known sources, such as quarry blasts, and study these using synthetic seismograms. A typical crust model with a sedimentary layer (Figure 1a) is chosen for this purpose (Bouchon, 1982).

The model is purely elastic, with no attenuation. The dispersion curves of fundamental mode Rayleigh waves and higher modes are plotted in Figure 1b. At 5 Hz there are a total of 57 modes. Energy distributions of the modes at each layer are shown in Figure 2 for frequency 1 Hz. The energy of each mode is normalized to 1. For the fundamental mode almost all the energy is confined to the top sedimentary layer. As the mode number goes up the energy tends to be distributed more evenly between layer.

Next we show the synthetic seismograms for a double-couple point source with a step time function. The source parameters are: strike 45° , dip 90° and rake 0° . Vertical displacement of Lg waves is calculated at a distance of 150 km with 0° azimuth at a 0–5 Hz frequency band. Different source depths (1 km, 10 km and 20 km) are considered (Figures 3a,b,c). The sources are located at the different layers of the model. Mode contributions from the fundamental mode—modes 1 to 10, modes 11 to 20, and modes 21 to 30—are compared with the summation of total modes. For the source at the depth of 1 km the amplitude of the fundamental mode is very large. It is not surprising because the shallow source excites the lower-order surface mode efficiently. Most parts of the Lg waves come from modes 1 to 10. Modes 11 to 20 have some contribution to the early part of the Lg phase. However, for the sources at the depths of 10 and 20 km, contributions to Lg can come from modes up to 30. For the shallow source Lg energy spreads over a longer time domain than the deep source.

In Figure 4 we compare the radial and vertical component of Lg waves with the source depth at 10 km. The radial component of Lg waves shows the same pattern as the vertical

component. This explains why the observed Lg waves look about the same on vertical and horizontal seismograms.

Comparison With Data

To compare the synthetic seismogram of Lg waves with the observed data, two quarry blasts from Leningrad recorded at the FINESA array were chosen. The velocity and attenuation models for Scandinavian crust given by Toksöz *et al.* (1990), and are plotted in Figures 5 and 6, respectively. The feature of the attenuation model is that Q_p and Q_s have the same form of frequency dependence,

$$Q = Q_o f^\xi \quad (5)$$

with different values of Q_o and ξ at each layer. It is assumed $Q_p = 2Q_s$. The quarry blast is modeled as a vertical point force at a depth of 40 m. The synthetic and observed seismograms at distances of 200 and 250 km are compared in Figures 7a and 7b, respectively. Since the site and instrument responses are not known exactly at very high frequencies, both synthetic and observed seismograms are band pass filtered between 0.5 to 5.0 Hz. Furthermore it is important to keep in mind that the synthetic seismograms include only the Lg and Rg waves and not the direct (Pg, Sg), refracted (Pn, Sn), or reflected body waves (PmP, SmS). The comparisons should be limited to Lg and Rg waves. Agreement between the observed Lg and Rg seismograms and the synthetics is very good, especially when we look at the relative amplitudes of Lg and Rg waves and the time durations of these phases. Since no scattering is

included in synthetics, there is no scattered coda in the synthetic models. Given the quality of the agreement, we can also state that for these paths the frequency dependent Q model is consistent with the observations. Mode analysis of Lg waves for a distance of 200 km (Figure 8) reveals that modes 1 to 14 make up most parts of the Lg phase.

CRUST MODEL WITH LATERAL HETEROGENEITY

Lg waves, interpreted as a superposition of higher modes surface waves, are sensitive to variation in crustal structure. Although this problem has been looked at for the simpler problem of SH waves (Kennett and Mykkeltveit, 1984; Campillo, 1987), no such studies have been carried out for the P-SV case. Since most observational data are in the form of vertical component seismograms, it is important to carry out this study. In this section we first outline the observations of the Lg phase across the regions with strong lateral variations of the crustal structure, and then use the coupled mode method to calculate the surface wave mode propagation in laterally heterogeneous crust. The lateral structures considered include a sediment filled basin, a thinned crust due to shallowed Moho ("Moho bump") that would result from crustal stretching. As an application we concentrate on the modeling of the extinction of the Lg phase across the central graben of the North Sea.

Observations of Lg in Strong Laterally Varying Crust

We focus observations at the area where Lg waves are strongly attenuated or become completely extinct. These areas are associated with active tectonic regions. For paths crossing the Tibetan Plateau the Lg phase was not observed (Ruzaikin *et al.*, 1977; Ni and Barazangi, 1983). There are three possibilities for the absence of Lg: (1) change in the crustal structure on the margins of the Tibetan Plateau disrupting the waveguide for the Lg; (2) a complex velocity structure inside the thickened crust; and (3) high attenuation in the crust. The Lg waves crossing the Turkish and Iranian Plateaus were highly attenuated (Kadinsky-Cade *et al.*, 1981). This may also be due to the above causes associated with a partial underthrusting of the Arabian Continental plate beneath the Iranian and Turkish continental blocks. The Lg phase was not observed when the path of propagation crosses the southern Caspian Sea and the Black Sea (Kadinsky-Cade *et al.*, 1981). These are consistent with the evidence of oceanic-type crustal structure beneath these seas. An interesting observation is that Lg propagated efficiently when the direction is parallel to the strike of the Andes and the Lg phase was not observed for paths crossing the Andes (Chinn *et al.*, 1980).

Another region of Lg observations is near Denmark and the North Sea (Gregersen, 1984). The poor propagation of Lg across the North Sea is similar to that observed across a sedimentary basin in eastern Greenland. The sedimentary basin in eastern Greenland is in a similar tectonic setting, along a passive continental margin, to that of the graben in the North Sea. Both developed before seafloor spreading separated Greenland from Europe (Barton and

Wood, 1984).

Method of Coupled Modes

The method of coupled modes was first used for seismological purposes by Kennett (1984). In this application to 2-D laterally varying structure, we neglect body waves and restrict calculations to the modal part of the wavefield. Following Kennett (1984) and using the Cartesian (x, z) coordinate system we express the wavefield as a sum of modes travelling both in the positive and the negative x direction with the modal coefficient dependent on x .

$$W(x, z) = \sum_{n=0}^N [c_n^+(x) e^{ik_n x} W_n(k_n, z) + c_n^-(x) e^{-ik_n x} W_n(-k_n, z)] \quad (6)$$

where $W_n(k_n, z)$ is the displacement eigenfunction associated with wavenumber k_n . N is the total number of modes at frequency ω . The details of the method are given in Appendix A. Using the equation of motion and orthogonality of the eigenfunctions, we consider the reflection and transmission problem of the heterogeneous region confined between x_l and x_r as shown in Figure 9. We obtain the coupled Ricatti equations:

$$\frac{\partial R}{\partial x_l} + RB^{++} - B^{--}R + RB^{+-}R - B^{-+} = 0 \quad (7)$$

$$\frac{\partial S}{\partial x_l} + SB^{++} + SB^{+-}R = 0 \quad (8)$$

where R and S are mode reflection and transmission matrices with initial conditions

$$\begin{aligned} S(x_r, x_r) &= I \\ R(x_r, x_r) &= 0 \end{aligned} \tag{9}$$

where I is the identity matrix. Coefficients B^{++} , B^{+-} , B^{-+} and B^{--} depend on heterogeneity, as explained in the appendix.

After we calculate the mode transmission matrix at each frequency, the displacement in frequency domain can be obtained by adding all the transmitted modes together. For example, vertical displacement due to a point explosion source across a heterogeneous region with the mode transmission matrix $S(\omega)$ can be written explicitly as:

$$u_z(\vec{r}, \omega) = \sum_{n=0}^N \left[\sum_{m=0}^N s_{mn}(\omega) r_2^m(z) e^{ik_m D} \right] \sqrt{\frac{2}{\pi k_n D}} \frac{e^{i\frac{\pi}{4}}}{8cU I_1} [k_n r_1(z_s) + \frac{dr_2}{dz} |_{z_s}] M(\omega). \tag{10}$$

The seismogram in the time domain is obtained by the inverse Fourier transform.

Lg Waves Across a Sedimentary Basin

We apply the coupled mode method to the Lg waves that cross a basin (Figure 9). The reference model is the central France model [Bouchon, 1982 (Fig. 1a)]. There is no intrinsic attenuation in this model. The basin is modeled as a block of sedimentary layers. A sedimentary basin of width W , and a thickness of 5 km is below the top layer, as shown in Figure 9. This kind of model can be found in Kennett's paper (1984). The source is an impulse point explosion source at a depth of 1 km. The coupled Ricatti equations are

solved numerically by the Runge-Kutta method with initial conditions given in equation 9 to obtain a Rayleigh mode transmission matrix.

The synthetic seismogram is calculated at a distance of 150 km at a frequency band of 0–2.5 Hz. Lg seismograms for the reference structure (without sedimentary basin, $W = 0$) and those crossing the 20 km wide and the 40 km wide basins are shown in Figure 9b. The fundamental mode ($n = 0$) is not included in these seismograms. The waveform change reflects the mode conversion. There is substantial attenuation of the Lg waves across the basin. In Tables 1, 2, 3 and 4 we list the Rayleigh mode transmission matrix at frequencies 0.5, 1.0, 1.5 and 2.0 Hz. In these tables the absolute value of each complex element of the matrices are shown and discretized with unity represented by 100. Each column of the matrix shows the transmission amplitude of modes corresponding to the incidence of the pure mode of that column number. The fundamental mode is almost totally transmitted through the basin because most of the energy of the fundamental mode was confined near the surface, especially at high frequencies. For the 40 km wide basin the transmission is poor at high frequencies and high mode numbers. It is obvious from the band-limited two digits of the transmission matrix that the most Rayleigh mode conversion occurs by energy transfer between the neighboring modes.

From the mode composition of Lg waves it is expected that there should be more attenuation for a deeper source, which concentrates more energy in higher modes with poor transmission. The Lg phase as well as the Rg phase transmitted across the basin are shown

in Figure 9c. The basin has little effect on the Rg phase. Because of the shallow ($h = 1$ km deep) source, the fundamental mode (Rg) has the most energy. The shape and amplitude of seismograms dominated by the Rg do not show any change. Please note that since there is no intrinsic attenuation ($Q = \infty$) in the model, Rg looks stronger than what it would be in the case of the real earth with strong attenuation near the surface.

The North Sea Case

An excellent data set for the study of Lg attenuation comes from seismic refraction experiments in the central North Sea area recorded at the NORSAR array in Norway. The vertical component seismograms and the location of the shots on the map of the North Sea are shown in Figures 10a and 10b, respectively [from Kennett and Mykkeltveit (1984)]. Plotted seismograms are band-pass filtered between 1.5 and 5.0 Hz and each trace is normalized to its own maximum amplitude. The paths that cross the central graben (shot D1, D2 and F4) show no distinct Lg arrivals. The attenuation of Lg across the central graben is also observed by Gregersen (1984) from the study of regional seismic events.

In order to understand the extinction of the Lg wave cross the central graben we used a simplified structural model of the central graben. A profile of the crustal structure of the central graben was obtained by a long-range seismic reflection and refraction experiments (Barton and Wood, 1984). A cross-section of the structure with velocity contours is shown in Figure 11a. The thickening of the sediments and thinning of the crust is clearly shown in

this figure. Our simplified reference velocity model of the North Sea crust has three layers with a 2 km thick sedimentary layer on top (Figure 11b). The central graben is represented by a rectangular block of sediment concentrated down to 7 km. The thinning of the crust is done by raising the Moho from 30 km to 20 km, as a rectangular block. The model used for calculations is shown by Figure 11c. A similar model was also used by Kennett and Mykkeltveit (1984) to calculate a Love modes transmission matrix at 1 Hz.

Lg waves propagate with little attenuation across the North Sea paths without the central graben, as shown in Figure 10a. We calculated Lg propagation using the simplified central graben model, shown in Figure 11c. The source is an impulse point explosion at a depth of 1 km and the distance is 600 km. The seismograms bandpass-filtered between 0.8 and 2.4 Hz are shown in Figure 12 for three values of basin width: $W = 0$ (reference model), $W = 30$ km and $W = 60$ km. In these calculations we included attenuation. In the reference structure, Q_s equals 300, 1500, and 2000 for layer 1, 2 and 3, respectively. It is assumed that $Q_p = 2Q_s$, and in all cases Q is independent of frequency. Both 30 km and 60 km wide central graben models significantly attenuate the Lg phase. The actual central graben is about 100 km wide, but with much smoother change in crustal thickness than our simplified model. The attenuation effects of the central graben are increased by our block-like model. Thus, getting significant attenuation with a 60 km wide model is not surprising.

We investigated the relative effects of different aspects of lateral structural change on Lg phase propagation. These include having only the sedimentary basin, the Moho bump,

and the combination of the two. The results are shown in Figure 13. The Moho bump has a greater effect on Lg attenuation than the sedimentary basin thickening. We note that in our model the Moho bump is 10 km in height but the sedimentary basin is only 5 km deep. The higher-order modes are more strongly affected by the Moho bump and the lower-order modes by basin thickening.

To compare the theoretical results with the observation shown in Figure 10, we calculated Lg wave synthetics as a function of distance. Two sets of seismograms were calculated, the first set using the flat layered reference model shown in Figure 11b, and the second set with the graben (Figure 11c) centered at $x = 700$ km distance. Both models have the intrinsic attenuation used in previous figures. The sources are explosions at 1 km depth. Figure 14 shows the Lg synthetic seismograms for both "reference" and "graben" models in the distance range of 554 km to 882 km, corresponding to the distances of observed seismograms (Figure 10a). In the synthetic seismograms the amplitudes are normalized to the same maximum amplitude at 554 km.

Intrinsic attenuation reduces the amplitude of Lg waves, as shown in Figure 14a, for the reference model. However, a clear Lg phase, with longer duration due to dispersion is visible at 882 km distance. With the central graben, the Lg waves become almost completely extinct once they cross the graben. The synthetic Lg seismograms shown in Figure 14b are very similar to the observed one shown in Figure 10a. The extinction of Lg across the North Sea Central Graben can be explained by the lateral structure change due to crustal thinning.

From a computational view point, the coupled mode method is time consuming because at each frequency we have two N^2 coupled first order differential equations to solve, and N increases rapidly as frequency goes up (N is the number of modes at a given frequency). To obtain a realistic time domain seismogram we have a large number of frequencies. For example, for the North Sea reference model, $N = 43$ at a frequency of 2.5 Hz. Fortunately the computations are independent at each frequency, and calculations can be made efficiently on a parallel machine. Using the 64 nodes of the nCUBE at the Earth Resources Laboratory (ERL), the North Sea model with the 60 km wide central graben took 3-1/2 hours of CPU time.

CONCLUSIONS

Mode summation provides a method to synthesize seismograms of Lg wave propagation in the flat-layered or laterally inhomogeneous crust. Synthetic Lg and Rg waves, calculated using a flat-layered crustal model of Fennoscandia with frequency dependent attenuation, are in good agreement with observations of quarry blasts recorded at the FINESA array. Mode analysis of composition of Lg phase shows that as the source goes deeper, the higher modes become important. With the coupled mode method, synthetic Lg waves show an attenuation and the modes conversion across the basin model. Using a model in which there is a thickening sedimentary layer and crustal thinning, synthetic Lg wave seismograms explain the observed extinction of Lg waves across the central graben of the North Sea.

ACKNOWLEDGMENTS

This research was supported by the Defense Advanced Research Projects Agency through contract F19628-81-K-0020, administered by the Air Force Geophysics Laboratory. We thank Bata Mandal and Anton Dainty for valuable discussions on the Lg wave. The calculations were carried out using ERL's nCUBE computer. We thank Ted Charrette for helping us implement our code on the nCUBE.

REFERENCES

- Aki, K. and Richards, P.G. (1980). *Quantitative Seismology*, W. H. Freeman and Company.
- Barton, P. and Wood, R. (1984). Tectonic evolution of the North Sea basin: crustal stretching and subsidence. *Geophys. J.R. astr. Soc.*, 79, 987-1022
- Bollinger, G.A. (1979). Attenuation of the Lg Phase and the determination of mb in the southeastern United States, *Bull. Seismol. Soc. Am.*, 69, 45-63.
- Bostock, M.G. and Kennett, B.L.N. (1990). The effect of 3-D structure on Lg propagation patterns, *Geophys. J. Int.*, 101, 355-365.
- Bouchon, M. (1982). The complete synthesis of seismic crustal phases at regional distances, *J. Geophys. Res.*, 87, 1735-1741.
- Campillo, M. (1987). Lg wave propagation in a laterally varying crust and the spatial distribution of the quality factor in central France, *J. Geophys. Res.* 92, 12604-12614.
- Campillo, M., Plantet, J.L., and Bouchon, M. (1985). Frequency-dependent attenuation in the crust beneath central France from Lg waves: Data analysis and numerical modeling, *Bull. Seismol. Soc. Am.*, 75, 1395-1411.
- Cara, M., Minster, J.B., and LeBras, R. (1981). Multimode analysis of Rayleigh-type Lg, Part II. Application to Southern California and the Northwestern Sierra Nevada, *Bull. Seismol. Soc. Am.*, 71, 985-1002.
- Chavez, D.E. and Priestley, K.K. (1986). Measurement of frequency-dependent Lg attenuation in the Great Basin, *Geophys. Res. Lett.*, 13, 551-554.

- Chinn, D.S., Isacks, B.L., and Barazangi, M. (1980). High-frequency seismic wave propagation in western South America along the continental margin, in the Zazca Plate and across the Altiplano, *Geophys. J. R. astr. Soc.*, 60, 209-244.
- Dainty, A.M. (1981). A Scattering model to explain seismic Q observations in the lithosphere between 1 and 30 Hz, *Geophys. Res. Lett.*, 8, 1126-1128.
- Dwyer, J.J., Herrmann, R.B., and Nullit, O.W. (1983). Spatial attenuation of the Lg wave in the central United States, *Bull. Seismol. Soc. Am.*, 73, 781-796.
- Gregersen, S. (1984). Lg-wave propagation and crustal structure differences in Denmark and the North Sea, *Geophys. J. R. astr. Soc.*, 79, 217-234.
- Hasegawa, H.S. (1985). Attenuation of Lg Waves the Canadian Shield, *Bull. Seismol. Soc. Am.*, 75, 1569-1528.
- Herrmann, R.B. and Kijko, A. (1983). Modelling some empirical vertical component Lg relations, *Bull. Seismol. Soc. Am.*, 73, 157-171.
- Jones, F.B., Long, L.T., and McKee, J.H. (1977). Study of the attenuation and azimuthal dependence of seismic wave propagation in the southeastern United States, *Bull. Seismol. Soc. Am.*, 67, 1503-1513.
- Kennett, B.L.N. (1984). Guided wave propagation in laterally varying media, I: Theoretical developments, *Geophys. J. R. astr. Soc.*, 79, 253-255.
- Kennett, B.L.N. (1986). Lg waves and structural boundaries, *Bull. Seismol. Soc. Am.*, 76, 1133-1141.

- Kennett, B.L.N. and Mykkeltveit, S. (1984). Guided wave propagation in laterally varying media, II: Lg waves in northwestern Europe, *Geophys. J. R. astr. Soc.*, *79*, 257-267.
- Knopoff, L., Schwab, F., and Kausel, E. (1973). Interpretation of Lg, *Geophys. J.*, *33*, 389-404.
- Mitchell, B.J. (1980). Frequency dependence of shear wave internal friction in the continental crust of eastern North America, *J. Geophys. Res.*, *85*, 5212-5218.
- Ni, J. and Barazangi, M. (1983). High-frequency seismic wave propagation beneath the Indian Shield, Himalayan Arc, Tibetan Plateau and surrounding regions: High uppermost mantle velocities and efficient Sn propagation beneath Tibet, *Geophys. J. R. astr. Soc.*, *72*, 665-689.
- Nicolas, M., Massinon, B., Mechler, P., and Bouchon, M. (1982). Attenuation of regional phases in Western Europe, *Bull. Seismol. Soc. Am.*, *72*, 2089-2106.
- Nuttli, O.W. (1980). The excitation and attenuation of seismic crustal phases in Iran, *Bull. Seismol. Soc. Am.*, *70*, 469-485.
- Nuttli, O.W. (1981). On the attenuation of Lg waves in Western and Central Asia and their use as a discrimination between earthquake and explosions, *Bull. Seismol. Soc. Am.*, *71*, 249-261.
- Oliver, J. and Ewing, M. (1957). Higher modes of continental Rayleigh waves, *Bull. Seismol. Soc. Am.*, *47*, 187-204.
- Oliver, J. and Ewing, M. (1958). Normal modes of continental surface waves, *Bull. Seismol.*

Soc. Am., 48, 33-49.

Olsen, K.H., Braile, L.W., and Stewart, J.N. (1983). Modeling short-period crustal phases (Pg-Lg) for long-rang refraction profiles, *Phys. Earth Planet. Interiors*, 31, 334-347.

Panza, G.F. and Calcagnile, G. (1975). Lg, Li and Rg from Rayleigh modes, *Geophys. J.*, 40, 475-487.

Press, F. and Ewing, M. (1952). Two slow surface waves across North America, *Bull. Seismol. Soc. Am.*, 42, 219-228.

Ruzaikin, A.I., Nersesov, I.L., Khalturin, V.I., and Molnar, P. (1977). Propagation of Lg and lateral variations of crustal structure in Asia, *J. Geophys. Res.*, 82, 307-316.

Street, R.L. (1976). Scaling Northeastern United States, Southeastern Canadian earthquakes by their Lg waves, *Bull. Seismol. Soc. Am.*, 66, 1525-1537.

Toksöz, M.N., Wu, R.S., and Schmitt, D.P. (1987). Physical mechanisms contribution to seismic attenuation in the crust, *Proc. NATO ASI "Strong Ground Motion Seismology"*, 225-247.

Toksöz, M.N., Mandal, B., and Dainty, A.M. (1990). Frequency dependent attenuation in the crust, *Geophys. Res. Lett.*, 17, 973-976.

APPENDIX

Method of Coupled Modes

In this appendix we present the theoretical equations for the coupled modes as applied to Rayleigh waves following Kennett (1984) and then briefly describe the numerical implementation for calculating the Lg and Rg synthetic seismograms.

In the Cartesian coordinate system in which z is the depth variable, we introduce displacement vector $W = (u, v, w)$ and stress vector $T = (t_{xx}, t_{xy}, t_{xz})$. The equation of motion, in terms of W and T and keeping all derivatives with respect to x on the left-hand side, can be written as:

$$\frac{\partial}{\partial x} \begin{pmatrix} W \\ T \end{pmatrix} = \begin{pmatrix} A_{ww} & A_{wt} \\ A_{tw} & A_{tt} \end{pmatrix} \begin{pmatrix} W \\ T \end{pmatrix} \quad (\text{A.1})$$

where A_{ww} , A_{wt} , A_{tw} and A_{tt} are operators which depend on $\frac{\partial}{\partial y}$, $\frac{\partial}{\partial z}$, frequency ω and elastic constant λ and μ .

In the two-dimensional (2-D) situation where the structure is independent of y , the wavefield, restricted to the modal part, can be expressed as a sum of modes travelling in both the positive x and negative x directions:

$$W(x, z) = \sum_{n=1}^N [c_n^+(x) e^{ik_n x} W_n(k_n, z) + c_n^-(x) e^{-ik_n x} W_n(-k_n, z)] \quad (\text{A.2})$$

$$T(x, z) = \sum_{n=1}^N [c_n^+(x) e^{ik_n x} T_n(k_n, z) + c_n^-(x) e^{-ik_n x} T_n(-k_n, z)] \quad (\text{A.3})$$

where N is the mode number at a given frequency. $W_n(k_n, z)$ is the displacement eigenfunction. Stress vector $T_n(k, z)$ can be obtained from $W_n(k_n, z)$. We assume that the model

consists of a region of heterogeneity superimposed on a stratified medium, it is easy to work in terms of the modes in the reference structure. The orthogonality of the eigenfunctions at a fixed frequency requires

$$i \int_0^\infty [W_p(k_p, z)T_q(-k_q, z) - T_p(k_p, z)W_q(-k_q, z)]dz = \delta_{pq} \quad (\text{A.4})$$

$$i \int_0^\infty [W_p(k_p, z)T_q(k_q, z) - T_p(k_p, z)W_q(k_q, z)]dz = 0. \quad (\text{A.5})$$

After some algebra, we get:

$$\begin{aligned} \frac{\partial}{\partial x}(c_m^+ e_m) &= i \int_0^\infty dz \sum_{n=0}^N [T_m^-(A_{ww}W_n - A_{wt}T_n) - W_m^-(A_{tw}W_n + A_{tt}T_n)]c_n^+ e_n \\ &+ i \int_0^\infty dz \sum_{n=0}^N [T_m^-(A_{ww}W_n^- - A_{wt}T_n^-) - W_m^-(A_{tw}W_n^- + A_{tt}T_n^-)]c_n^- e_n^- \quad (\text{A.6}) \end{aligned}$$

For brevity we set $W_n^- = W_n(-k_n, z)$, $T_n^- = T(-k_n, z)$, $e_n = e^{ik_n x}$ and $e_n^- = e^{-ik_n x}$.

In the absence of heterogeneity, c_m^+ is a constant and c_m^- equals zero. In the reference structure the corresponding operators are A_{ww}^0 , A_{wt}^0 , A_{tw}^0 and A_{tt}^0 . The effect of heterogeneity, which only depends on the local departures from the reference structure, can be expressed by:

$$\begin{aligned} \Delta A_{ww} &= A_{ww} - A_{ww}^0 \\ \Delta A_{wt} &= A_{wt} - A_{wt}^0 \\ \Delta A_{tw} &= A_{tw} - A_{tw}^0 \\ \Delta A_{tt} &= A_{tt} - A_{tt}^0 \end{aligned} \quad (\text{A.7})$$

For the laterally heterogeneous model the modal equations are

$$\frac{\partial c_m^+}{\partial x} = \sum_{n=0}^N iK_{mn}e_m^- e_n^+ c_n^+ + \sum_{n=0}^N iL_{mn}e_m^- e_n^- c_n^- \quad (\text{A.8})$$

$$\frac{\partial c_m^-}{\partial x} = - \sum_{n=0}^N i L_{mn} e_m c_n c_n^+ - \sum_{n=0}^N i K_{mn} e_m e_n^- c_n^- \quad (\text{A.9})$$

where

$$K_{mn} = \int_0^\infty dz [T_m^- (\Delta A_{ww} W_n + \Delta A_{wt} T_n) - W_m^- (\Delta A_{tw} W_n + \Delta A_{tt} T_n)] \quad (\text{A.10})$$

$$L_{mn} = \int_0^\infty dz [T_m^- (\Delta A_{ww} W_n^- + \Delta A_{wt} T_n^-) - W_m^- (\Delta A_{tw} W_n^- + \Delta A_{tt} T_n^-)]. \quad (\text{A.11})$$

Introducing two new N dimensional vectors: $C^+ = (c_m^+)$, $C^- = (c_m^-)$, we obtain a more compact form of modal equations:

$$\frac{\partial}{\partial x} \begin{pmatrix} C^+ \\ C^- \end{pmatrix} = \begin{pmatrix} B^{++} & B^{-+} \\ B^{+-} & B^{--} \end{pmatrix} \begin{pmatrix} C^+ \\ C^- \end{pmatrix} \quad (\text{A.12})$$

where

$$\begin{aligned} (B^{++})_{ij} &= i K_{ij} e_i^- e_j \\ (B^{+-})_{ij} &= i L_{ij} e_i^- e_j^- \\ (B^{-+})_{ij} &= -i L_{ij} e_i e_j \\ (B^{--})_{ij} &= -i K_{ij} e_i e_j^- \end{aligned} \quad (\text{A.13})$$

We assume that the region of heterogeneity is restricted between x_l and x_r , as shown in Figure 9a, and consider the surface wave incident from the left. Defining transmission matrix $S(x_r, x_l)$ and reflection matrix $R(x_r, x_l)$ as:

$$\begin{aligned} C^+(x_r) &= S(x_r, x_l) C^+(x_l) \\ C^-(x_l) &= R(x_r, x_l) C^+(x_l) \end{aligned} \quad (\text{A.14})$$

we obtain the coupled Ricatti equations for R and S :

$$\frac{\partial R}{\partial x_l} + RB^{++} - B^{--}R + RB^{+-}R - B^{-+} = 0 \quad (\text{A.15})$$

$$\frac{\partial S}{\partial x_l} + SB^{++} + SB^{+-}R = 0. \quad (\text{A.16})$$

We need to integrate these equations starting at x_r with the initial conditions:

$$\begin{aligned} S(x_r, x_r) &= I \\ R(x_r, x_r) &= 0 \end{aligned} \quad (\text{A.17})$$

where I is the identity matrix.

For the P-SV case, the equation of motion is:

$$\frac{\partial}{\partial x} \begin{pmatrix} u \\ w \\ t_{xx} \\ t_{xz} \end{pmatrix} = \begin{pmatrix} 0 & -\lambda(\lambda + 2\mu)^{-1}\partial_z & -(\lambda + 2\mu)^{-1} & 0 \\ -\partial_z & 0 & 0 & \mu^{-1} \\ -\rho\omega^2 & 0 & 0 & -\partial_z \\ 0 & -\rho\omega^2 - \partial_z(\nu\partial_z) & -\partial_z[\lambda(\lambda + 2\mu)^{-1}] & 0 \end{pmatrix} \begin{pmatrix} u \\ w \\ t_{xx} \\ t_{xz} \end{pmatrix} \quad (\text{A.18})$$

where $\nu = \frac{4\mu(\lambda+2\mu)}{\lambda+2\mu}$.

The coefficients of K_{ij} and L_{ij} in the terms of $\Delta\rho$, $\Delta\lambda$ and $\Delta\mu$ are

$$\begin{aligned} K_{ij} = \int_D dz [& \Delta\rho\omega^2(r_1^i r_1^j + r_2^i r_2^j) - \Delta\lambda(k_i r_1^i + \frac{\partial r_2^i}{\partial z})(k_j r_1^j + \frac{\partial r_2^j}{\partial z}) \\ & - \Delta\mu(k_i r_2^i - \frac{\partial r_1^i}{\partial z})(k_j r_2^j + \frac{\partial r_1^j}{\partial z}) - 2\Delta\mu(k_i k_j r_1^i r_1^j - \frac{\partial r_2^i}{\partial z} \frac{\partial r_2^j}{\partial z})] \end{aligned} \quad (\text{A.19})$$

$$\begin{aligned} L_{ij} = \int_D dz [& \Delta\rho\omega^2(r_1^i r_1^j + r_2^i r_2^j) - \Delta\lambda(-k_i r_1^i + \frac{\partial r_2^i}{\partial z})(k_j r_1^j + \frac{\partial r_2^j}{\partial z}) \\ & - \Delta\mu(-k_i r_2^i - \frac{\partial r_1^i}{\partial z})(k_j r_2^j + \frac{\partial r_1^j}{\partial z}) - 2\Delta\mu(-k_i k_j r_1^i r_1^j - \frac{\partial r_2^i}{\partial z} \frac{\partial r_2^j}{\partial z})] \end{aligned} \quad (\text{A.20})$$

where D is the region of heterogeneity in the z direction. k is wavenumber. r_1, r_2 are the radial (x) and vertical (z) displacement eigenfunctions of the Rayleigh wave.

Since each frequency is independent in the method, this provides a natural level at which to parallelize the algorithm. The approach used here is the master/slave algorithm. The master reads the input file, calculates some of the global variables and passes them to the slaves. Then each slave is given a frequency to work on. At each frequency the coupled Ricatti equation is solved numerically by the Runge-Kutta method. When finished, the slave returns its results to the master program, then queues up for more work. After all the frequencies are calculated, the data which has been collected by the master program is inverse-Fourier transformed into time domain seismograms.

MODE	F	1	2	3	4	5
F	95	3	2	5	3	5
1	2	94	22	13	3	0
2	2	21	93	13	3	0
3	4	11	11	95	2	0
4	0	2	2	2	98	0
5	7	1	2	2	1	99

(a)

MODE	F	1	2	3	4	5
F	92	4	5	8	1	2
1	4	84	41	15	0	0
2	4	40	84	19	2	0
3	5	13	17	93	2	0
4	0	0	1	4	96	1
5	3	1	0	2	2	98

(b)

Table 1: The mode transmission matrices of the basin model at 0.5 Hz. The absolute value of each complex element of the matrices are shown and discretized with unity represented by 100. (a) 20 km wide basin. (b) 40 km wide basin.

MODE	F	1	2	3	4	5	6	7	8	9	10	11
F	99	5	0	0	0	0	0	0	0	0	0	0
1	4	64	13	16	4	7	11	10	5	2	2	0
2	0	14	86	29	21	11	3	1	1	1	1	0
3	0	17	29	72	33	20	7	1	2	1	1	1
4	0	4	20	32	80	19	9	2	0	0	0	1
5	0	7	10	18	18	89	8	4	3	2	0	0
6	0	12	2	6	8	8	91	8	8	6	1	1
7	0	10	1	0	1	5	9	91	14	11	3	4
8	0	4	1	2	1	4	9	14	89	18	8	4
9	0	2	1	1	0	2	7	13	19	87	18	1
10	0	2	1	1	0	0	1	3	9	19	90	16
11	0	1	2	4	3	1	2	5	4	3	17	89

(a)

MODE	F	1	2	3	4	5	6	7	8	9	10	11
F	98	5	0	0	0	0	0	0	0	0	0	0
1	5	40	15	15	5	13	7	3	6	3	3	0
2	0	17	61	54	24	5	4	0	2	2	1	1
3	0	15	53	36	42	12	2	1	1	1	1	0
4	0	6	23	41	72	23	6	1	1	1	0	1
5	0	13	4	11	22	85	10	2	1	3	1	0
6	0	7	3	2	5	9	88	11	6	2	2	2
7	0	3	1	1	1	3	12	86	20	8	3	3
8	0	6	2	1	2	1	7	21	80	27	7	1
9	0	3	2	1	2	4	2	9	29	73	29	3
10	0	2	0	1	0	0	3	4	8	31	78	24
11	0	0	1	1	2	0	3	3	2	4	26	78

(b)

Table 2: The mode transmission matrices of the basin model at 1.0 Hz. The absolute value of each complex element of the matrices are shown and discretized with unity represented by 100. (a) 20 km wide basin. (b) 40 km wide basin.

MODE	F	1	2	3	4	5	6	7	8	9	10	11	12	13	14	15	16	17
F	99	1	0	0	0	0	0	0	0	0	0	0	0	0	0	0	0	0
1	1	40	9	15	22	18	6	2	4	2	0	1	1	1	1	1	0	1
2	0	9	75	31	12	15	15	10	5	1	0	0	0	0	0	0	0	0
3	0	15	31	64	20	4	13	13	9	3	0	0	0	0	0	0	0	0
4	0	21	12	19	70	30	14	8	8	5	0	1	1	1	0	1	1	0
5	0	17	15	4	30	53	40	24	8	3	2	0	1	2	0	1	1	1
6	0	6	15	12	13	39	65	30	16	3	1	1	0	1	0	0	0	1
7	0	2	10	12	7	23	29	76	20	8	1	1	0	0	0	0	0	0
8	0	3	4	8	8	7	16	20	81	14	6	3	1	0	1	1	1	1
9	0	2	1	2	4	3	3	8	14	84	11	9	5	1	1	1	1	2
10	0	1	0	0	0	2	1	2	7	12	88	11	8	5	1	2	1	1
11	0	1	0	0	1	0	1	1	4	10	12	86	13	10	4	1	2	0
12	0	0	0	0	2	2	0	0	1	6	9	13	85	16	11	3	2	3
13	0	1	0	0	1	2	1	0	0	1	6	12	17	79	23	14	5	5
14	0	2	0	0	1	1	1	0	1	2	1	5	12	24	74	27	18	8
15	0	1	0	0	1	1	0	1	1	2	2	2	4	15	29	65	36	23
16	0	1	0	0	1	2	1	0	2	1	1	3	3	6	19	37	59	36
17	0	1	0	0	0	2	2	0	2	3	1	0	4	6	9	23	36	69

(a)

MODE	F	1	2	3	4	5	6	7	8	9	10	11	12	13	14	15	16	17
F	99	1	0	0	0	0	0	0	0	0	0	0	0	0	0	0	0	0
1	1	20	14	12	11	8	1	3	0	2	0	0	0	0	0	0	1	1
2	0	13	60	41	1	24	9	3	4	1	1	0	1	0	0	0	0	0
3	0	12	41	45	26	12	17	7	3	3	1	1	0	0	0	0	0	0
4	0	11	1	26	45	39	19	16	6	3	1	1	2	0	1	0	1	0
5	0	8	23	12	38	34	38	14	5	3	1	1	1	1	1	0	0	0
6	0	1	9	16	18	38	58	35	12	3	1	1	1	1	0	1	1	0
7	0	3	2	7	16	13	35	69	25	4	2	1	1	0	1	0	1	0
8	0	0	4	3	5	5	12	25	73	18	4	1	2	0	0	1	1	2
9	0	1	1	3	3	2	3	4	19	74	17	8	0	3	0	1	1	0
10	0	0	1	0	1	1	1	2	5	17	79	17	8	1	3	1	1	1
11	0	0	0	0	1	1	1	1	1	9	18	76	19	7	4	2	2	0
12	0	0	0	0	2	1	1	1	2	0	9	20	76	23	4	6	2	3
13	0	0	1	0	1	1	1	0	0	4	1	8	25	64	31	3	8	4
14	0	1	1	0	2	1	1	1	1	0	4	5	5	33	55	36	4	12
15	0	0	1	0	1	1	1	1	1	1	3	7	4	37	45	42	12	12
16	0	1	0	0	1	0	1	1	1	1	3	2	9	4	43	37	44	44
17	0	1	0	0	0	1	0	1	3	0	2	0	4	5	12	13	45	29

(b)

Table 3: The mode transmission matrices of the basin model at 1.5 Hz. The absolute value of each complex element of the matrices are shown and discretized with unity represented by 100. (a) 20 km wide basin. (b) 40 km wide basin.

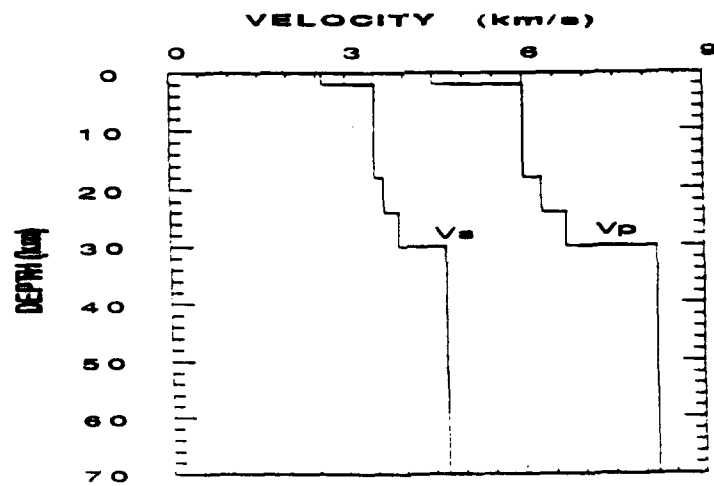
MODE	F	1	2	3	4	5	6	7	8	9	10	11	12	13	14	15	16	17	18	19	20	21	22	23
F	99	0	0	0	0	0	0	0	0	0	0	0	0	0	0	0	0	0	0	0	0	0	0	0
1	0	61	23	2	4	4	3	3	2	2	2	2	1	1	1	1	1	0	0	0	0	1	1	1
2	0	22	12	5	12	17	14	5	2	3	3	1	2	2	1	1	1	1	0	0	0	1	1	0
3	0	2	5	78	29	17	4	15	10	7	3	3	2	0	0	1	0	0	0	0	0	0	0	0
4	0	4	12	29	57	31	7	14	12	10	4	3	3	1	0	1	1	0	0	0	0	0	0	0
5	0	4	17	17	31	65	26	7	4	7	6	1	2	2	1	1	1	0	0	0	0	0	0	0
6	0	4	14	4	7	25	60	34	17	11	6	5	1	1	2	2	1	1	1	0	0	0	0	0
7	0	3	5	15	14	6	34	54	29	23	10	1	3	2	0	1	1	0	1	1	0	0	0	0
8	0	2	2	10	12	4	16	29	76	22	15	5	1	2	1	0	0	0	0	0	0	0	0	0
9	0	2	3	7	10	7	11	23	22	76	21	12	2	2	2	1	0	1	0	0	0	0	0	0
10	0	2	3	3	3	5	6	10	15	21	77	20	10	3	1	2	1	0	1	1	0	0	0	1
11	0	2	1	3	3	1	5	2	5	12	20	78	18	10	6	2	0	1	0	2	2	0	0	1
12	0	1	2	2	3	2	1	3	1	3	11	18	78	17	12	8	3	1	1	1	3	1	0	0
13	0	1	2	0	1	2	1	2	2	2	4	11	17	81	15	13	8	1	2	1	2	3	0	2
14	0	1	1	0	0	1	2	0	1	2	1	6	13	15	85	15	11	4	0	2	1	3	1	2
15	0	1	1	1	1	1	2	1	0	2	2	2	9	14	16	80	19	11	3	2	1	3	3	1
16	0	1	1	0	0	1	1	1	0	0	2	1	3	9	12	20	75	21	13	1	4	4	1	4
17	0	0	1	0	0	0	1	0	1	1	1	1	1	1	4	12	22	74	25	12	3	1	4	2
18	0	0	1	0	0	0	2	1	0	1	2	1	1	2	1	4	14	25	71	25	6	1	10	2
19	0	0	1	0	0	0	1	1	0	0	2	3	1	1	2	3	1	13	26	69	24	1	10	1
20	0	0	1	0	0	0	1	1	0	0	1	3	4	3	1	2	5	3	6	25	65	24	1	20
21	0	1	1	0	0	0	0	0	0	0	1	0	2	4	4	4	1	7	10	1	25	60	30	3
22	0	1	1	0	0	0	0	0	0	0	0	0	0	0	1	4	4	1	8	13	0	31	58	33
23	0	1	0	0	0	0	0	0	0	1	2	2	1	2	2	1	1	4	2	11	20	4	34	45

(a)

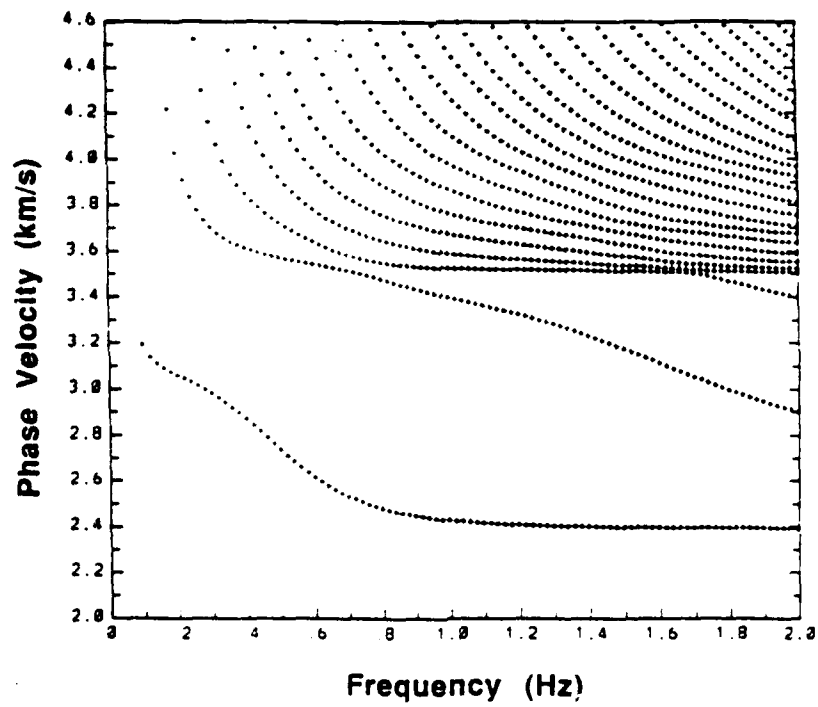
MODE	F	1	2	3	4	5	6	7	8	9	10	11	12	13	14	15	16	17	18	19	20	21	22	23
F	99	0	0	0	0	0	0	0	0	0	0	0	0	0	0	0	0	0	0	0	0	0	0	0
1	0	43	17	1	3	4	4	3	2	1	1	1	1	0	0	1	0	0	0	0	0	0	0	1
2	0	16	9	0	3	6	1	3	3	2	1	2	2	1	1	2	1	1	1	0	0	0	0	1
3	0	1	1	69	39	15	13	8	4	7	3	2	1	1	1	0	1	0	0	0	0	0	0	0
4	0	3	3	39	45	35	9	14	1	4	5	0	2	0	1	0	0	0	0	0	0	0	0	0
5	0	4	6	15	35	56	23	11	12	7	4	0	1	0	1	1	0	0	0	0	0	0	0	0
6	0	4	1	13	9	23	55	31	9	8	7	2	2	0	1	1	0	0	0	0	0	0	0	0
7	0	3	3	8	14	10	31	40	38	24	5	8	1	3	1	1	1	1	1	1	0	0	0	0
8	0	2	3	4	1	11	9	37	62	35	15	3	4	1	2	0	1	0	1	0	0	0	0	0
9	0	1	2	7	4	7	8	23	35	60	30	6	5	2	1	1	0	0	0	1	0	0	0	0
10	0	1	2	3	5	4	7	5	15	29	64	25	5	4	3	1	1	0	1	1	1	0	0	0
11	0	1	2	2	0	4	2	8	3	6	25	65	23	6	1	4	1	1	0	1	1	1	1	0
12	0	1	2	1	2	0	3	1	4	5	5	24	65	23	12	0	5	0	2	1	2	2	0	0
13	0	0	1	1	0	1	0	3	1	2	4	7	24	70	23	14	0	4	0	2	3	0	2	0
14	0	0	1	1	1	0	1	1	2	1	4	1	12	24	75	22	8	3	2	2	1	2	1	0
15	0	1	2	0	0	1	1	1	0	1	2	5	0	14	22	67	26	4	5	0	2	3	1	2
16	0	0	1	1	0	1	0	1	1	0	1	2	5	0	9	27	60	26	3	7	3	1	5	1
17	0	0	1	0	0	0	1	1	0	1	0	1	0	5	4	5	27	59	32	4	5	6	1	4
18	0	0	1	0	0	0	0	1	1	0	1	0	2	0	2	6	3	33	51	31	7	3	8	2
19	0	0	0	0	0	0	1	1	1	1	1	2	1	2	3	0	8	4	33	45	30	12	4	9
20	0	0	0	0	0	0	0	1	1	0	2	2	2	4	1	3	4	6	7	31	40	23	16	4
21	0	0	0	0	0	0	0	0	0	1	0	1	2	0	3	4	2	6	3	12	25	41	34	14
22	0	0	0	0	0	0	0	0	0	0	0	1	1	3	2	2	5	1	8	4	16	35	39	26
23	0	1	1	0	0	0	0	0	0	0	1	0	1	1	0	2	1	5	3	9	4	14	27	14

(b)

Table 4: The mode transmission matrices of the basin model at 2.0 Hz. The absolute value of each complex element of the matrices are shown and discretized with unity represented by 100. (a) 20 km wide basin. (b) 40 km wide basin.



(a)



(b)

Figure 1: (a) A typical crust velocity model with sediment layer. (b) Rayleigh wave dispersion curve corresponding to velocity model (a).

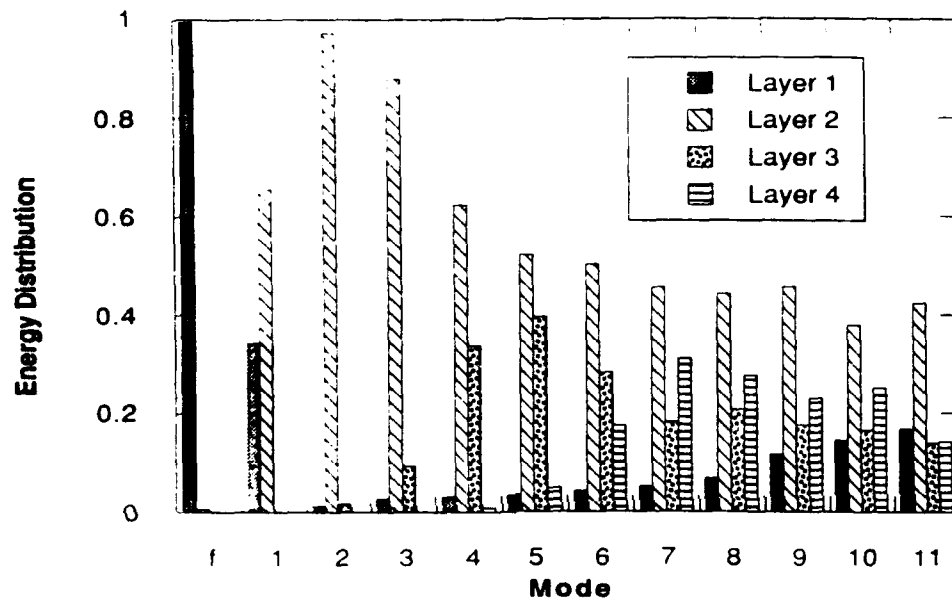
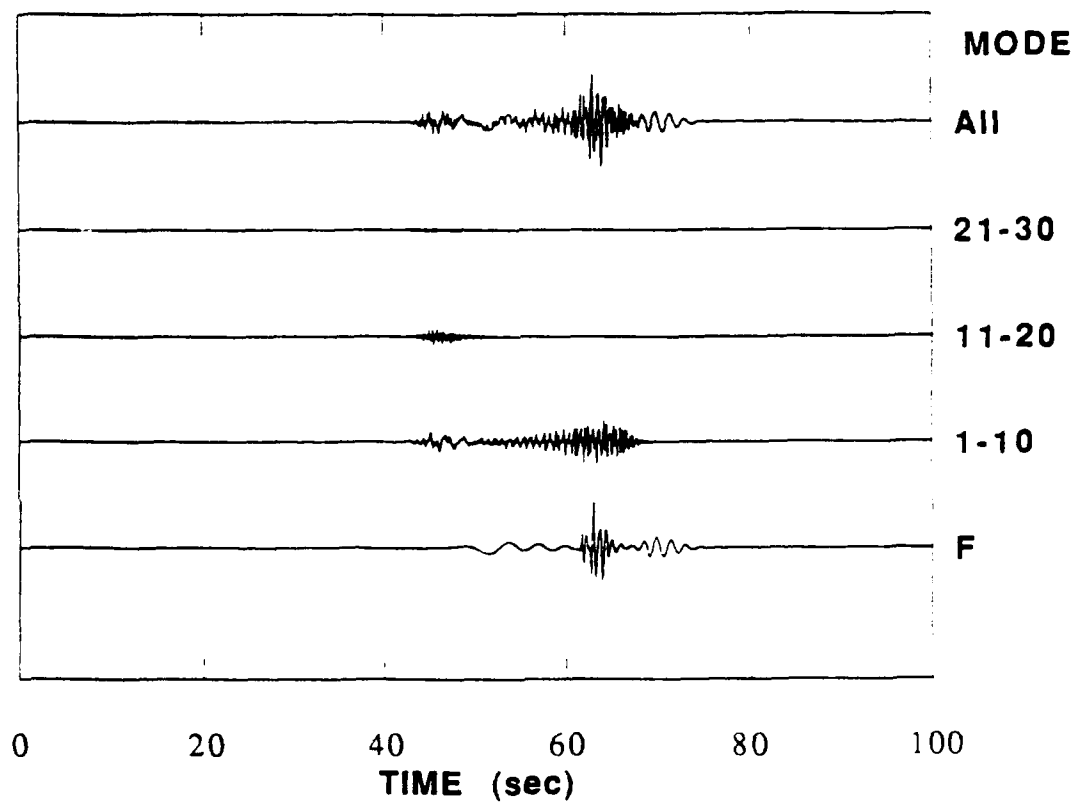
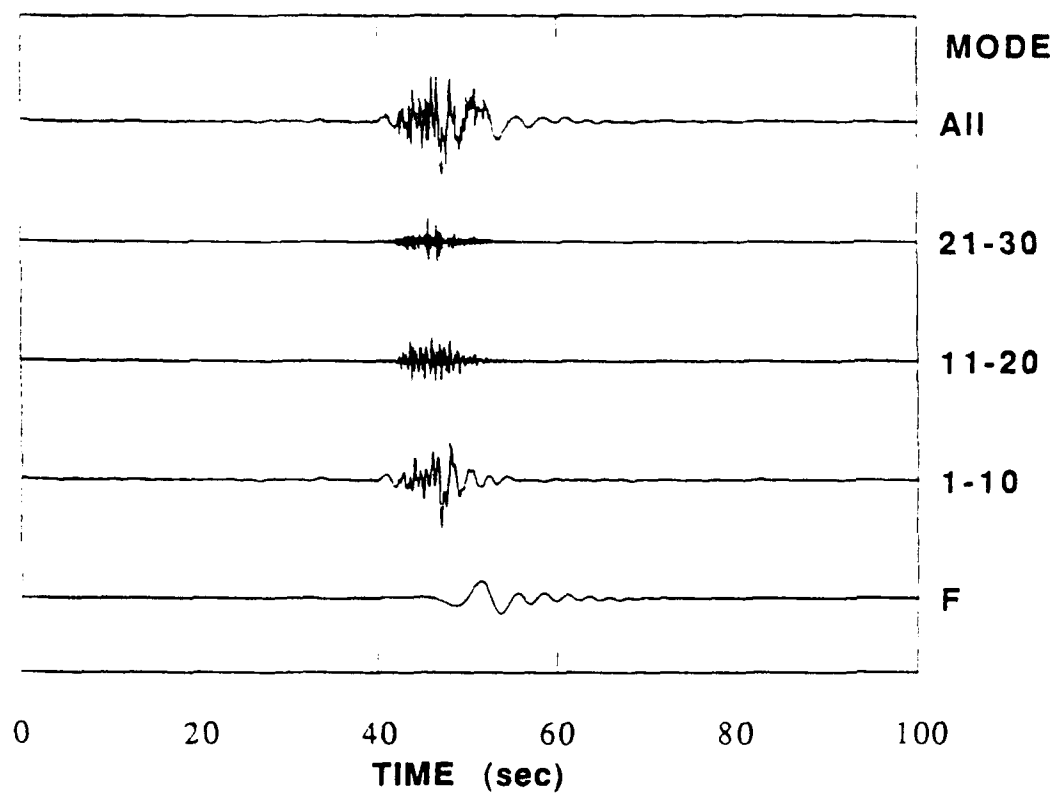


Figure 2: Energy layer distribution for different modes at 1 Hz. Energy of each mode is normalized to 1.



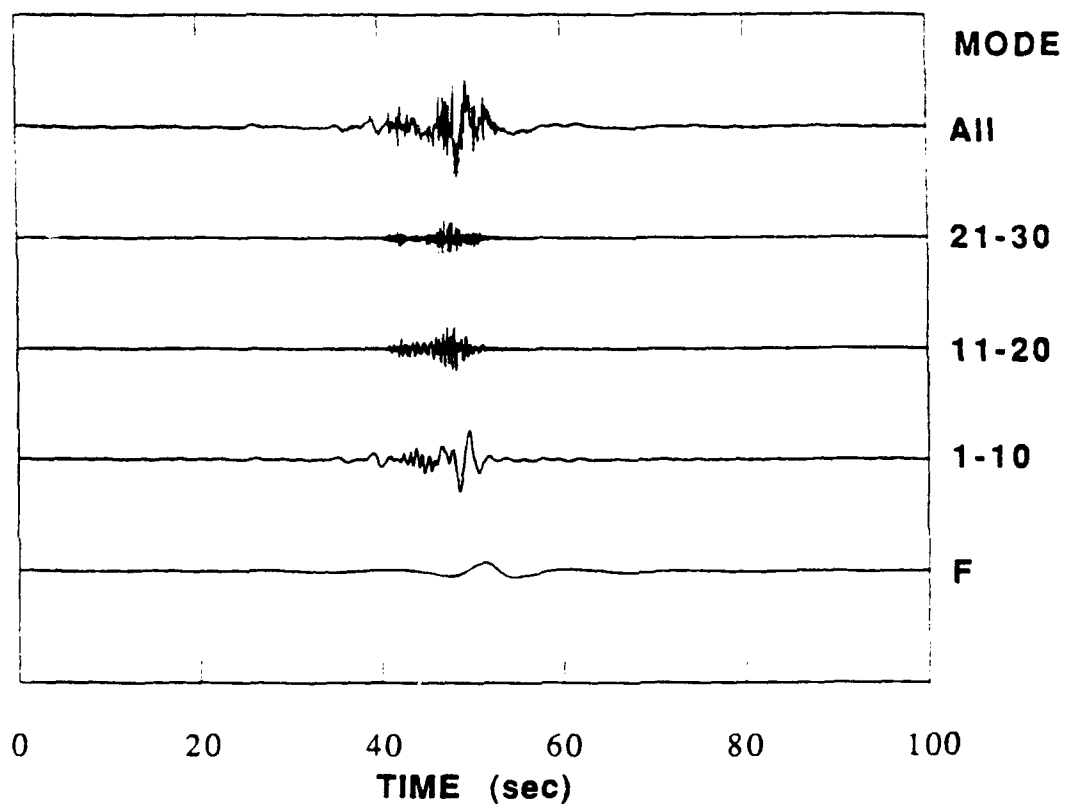
(a)

Figure 3a: Synthetic vertical component seismograms of Lg and Rg by mode summation. Contributions from fundamental mode, modes 1 to 10, modes 11 to 20 and modes 21 to 30 are compared with total mode summation. Source depth 1 km.



(b)

Figure 3b: Same as Figure 3a with source depth 10 km.



(c)

Figure 3c: Same as Figure 3a with source depth 20 km.

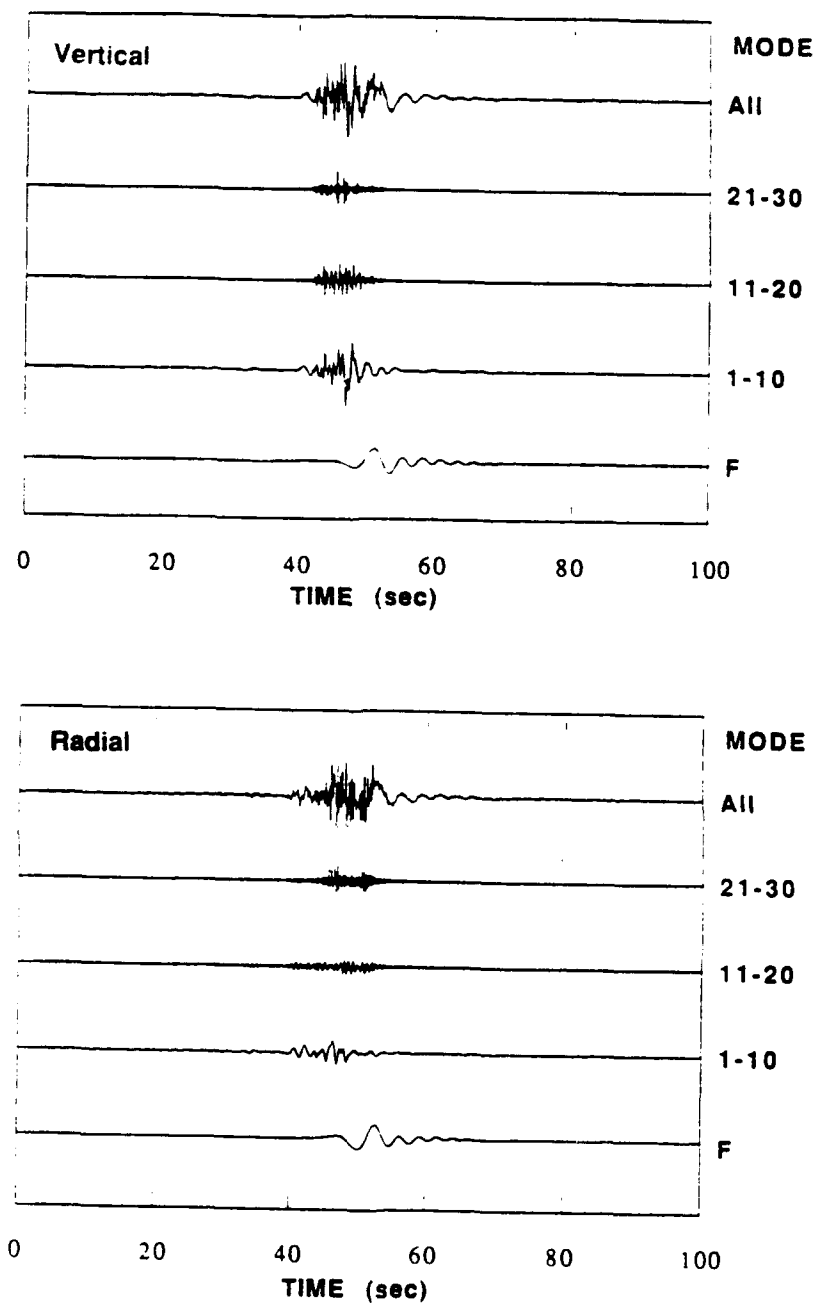


Figure 4: Synthetic vertical (top) and radial (bottom) component seismograms of Lg and Rg with source depth 10 km by mode summation. Contributions from fundamental mode, modes 1 to 10, modes 11 to 20 and modes 21 to 30 are compared with total mode summation.

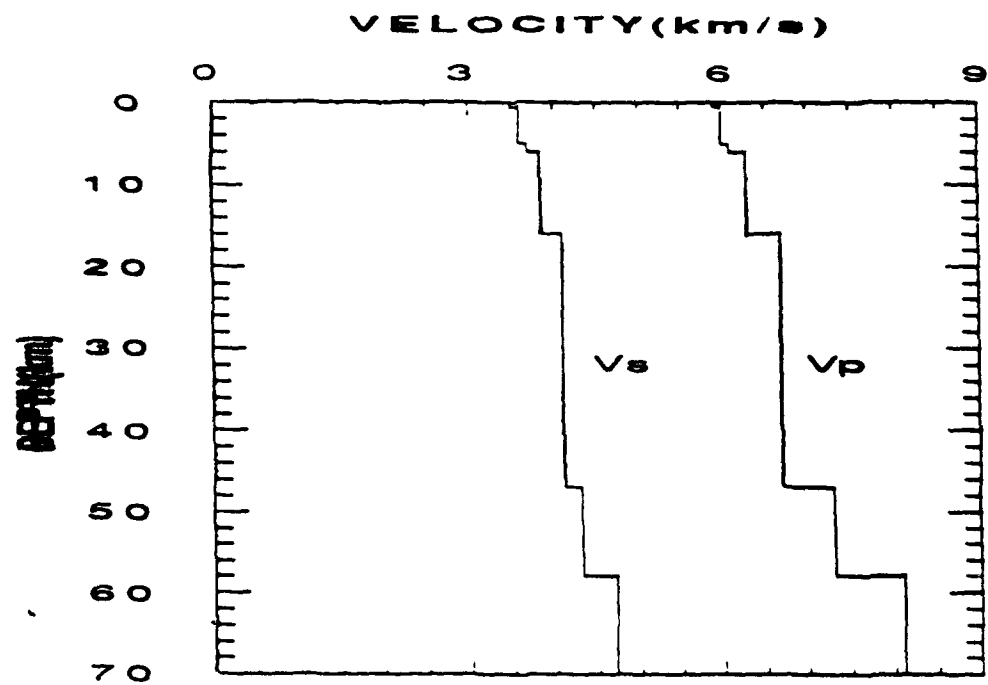


Figure 5: Velocity model for Scandinavia.

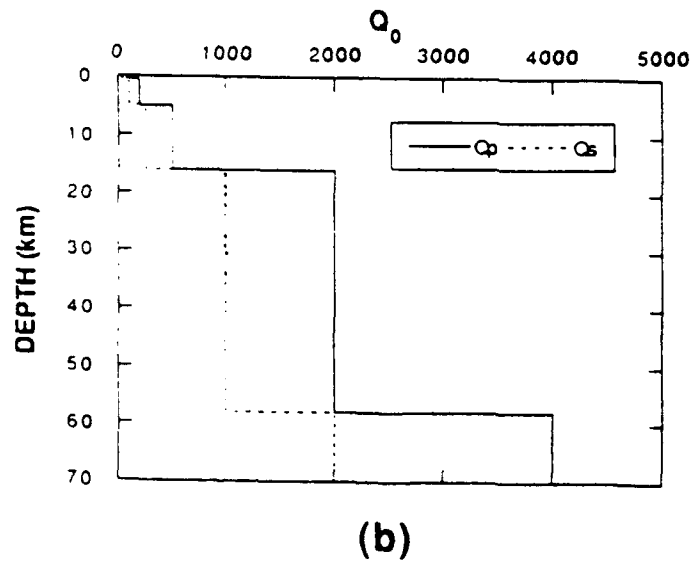
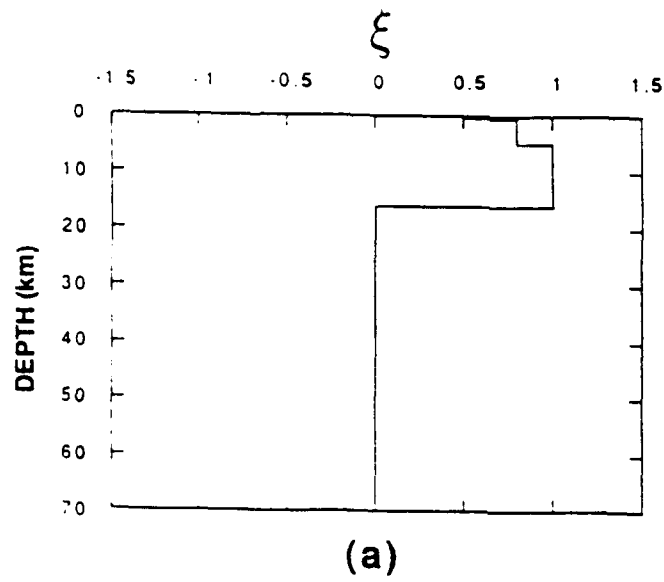
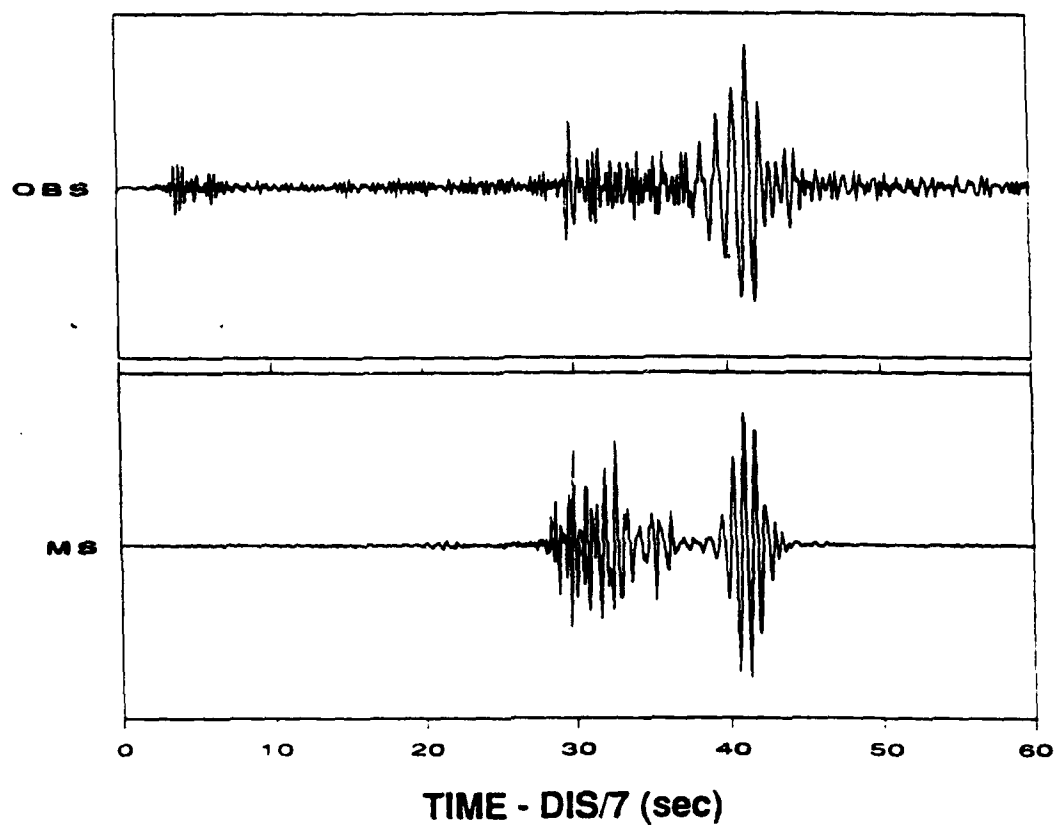
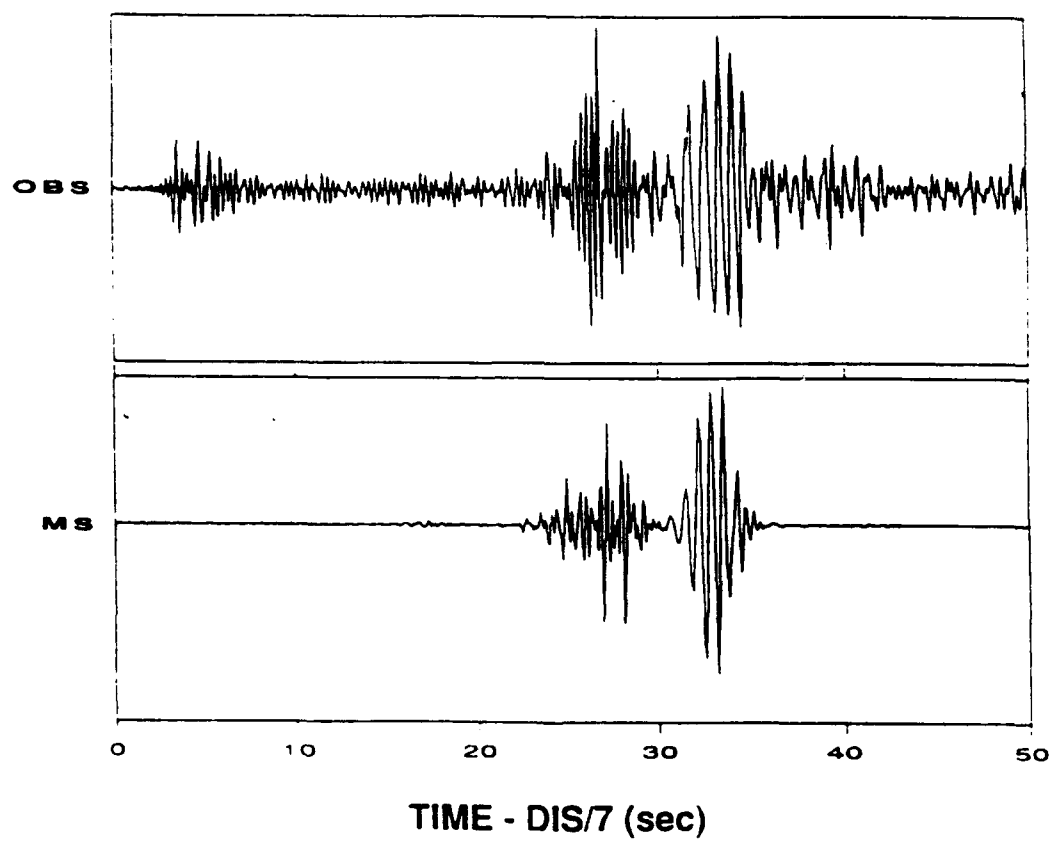


Figure 6: Frequency dependent Q model for Scandinavia. $Q = Q_0 f^\xi$ (a) ξ versus depth. (b) Q_0 versus depth. It is assumed that $Q_P = 2Q_S$.



(a)

Figure 7a: Comparison of observed and synthetic seismograms of Lg and Rg waves for quarry blast at Leningrad recorded at the FINESA array. Distance 250 km.



(b)

Figure 7b: Same as Figure 7a with distance 200 km.

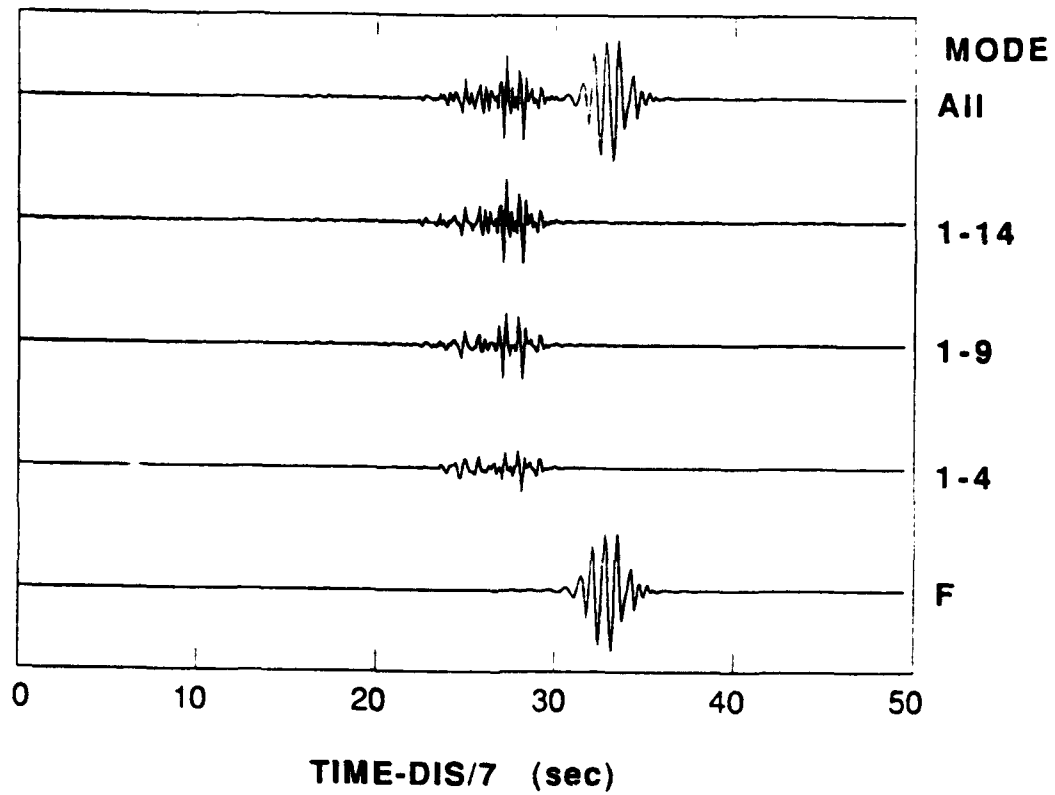
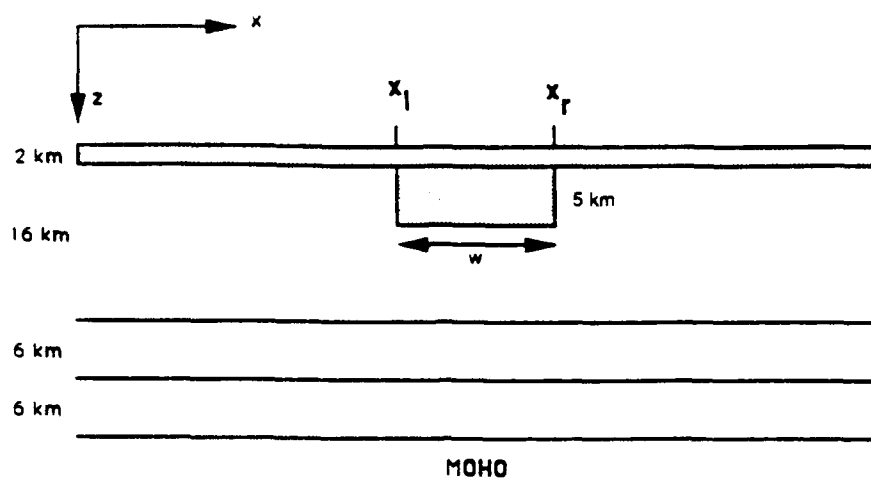
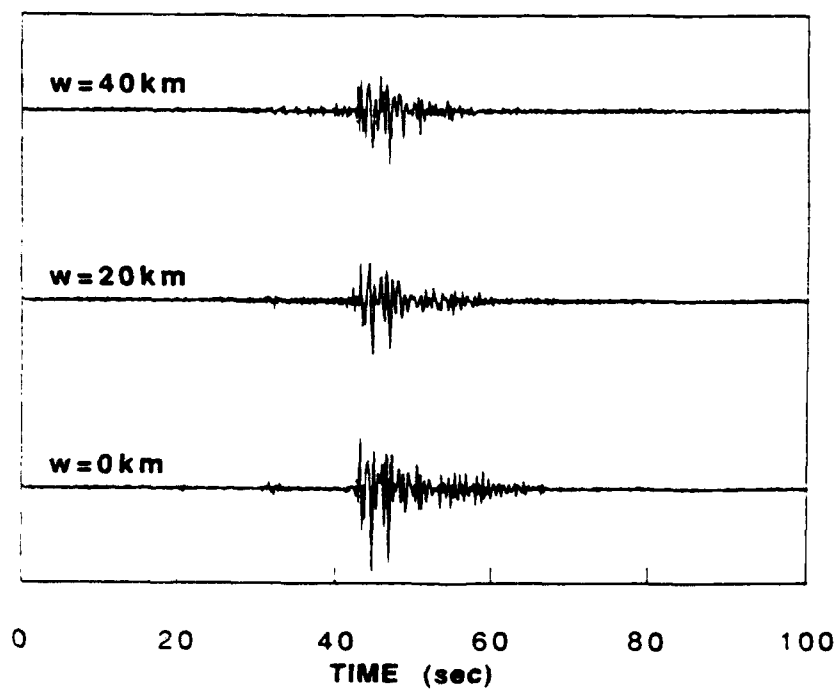


Figure 8: Mode analysis of quarry blast recorded at the FINESA array at distance 200 km. Summation of fundamental mode, modes 1 to 4, modes 1 to 9, modes 1 to 14 and all modes are shown.

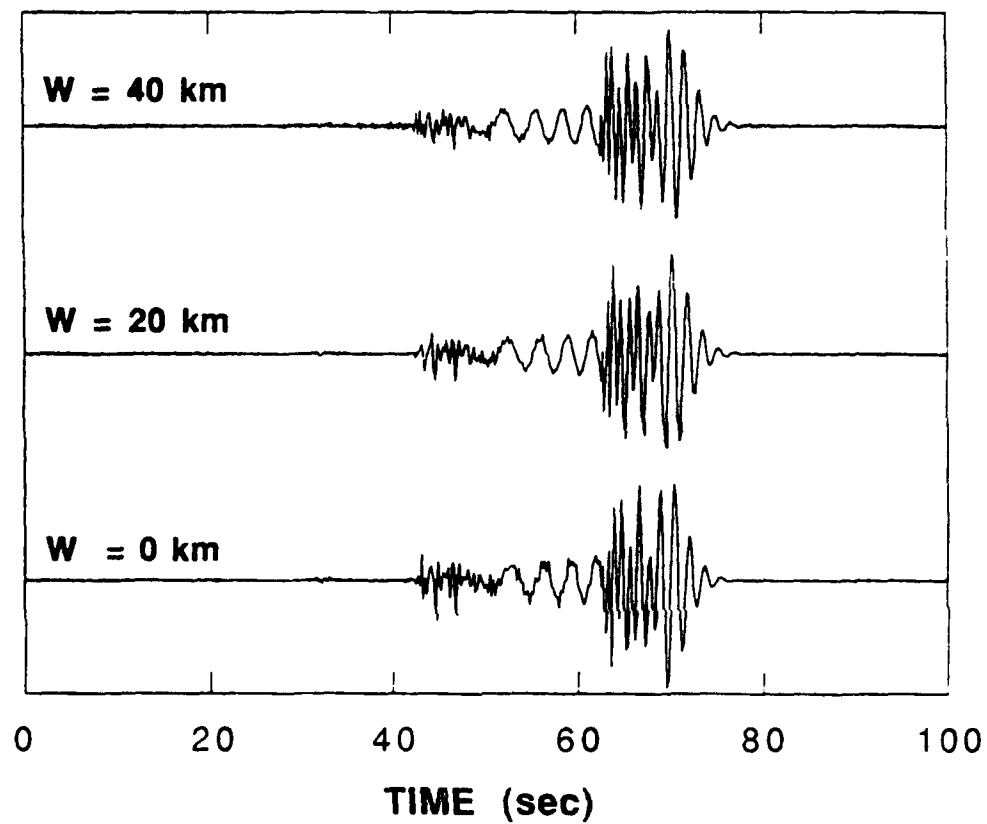


(a)



(b)

Figures 9a,b: Propagation of Lg and Rg waves across a sedimentary basin. (a) The basin model. (b) The vertical component seismograms for Lg phase computed by the coupled mode method in the frequency range 0-2.5 Hz. The cases of no basin ($W = 0$), a 20 km wide basin and a 40 km wide basin are shown.



(c)

Figure 9c: The vertical component seismograms for Lg and Rg phase computed by coupled mode method in the frequency range 0-2.5 Hz. The cases of no basin ($W = 0$), a 20 km wide basin and a 40 km wide basin are shown.

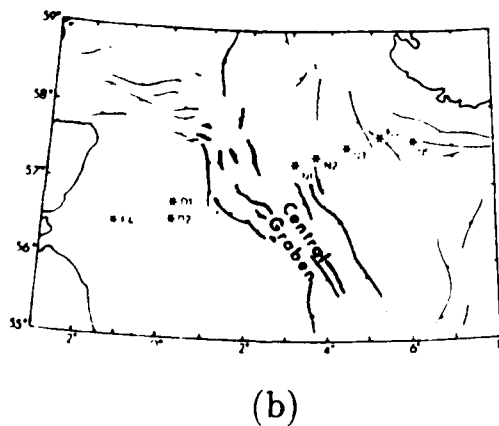
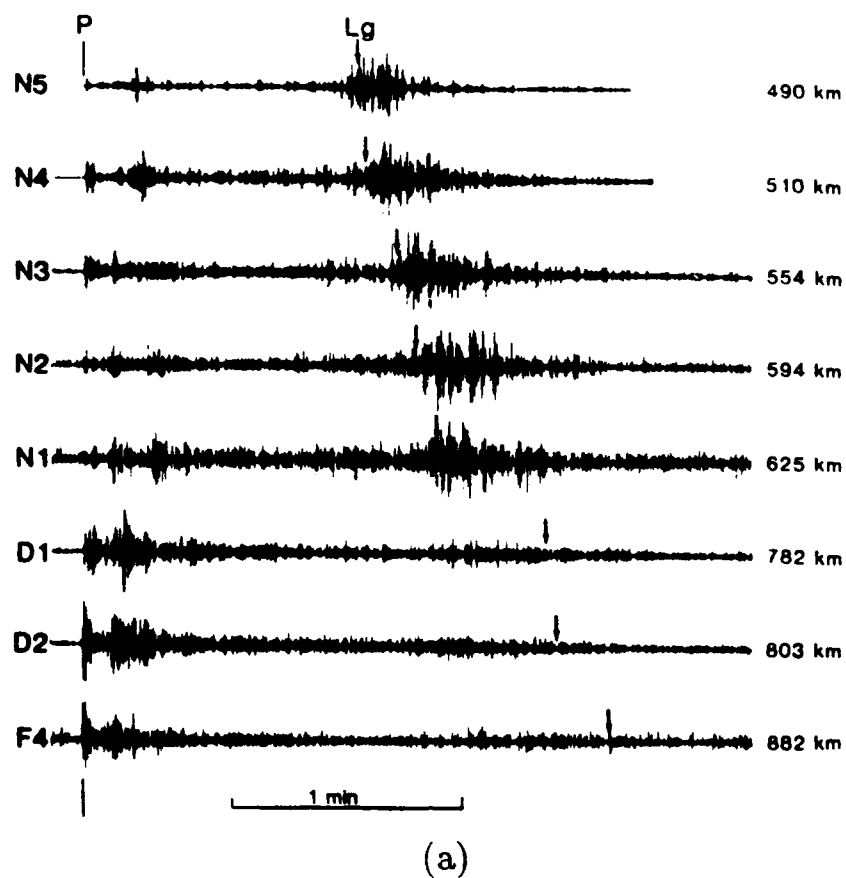


Figure 10: (a) Seismograms from the refraction shots in the central graben zone. Each trace is normalized to its maximum amplitude and aligned on the P-wave onsets. An arrow indicates a group velocity of 3.5 km/s corresponding to Lg arrivals. (b) map of the central North Sea basin and the position of the shots (star). (After Kennett and Mykkeltveit, 1984.)

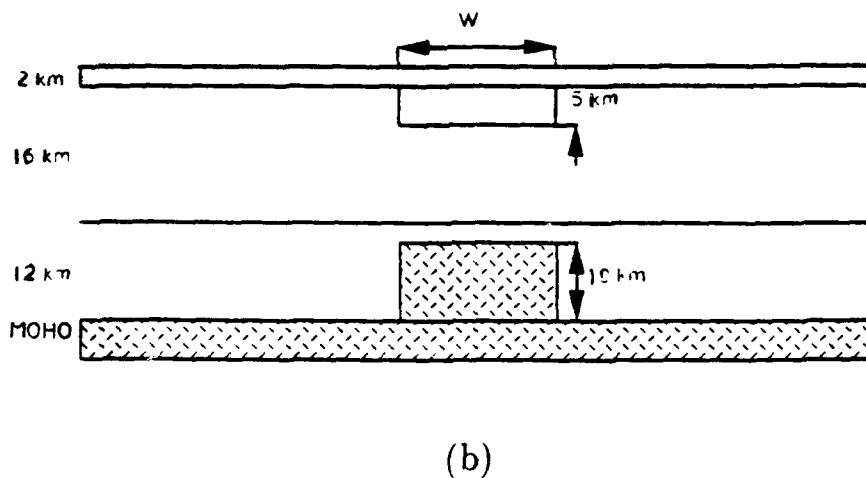
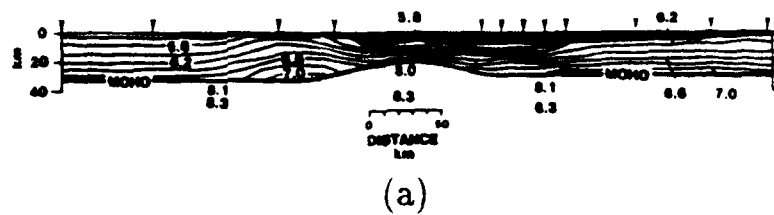


Figure 11: (a) Cross-section of structure across the central graben with velocity contour. Sediments slashed. (After Barton and Wood, 1984.) (b) Reference velocity structure used to model the central graben of the North Sea. (c) Illustration of the model for the central graben crustal pinch.

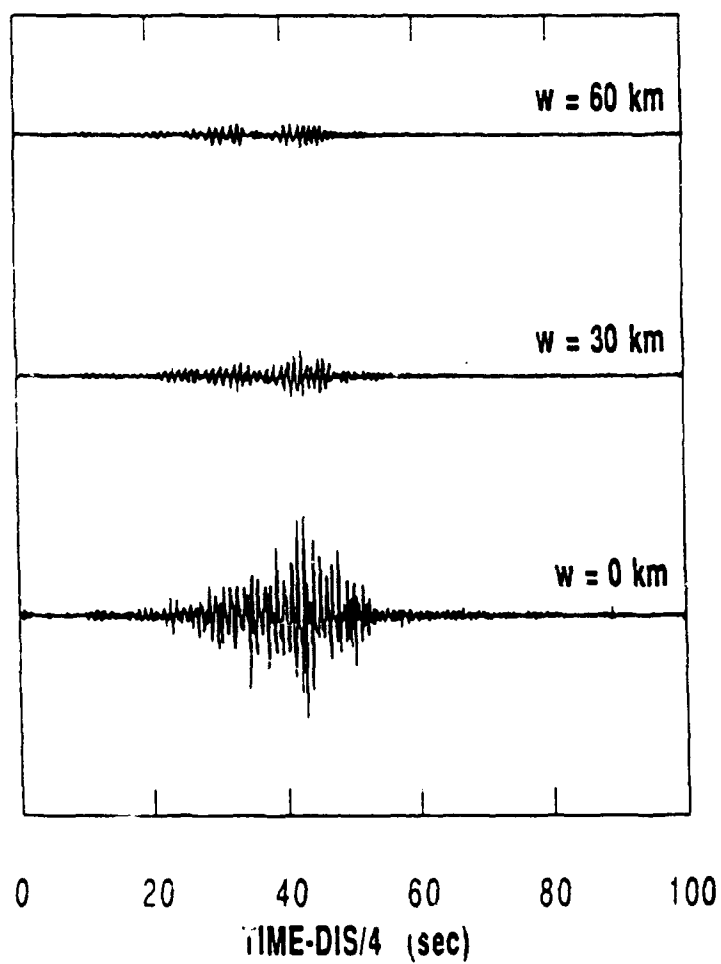


Figure 12: The vertical component seismograms for the Lg phase across the central graben of the North Sea model. Distance is 600 km. The case of 0, 30 km and 60 km wide central graben are shown.

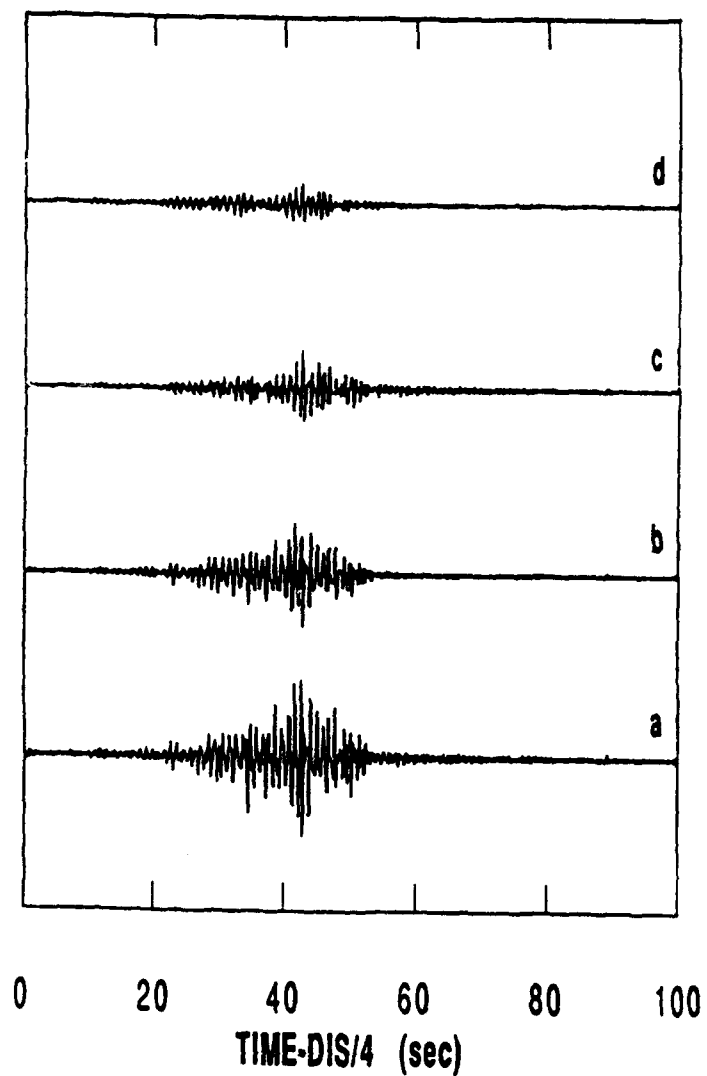


Figure 13: Effects of the lateral structure changes on Lg wave propagation in the North Sea case. a: flat-layered. b: sedimentary basin thickening. c: Moho uplift. d: both sedimentary basin thickening and Moho uplift. Distance is 600 km. Width of structure variation is 30 km.

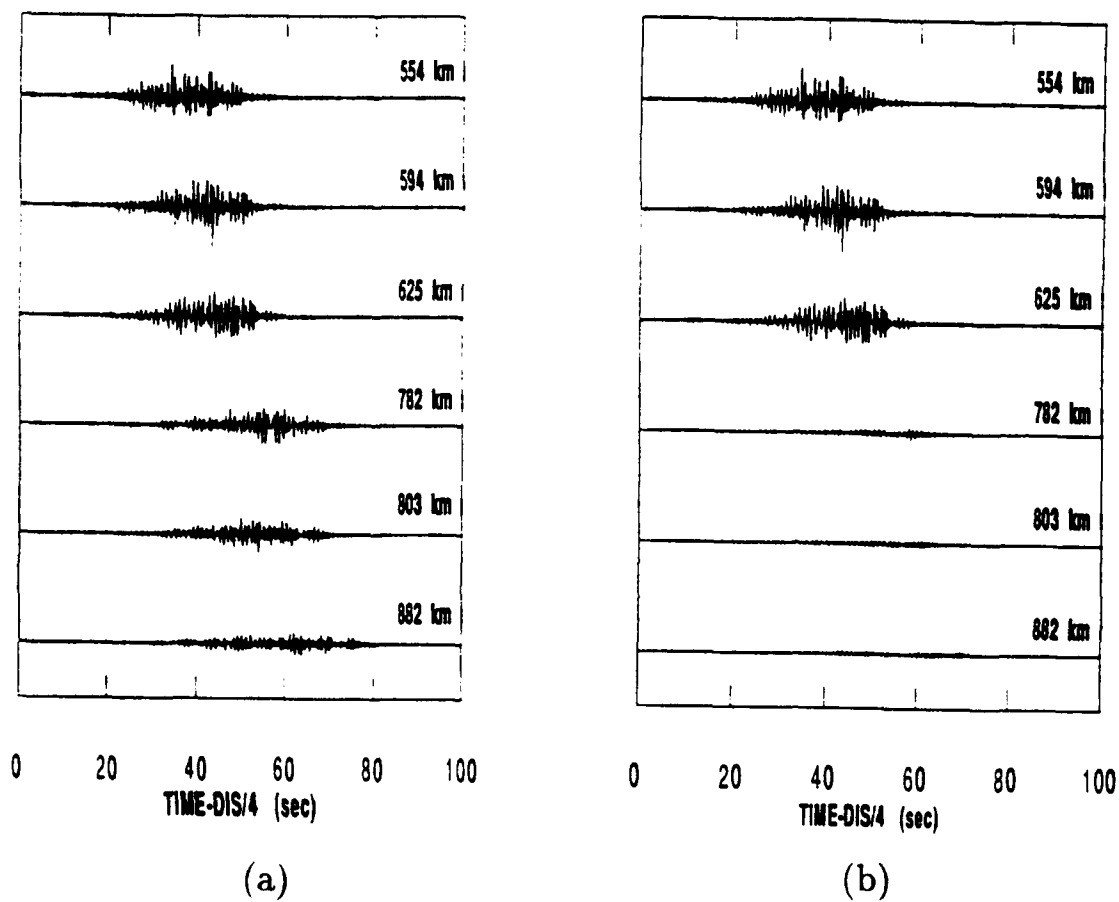


Figure 14: Vertical components of synthetic seismograms in the North Sea area. The distances is indicated at the end of each trace. The time axis is the reduced time-scale using 4 km/sec velocity. (a) Without the central graben. (b) With the 60 km wide central graben.

**REFLECTIONS FROM A RANDOMLY GROOVED
INTERFACE: ULTRASONIC MODELING AND
FINITE-DIFFERENCE CALCULATION AND
ATTENUATION OF Lg WAVES**

by

Craig A. Schultz and M. Nafi Toksöz

Earth Resources Laboratory

Department of Earth, Atmospheric, and Planetary Sciences

Massachusetts Institute of Technology

Cambridge, MA 02139

ABSTRACT

This study utilizes ultrasonic water tank modeling to examine three-dimensional scattering trends from a random set of parallel grooves, and compares this with theoretical results obtained from two-dimensional finite-difference calculations. Ultrasonic laboratory modeling is carried out using computer-controlled source and receivers with an aluminum block submerged in a water tank. The block's upper interface is plane for the reference model and grooved for the test model. The grooves measure about one-third the center source wavelength and have a Gaussian distribution with a mean of 1 wavelength and a standard deviation of $1/3$ wavelength. This experiment places both the source and receiver at the water's surface with the receiver array in the horizontal plane. The receiver line is then positioned at various angles to grooves. A staggered-grid finite-difference scheme is used for theoretical computations and comparisons with laboratory data. These theoretical results matched experimental data well for both the plane interface and the grooved model. Specifically, this study shows that scattering mechanisms are different for propagation normal to grooves than those parallel to the grooves. In the first case scattering takes place in the form of point diffractors. This causes reduction of the specular reflections. Amplitudes decrease by more than 60%, relative to a plane interface, when the incidence angle exceeds 45° . "Snapshots" of finite-difference synthetics helped to clarify details of scattering. In the second case, where the wave front is parallel to the grooves, scattering takes the form of guided head waves and continuous diffractions giving rise to constructive and destructive

interference. This gives the illusion of "broken" reflectors at depth. Amplitude differences appear as large oscillations about a zero mean as head waves refract individually along each groove radiating energy back into the sagital plane.

INTRODUCTION

The scattering of a seismic wave from irregular interfaces has become a topic of critical importance in understanding nonuniform, low amplitude arrivals which tend to complicate ocean seismograms. A number of basic theoretical approaches have been developed to model this scattering. When interface irregularities are small with respect to the seismic wavelength, small perturbations to velocity and density allow a single scattering approximation. Kennett (1972) and Kuperman and Schmidt (1989) have applied the Born approximation to 2-D cases. Prange (1989) has perturbed material parameters and interface height to describe 3-D scattering from randomly rough interfaces in terms of simple matrix operators. Both techniques have the advantage of separating the scattered wavefield from the background field. However, when the size of an interface irregularity approaches the incoming wavelength and impedance contrasts are large, the above approximations break down and complete waveform modeling must be introduced to understand the multiply scattered waves. This involves implementing full waveform numerical techniques such as the discrete wavenumber-boundary integral (Bouchon *et al.*, 1989), boundary element (DeSanto, 1985; Campillo and Bouchon, 1985; Paul and Campillo, 1988), or finite-difference (Virieux, 1986; Bayliss *et al.*, 1986; Stephen, 1988) methods. Stephen (1988) gives an excellent summary of current acoustic-elastic finite-difference techniques, and Axilrod *et al.* (1990) compares run time and accuracy between the various discrete wavenumber techniques. Although computational constraints usually require two-dimensionality, spreading factor corrections can

give reasonable amplitude data for comparison with three-dimensional point sources. Unfortunately, the inability of full waveform techniques to model three-dimensionally irregular interfaces is difficult to avoid. In this respect ultrasonic modeling has become an important tool for 3-D modeling, approaching the geometrical, source, noise, and material property control enjoyed by the numerical techniques above.

This study utilizes ultrasonic water tank modeling to examine three-dimensional scattering phenomena from a random set of deeply cut parallel grooves, labeled as a "random diffraction grating," and compares them with theoretical results obtained from numerical calculations. These grooves measure about one-third the incoming wavelength and have a Gaussian spatial distribution. These properties place the interface in the "full waveform zone" of Aki and Richard's scattering classification (Aki and Richards, 1980). Finite-difference modeling is therefore incorporated in the two-dimensional scattering case, with a seismic line perpendicular to groove strike. These synthetics also avoid the source-receiver effects that arise in the experimental data. Amplitude versus distance (*AVD*) curves then show the reflected amplitude variations in both the two- and three-dimensional grooved cases.

The random diffraction grating, in this case with "V" shaped grooves, may be related to many different structural regions. In extensional zones, such as the Basin and Range province of the western United States, extensive normal faulting occurs over short distances. This may leave jagged boundaries between the layers severed by faulting. Mid-ocean ridges and continental rifting areas with extensional faulting may similarly result in irregular interfaces,

giving the effect of elongated grooves. In addition, poorly understood deep boundaries, such as the Mohorovičić discontinuity, may be highly irregular, possibly explaining coherent noise encountered on short-period seismograms. Similar situations exist in all frequency ranges including the ultrasonic range investigated here.

ULTRASONIC MODEL DESCRIPTION

Ultrasonic modeling is carried out in our in-house water tank, where computer-controlled transducer holders can move the source and the receiver in all coordinate directions. An aluminum block with 30×30 cm area and 15 cm height is used as the ultrasonic tank model. This model has physical properties similar to upper crustal rocks, thus giving a large impedance contrast with water and large reflected amplitudes.

Figure 1 shows a two-dimensional view of the block studied. Figure 1a shows the control case with a plane interface on both the upper and lower boundaries. Figure 1b illustrates the block with an irregular upper interface. The interface consists of parallel "V" shaped grooves, each with a constant depth of 3 mm and a 60° lower acute angle. The grooves form a Gaussian distribution with a 1 cm average standard deviation of 3 mm, and the constraint that grooves do not overlap. Due to this spatial randomness the interface is termed a "random diffractor grating." Although the slope discontinuities and steepness of each groove allow for local multiple scattering effects, we focus only on the interference caused by the groove distribution as a whole.

EXPERIMENTAL METHODS

Ultrasonic water tank modeling involves submerging a structure, in this case the aluminum block described above, in a water tank. Although the tank is of finite dimension, any reflection from its sides arrives outside the desired time window. Piezoelectric transducers act as the source and receiver. A vertically polarized cylindrical transducer generates the sharp pulse that is important in resolving multiple scattered trends. However, in making the source impulsive, the source radiation pattern becomes a strong function of the angle from the axis. This pattern will be important later in comparing experimental amplitudes with synthetic results. For now we only note that a large amplitude oriented downward in the radiation pattern renders amplitudes in the first few traces useless. These traces are therefore muted from the ultrasonic results.

Placing the transducers just beneath the surface eliminates scattering from the source and receiver supports. Unfortunately, this source position distorts recorded wave amplitudes as the incident and surface reflected waves interact near the receiver. The analysis of this effect discussed in detail in the next section, shows that, although the surface distorts the appearance of the seismogram as a function of source receiver separation, it has little effect on the comparison of relative amplitudes between different interfaces.

The experiments involve a single source and a line of multiple receivers. As shown in Figure 1, the source is positioned over the interface, 5 cm from the block's edge. The receiver array begins at the source and extends 5 cm past the opposite corner with 2.85 mm

spacing. The source wavelet is a narrow band pulse with 0-300 kHz frequency range and peak amplitude at 185 kHz. The center wavelength measures 1 cm and varies from 1.5 to .5 cm over the effective frequency range of the source. The grooves therefore range from one-fifth to three-fifths the width of the incoming wavefield. All traces are averaged over 1,024 source sweeps, reducing random noise amplitudes far below that of the scattered field.

Plane Interface

Figure 2a shows the experimental results from the plane interface control block. The reflected wave appears earliest in the seismogram with the largest amplitude. Other phases are identified by looking at their apparent velocities. Refracted P-wave energy is barely identifiable at this scale, while the shear head wave exhibits much larger excitation. This is common with acoustic-elastic boundaries as normal displacement and normal tractions at the boundary have major components in the direction of shear head wave displacement. Due to its phase shift and large amplitude, this head wave interferes with the reflected wave amplitudes destructively and then constructively over a large distance. Reflected amplitudes cannot be studied in this range.

Following the primary reflection, diffractions occur from both corners of the block. The hyperbolic trend and limiting water velocity at large distances identify the diffraction nearest the source. The opposite corner diffraction appears at about 265 μs . The low energy bottom of the block reflection arrives at 190 μs . Due to the high acoustic impedance, one

reverberation from within the block is also observed at 230 μs . The first water multiple is muted along the top of the seismogram starting at 250 μs .

Grooved Interface

Three groove geometries are studied in this section. We begin by examining the two-dimensional diffraction grating. Turning to the limiting 3-D case, with the grooves parallel to the seismic line, we take advantage of the simplified geometry to understand the different style of scattering. These two limiting cases become very valuable because they form a tool for explaining scattering phenomena observed in the third case, where the grooves strike is diagonal to the source-receiver line.

Perpendicular to the Grooves

Figure 3a shows the seismogram recorded along a receiver line oriented perpendicular to the groove strike. The primary reflected wave still dominates the seismogram. However, its amplitude varies nonuniformly as scattered energy interacts with and trails the initial reflection. These scattered arrivals persist until the seismogram ends. Comparing these traces to those in the plane interface case suggests that the grooves completely obstruct both *S* and *P* head wave propagation. Some of this energy most likely appears as time-delayed low energy arrivals.

Scattered energy, immediately following the primary reflection, exhibits distinct trends.

Hyperbolic arrivals (all originating within the primary reflection) appear, paralleling the trend of the corner diffraction identified in the control case. Since each hyperbola follows a *point diffractor trajectory* with a limiting water velocity, these arrivals appear to be multiple scattered diffractions originating from the grooves. The difficulty in correlating any one diffraction with a specific scatterer suggests that each groove acts as a complex multiple diffractor. Furthermore, the energy coalesces into a narrow wedge of high amplitude trailing the primary reflection, causing a large amount of interference. Although the bottom of the block reflections are still identifiable, the larger amplitude diffractions muffle their presence. Migration may act as a tool in bringing out the bottom of the block reflector as diffractions collapse back into grooved secondary sources.

Parallel to the Grooves

The simplest three-dimensional case arises when the seismic line extends parallel to the groove strike. As shown in Figure 4a, scattered energy appears following a large amplitude reflection from the irregular boundary. The trends, although taking the form of continuous hyperbolic curves, differ greatly from the two-dimensional situation. The hyperbolas do not originate within the primary reflected wave. Instead, they intersect the first trace with a distinct time delay and tend to parallel the primary reflection at small offsets. At larger offsets, these trends converge on the primary reflection instead of diverging like the point diffractors in the two-dimensional case. This smears the primary reflected wavelet so that

it shows little similarity to the incident wavelet. The convergence of these hyperbolas to one another results in additional interference, giving the appearance of broken reflectors at depth, not an irregular interface.

The *S* head wave is still prominent in the profile. At later times secondary arrivals paralleling the initial head wave branch also appear. Each later branch can be traced back to its origin which lies within the trailing hyperbolas described above. This intersection with the hyperbolas smears the constructive-destructive interference between the primary reflected and earliest head wave to larger times.

The above observations suggest that each individual groove acts as a continuous diffractor of energy. The geometry for a continuous groove diffractor allows a number of paths to exist, each having slower moveout than the primary reflected arrival. This explains the observed convergence of individual hyperbolas at large distances. In addition, the parallel head wave arrivals and the extension of constructive head wave interference both suggest that each groove acts as a head wave guide, continuously releasing energy back into the vertical plane of the receiver array.

Diagonal to the Grooves

Utilizing our knowledge from the two limiting cases described above, one can understand scattered trends recorded at intermediate receiver array azimuths. We now describe the trends on a seismic line positioned diagonal to the grooves.

Figure 4b shows the seismic data recorded with a receiver line oriented 45° to groove strike. The trends display more complexity than the first two cases. The primary reflection contains the largest amplitude, and scattered arrivals again form hyperbolic trends. Some hyperbolas never intersect the primary reflection but instead intersect the first trace with some time delay. Other trends originate within the primary reflection and appear more as point diffractions from the interface. In both cases the hyperbolas are divergent from the primary reflection branch, with a slope between the limiting cases studied previously. Head waves also appear, but they dissipate within a few traces after they are formed.

The two limiting cases above suggest an explanation for these observed trends. Components of both cases are clearly present, suggesting that scattering from a random diffraction grating can be explained in terms of the multiple point diffraction and head wave obstruction observed in the two-dimensional case along with the continuous diffraction and head wave guidance for the case parallel to the grooves. More specifically, shooting diagonal to the grooves gives the appearance of 45° dipping reflectors at depth as each groove continuously diffracts energy. However, some diffractions give the impression of interface origin. The slight persistence of head waves suggests that energy radiates into the sagittal plane as groove-guided refractions cross underneath the receiver line. Head waves propagating parallel to the seismic line are obstructed.

Amplitude Versus Distance

In this section we investigate how a random diffraction grating changes reflected wave amplitude with distance from the source. *AVD* curves for the grooved interface are compared with the amplitude curve for a plane reflector. More useful, however, is the "relative difference" in amplitude between the plane and grooved reflection. This gives an accurate measure of amplitude variation induced by the random diffraction grating.

Figure 5a shows the *AVD* curve for the plane layer control case. Destructive and constructive interference of the shear refraction affects amplitudes from the critical angle at 30° to about 40° , as marked on the graph. In the scattered cases, this destructive null and constructive buildup is greatly reduced, causing amplitude differences as high as 100% in this range. Therefore, amplitudes in this region are not studied. The measured amplitude over the two-dimensional grooved interface is also shown. Comparing the primary scattered reflection to the control case reveals a decrease in reflected amplitudes at most offsets. The reflection amplitude rises above the control case only during the *S* head wave interference zone. Notice that the grooved interface also appears to shift the head wave interference zone to larger incident angles. (Part of this offset appears to result from a difference in velocity between the two blocks and will be corrected in any future work. However, another portion of this offset may also represent anisotropy created directly by the grooved interface. This is supported by the smaller lag in crossover distance when shooting diagonal to the grooves in the next section.) The relative difference between the two curves, also shown in Figure 5a,

strongly depends on offset. Waves near normal incidence lose an average of 10–15% of their amplitude. At angles greater than 40° the difference quickly climbs to values as large as 60%. Clearly, increasing the incident angle greatly reduces reflected amplitudes.

Figure 5b plots the *AVD* curves for the three-dimensional geometries studied. In the limiting case, parallel to groove strike, an average of 15% loss in amplitude is recorded at small incident angles, most likely resulting from interference with diffractions from the nearest grooves. At larger angles, amplitudes start oscillating rapidly about the plane *AVD* curve causing relative differences larger than 80%. This oscillation is apparently due to the multiply refracted *S* head wave arrivals crossing the primary reflection. Turning to the intermediate case, with grooves striking 45° under the seismic line, scattering causes reflected amplitudes to rise by about 15% at lower incident angles. The amplitude decreases below the control case only after the refractive critical angle. At large angles amplitudes are very similar to the two-dimensional case, approaching 50–60% lower amplitude at angles greater than 45° .

In all cases, the *AVD* curves establish 10–15% amplitude variations at low angles of incidence. Increasing the incident angle reduces amplitudes by as much as 60%. Although this maximum deviation of 60% appears similar between models, *AVD* signatures vary greatly between different groove azimuths.

COMPARISON WITH FINITE-DIFFERENCE

Two-dimensional finite-difference techniques allow full waveform modeling in both water and the aluminum block. In addition, source-receiver distortions, which noticeably affect experimental data, are not present in these synthetics. In the next section we investigate the nature of distortions present in the experimental tank. These distortions are then applied, using various approximations, to the finite-difference synthetics. Amplitudes are then compared to the experimental results of the previous section.

Finite-Difference Algorithm

One of the fundamental problems with the finite-difference technique occurs when modeling a sharp interface between two media with widely varying elastic constants. Two difficulties in particular arise when dealing with the acoustic-elastic boundary on a non-staggered grid. First, a boundary condition with continuous normal stress and displacement must be applied. For a non-staggered grid this boundary condition must be set up artificially by the programmer. Second, large impedance contrasts can cause large instabilities at the interface rendering some results useless (Stephen, 1988). Fortunately, the staggered grid solves these two problems naturally by offsetting horizontal and vertical displacement grids; no explicit boundary condition is required. However, the boundary condition is not absolutely abrupt and is approximated over one finite grid spacing, allowing some averaging to occur. The models in this paper were created using a stress-displacement finite-difference algorithm.

This algorithm was adapted to an nCUBE2 multiple instruction, multiple data, parallel processor.

This staggered-grid scheme is stable for the high impedance contrast, acoustic-elastic boundary encountered in this study. First-order absorbing boundaries developed by Lindman (1975) and later introduced to geophysics by Randall (1989) are implemented. These boundaries give reflection amplitudes less than one percent the incident wave amplitude at all angles less than 90° .

The synthetic model parameters were chosen to minimize grid dispersion. The grid measures 960 by 813 points with a grid spacing of .375 mm. The time increment is approximately .03 μs , where the actual sampled time interval is .4 μs . Therefore the shortest wavelength of 5.0 mm is sampled with 13 grid points. The smallest time period is sampled 110 times, which is well within the stability limits. A windowed Ricker wavelet with a 0–300 kHz frequency range and 185 kHz peak amplitude is used to approximate the transducer source wavelet.

Numerical Results

Figure 6 shows two finite-difference time slices of a wave reflecting from the plane-bounded block (Figure 1a). The grey scale plots vertical displacement resulting from a vertical point source and is scaled to one-half the maximum amplitude on the grid. Each feature present in the experimental data is identified in Figure 6. Figure 7 gives similar time slices for the random diffraction grating. Scattered energy takes the form of large amplitude diffractions

trailing the primary reflected wave. A large amount of reverberative energy trapped within the block also results from transmission through the irregular boundary. A few broken multiple head waves project from the primary reflected wave like faint spears. This suggests that each groove acts as its own secondary source for head wave energy, which the remaining grooves quickly obstruct.

Figure 2b presents the synthetic pressure record for the plane-bounded aluminum block and compares this with the experimental recordings. The synthetic emphasizes diffractions and refractions created by the block corners, again demonstrating how a slope discontinuity can create head waves and diffractive waves. Figure 3b illustrates synthetics recorded over the grooved interface. Scattered trends are accentuated. These trends are similar to those observed in the experimental data with a narrow zone of coalescing diffractions trailing the primary reflected wave. Lower amplitude, backscattered energy appears sloping toward a larger offset. Figure 8 gives the pressure field recorded over the same block, but with a volume source. The volume source, in comparison to the vertical point source, creates much greater backscattered diffractive energy at a large offset. Note that, although a three-dimensional spreading factor (discussed below) has been applied to both seismograms, the scattered amplitudes exhibit higher amplitude than the experimental case. Two additional first-order tank distortions must be applied to the finite-difference results before the primary reflected and later scattered arrival amplitudes can be compared to the experimental data of the previous section.

A total of three corrections applied to the volume source synthetics for comparison with experimental data. The first correction accounts for the transducer source radiation pattern and the receiver sensitivity pattern; both vary strongly as a function of inclination. We assume that the energy contributing to the primary reflected amplitude comes from a small zone about the path that a plane-reflected wave would follow. Each trace is multiplied by a single scaling factor based on the transducer source amplitude in the direction of that path. This geometrical correction is valid only in the vicinity of the primary-reflected wave as later scattered arrivals do not follow this assumed path. This correction demonstrates the distortion of experimental scattered arrivals as a function of a ray's emergence from the source. Notice that the amplitude of head waves and the bottom of the block reflections are not properly corrected because these paths also differ from the specular field. The second correction, already implemented above, involves correcting the 2-D synthetic data for 3-D spreading. If the scattered wave travels exclusively in the water, multiplying amplitudes by an $r^{-1/2}$ factor corrects for spreading of the specular wavefield. In this case, r is the total distance traveled in the water.

The third correction factor involves correcting for wavefield interference at the water's surface. The boundary conditions at the free surface give the pressure field near the receiver.

$$P = \exp[-i\omega t + ik_x x](\exp[ik_z z] - \exp[-ik_z z]), \quad (1)$$

assuming a plane incident wave with wavenumber $\underline{k} = (k_x, k_z)$. Taking z to be small the

pressure depends only on vertical wavenumber and receiver depth,

$$P \propto |k|z \cos(\alpha), \quad (2)$$

where α is the incident angle of the wave impinging on the receiver, measured from normal. Notice that the pressure field goes to zero at the surface as expected. This correction is applied using the geometrical ray angle approximation summarized above for the first correction. Expression (2) shows no amplitude distortion at normal incidence but accounts for one-half the wave amplitude at a 60° incident angle. This corresponds to the last receiver on the profile. Note that the relative difference in amplitude due to scattering is not changed (to first-order) by the above distortions in the tank since the distortions appear as identical multiplicative factors in both the scattered and the plane layer case (the corrections factor out and cancel in the relative difference calculation).

It is important to emphasize that the corrections implemented above apply only in the vicinity of the first-reflected energy. It is difficult to determine the exact path a scattered wave traverses in traveling from source to receiver. Therefore, these corrections hold only near the specular field. Since finite-difference avoids these distortions, it may be useful for future amplitude analysis. However, the correction for spherical spreading is a good approximation only where an unperturbed wave travels exclusively in water. The 3-D spreading of diffractions are also left uncorrected. In addition, waves traveling through any part of the block, such as the bottom of the block reflections, are under-corrected.

Figures 9a and 9b show the two-dimensional experimental *AVD* curves overlaid on the

corrected finite-difference results. For a plane layer (Figure 9a) the curves agree within 15% at most angles. In the area of head wave interference, rapid changes in amplitude cause larger differences. Comparing the results for the random diffraction grating with the synthetics (Figure 9b), they match very well at wide angles. A larger disagreement, however, occurs at low incident angles where finite-difference predicts greater than 30% lower amplitudes in some regions. These differences may result from rapid changes in the transducer radiation pattern and slight variations between the filtered Ricker wavelet and the transducer wavelet. Figure 9c shows the *AVD* signature predicted by finite-difference. As expected, finite-difference predicts 5–10% more scattering about the lower incident angles than experimental data. The synthetics support a maximum amplitude change of 60% for wide angle reflections approaching 60°.

Discussion

Ultrasonic water tank experiments reveal that waves scattered from a random diffraction grating can be understood in terms of two simple models. First, in the case where the incoming wavefield travels perpendicular to the grooves, scattering takes place in the form of point diffractors and obstructed refractions. Amplitude variations relative to the the control case of a plane reflector average about 10–15% at lower incident angles (0–20°) and rise as high as 60% at angles greater than 45°. Second, in the case where the receiver array is parallel to the grooves, scattering takes the form of guided head waves and continuous diffractions,

giving the illusion of broken reflectors at depth. The relative differences reach magnitudes similar to the two-dimensional case above. However, at a large offset this difference takes the form of large oscillations about zero as multiple head waves intersect the primary-reflected wave. Diagonal to the grooves, scattering becomes a combination of trends identified in the two limiting cases above, and amplitudes show an *AVD* signature similar to the two-dimensional case.

Finite-difference modeling gives primary reflected wave amplitudes that match experimental results to within 15% over most angles in both the plane and grooved cases. However, in some small offset regions over the grooved interface, finite-difference predicted 30–40% lower amplitudes than were observed. Larger differences were also observed due to rapid variation in head wave interference zones.

Numerical calculations have since been carried out for models with different velocities, including cases where the shear velocity of the solid is above and below the *P*-velocity in water. These show distinct trends in amplitude variation and have implications for *AVD* analysis. Further studies may include the frequency analysis of diffracted and transmitted waves at the interface. In addition, the effect of migration on reducing scattered noise may serve as an interesting test for the resolving power of techniques such as Kirchhoff migration. Although this study keeps groove geometry constant to allow for careful comparison with experimental data, further studies will use more general, random interfaces to study scattering amplitudes and trends.

ACKNOWLEDGMENTS

This research was partially supported by the Defense Advanced Research Projects Agency through contract #F19628-89-K-0020, administered by the Phillips Laboratory (formerly the Geophysics Laboratory) of the Air Force Systems Command.

References

- Aki, K. and P. Richards, 1980, *Quantitative Seismology—Theory and Methods*, W. H. Freeman, San Francisco, 721–796, 1980.
- Axilrod, H.D. and J.F. Ferguson, 1990, SH-wave scattering from a sinusoidal grating: An evaluation of four discrete wavenumber techniques, *Bull. Seism. Soc. Am.*, 644–655.
- Bayliss, A., K.E. Jordan, J. LeMesurier, and E. Turkel, 1986, A fourth-order accurate finite-difference scheme for the computation of elastic waves, *Bull. Seism. Soc. Am.*, 76, 1115–1132.
- Bouchon, M., M. Campillo, and S. Gaffet, 1989, A boundary integral equation-discrete wavenumber representation method to study wave propagation in multilayered media having irregular interfaces, *Geophysics*, 54, 1134–1140.
- Campillo, M. and M. Bouchon, 1985, Synthetic SH seismograms in a laterally varying medium by the discrete wavenumber method, *Geophys. J. R. astr. Soc.*, 83, 307–317.
- DeSanto, J., 1985, Exact spectral formalism from rough-surface scattering, *J. Opt. Soc. Am.*, 12, 2202–2207.
- Kennett, B.L.N., 1972, Seismic wave scattering by obstacles on interfaces, *Geophys. J. R. astr. Soc.*, 28, 249–266.
- Kuperman, W. and H. Schmidt, 1989, Self-consistent perturbation approach to rough surface scattering in stratified elastic media, submitted to *J. Acoust. Soc. Am.*

- Lindman, E., 1975, Free-space boundary conditions for the time dependent wave equation, *J. Comp. Phys.*, 18, 66-78.
- Paul, A. and M. Campillo, 1988, Diffraction and conversion of elastic waves at a corrugated interface, *Geophysics*, 53, 1425-1424.
- Prange, M.D., 1989, Perturbation approximation of 3-D seismic scattering, submitted to *Geophysical Journal*.
- Randall, C., 1989, Absorbing boundary condition for the elastic wave equation: Velocity-stress formulation, *Geophys.*, 54, 1141-1152.
- Shortt, E.R., 1986, Laboratory borehole modeling, Full Waveform Acoustic Logging consortium, 461-470.
- Stephen, R.A., 1988, A review of Finite difference methods for seismo-acoustics problems at the seafloor, *Review of Geophysics*, 26, 445-458.
- Tang, X-M., 1989, Elastic wave radiation and diffraction of a piston source, *JASSA*, in press.
- Virieux, J., 1986, P-SV Wave Propagation in heterogeneous media: Velocity-stress finite-difference method, *Geophysics*, 51, 889-901.

APPENDIX A. ABSORBING BOUNDARY CONDITIONS

The paraxial approximation to the one-way equation is the foundation for absorbing boundaries on a non-staggered grid. This method is known in electromagnetic theory as the Enquist-Majda absorbing boundary. In elastodynamics it is better known as the Clayton-Enquist absorbing boundary. Unfortunately, the second-order Clayton-Enquist scheme is unstable for our staggered differencing scheme (when applied to the displacement field). However, the Lindman boundary condition referenced in the text is stable for a *homogeneous* elastic medium represented on a staggered grid. Unfortunately, the use of potentials makes it unstable when inhomogeneous boundary conditions are present. The water tank has water bounding all sides of a solid object. Therefore, the homogeneity requirement is satisfied and only the acoustic portion of the boundary condition is implemented.

The Lindman absorbing boundary condition attempts to adapt the one-way wave equation to larger incident angles, where the paraxial approximation breaks down. The one-way wave equation for a wave traveling in the negative x direction (applicable to the left grid boundary) can be written as

$$\left[\frac{1}{\cos \theta} \partial_x + i \frac{\omega}{c} \right] \phi(\mathbf{r}, \omega) = 0, \quad (3)$$

where θ is the angle between the incoming wavenumber and the normal to the boundary surface, c is the velocity of acoustic medium, and $k_x = \omega \cos \theta / c$. Approximating $[\cos \theta]^{-1}$

by the rational expression

$$[\cos \theta]^{-1} \simeq 1 + \sum_{i=1}^n \frac{\alpha_i \sin^2 \theta}{1 - \beta_i \sin^2 \theta}, \quad (4)$$

where α_i and β_i are constants to be determined. Substituting $\sin^2 \theta \equiv (ck_z/\omega)^2$, letting $k_y = 0$, and converting back to the time domain,

$$\left[\partial_x - \frac{1}{c} \partial_t \right] = - \sum_{i=1}^n h_i(\mathbf{r}, t) \quad (5)$$

where

$$\ddot{h}_i(\mathbf{r}, t) - \beta_i c^2 \partial_{zz} h_i(\mathbf{r}, t) = \alpha_i c^2 \partial_{zzx} \phi(\mathbf{r}, t), \quad (6)$$

and h_i is now independent of the angle of incidence and can be applied to any wave incident on the boundary. Lindman (1975) calculated the constants that minimize the reflection coefficient over the widest range of angles. Expansion to $n = 3$ gives reflection coefficients less than one percent for all incident angles less than 89° . In this case the constants become $\alpha_i = 0.3264, 0.1272, 0.0309$ and $\beta_i = 0.7375, 0.98384, 0.9996472$. Once the potential has been calculated, its gradient gives the displacement boundary value actually assigned to the grid's edge.

Large amplitude bursts from the grid corners are almost always a large problem in any finite-difference code. They are also poorly documented. We note that one stable scheme involves approximating equation A-11 directly (Sergio Kostek, pers. comm.). The left-hand side of A-4 represents the two-way wave equation. We approximate the left side with the

one-way wave equation and set the right-hand side of A-4 to zero,

$$\dot{h}_i(\underline{r}, t) - c\sqrt{(\beta_i)}\partial_z h_i(\underline{r}, t) = 0. \quad (7)$$

This is implemented with a forward difference scheme and is good to first order in grid spacing. Note that the sign preceding the second term in A-5 changes for opposite corners of the grid.

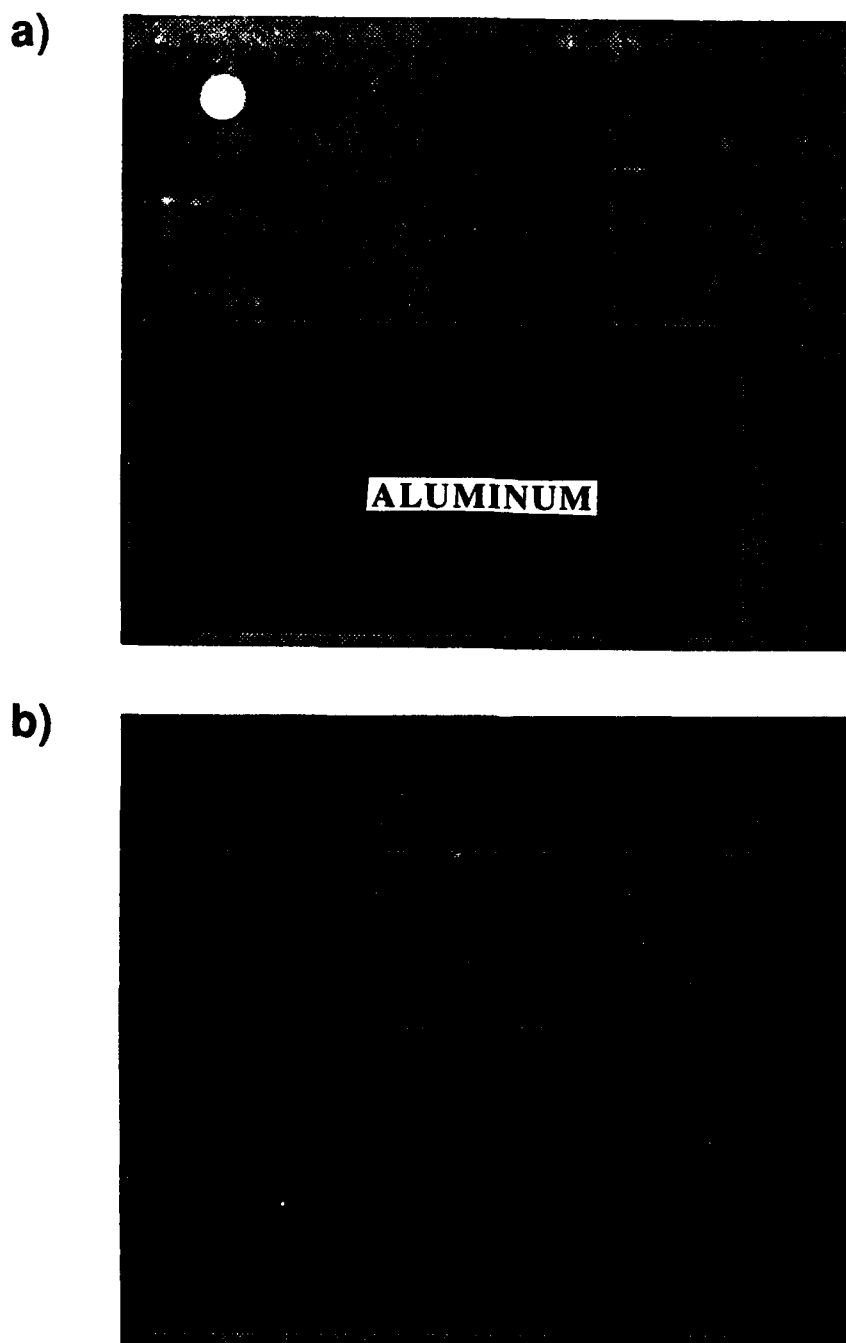


Figure 1: Two-dimensional cross-section of block geometry used for ultrasonic water tank and finite-difference modeling. (a) The control case with an upper and lower plane boundary. (b) The randomly grooved interface, looking down the strike of the grooves. The boundary in both cases is acoustic-elastic.

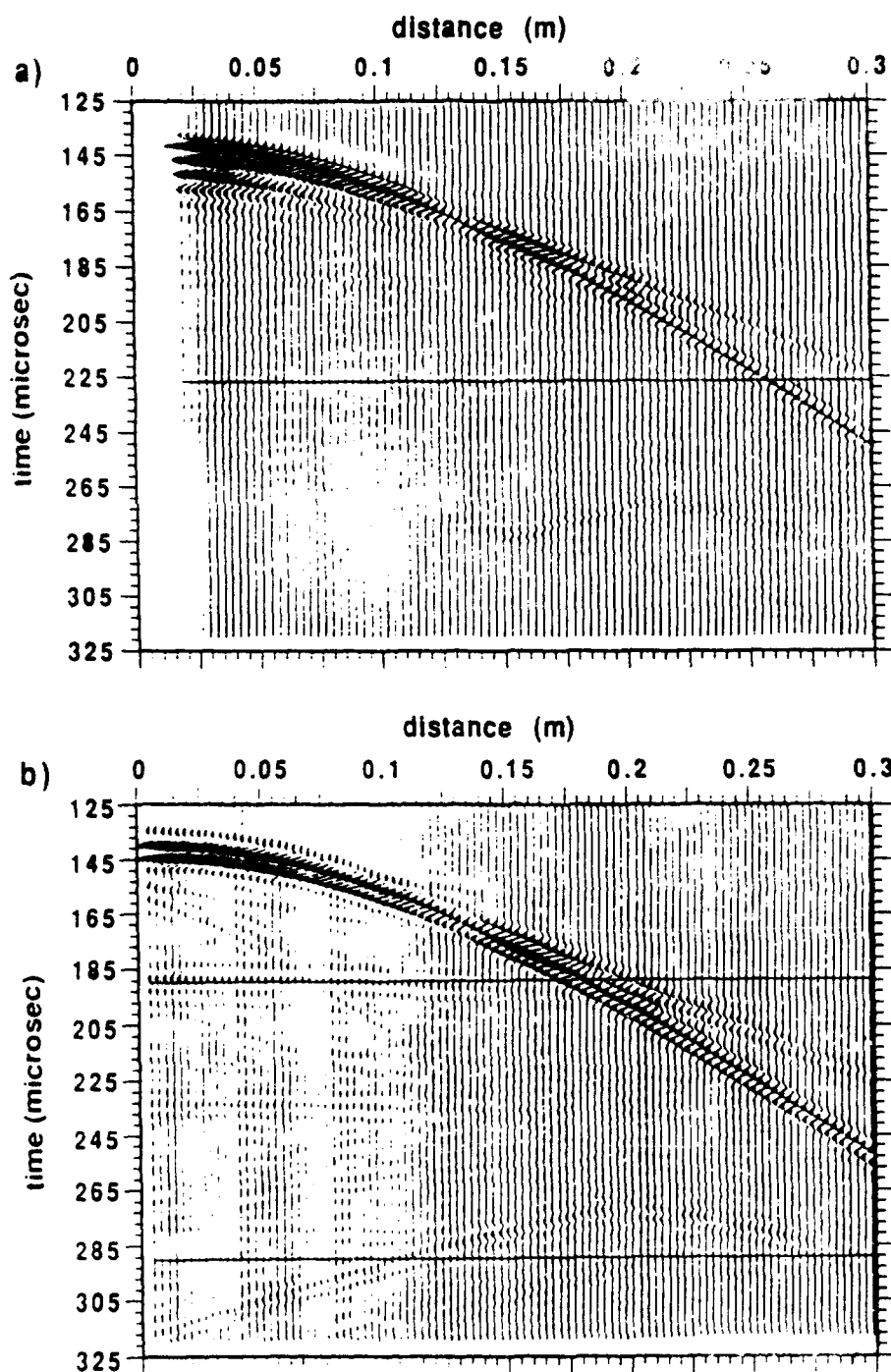


Figure 2: Seismogram recorded 10 cm above the smooth interface using a small pinhead transducer. The record starts at 125 microseconds, truncating the direct arrival. Amplitudes are trace normalized to 1.0 and all recordings over the grooved interface are scaled with this same factor. (a) corresponds to the experimental control case while (b) corresponds to finite-difference synthetics.

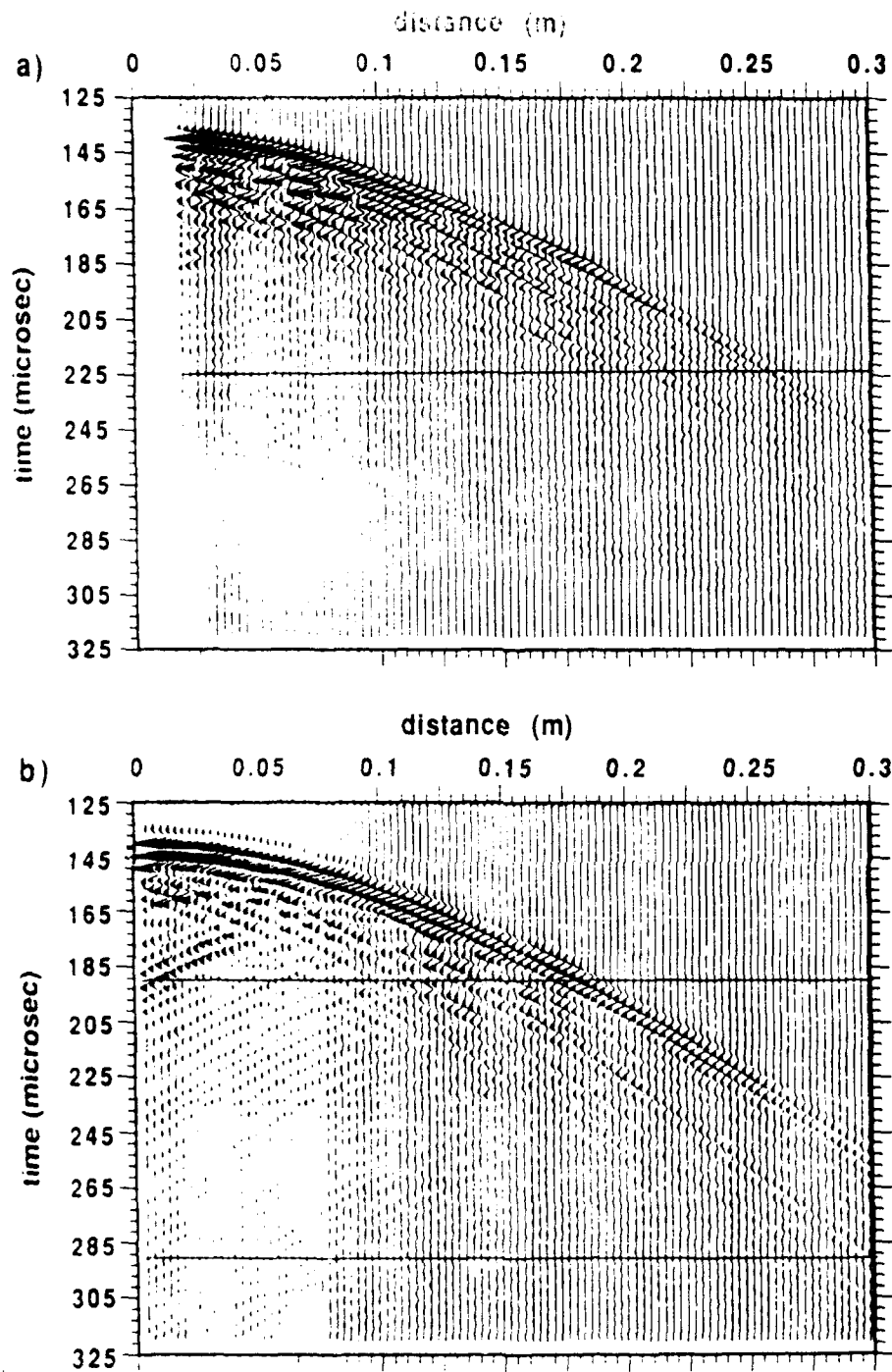


Figure 3: Similar to Figure 2 but for the two-dimensional case with the seismic line oriented perpendicular to the groove strike. (a) corresponds to the experimental results and (b) to the finite-difference synthetics.

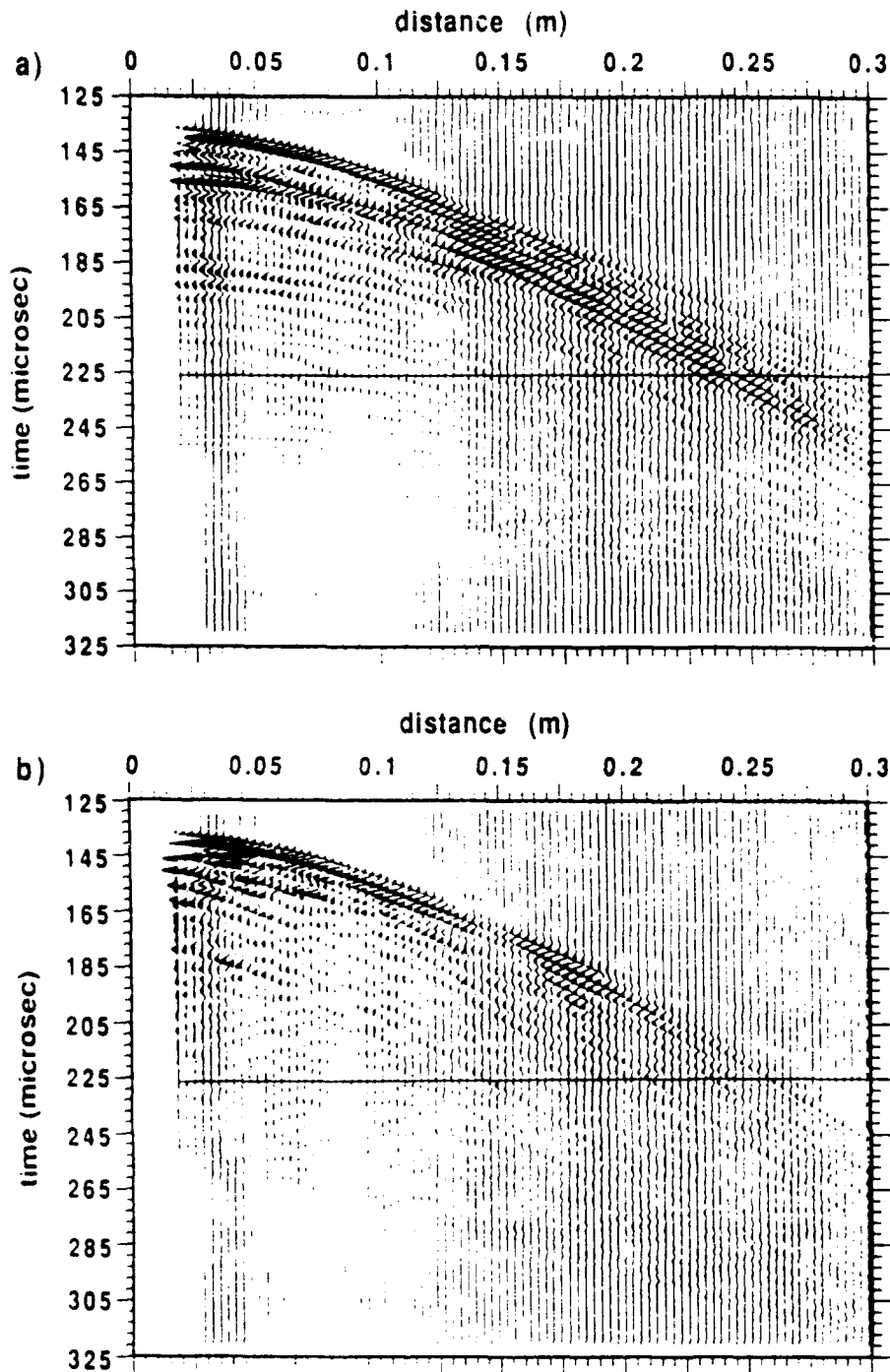


Figure 4: Similar to Figure 2 but for (a) the simplest three-dimensional experimental case with the seismic line parallel to the grooves, and (b) the more complex experimental case of a seismic line oriented at 45° with respect to groove strike.

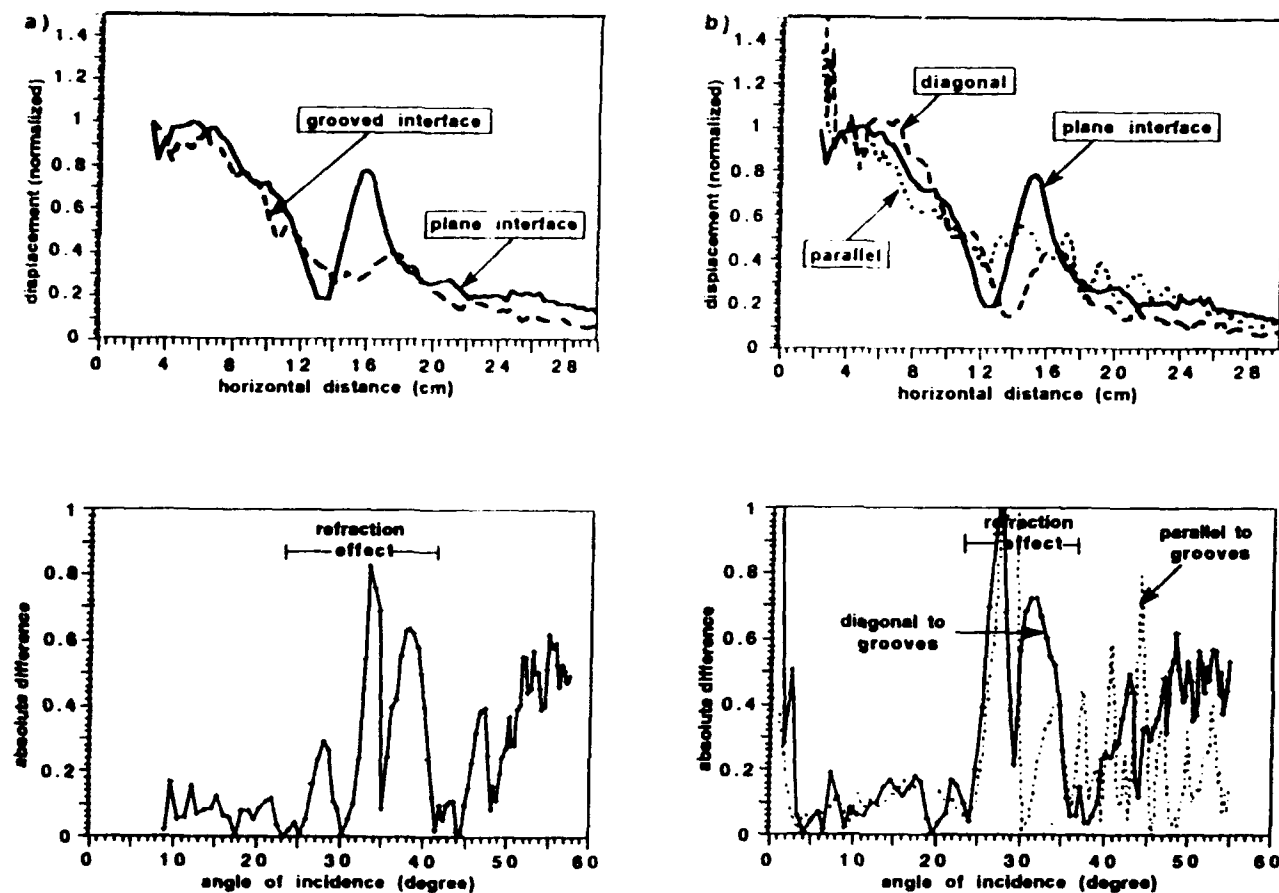
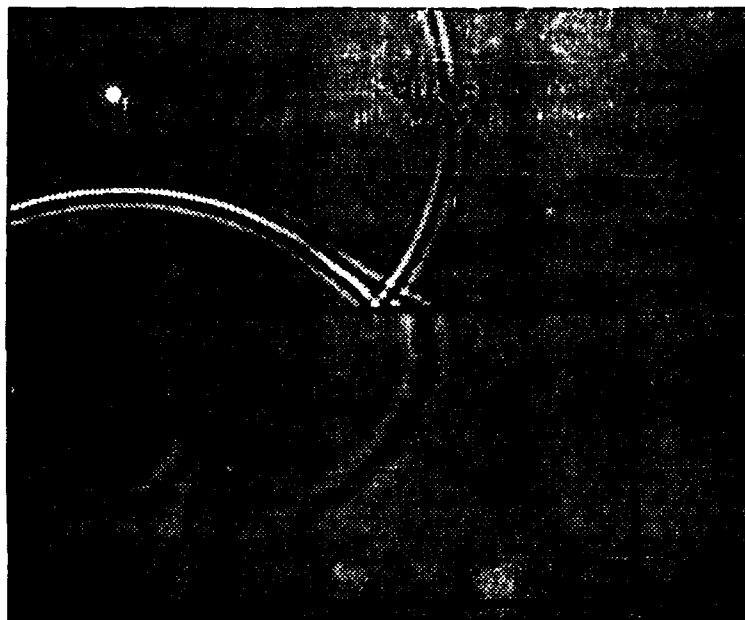


Figure 5: Wavefield amplitude in the acoustic medium versus distance from the source for a primary reflected wave: (a) Plots the experimentally derived curves for both the plane interface and the two-dimensional grooved surface along with their relative difference as a function of incidence angle. (b) is similar to (1), except the curves are for a seismic line oriented both parallel and 45° to groove strike.

a)



b)

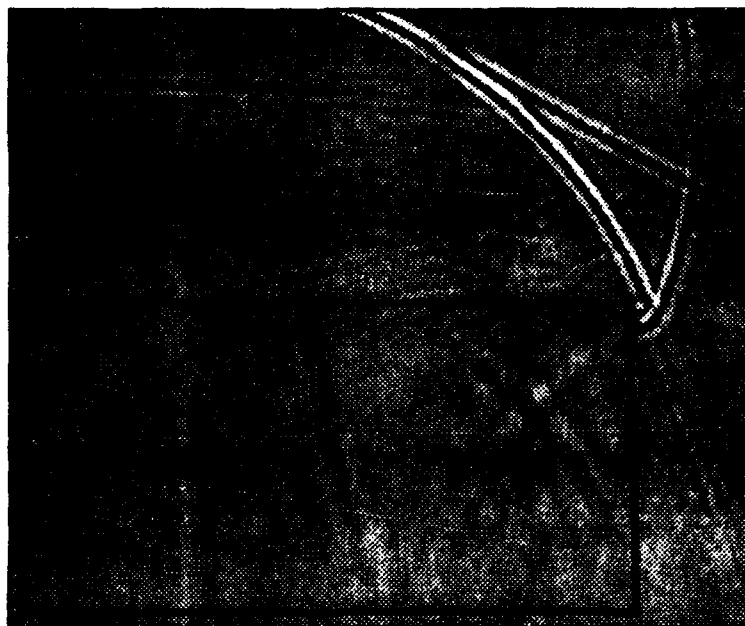
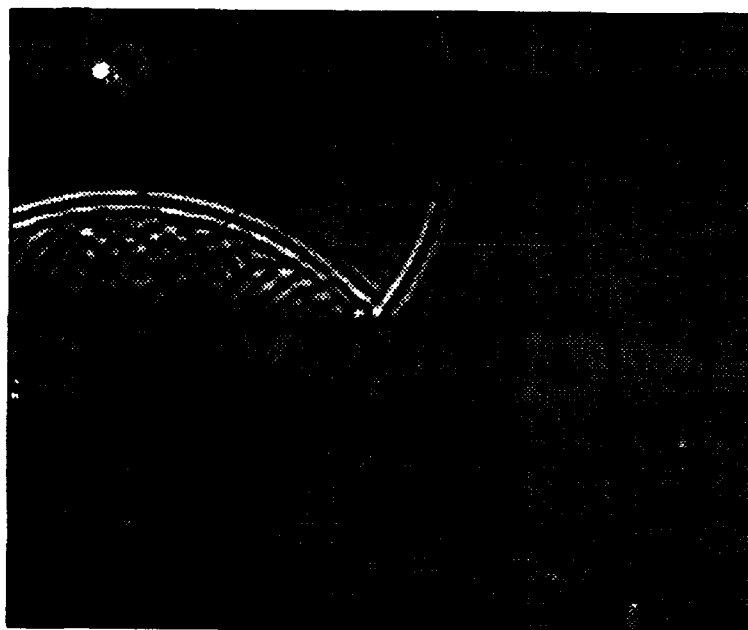


Figure 6: Two finite-difference time slices showing the vertical displacement from a vertical point source. The source receiver geometry is identical to that of the experimental models (Figure 1).

a)



b)

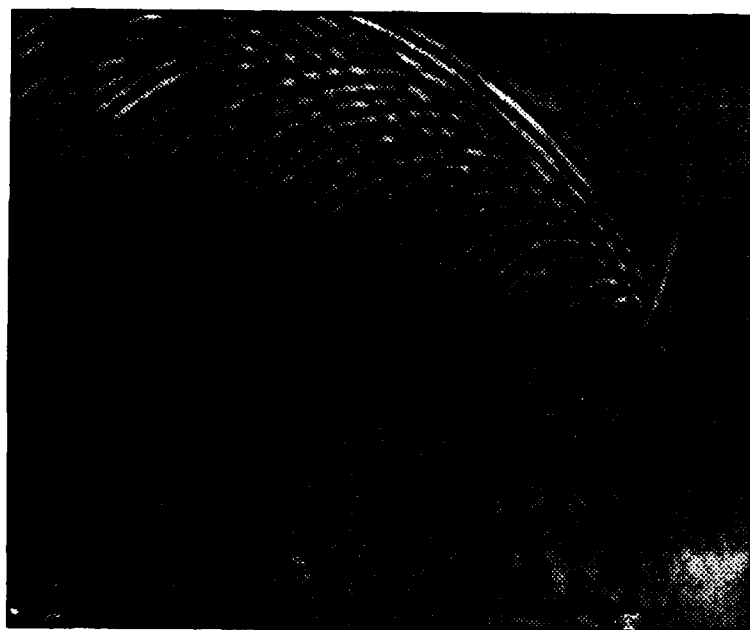


Figure 7: Similar to Figure 6, but for the two-dimensional random diffraction grating.

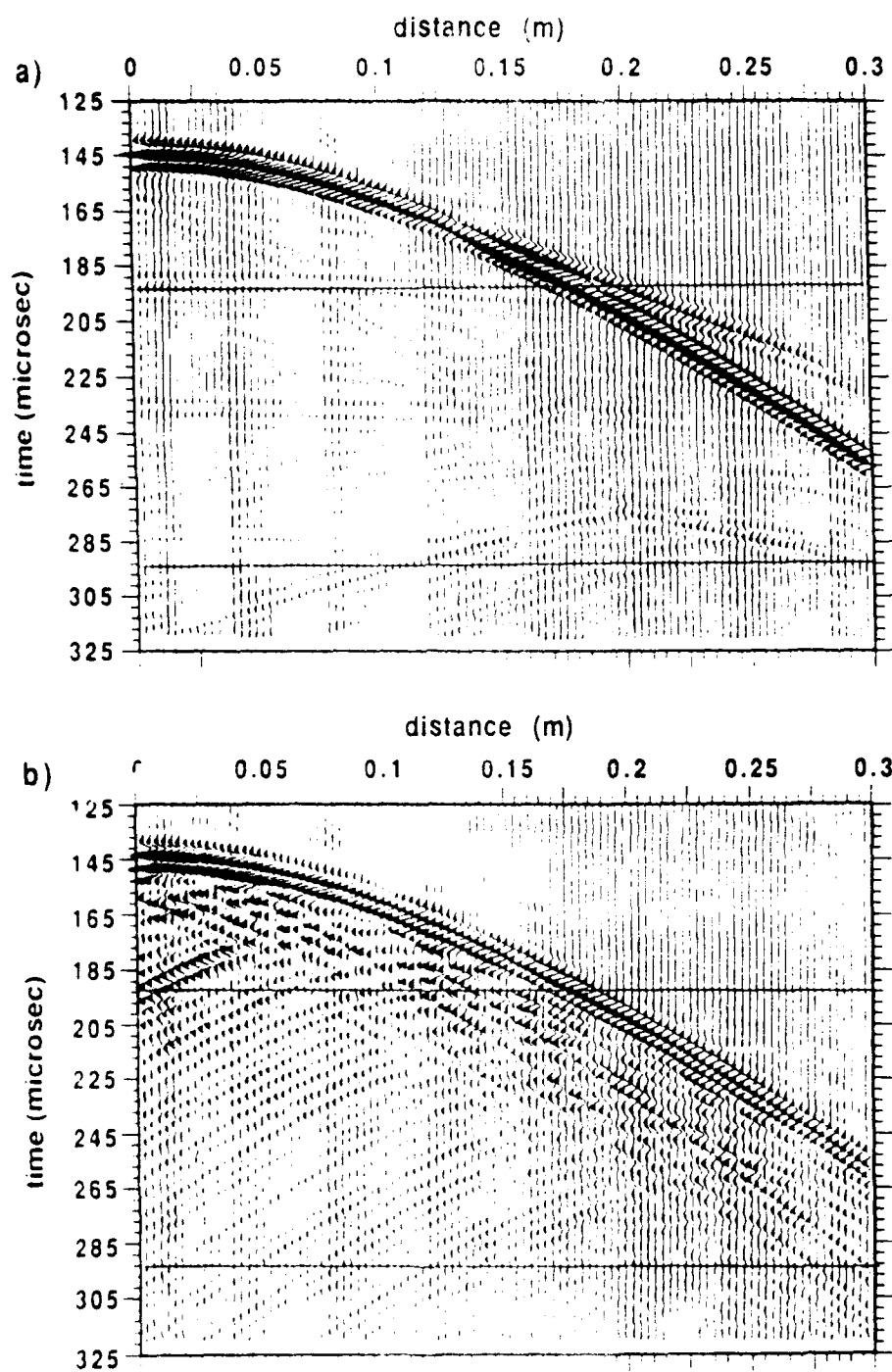


Figure 8: Synthetic seismograms for a volume source over both (a) a flat interface and (b) the two-dimensional grooved interface. Note the large increase in backscattered energy.

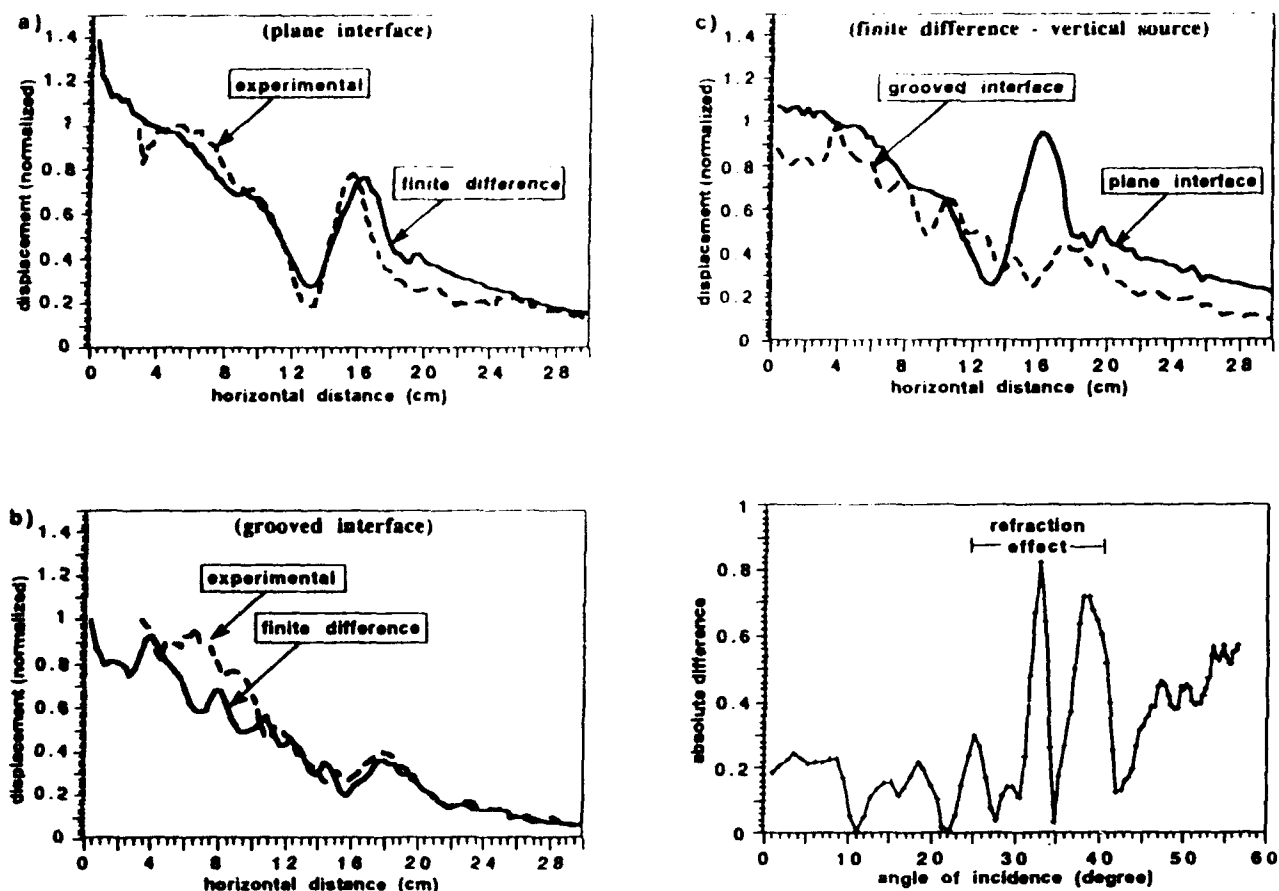


Figure 9: Shows the comparison of finite-difference amplitudes (corrected for the experimental distortions) with ultrasonic tank results. The plane layer (a) and the grooved interface (b) cases both match very well. (c) compares the predicted AVD curves predicted by these finite-difference synthetics and gives their relative difference.

**SYNTHETIC CODA WAVE MODELING AND
SEPARATION OF SCATTERING EFFECT FROM
INTRINSIC ATTENUATION**

by

Chengbin Peng and M. Nafi Toksöz

Earth Resources Laboratory

Department of Earth, Atmospheric, and Planetary Sciences

Massachusetts Institute of Technology

Cambridge, MA 02139

and

Anton M. Dainty

Phillips Laboratory

Seismology Branch (PL/GPEH)

Hanscom AFB, MA 01731

ABSTRACT

The spatial energy density distribution in 2-D random medium is derived for a point source using the radiative transfer theory. Synthetic data calculated by an exact discretized theory for 2-D and 3-D acoustic media are used to test our (2-D) and Wu's (3-D) radiative transfer theory. The results show that the energy transfer theory gives reasonable results and allows the separation of scattering effect from anelastic attenuation in the case of high seismic albedo (strong scattering) and sufficiently large observation range (the range must be longer than the extinction length). The 2-D theory is applied to R_g data from Maine.

INTRODUCTION

Energy losses of seismic waves can be due to anelasticity (frequency independent or frequency dependent), or frequency dependent scattering (Aki and Chouet, 1975; Aki, 1980; Toksöz and Johnson, 1981; Sato, 1982, 1984; Toksöz et al., 1990; Campillo, 1990). The latter is an energy redistribution process in space, and is difficult to separate from the anelastic attenuation. If there is no scattering, the energy intensity after geometrical correction will exponentially decay in space due to anelastic attenuation. Unfortunately, scattering is strong in the Earth at the local scale (0-100 Km), especially in tectonically active areas, and scattering attenuation can make a large contribution to the apparent attenuation (Wu and Aki, 1988; Toksöz et al., 1988). In general, an exponential form will not fit the data: because of

scattering, the received energy near the source may actually increase and reach a maximum value, then decay with distance, and will only fit an exponential in the far field (Wu, 1985). In this case, the geometrical-spreading corrected energy distribution will have an arch shape as a function of distance, i.e., there is an maximum at non-zero distance (Figure 1); and is critically dependent on two parameters: extinction length (the distance over which unit incident wave intensity is attenuated by e^{-1} due to both scattering and anelastic attenuation) and seismic albedo (the ratio of extinction length to scattering length; the scattering length is defined similarly to the extinction length). The theoretical formulation and plots of this arch shape can be found in reference texts such as Ishimaru (1978). Wu and Aki (1988) were among the first to recognize its usefulness in seismology; recently Zeng et al. (1990) developed a general theory of which Wu's formulation is a special case. Theoretically, by matching the observed data with the theory, we can uniquely obtain the scattering coefficient and absorption coefficient, thus separating out the scattering effect in the apparent attenuation.

One of the most effective methods of computing intensities in multiple scattering situations is the radiative transfer theory. The objective of this paper is to numerically study the ability of this theory to accurately predict the variation of intensity with distance in multiple scattering situations and thereby to separate scattering and intrinsic attenuation. We extend this theory to the case of two dimensional wave scattering. We test this case and the three dimensional case of Wu (1985) using synthetic seismograms calculated for a discrete

scattering media by an exact method (Peng et al., 1992). As a practical example, we apply the 2-D transfer theory to R_g waves from a USGS refraction experiment in Maine, U.S.A.

THE SPATIAL ENERGY TRANSFER (SET) THEORY

In this section, radiative transfer theory is applied to the problem of finding the variation of intensity of scattered energy (coda) with distance from a point continuous and isotropic source; we call this Spatial Energy Transfer (SET) theory.

For multiple scattering to be well approximated by radiative energy transfer theory requires that (Ishimaru, 1978): (1) the locally modified far field approximation is valid, (2) the correlation function of the scattered wave varies slowly with distance. Also we ignore wave conversion. Under these assumptions, the mutual coherence function in multiple scattering theory is the Fourier transform of the specific intensity in transfer theory. The great advantage of the radiative transfer theory is that it gives analytical formulations that may be efficiently calculated. This is an important consideration for parameter estimation or inversion, for example.

Below, we first derive expressions for the 2-D case, which has not been treated in the literatures. Then we test both the 2-D and 3-D cases against synthetic data calculated by exact formulations.

Seismic Wave Energy Transfer in 2-D Random Medium

The two dimensional energy transfer equation can be written in the frequency domain as (Ishimaru, 1978)

$$\frac{dI(\vec{r}, \hat{s})}{ds} = -\rho\sigma_t I(\vec{r}, \hat{s}) + \frac{\rho\sigma_s}{2\pi} \int_{2\pi} p(\hat{s}, \hat{s}') I(\vec{r}, \hat{s}') d\theta + \varepsilon(\vec{r}, \hat{s}) \quad (1)$$

where $I(\vec{r}, \hat{s})$ is the specific intensity, which is the average power flux density within a unit frequency band for a unit angle; ρ is the number density of the scatterers and will be taken as a constant because we only deal with wave propagation in spatially stationary media; σ_t is the total cross section of a scatterer; σ_s is the scattering cross section of a scatterer; $p(\hat{s}, \hat{s}')$ is the phase function; and $\varepsilon(\vec{r}, \hat{s})$ is the interior source. The first term in (1) represents the energy attenuation due to absorption and scattering, the second term represents the energy increment from other directions due to scattering, and the third term is the energy increase due to interior sources.

To solve (1), we follow a similar procedure to that of Wu (1985) for the 3-D case, assuming a continuous source in time.

Using average intensity $U(r)$

$$U(\vec{r}) = \frac{1}{2\pi} \int_{2\pi} I(\vec{r}, \hat{s}) d\theta \quad (2)$$

the solution of (1) is

$$U(\vec{r}) = \int_v \left[\frac{\rho\sigma_s}{2\pi} \int_{2\pi} p(\hat{s}, \hat{s}') I(\vec{r}', \hat{s}') d\theta' + \varepsilon(\vec{r}', \hat{s}) \right] \frac{\exp(-\rho\sigma_t |\vec{r} - \vec{r}'|)}{2\pi |\vec{r} - \vec{r}'|} dv \quad (3)$$

where $d\theta = da / |\vec{r} - \vec{r}'|$, $dads = dv$. Here we have assumed no external incident waves other than the interior source.

For isotropic scattering, $p(\hat{s}, \hat{s}')$ is constant. Then

$$U(\vec{r}) = \int_v G_0(\vec{r} - \vec{r}') [\rho\sigma_s U(\vec{r}') + \epsilon(\vec{r}', \hat{s})] dv \quad (4)$$

Here

$$G_0(r) = \frac{\exp(-\rho\sigma_t r)}{2\pi r} \quad (5)$$

Consider the radiation from a point source with power P_0 , i.e.,

$$\epsilon(\vec{r}) = \frac{P_0}{2\pi} \delta(\vec{r} - \vec{r}') \quad (6)$$

then

$$U(\vec{r}) = \frac{P_0}{2\pi} G_0(\vec{r}) + \rho\sigma_s \int_v G_0(\vec{r} - \vec{r}') U(\vec{r}') dv \quad (7)$$

If we denote by $G(\vec{r})$ the intensity $U(\vec{r})$ when the source is located at the origin with power $P_0 = 2\pi$, we obtain

$$G(\vec{r}) = G_0(\vec{r}) + \rho\sigma_s \int_v G_0(\vec{r} - \vec{r}') G(\vec{r}') dv \quad (8)$$

Define $\rho\sigma_s = \eta_s$, the scattering coefficient, $\rho\sigma_t = \eta_e$, the extinction coefficient. The equivalent lengths (scattering length and extinction length) are the reciprocals of the coefficients.

The above equation can be then written as

$$G(\vec{r}) = G_0(\vec{r}) + \eta_s \int_v G_0(\vec{r} - \vec{r}') G(\vec{r}') dv \quad (9)$$

Taking the Fourier transform in space, we get,

$$G(\vec{K}) = \frac{G_0(\vec{K})}{1 - \eta_s G_0(\vec{K})} \quad (10)$$

Inverse Fourier transform yields,

$$G(\vec{r}) = \frac{1}{(2\pi)^2} \int_{-\infty}^{\infty} \frac{G_0(\vec{K})}{1 - \eta_s G_0(\vec{K})} \exp(i\vec{K} \cdot \vec{r}) d\vec{K} \quad (11)$$

It is easy to find

$$G_0(\vec{K}) = \int_{-\infty}^{\infty} G_0(\vec{r}) \exp(-i\vec{K} \cdot \vec{r}) d\vec{r} = \frac{1}{\sqrt{K^2 + \eta_e^2}} \quad (12)$$

Then we obtain

$$G(\vec{r}) = \frac{1}{2\pi} \int_0^{\infty} \frac{K J_0(Kr)}{\sqrt{K^2 + \eta_e^2} - \eta_s} dK \quad (13)$$

Let $B_0 = \frac{\eta_s}{\eta_e}$, the seismic albedo; $D_e = \eta_e r$, the numerical extinction distance (Wu, 1985), and define the normalized (meaning correction for geometrical spreading) energy density $G_n(r) = 2\pi r G(r)$, then

$$G_n(\vec{r}) = D_e \int_0^{\infty} \frac{s J_0(D_e s)}{\sqrt{s^2 + 1} - B_0} ds \quad (14)$$

In an alternative form which is numerically stable for computation, (14) can be decomposed as,

$$G_n = D_e B_0 K_0 \left(D_e \sqrt{1 - B_0^2} \right) + e^{-D_e} + D_e^2 B_0^2 \int_0^{\infty} \frac{x J_0(x)}{(x^2 + D_e^2 - D_e^2 B_0^2) \sqrt{x^2 + D_e^2}} dx \quad (15)$$

The first two terms describe the energy decrease due to scattering and intrinsic attenuation, and the third term represents the energy increase due to multiple scattering.

Figure 1(a) shows the theoretical normalized energy intensity curve. Compared with its 3-D counterpart shown in Figure 1(b) (Wu, 1985), for the same B_0 , Figure 1(a) decays with distance more rapidly at large distance and has a maximum at shorter distance. This is due to the loss of freedom in the 2-D case (energy can't arrive at the receiver from the out-of-plane direction). The shape of $G_n(r)$ is sensitive to the seismic albedo of the medium, especially for $B_0 > 0.5$ (i.e., the scattering coefficient is greater than the attenuation coefficient). The arch shape of the energy transfer curves (Figure 1) is determined by B_0 and $L_e = 1/\eta_e$. By matching the theoretical curves with observations, one can infer the seismic albedo and extinction length. Other parameters can be calculated by the following two relationships:

$$\eta_e = \eta_a + \eta_s$$

$$B_0 = \frac{\eta_s}{\eta_a + \eta_s} \quad (16)$$

where η_a is the absorption coefficient.

Test of Spatial Energy Transfer Technique (SET)

Unlike anelastic attenuation, the scattering attenuation is an energy redistribution in time and space. The wave energy is scattered by the heterogeneities from the propagation direction to other directions, and may be re-scattered back to the propagation direction and arrive at the receiver at a later time. This is expressed in Figure 1 by the arch shape of the curves at high seismic albedo. This observation can be used to separate the scattering coefficient

from the absorption coefficient (Wu and Aki, 1988; Frankel and Wennerberg, 1987; Toksöz et al., 1988, Hoshiha, 1991).

The essence of the spatial energy transfer technique (SET) is to match the energy intensity distribution in space at a set of frequencies with the theoretical curves of Figure 1. The energy intensity can be obtained by taking the square of the Fourier transform of all (or part) of a seismogram after geometrical correction. By using the Fourier transform, we turn the transient source into a continuous harmonic source at a practical frequency. In this section we test this technique using exact synthetic seismograms calculated for discrete scattering media. We will particularly focus on the estimation of intrinsic Q , both because it is an important quantity in the earth and because the comparison of the model and the estimate is unambiguous.

2-D case

Synthetic seismograms are computed by the method of Peng et al. (1992). The model has a constant velocity background with 600 homogeneously and randomly distributed isotropic scatterers in a 50 Km \times 50 Km area. The size of the scatterers is 1/16 of the wavelength associated with the central frequency. The background velocity is 5.0 Km/s, the velocity of the scatterers is 2.0 Km/s and the intrinsic Q is 100. The source time history is the derivative of a Gabor wavelet with central frequency 1 Hz. Figure 2 shows one of the eight sections of complete synthetic seismograms, together with the scattering contributions. After Fourier

transform of whole seismogram being taken, an average is performed over receivers that are located at a given radius around the source to get a statistically reasonable data set for the SET technique.

Figure 3 shows the measured intensity (hereafter called numerical intensity) and best theoretical fit in the frequency band 0.6-2.6 Hz. Generally the fit is very good except at 2.6 Hz, where the source energy is very small.

Table 1 lists the estimated seismic albedo B_0 , extinction length L_e , scattering length L_s , absorption length L_a , intrinsic Q and the error in Q estimation. The SET technique shows a reasonable ability to separate the scattering effect from intrinsic attenuation at high frequency. It underestimates the anelastic Q at low frequency, probably because in this case the extinction length is close to or larger than the maximum source receiver distance and the shape of the normalized energy intensity curve is insensitive to the seismic albedo and extinction length (or trade-off between these two parameters). The seismic albedo estimated by SET in this case increases with increase of frequency, and the extinction length and the scattering length decrease with increase of frequency with negative power slightly greater than 1. This probably means that the derived parameters are tending to the correct answer at high frequencies - the scattering length is expected to be constant with frequency for point scatterers (Dainty, 1981)

3-D case

The model and physical parameters chosen for synthetics (Peng et al., peng) is similar to the 2-D case except in the 3-D case 600 scatterers are randomly distributed in a volume of $50 \times 50 \times 50 \text{ Km}^3$. The fraction of volume occupied by scatterers is much smaller than the fraction of area in the 2-D case. Thus the multiple scattering is correspondingly much weaker. Figure 4 shows the numerical intensity from the synthetics and its best theoretical fit by Wu's 3-D formulation of SET theory (Wu, 1985; Wu and Aki, 1988) in the frequency range between 0.6-2.6 Hz for 3-D acoustic wave scattering. Table 2 lists the estimated parameters, B_0 , L_e , L_s , L_a and estimated intrinsic Q as well as the error in intrinsic Q estimation. Again the SET technique gives a reasonable separation of intrinsic attenuation and scattering attenuation at high frequency. The problem of the extinction length being close to the source-receiver separation (aperture of observational array) is particularly evident in this case - good estimates of the extinction length are probably only being acquired at the high frequencies.

Summary

These two numerical tests show that the Spatial Energy Transfer (SET) technique has a reasonable ability to separate the scattering attenuation and anelastic attenuation for certain combinations of the seismic albedo and extinction length. In the case of strong scattering ($B_0 \gg 0.5$, the 2-D case), the quality of parameter estimation as indicated by estimation

of intrinsic attenuation is good provided that the aperture of seismic array is significantly greater than the extinction length. In the case of weaker scattering ($B_0 < 0.5$, the 3-D example), the seismic albedo decreases with increase of frequency, and the estimation of parameters, as shown by the case of intrinsic Q , is subject to larger error due to insensitivity or trade-off in the SET technique. In this case, no maximum exists anywhere.

USGS REFRACTION DATA IN MAINE

We test the usefulness of the SET technique by applying it to some observed data. The data comes from a refraction survey conducted in Maine by the USGS; a complete description can be found in Murphy and Luetgert (1986, 1987). We use only a subset of the experimental data shown in Figure 5 after 1-10 Hz bandpass filtering and 10 second time windowing. This data has previously been interpreted by Reiter et al. (1988) and Toksöz et al. (1988). In this data set, the R_g phase is particularly well recorded, and is very suitable for the application of our 2-D SET technique. We intend to compare the attenuation estimates by the SET technique to those of Reiter et al. (1988) and Toksöz et al. (1988). We also obtain other parameters which cannot be determined by the methods used before.

Shown in Figure 6 is the measured energy intensity (black circles) and the best fit by our 2-D energy transfer theory (empty triangles) in the frequency range 2.0-5.5 Hz. Generally the fit is good with the correlation coefficient greater than 0.80. Table 3 lists the estimated seismic albedo, extinction length, scattering length, absorption length, and apparent and

intrinsic Q . It should be noted, however, that scattering of R_g to body waves (P or S) could appear as intrinsic attenuation, since this type of wave conversion is not included in our theory. The seismic albedo is less than 0.5 except at 2.5 and 3.0 Hz, suggesting the scattering effect is weak compared to the intrinsic attenuation for this data, thus the exponential formulation used in Reiter et al. (1988) and Toksöz et al. (1988) is applicable. This contrasts with the 2-D synthetic case where scattering is very strong, but is similar to the 3-D case. The extinction length decreases with frequency. Based on our experience with the synthetic examples, parameter estimation will certainly be worse at low frequencies due to the extinction length being of the same order as the observation distance. At high frequency (above 3 Hz), the attenuation (extinction) Q^{-1} (solid circle) agrees well with that estimated by Toksöz et al. (1988) (open circle) as shown in Figure 7a, while it is not true for points associated with low frequencies. Figure 7b shows the intrinsic attenuation as a function of frequency; the high frequency portion can be fitted by a power law with a power index $\zeta \approx 0.90$. This is larger than that predicted by the fluid flow relaxation model (0.5, Toksöz et al. 1988) but does indicate frequency-dependent attenuation. We also have not considered depth-dependent attenuation properties in this study, as was done by Toksöz et al. Because of the large error of the SET technique in separating scattering effect from intrinsic attenuation at low frequency, the low frequency portion in Figure 7b is least reliable and does not fit the power law.

SUMMARY AND CONCLUSIONS

In this paper, we have extended the energy transfer theory to 2-D wave scattering and given two numerical studies of the SET technique. We have applied this technique to the USGS refraction data in Maine to study the attenuation of the R_g wave and compared our results with previous work. Summing up,

- Numerical tests show that the Spatial Energy Transfer (SET) technique has a reasonable ability to separate the scattering attenuation and anelastic attenuation at high albedos and extinction lengths shorter than the observation range.
- The 2-D energy transfer theory fits the field data. The attenuation estimated by the SET technique in the Maine data is consistent with the results obtained by other methods at high frequency.

ACKNOWLEDGEMENTS

We are grateful to Prof. Ru-Shan Wu of the Institute of Geophysics, Chinese Academy of Sciences for stimulating our research interest in radiative transfer theory. B. Mandal and E. Reiter helped with the Maine data. This work is partially supported by the ERL/nCUBE Geophysical Center for Parallel Processing at MIT and partially supported by the Defense Advanced Research Projects Agency through contract # F19628-89-K-0020 administrated by the Phillips Laboratory (formerly the Geophysics Laboratory) of the Air Force Systems

Command. The first author also holds an nCUBE fellowship.

REFERENCES

- Aki, K. and Chouet, B. (1975). Origin of coda wave: source, attenuation and scattering effects, *J. Geophys. Res.* **80**, 3322-3342.
- Aki, K. (1980). Scattering and attenuation of shear waves in the lithosphere, *J. Geophys. Res.* **85**, 6496-6504.
- Campillo, M. (1990). Propagation and attenuation characteristic of the Crustal phase Lg, *PAGEOPH* **132**, 1-19.
- Dainty, A. M. (1981). A scattering model to explain seismic Q observations in the lithosphere between 1 and 30 Hz, *Geophys. Res. Lett.* **8**, 1126-1128.
- Frankel, A. and Wennerberg, L. (1987). Energy-flux model of seismic coda: separation of scattering and intrinsic attenuation, *Bull. Seis. Soc. Am.* **77**, 1223-1251.
- Hoshiba, M. (1991). Simulation of multiple scattered coda wave excitation adopting energy conservation law, *Phys. Earth Planet Inter.*, **67**, 123-136.
- Ishimaru, A. (1978). Wave propagation and scattering in random media, Vol. 1 and 2, Academic Press, New York.
- Murphy, J. M. and Luetgert, J. H. (1986). Data report for the Maine-Quebec cross-strike seismic refraction profile, USGS open file report, **86-47**, United States Geological Survey.
- Murphy, J. M. and Luetgert, J. H. (1987). Data report for the Maine-Quebec along-strike

- seismic-refraction profile, USGS open file report, **86-133**, United State Geological Survey.
- Reiter, E., Toksöz, M. N. and Dainty, A. M. (1988). Influence of scattering on seismic waves: velocity and attenuation of upper crust in southeast Maine, Rept. AFGL TR-88-0094, **56**, Air Force Geophysics Laboratory, ADA199131.
- Sato, H. (1982). Attenuation of S waves in the lithosphere due to scattering by its random velocity structure, *J. Geophys. Res.* **87**, 7779-7785.
- Sato, H. (1984). Attenuation and envelope formation for three component seismograms of small local earthquakes in randomly inhomogeneous lithosphere, *J. Geophys. Res.* **89**, 1221-1241.
- Toksöz, M. N., Mandal, B. and Dainty, A. M. (1990). Frequency-dependent attenuation in the crust, *Geophys. Res. Lett.* **17**, 973-976.
- Toksöz, M. N., Dainty, A. M., Reiter, E. and Wu, R.S.(1988). A model for attenuation and scattering in the earth's crust, *PAGEOPH*, **128**, 81-100.
- Toksöz, M. N. and Johnston, D. H. (1981). Seismic wave attenuation, *Geophysics reprint series*, **2**, Society of Exploration Geophysics.
- Wu, R. S. (1985). Multiple scattering and energy transfer of seismic waves -separation of scattering effect from intrinsic attenuation-I. Theoretical modeling, *Geophys. J. R. astr. soc.* **82**, 57-80.
- Wu, R. S. and Aki. K. (1988). Multiple scattering and energy transfer of seismic waves...II. Application of the theory to Hindu Kush Region, *PAGEOPH*, **128**, 49-80.

Zeng, Y., Su, F. and Aki, K., 1990, Scattering wave energy propagation in a medium with randomly distributed isotropic scatterers: J. Geophys. R. **96**, 607-619.

Table 1: Estimated parameters by matching the synthetic and theoretical energy transfer in space in 2-D case

Freq.(Hz)	B_0	L_e (Km)	L_s (Km)	L_a (Km)	Intrinsic Q	True Q	Error
0.6	0.80	12.33	15.42	61.66	46.50	100	53.50%
0.8	0.75	13.67	18.63	51.25	51.52	100	48.48%
1.0	0.83	8.67	10.40	52.00	65.43	100	34.57%
1.2	0.85	6.33	7.48	41.30	62.30	100	37.70%
1.4	0.89	5.00	5.60	46.87	82.46	100	17.54%
1.6	0.89	4.33	4.87	39.39	79.21	100	20.79%
1.8	0.90	3.33	3.68	35.72	80.78	100	19.22%
2.0	0.93	3.17	3.42	43.18	119.38	100	19.38%
2.2	0.92	3.00	3.23	40.90	113.10	100	13.10%
2.4	0.89	3.50	3.93	31.82	95.96	100	4.04%
2.6	0.92	3.00	3.23	40.91	133.66	100	33.66%

$$Q_s = \frac{\omega L_s}{v}$$

$$Q_a = \frac{\omega L_a}{v}$$

$$Q = \frac{\omega L_e}{v}$$

$$Q^{-1} = Q_a^{-1} + Q_s^{-1}$$

where v is velocity and ω is angular frequency.

Table 2: Estimated parameters by matching the synthetic and theoretical energy transfer in space in 3-D case

Freq.(Hz)	B_0	L_e (Km)	L_s (Km)	L_a (Km)	Intrinsic Q	True Q	Error
0.6	0.87	8.67	9.96	66.67	50.26	200	74.87%
0.8	0.88	8.67	9.85	72.22	72.60	200	63.70%
1.0	0.79	16.66	21.18	78.13	98.17	200	50.92%
1.2	0.74	28.00	37.67	109.10	164.50	200	17.75%
1.4	0.62	26.67	43.01	70.18	132.28	200	33.86%
1.6	0.66	18.00	27.14	53.46	107.50	200	46.25%
1.8	0.61	16.33	26.77	41.88	94.73	200	52.64%
2.0	0.54	30.33	57.59	64.08	161.06	200	19.47%
2.2	0.66	18.00	27.13	53.46	147.81	200	26.10%
2.4	0.45	34.67	76.47	63.42	191.25	200	4.38%
2.6	0.46	29.67	64.49	54.94	179.50	200	10.25%

Table 3: Estimated parameters by matching the observed (R_g) and theoretical energy transfer in space(USGS Refraction Data in Maine.1986)

Freq.(Hz)	B_0	L_e (Km)	L_s (Km)	L_a (Km)	Apparant Q	Intrinsic Q
2.0	0.45	14.33	32.09	25.90	76.63	138.52
2.5	0.65	9.33	14.43	26.42	63.17	178.85
3.0	0.75	4.00	5.33	16.00	32.64	130.56
3.5	0.18	4.00	22.20	4.88	38.25	46.64
4.0	0.25	2.68	10.52	3.57	29.14	39.03
4.5	0.13	3.00	23.07	3.45	36.88	42.39
5.0	0.36	3.00	8.33	4.68	40.97	64.02
5.5	0.05	4.00	75.00	4.23	60.10	63.49

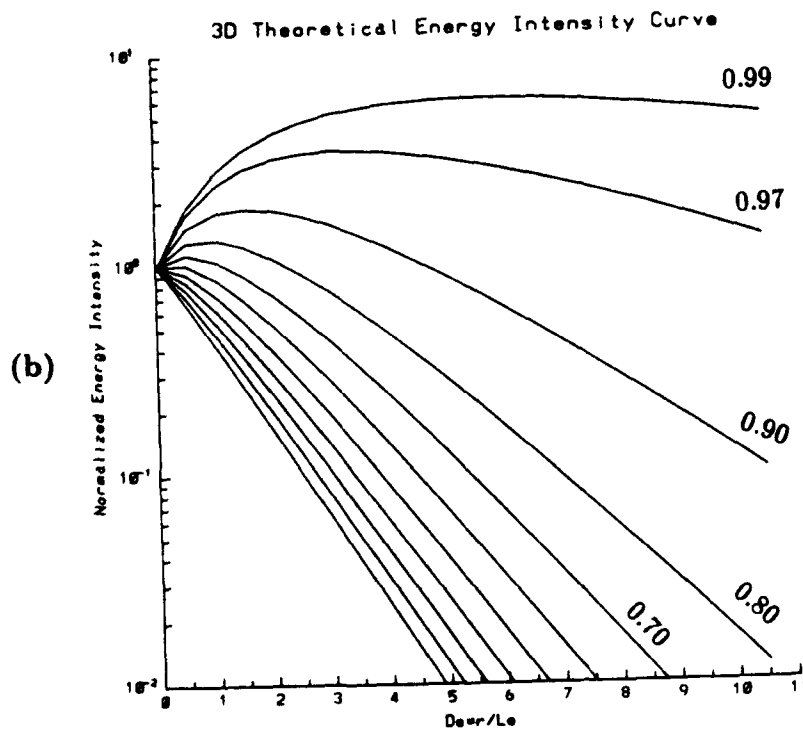
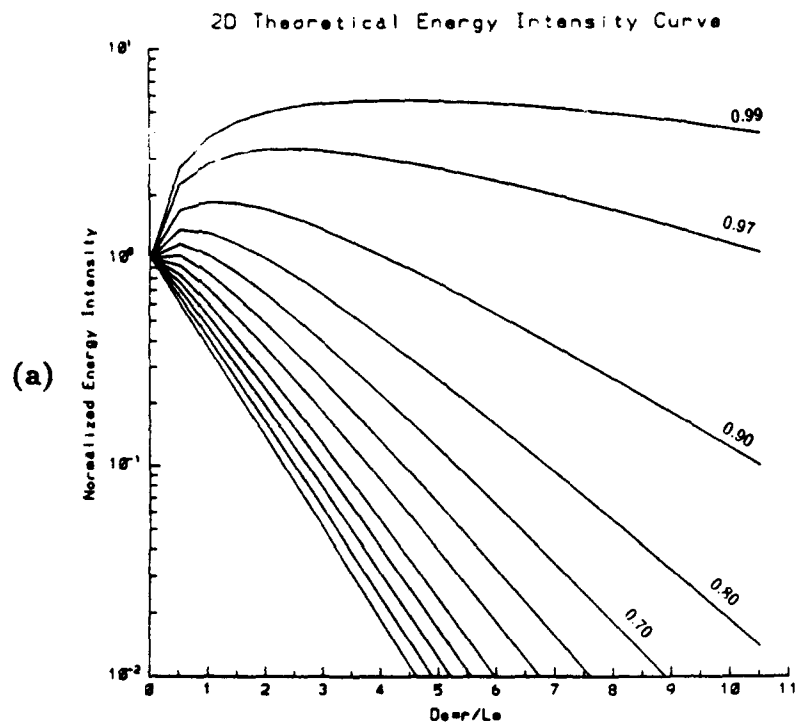


Figure 1: Theoretical normalized (i.e., corrected for geometric spreading) energy intensity curve: (a) 2-D case, (b) 3-D case.

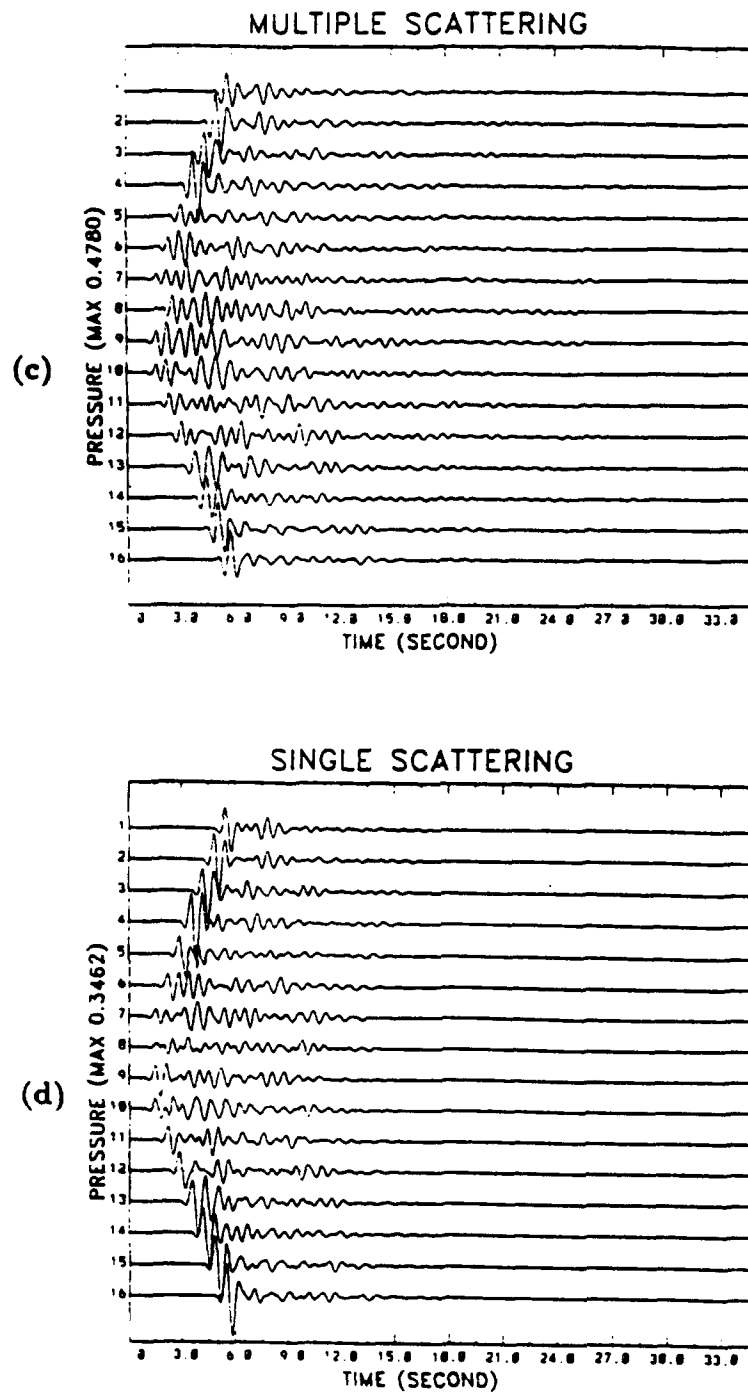


Figure 2: Synthetic whole waveforms (a), total scattering contributions (b), multiple scattering contributions (c) and single scattering contributions (d) along a cross section through the point source.

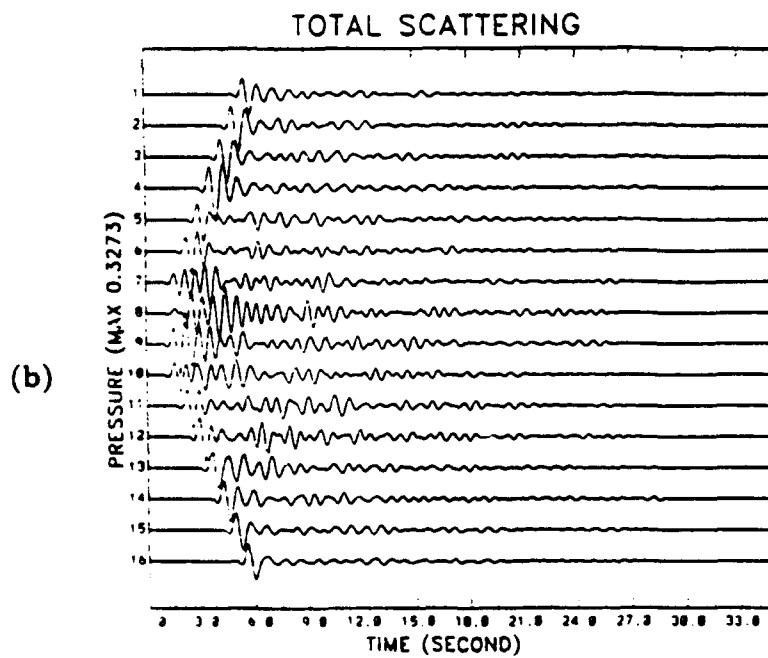
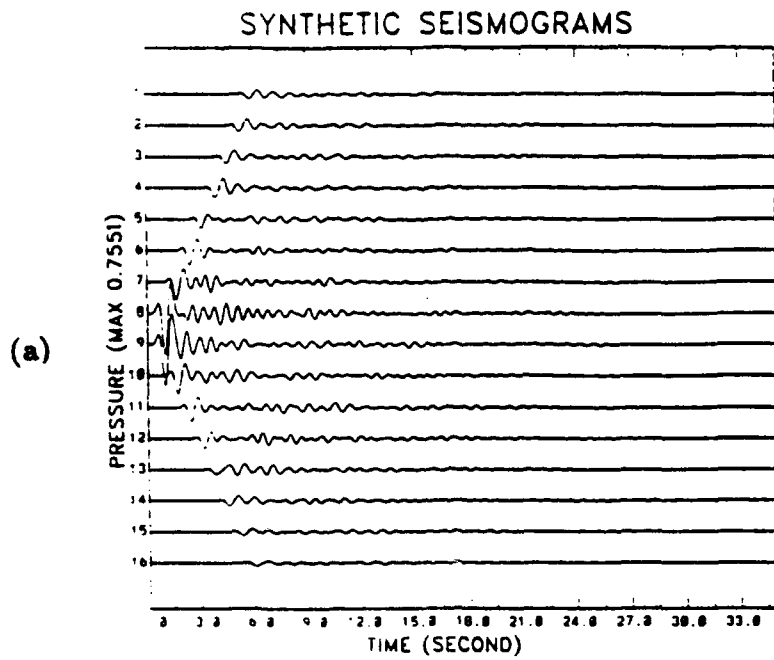


Figure 2, continued.

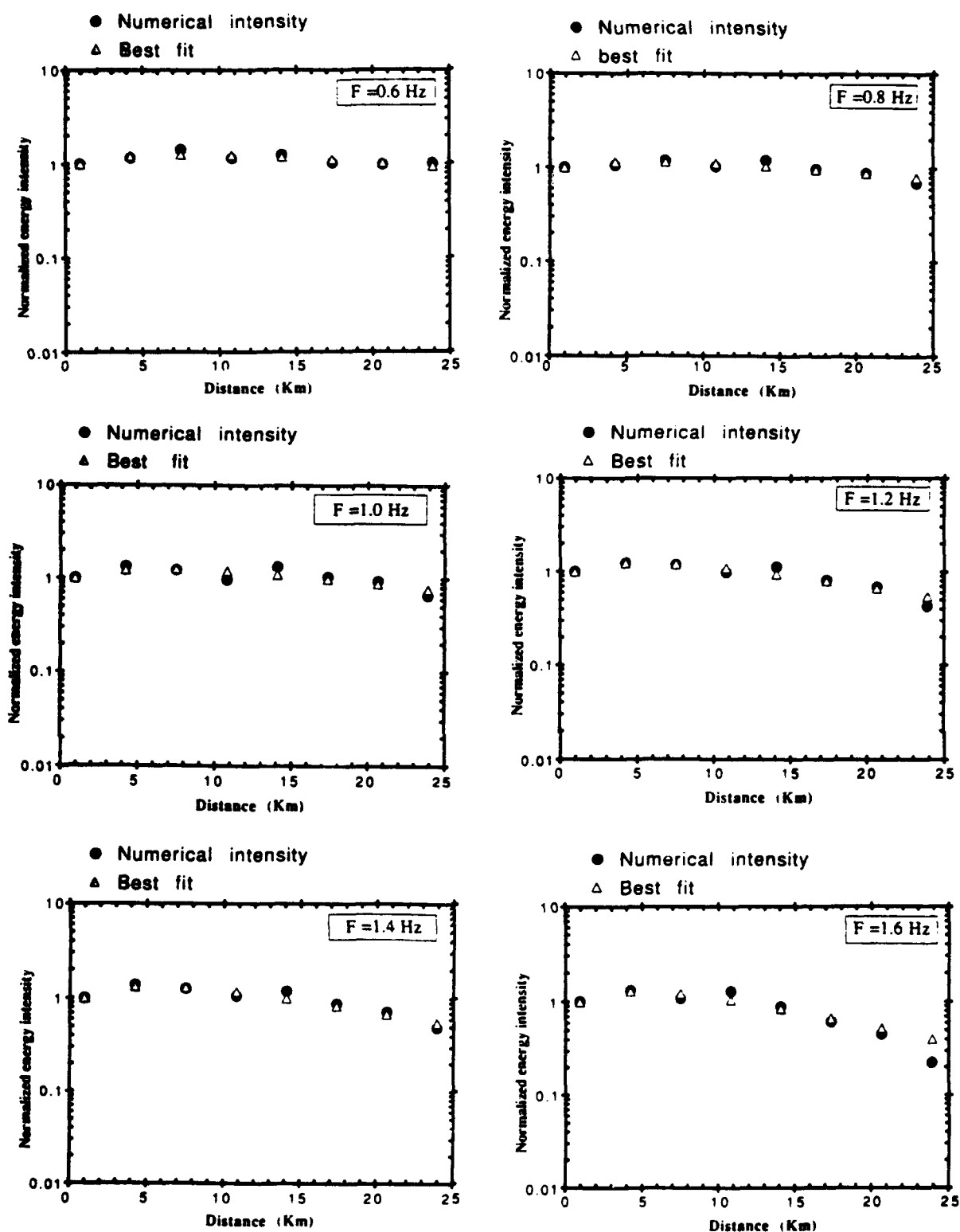


Figure 3: The observed intensity (from synthetic data, referred as numerical intensity in the figures) and the best theoretical fit in the frequency range between 0.6–2.6 Hz for the 2-D case.

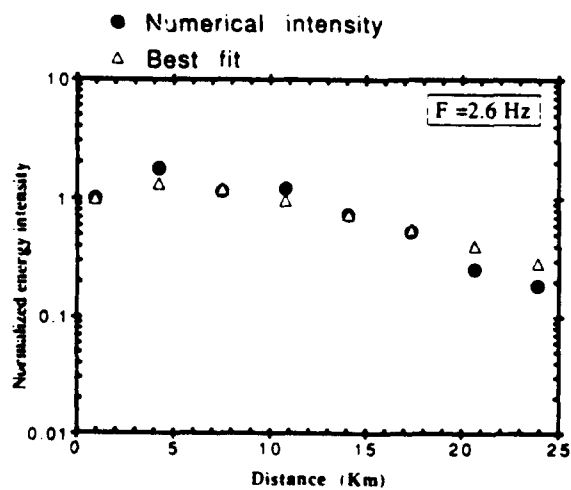
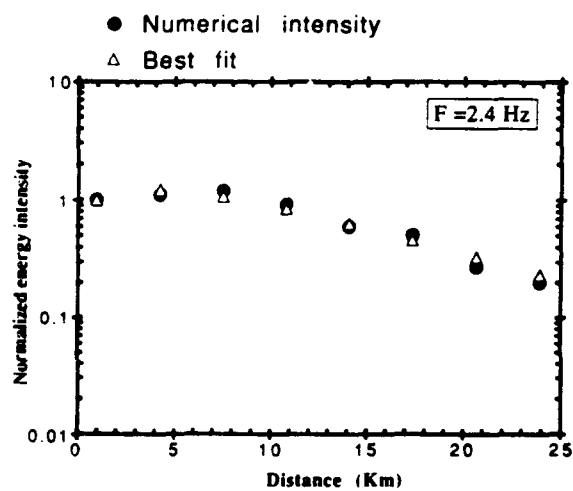
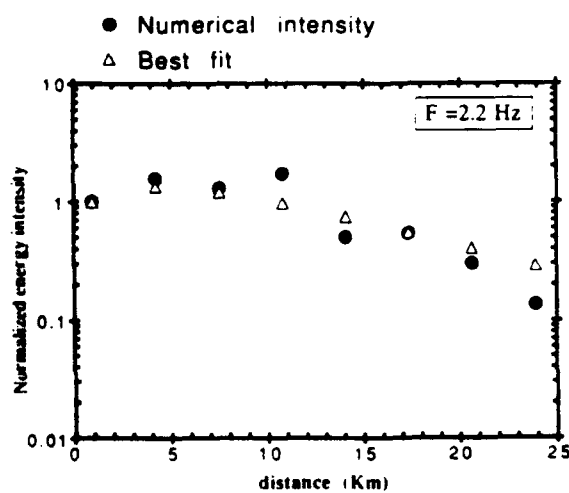
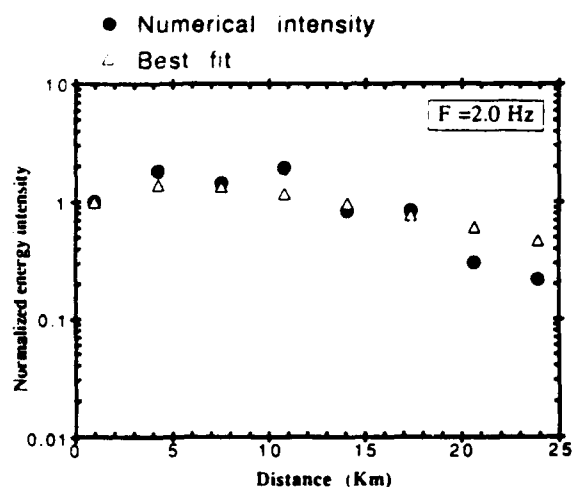
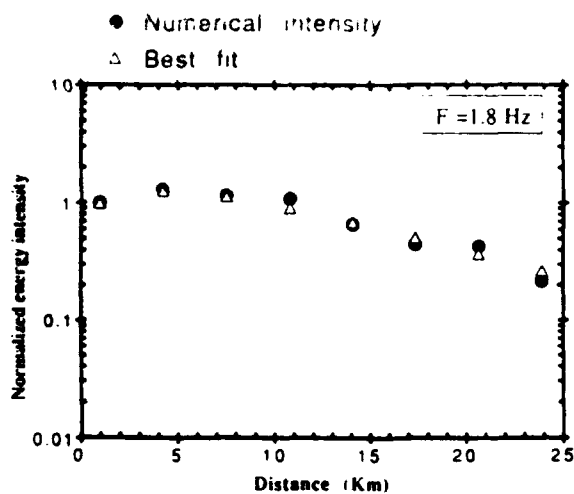


Figure 3, continued.

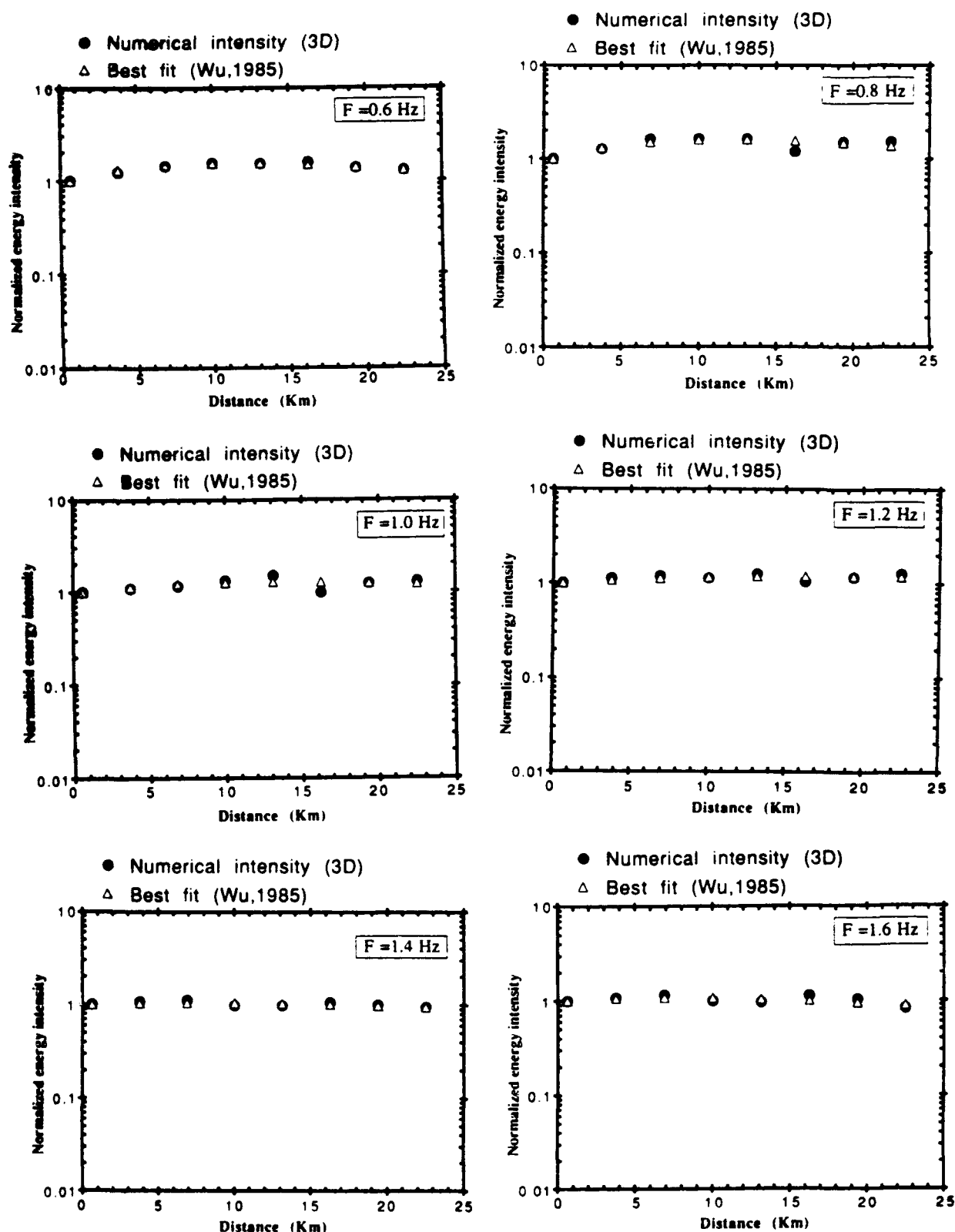


Figure 4: The observed intensity (from synthetic data, referred as numerical intensity in the figures) and the best theoretical fit in the frequency range between 0.6-2.6 Hz for the 3-D case.

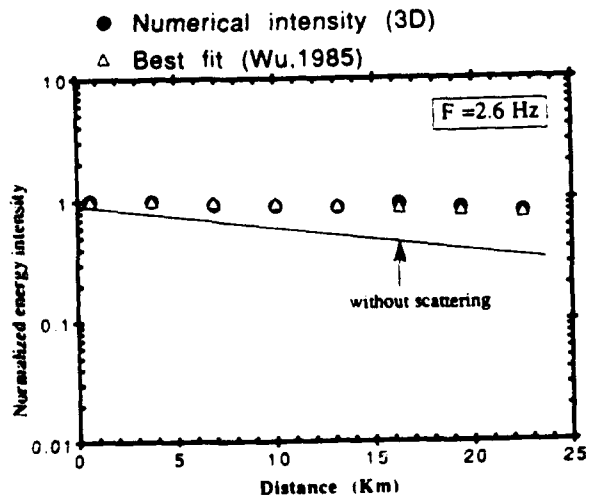
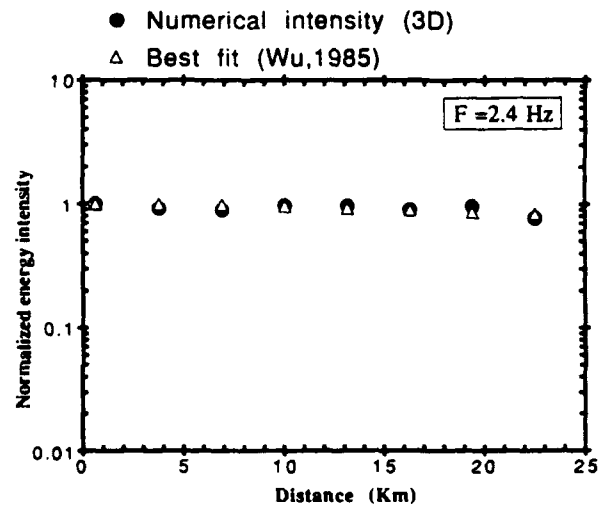
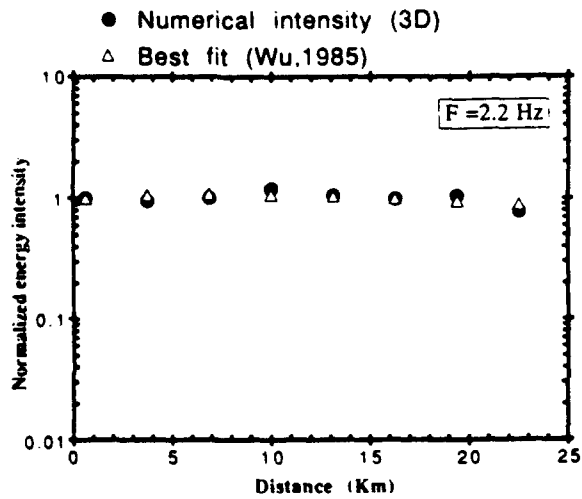
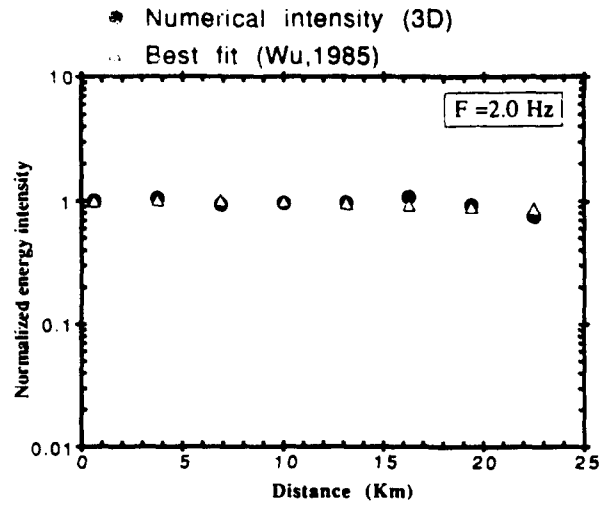
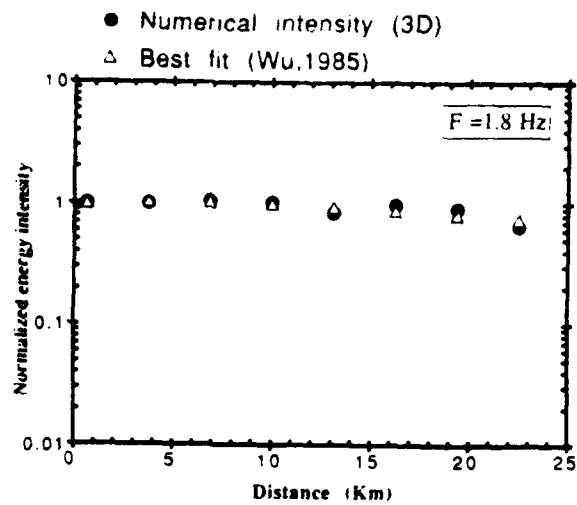


Figure 4, continued.

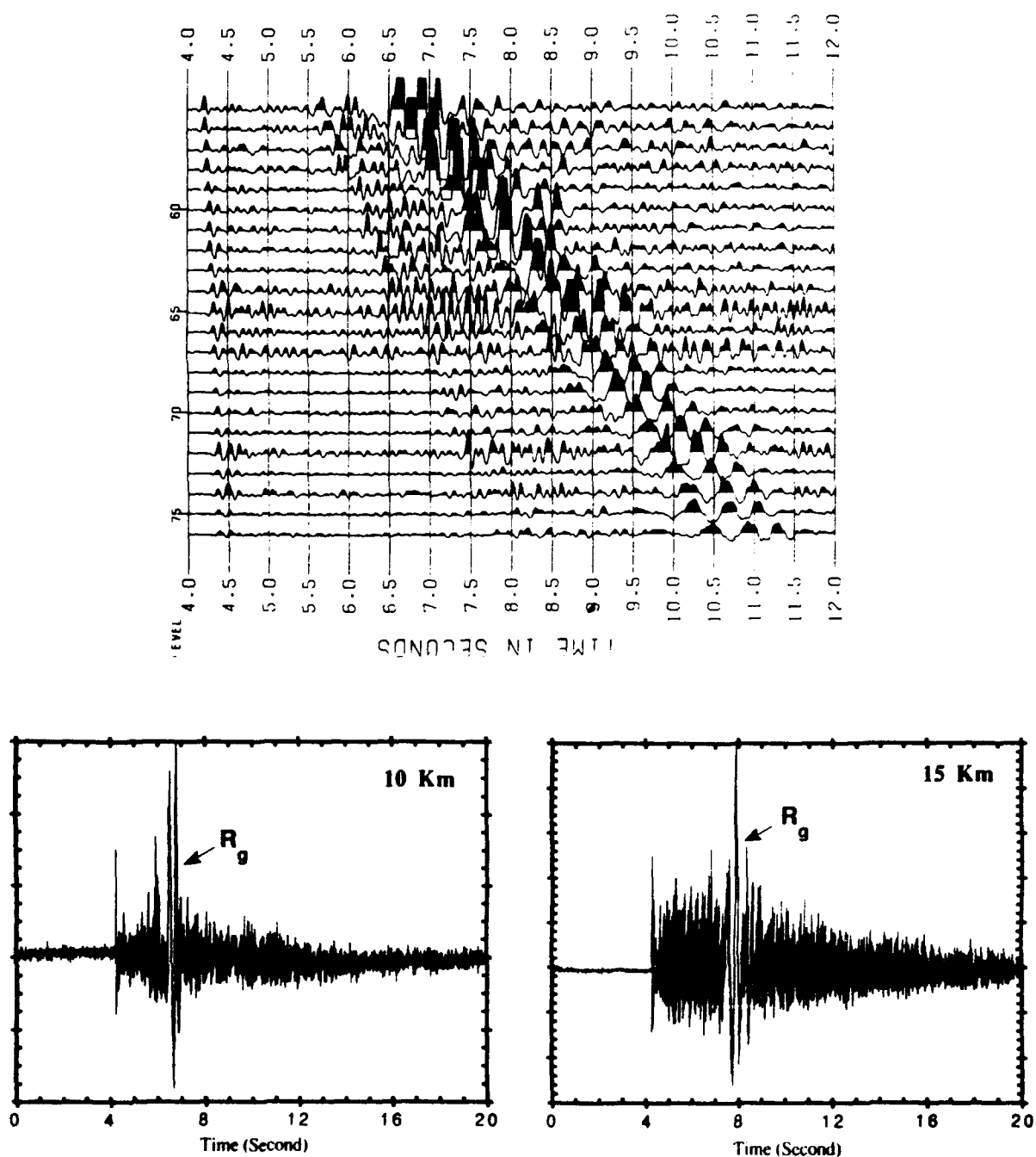


Figure 5: A subset of the USGS refraction data in Maine after 1-10 Hz bandpass filtering and moveout correction of the first arrival. The source-receiver distance ranges from 11.0 km to 30.0 km. Also shown here are two original traces at 10 km and 15 km offsets. The dominant phase here is R_g wave.

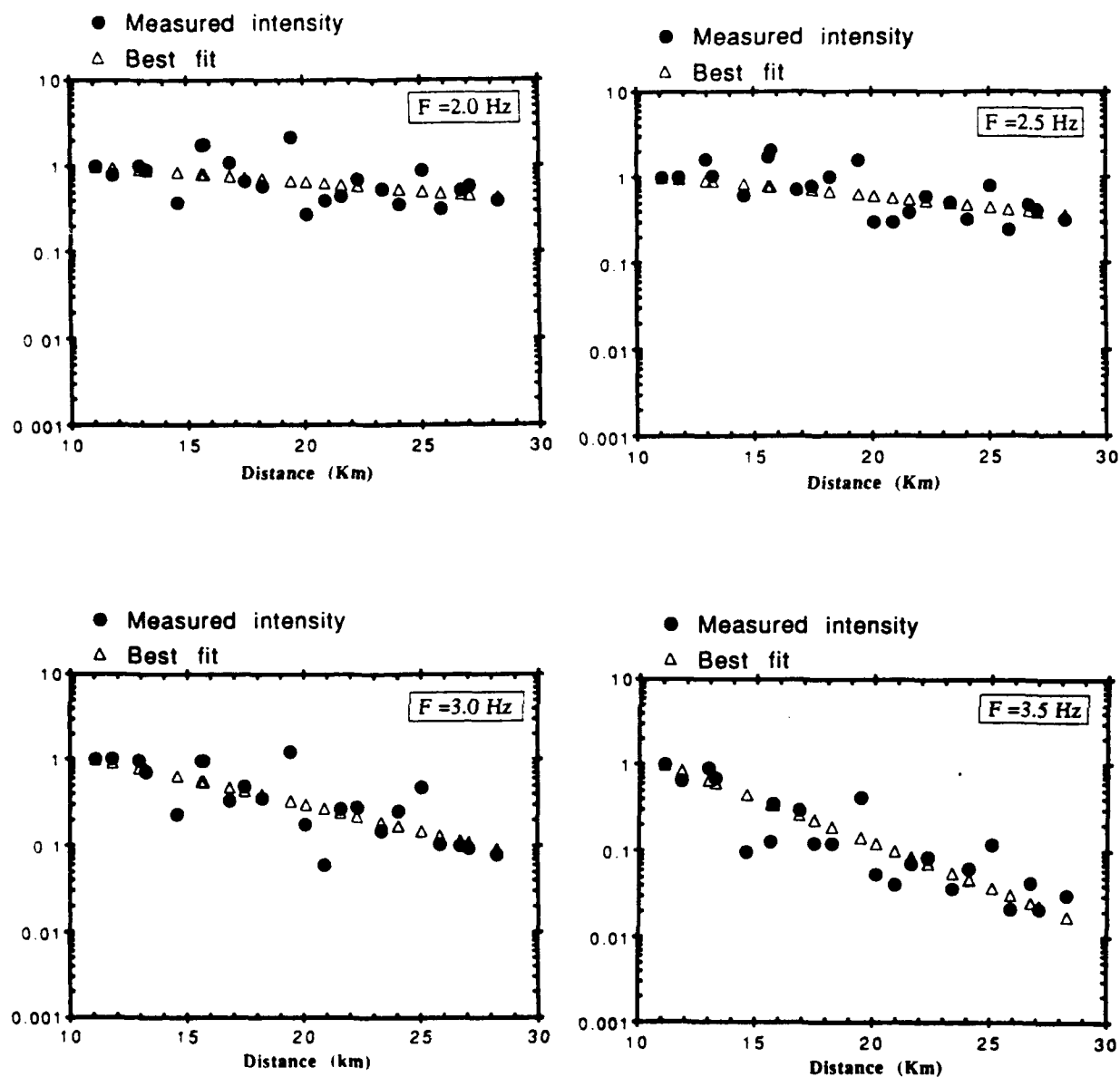


Figure 6: The measured R_g intensity and its best theoretical fit by the 2-D radiative energy transfer theory. Frequencies range from 2.0 Hz to 5.0 Hz.

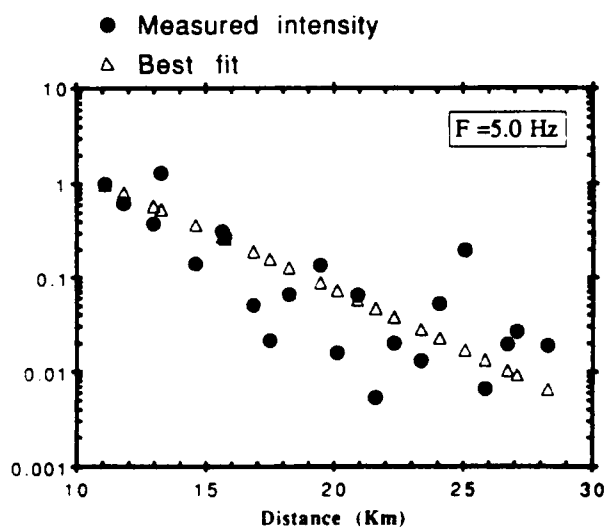
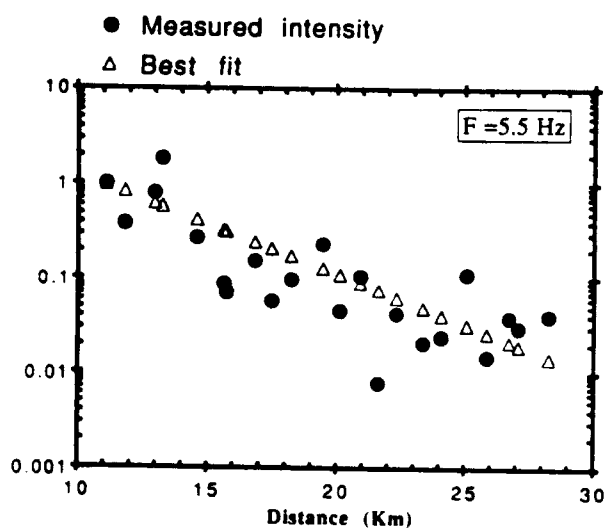
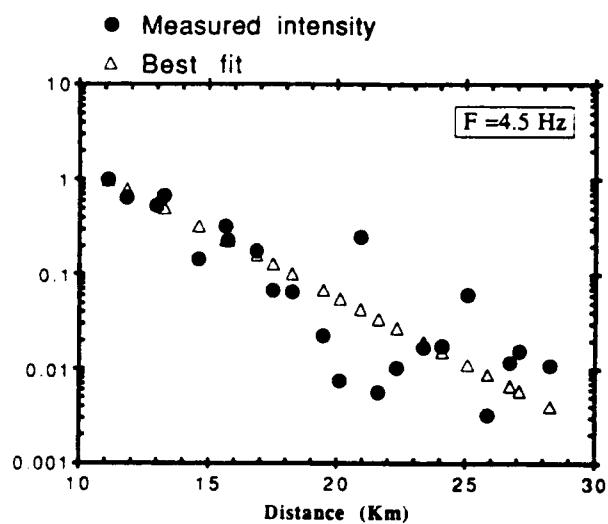
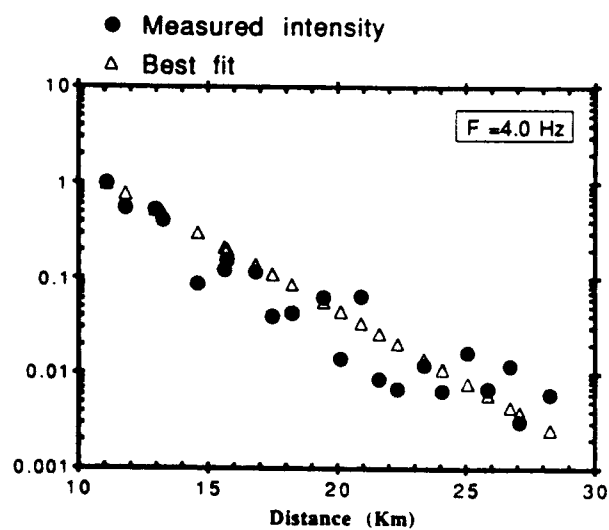


Figure 6, continued.

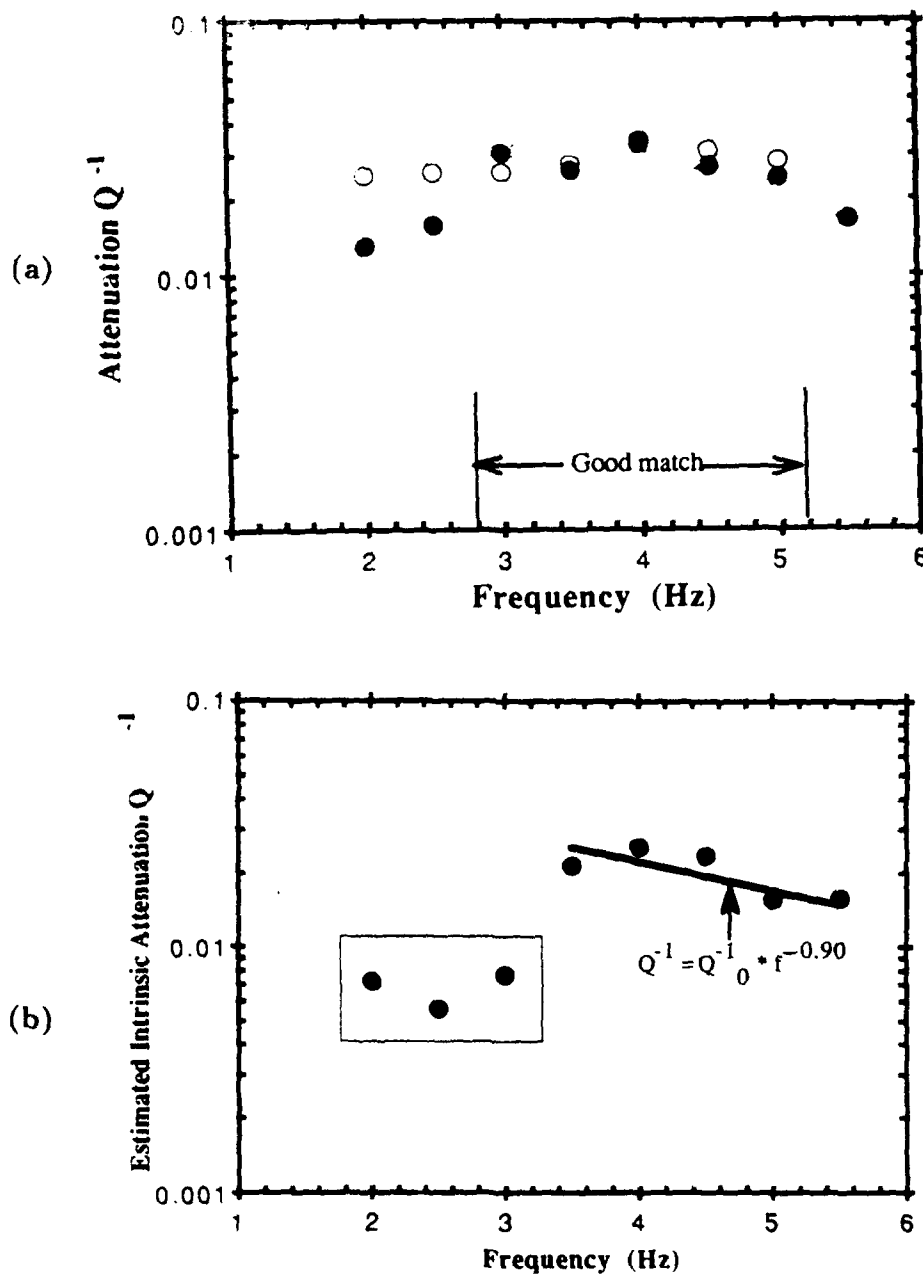


Figure 7: (a) Apparent attenuation estimated by the SET technique (black circles) and by Toksöz et al. (1988) (open circles). (b) Estimated intrinsic attenuation. The solid line is the fit by a power law model only for the high frequencies. The highlighted three points at low frequency do not fit the power law.

DISTRIBUTION LIST

Prof. Thomas Ahrens
Seismological Lab, 252-21
Division of Geological & Planetary Sciences
California Institute of Technology
Pasadena, CA 91125

Prof. Keiiti Aki
Center for Earth Sciences
University of Southern California
University Park
Los Angeles, CA 90089-0741

Prof. Shelton Alexander
Geosciences Department
403 Deike Building
The Pennsylvania State University
University Park, PA 16802

Dr. Ralph Alewine, III
DARPA/NMRO
3701 North Fairfax Drive
Arlington, VA 22203-1714

Prof. Charles B. Archambeau
CIRES
University of Colorado
Boulder, CO 80309

Dr. Thomas C. Bache, Jr.
Science Applications Int'l Corp.
10260 Campus Point Drive
San Diego, CA 92121 (2 copies)

Prof. Muawia Barazangi
Institute for the Study of the Continent
Cornell University
Ithaca, NY 14853

Dr. Jeff Barker
Department of Geological Sciences
State University of New York
at Binghamton
Vestal, NY 13901

Dr. Douglas R. Baumgardt
ENSCO, Inc
5400 Port Royal Road
Springfield, VA 22151-2388

Dr. Susan Beck
Department of Geosciences
Building #77
University of Arizona
Tucson, AZ 85721

Dr. T.J. Bennett
S-CUBED
A Division of Maxwell Laboratories
11800 Sunrise Valley Drive, Suite 1212
Reston, VA 22091

Dr. Robert Blandford
AFTAC/TT, Center for Seismic Studies
1300 North 17th Street
Suite 1450
Arlington, VA 22209-2308

Dr. G.A. Bollinger
Department of Geological Sciences
Virginia Polytechnical Institute
21044 Derring Hall
Blacksburg, VA 24061

Dr. Stephen Bratt
Center for Seismic Studies
1300 North 17th Street
Suite 1450
Arlington, VA 22209-2308

Dr. Lawrence Burdick
Woodward-Clyde Consultants
566 El Dorado Street
Pasadena, CA 91109-3245

Dr. Robert Burrige
Schlumberger-Doll Research Center
Old Quarry Road
Ridgefield, CT 06877

Dr. Jerry Carter
Center for Seismic Studies
1300 North 17th Street
Suite 1450
Arlington, VA 22209-2308

Dr. Eric Chael
Division 9241
Sandia Laboratory
Albuquerque, NM 87185

Prof. Vernon F. Cormier
Department of Geology & Geophysics
U-45, Room 207
University of Connecticut
Storrs, CT 06268

Prof. Steven Day
Department of Geological Sciences
San Diego State University
San Diego, CA 92182

Marvin Denny
U.S. Department of Energy
Office of Arms Control
Washington, DC 20585

Dr. Zoltan Der
ENSCO, Inc.
5400 Port Royal Road
Springfield, VA 22151-2388

Prof. Adam Dziewonski
Hoffman Laboratory, Harvard University
Dept. of Earth Atmos. & Planetary Sciences
20 Oxford Street
Cambridge, MA 02138

Prof. John Ebel
Department of Geology & Geophysics
Boston College
Chestnut Hill, MA 02167

Eric Fielding
SNEE Hall
INSTOC
Cornell University
Ithaca, NY 14853

Dr. Mark D. Fisk
Mission Research Corporation
735 State Street
P.O. Drawer 719
Santa Barbara, CA 93102

Prof Stanley Flatte
Applied Sciences Building
University of California, Santa Cruz
Santa Cruz, CA 95064

Dr. John Foley
NER-Geo Sciences
1100 Crown Colony Drive
Quincy, MA 02169

Prof. Donald Forsyth
Department of Geological Sciences
Brown University
Providence, RI 02912

Dr. Art Frankel
U.S. Geological Survey
922 National Center
Reston, VA 22092

Dr. Cliff Frolich
Institute of Geophysics
8701 North Mopac
Austin, TX 78759

Dr. Holly Given
IGPP, A-025
Scripps Institute of Oceanography
University of California, San Diego
La Jolla, CA 92093

Dr. Jeffrey W. Given
SAIC
10260 Campus Point Drive
San Diego, CA 92121

Dr. Dale Glover
Defense Intelligence Agency
ATTN: ODT-1B
Washington, DC 20301

Dr. Indra Gupta
Teledyne Geotech
314 Montgomery Street
Alexandria, VA 22314

Dan N. Hagedorn
Pacific Northwest Laboratories
Battelle Boulevard
Richland, WA 99352

Dr. James Hannon
Lawrence Livermore National Laboratory
P.O. Box 808
L-205
Livermore, CA 94550

Dr. Roger Hansen
HQ AFTAC/TTR
Patrick AFB, FL 32925-6001

Prof. David G. Harkrider
Seismological Laboratory
Division of Geological & Planetary Sciences
California Institute of Technology
Pasadena, CA 91125

Prof. Danny Harvey
CIRES
University of Colorado
Boulder, CO 80309

Prof. Donald V. Helmberger
Seismological Laboratory
Division of Geological & Planetary Sciences
California Institute of Technology
Pasadena, CA 91125

Prof. Eugene Herrin
Institute for the Study of Earth and Man
Geophysical Laboratory
Southern Methodist University
Dallas, TX 75275

Prof. Robert B. Herrmann
Department of Earth & Atmospheric Sciences
St. Louis University
St. Louis, MO 63156

Prof. Lane R. Johnson
Seismographic Station
University of California
Berkeley, CA 94720

Prof. Thomas H. Jordan
Department of Earth, Atmospheric &
Planetary Sciences
Massachusetts Institute of Technology
Cambridge, MA 02139

Prof. Alan Kafka
Department of Geology & Geophysics
Boston College
Chestnut Hill, MA 02167

Robert C. Kemerait
ENSCO, Inc.
445 Pineda Court
Melbourne, FL 32940

Dr. Max Koontz
U.S. Dept. of Energy/DP 5
Forrestal Building
1000 Independence Avenue
Washington, DC 20585

Dr. Richard LaCoss
MIT Lincoln Laboratory, M-200B
P.O. Box 73
Lexington, MA 02173-0073

Dr. Fred K. Lamb
University of Illinois at Urbana-Champaign
Department of Physics
1110 West Green Street
Urbana, IL 61801

Prof. Charles A. Langston
Geosciences Department
403 Deike Building
The Pennsylvania State University
University Park, PA 16802

Jim Lawson, Chief Geophysicist
Oklahoma Geological Survey
Oklahoma Geophysical Observatory
P.O. Box 8
Leonard, OK 74043-0008

Prof. Thorne Lay
Institute of Tectonics
Earth Science Board
University of California, Santa Cruz
Santa Cruz, CA 95064

Dr. William Leith
U.S. Geological Survey
Mail Stop 928
Reston, VA 22092

Mr. James F. Lewkowicz
Phillips Laboratory/GPEH
Hanscom AFB, MA 01731-5000(2 copies)

Mr. Alfred Lieberman
ACDA/VI-OA State Department Building
Room 5726
320-21st Street, NW
Washington, DC 20451

Prof. L. Timothy Long
School of Geophysical Sciences
Georgia Institute of Technology
Atlanta, GA 30332

Dr. Randolph Martin, III
New England Research, Inc.
76 Olcott Drive
White River Junction, VT 05001

Dr. Robert Masse
Denver Federal Building
Box 25046, Mail Stop 967
Denver, CO 80225

Dr. Gary McCartor
Department of Physics
Southern Methodist University
Dallas, TX 75275

Prof. Thomas V. McEvilly
Seismographic Station
University of California
Berkeley, CA 94720

Dr. Art McGarr
U.S. Geological Survey
Mail Stop 977
U.S. Geological Survey
Menlo Park, CA 94025

Dr. Keith L. McLaughlin
S-CUBED
A Division of Maxwell Laboratory
P.O. Box 1620
La Jolla, CA 92038-1620

Stephen Miller & Dr. Alexander Florence
SRI International
333 Ravenswood Avenue
Box AF 116
Menlo Park, CA 94025-3493

Prof. Bernard Minster
IGPP, A-025
Scripps Institute of Oceanography
University of California, San Diego
La Jolla, CA 92093

Prof. Brian J. Mitchell
Department of Earth & Atmospheric Sciences
St. Louis University
St. Louis, MO 63156

Mr. Jack Murphy
S-CUBED
A Division of Maxwell Laboratory
11800 Sunrise Valley Drive, Suite 1212
Reston, VA 22091 (2 Copies)

Dr. Keith K. Nakanishi
Lawrence Livermore National Laboratory
L-025
P.O. Box 808
Livermore, CA 94550

Dr. Carl Newton
Los Alamos National Laboratory
P.O. Box 1663
Mail Stop C335, Group ESS-3
Los Alamos, NM 87545

Dr. Bao Nguyen
HQ AFTAC/TTR
Patrick AFB, FL 32925-6001

Prof. John A. Orcutt
IGPP, A-025
Scripps Institute of Oceanography
University of California, San Diego
La Jolla, CA 92093

Prof. Jeffrey Park
Kline Geology Laboratory
P.O. Box 6666
New Haven, CT 06511-8130

Dr. Howard Patton
Lawrence Livermore National Laboratory
L-025
P.O. Box 808
Livermore, CA 94550

Dr. Frank Pilotte
HQ AFTAC/TT
Patrick AFB, FL 32925-6001

Dr. Jay J. Pulli
Radix Systems, Inc.
2 Taft Court, Suite 203
Rockville, MD 20850

Dr. Robert Reinke
ATTN: FCTVTD
Field Command
Defense Nuclear Agency
Kirtland AFB, NM 87115

Prof. Paul G. Richards
Lamont-Doherty Geological Observatory
of Columbia University
Palisades, NY 10964

Mr. Wilmer Rivers
Teledyne Geotech
314 Montgomery Street
Alexandria, VA 22314

Dr. George Rothe
HQ AFTAC/TTR
Patrick AFB, FL 32925-6001

Dr. Alan S. Ryall, Jr.
DARPA/NMRO
3701 North Fairfax Drive
Arlington, VA 22209-1714

Dr. Richard Sailor
TASC, Inc.
55 Walkers Brook Drive
Reading, MA 01867

Prof. Charles G. Sammis
Center for Earth Sciences
University of Southern California
University Park
Los Angeles, CA 90089-0741

Prof. Christopher H. Scholz
Lamont-Doherty Geological Observatory
of Columbia University
Palisades, CA 10964

Dr. Susan Schwartz
Institute of Tectonics
1156 High Street
Santa Cruz, CA 95064

Secretary of the Air Force
(SAFRD)
Washington, DC 20330

Office of the Secretary of Defense
DDR&E
Washington, DC 20330

Thomas J. Sereno, Jr.
Science Application Int'l Corp.
10260 Campus Point Drive
San Diego, CA 92121

Dr. Michael Shore
Defense Nuclear Agency/SPSS
6801 Telegraph Road
Alexandria, VA 22310

Dr. Matthew Sibol
Virginia Tech
Seismological Observatory
4044 Derring Hall
Blacksburg, VA 24061-0420

Prof. David G. Simpson
IRIS, Inc.
1616 North Fort Myer Drive
Suite 1440
Arlington, VA 22209

Donald L. Springer
Lawrence Livermore National Laboratory
L-025
P.O. Box 808
Livermore, CA 94550

Dr. Jeffrey Stevens
S-CUBED
A Division of Maxwell Laboratory
P.O. Box 1620
La Jolla, CA 92038-1620

Lt. Col. Jim Stobie
ATTN: AFOSR/NL
Bolling AFB
Washington, DC 20332-6448

Prof. Brian Stump
Institute for the Study of Earth & Man
Geophysical Laboratory
Southern Methodist University
Dallas, TX 75275

Prof. Jeremiah Sullivan
University of Illinois at Urbana-Champaign
Department of Physics
1110 West Green Street
Urbana, IL 61801

Prof. L. Sykes
Lamont-Doherty Geological Observatory
of Columbia University
Palisades, NY 10964

Dr. David Taylor
ENSCO, Inc.
445 Pineda Court
Melbourne, FL 32940

Dr. Steven R. Taylor
Los Alamos National Laboratory
P.O. Box 1663
Mail Stop C335
Los Alamos, NM 87545

Prof. Clifford Thurber
University of Wisconsin-Madison
Department of Geology & Geophysics
1215 West Dayton Street
Madison, WS 53706

Prof. M. Nafi Toksoz
Earth Resources Lab
Massachusetts Institute of Technology
42 Carleton Street
Cambridge, MA 02142

Dr. Larry Turnbull
CIA-OSWR/NED
Washington, DC 20505

DARPA/RMO/SECURITY OFFICE
3701 North Fairfax Drive
Arlington, VA 22203-1714

Dr. Gregory van der Vink
IRIS, Inc.
1616 North Fort Myer Drive
Suite 1440
Arlington, VA 22209

HQ DNA
ATTN: Technical Library
Washington, DC 20305

Dr. Karl Veith
EG&G
5211 Auth Road
Suite 240
Suitland, MD 20746

Defense Intelligence Agency
Directorate for Scientific & Technical Intelligence
ATTN: DTIB
Washington, DC 20340-6158

Prof. Terry C. Wallace
Department of Geosciences
Building #77
University of Arizona
Tuscon, AZ 85721

Defense Technical Information Center
Cameron Station
Alexandria, VA 22314 (2 Copies)

Dr. Thomas Weaver
Los Alamos National Laboratory
P.O. Box 1663
Mail Stop C335
Los Alamos, NM 87545

TACTEC
Battelle Memorial Institute
505 King Avenue
Columbus, OH 43201 (Final Report)

Dr. William Wortman
Mission Research Corporation
8560 Cinderbed Road
Suite 700
Newington, VA 22122

Phillips Laboratory
ATTN: XPG
Hanscom AFB, MA 01731-5000

Prof. Francis T. Wu
Department of Geological Sciences
State University of New York
at Binghamton
Vestal, NY 13901

Phillips Laboratory
ATTN: GPE
Hanscom AFB, MA 01731-5000

AFTAC/CA
(STINFO)
Patrick AFB, FL 32925-6001

Phillips Laboratory
ATTN: TSML
Hanscom AFB, MA 01731-5000

DARPA/PM
3701 North Fairfax Drive
Arlington, VA 22203-1714

Phillips Laboratory
ATTN: SUL
Kirtland, NM 87117 (2 copies)

DARPA/RMO/RETRIEVAL
3701 North Fairfax Drive
Arlington, VA 22203-1714

Dr. Michel Bouchon
I.R.I.G.M.-B.P. 68
38402 St. Martin D'Heres
Cedex, FRANCE

Dr. Michel Campillo
Observatoire de Grenoble
I.R.I.G.M.-B.P. 53
38041 Grenoble, FRANCE

Dr. Jorg Schlittenhardt
Federal Institute for Geosciences & Nat'l Res.
Postfach 510153
D-3000 Hannover 51, GERMANY

Dr. Kin Yip Chun
Geophysics Division
Physics Department
University of Toronto
Ontario, CANADA

Dr. Johannes Schweitzer
Institute of Geophysics
Ruhr University/Bochum
P.O. Box 1102148
4360 Bochum 1, GERMANY

Prof. Hans-Peter Harjes
Institute for Geophysics
Ruhr University/Bochum
P.O. Box 102148
4630 Bochum 1, GERMANY

Prof. Eystein Husebye
NTNF/NORSAR
P.O. Box 51
N-2007 Kjeller, NORWAY

David Jepsen
Acting Head, Nuclear Monitoring Section
Bureau of Mineral Resources
Geology and Geophysics
G.P.O. Box 378, Canberra, AUSTRALIA

Ms. Eva Johannisson
Senior Research Officer
National Defense Research Inst.
P.O. Box 27322
S-102 54 Stockholm, SWEDEN

Dr. Peter Marshall
Procurement Executive
Ministry of Defense
Blacknest, Brimpton
Reading FG7-FRS, UNITED KINGDOM

Dr. Bernard Masseron, Dr. Pierre Mechler
Societe Radioman
27 rue Claude Bernard
75005 Paris, FRANCE (2 Copies)

Dr. Svein Mykkeltveit
NTNF/NORSAR
P.O. Box 51
N-2007 Kjeller, NORWAY (3 Copies)

Prof. Keith Priestley
University of Cambridge
Bullard Labs, Dept. of Earth Sciences
Madingley Rise, Madingley Road
Cambridge CB3 0EZ, ENGLAND